Maynooth University
National University of Ireland Maynooth

An Assessment of Radiative, Energy and Carbon Dioxide Fluxes over Three Urban Locations in Dublin

Stephanie Keogh B.A, M.Sc

A Thesis submitted for the Degree of Doctor of Philosophy

Irish Climate Analysis and Research Units,
Department of Geography,
Maynooth University, National University of Ireland

August 2015

Head of Department:

Dr Jan Rigby

Research Supervisors:

Dr Rowan Fealy and Dr Gerald Mills

ABSTRACT

The urban form and function varies across and within cities serving to alter surface-atmosphere exchanges of radiation, turbulent heat and carbon dioxide. To date very few measurements of these exchanges are undertaken in the urban domain despite the growing number of urban dwellers worldwide. This thesis presents the first attempt at investigating these exchanges over an urban surface in Ireland. Radiometer and eddy covariance observations are examined for Dublin at 3 distinctive urban locations (suburban, urban, and urban-compact). The observational period (maximum 33 months) allowed for the investigation of both diurnal and seasonal trends of the turbulent sensible heat (Q_H), latent heat (Q_E) and carbon dioxide (F_C) fluxes.

Net radiation (Q*) was 7.5 and 10% greater in summer and winter at the suburban location when compared to an urban location. Q* was preferentially channelled into the Q_H in summer and the Q_E in winter at the suburban location while Q_H dominates in all seasons at the urban locations. In summer median Q_H is greater at the urban location (+38 W m^{-2}) while median Q_E is greater at the suburban location (+30 W m^{-2}). The storage heat flux (ΔQ_S) was reported as a significant component of the surface energy budget at all locations and is estimated using the Objective Hysteresis Model (OHM). The occurrence of unstable atmospheric conditions increased with increasing built and impervious surface cover fraction however neutral stratification was dominant.

Temporal analysis of the CO_2 flux indicates photosynthetic uptake in spring, summer and autumn at the well-vegetated suburban location, however the area is a net source of CO_2 annually (1.67 kg C m^{-2} $year^{-1}$). Temporal and directional analysis of the CO_2 flux at an urban location indicates significant contributions from traffic and the emissions are double than the suburban location on an annual basis (3.47 kg C m^{-2} $year^{-1}$). Inter-site differences in the mean daily release of carbon are greatest in the summer; the urban location reports values 5 times greater than those reported for the suburban location indicating the role of vegetation in modulating F_C (1.4 versus 7.1 g C m^{-2} day^{-1}).

ACKNOWLEDGEMENTS

It is a pleasure to thank all those who have made this thesis possible. I am incredibly grateful to my research supervisors, Dr Rowan Fealy and Dr Gerald Mills. This thesis would not have been possible without their expertise, direction and clarity of thought. They have bestowed upon me such wonderful opportunities to travel, learn, train, and to grow as a researcher. These experiences have most definitely benefitted the final thesis and broadened my horizons.

I am particularly grateful to the Maynooth University and the John and Pat Hume Scholarship which part-funded the thesis research and the Higher Education Authority (HEA) who funded the instrumentation. I would also like to sincerely thank colleagues in Maynooth University and University College Dublin, in particular Dr Priscilla Mooney, Catriona Duffy, Ciarán Pollard, Shaun Harrigan, Paul Alexander and Dr Tine Ningal. Each of you have so graciously shared your time, skills and wisdom with me throughout the thesis; I am deeply grateful to you all. I would like to say a special thanks to all of my other colleagues within ICARUS and the Department of Geography, it has been a supportive, collaborative and most of all entertaining work environment and I am very fortunate to have spent four years in your company. There are a number of international researchers and friends I would like to sincerely thank, without whom this thesis would not have been possible; Dr Simone Kotthaus , Dr Annika Nordbo, Olli Peltola, and Dr Matthias Mauder all of whom who shared valuable data, insights, skills and direction.

For their unyielding willingness to help me maintain the observation sites I would like to thank three key groups 1) the staff and pupils of St Pius X Girls National School, in particular the principal Miriam Marron, the secretary, Natasha Ryan and the caretaker Paul Lynott, 2) the Dublin City Council staff in Marrowbone Lane, in particular Brian McManus and 3) the staff of Dublin Institute of Technology, Kevin Street, in particular my lovely colleague Dr Keith Sunderland – not forgetting the vital support of Rowan, Gerald and Paul in this regard!

To my parents, Mel and Brian, I cannot thank you enough for the endless care, encouragement and love you have given me throughout my life – I could not ask for better parents. You both love life and exude such wonderful positivity that ultimately got me over the thesis finish line.

To my siblings Robert, Lesley Ann, Nicola and Rebecca, and to all of my wonderful friends – thank you for your friendship and for the belief you instilled in me to achieve my PhD. Most importantly thank you for getting me away from the desk when I needed a break, dance or a drink!

To the world's most wonderful husband, James – where do I begin? You have been truly amazing throughout ALL of my academic pursuits. You have shown me unyielding support (financial and emotional!), encouragement, and love - I will endeavour to do the same each and every day of our marriage. I love you with all my heart.

Stephanie

CONTENTS

List of Figures.....viii

List of Tables.....xv

List of Equations.....xvi

CHAPTER 1 INTRODUCTION.....1

1.1 RESEARCH BACKGROUND.....1

1.2 THE EDDY COVARIANCE MEASUREMENT TECHNIQUE.....5

1.3 RESEARCH AIMS AND OBJECTIVES.....7

1.4 THESIS OUTLINE.....8

CHAPTER 2 SCALE AND CONCEPTS USING EDDY COVARIANCE 11

2.1 ATMOSPHERIC BOUNDARY LAYER STRUCTURE AND DEPTH.....11

2.2 AIRFLOW IN THE ATMOSPHERIC BOUNDARY LAYER.....14

2.3 TURBULENT FLUXES AND THEIR DERIVATION.....19

2.4 THE SURFACE ENERGY BALANCE.....23

2.5 THE RADIATION BUDGET.....23

2.6 SURFACE HEAT FLUXES.....26

2.7 MEASUREMENT SOURCE AREAS.....28

2.7.1 The radiation source area.....28

2.7.2 The turbulent flux footprint.....29

2.8 ENERGY BALANCE CLOSURE.....31

2.9 DISCUSSION.....32

CHAPTER 3 LITERATURE REVIEW.....34

3.1 THE ATMOSPHERIC BOUNDARY LAYER OVER URBAN SURFACES.....35

3.1.1 Vertical scales of the UBL.....35

3.1.2 Airflow within the UBL.....37

3.1.3 Turbulence characteristics in the UBL.....43

3.2 IMPLEMENTING A CONCEPTUAL FRAMEWORK FOR URBAN BASED OBSERVATIONAL STUDIES.....44

3.3 THE RADIATION BUDGET OF THE URBAN SURFACE.....46

3.3.1 Urban geometry and its effects on the radiation budget.....47

3.3.2 Albedo and reflected shortwave radiation in urban areas.....48

3.3.3 Incoming shortwave radiation in urban areas.....51

3.3.4 Incoming and outgoing longwave radiation in urban areas.....53

3.3.5 Net all-wave radiation in urban areas.....55

3.4 THE ENERGY BUDGET OF THE URBAN SURFACE.....57

3.4.1 Diurnal trends in the turbulent fluxes of latent and sensible heat.....60

3.4.2 The Bowen ratio.....61

3.4.3 Seasonal trends in Q and the turbulent heat fluxes.....63*

3.5 MEASUREMENT SOURCES AREAS IN THE URBAN DOMAIN 64
3.5.1 Radiation and flux source areas *66*
3.6 THE STORAGE HEAT FLUX 69
3.6.1 Methods to estimate the storage heat flux: Residual of the SEB *69*
3.6.2 Methods to estimate the storage heat flux: Modelling techniques *70*
3.7 THE ANTHROPOGENIC HEAT FLUX 72
3.8 THE CO_2 FLUX IN URBAN DOMAIN 75
3.8.1 The temporal variability of the CO_2 flux *76*
3.9 DISCUSSION 80

CHAPTER 4 METHODOLOGY 83

4.1 INSTRUMENTS 84
4.1.1 Sonic anemometers (CSAT3 and WindMaster Pro) *85*
4.1.2 Open-path infrared gas analyser (Li7500) *87*
4.1.3 Enclosed-path infrared gas analyser (Li7200) *89*
4.1.4 Auxiliary meteorological instruments (NR01, HMP45C, FW, SK215, ARG100) *91*
4.2 DATA PROCESSING 96
4.2.1 Despiking the raw 10 Hz dataset *96*
4.2.2 Coordinate rotation *97*
4.2.3 Correction for time lags *99*
4.2.4 Detrending *100*
4.2.5 Ogive analysis *100*
4.3 EC CORRECTIONS 102
4.3.1 Spectral corrections *102*
4.3.2 Sonic corrections *105*
4.3.3 Open-path IRGA surface heating correction *107*
4.3.4 WPL correction *107*
4.4 SOFTWARE COMPARISON 109
4.5 DATA PROCESSING FOR DUBLIN EDDY COVARIANCE SITES 116
4.6 DATA QUALITY FLAGGING 118
4.7 POST-PROCESSING AND DATA QUALITY CONTROL 120
4.8 SURFACE ROUGHNESS AND FLUX FOOTPRINT CALCULATIONS 121
4.9 DISCUSSION 122

CHAPTER 5 SURFACE COVER AND ROUGHNESS PROPERTIES 125

5.1 SUBURBAN SITE – ST PIUS X 126
5.1.1 Site surrounds and surface cover of the suburban site *127*
5.1.2 Surface roughness properties of the suburban site *133*
5.2 URBAN SITE 1 – MARROWBONE LANE 136
5.2.1 Site surrounds and surface properties of urban site 1 ..... *139*
5.2.2 Surface roughness properties of urban site 1 ..... *143*

5.3 URBAN SITE 2 – KEVIN STREET 146
5.3.1 Site surrounds and surface properties of urban site 2 ..... *148*
5.3.2 Surface roughness properties of urban site 2 ..... *151*
5.4 DISCUSSION OF THE SITE CHARACTERISTICS 153

CHAPTER 6 RESULTS 158

6.1 RAW DATA AVAILABILITY FOR PROCESSING 158
6.2 METEOROLOGICAL CONDITIONS FOR THE THREE YEAR OBSERVATION PERIOD 159
6.3 THE RADIATION BALANCE 165
6.3.1 Suburban site radiation measurements *165*
6.4 INTER-SITE COMPARISON OF THE RADIATION BALANCE 175
6.5 TURBULENT FLUXES: DATA AVAILABILITY, DATA GAPS AND QUALITY FLAGS 180
6.6 ATMOSPHERIC STABILITY 183
6.7 TURBULENT FLUX FOOTPRINT 187
6.8 TURBULENCE, SURFACE DRAG AND FLOW DISTORTION 192
6.9 THE SURFACE ENERGY BUDGET 196
6.9.1 The storage heat flux coefficients *196*
6.9.2 The surface energy budget: temporal trends *198*
6.9.3 Inter-site comparison of turbulent heat fluxes *204*
6.9.4 The turbulent heat fluxes: spatial and directional variability *206*
6.9.5 Energy partitioning and energy balance closure *209*
6.9.6 The anthropogenic heat flux *213*
6.10 THE CO_2 FLUX 215
6.10.1 The temporal variability of F_C *215*
6.10.2 The spatial variability of F_C *220*
6.11 SUMMARY OF THE RESULTS 224

CHAPTER 7 DISCUSSION AND CONCLUSIONS 227

7.1 DISCUSSION OF THESIS FINDINGS 227
7.1.1 Radiation budget *227*
7.1.1 Turbulent flux footprint *231*
7.1.2 Turbulent heat fluxes *232*
7.1.3 The energy balance ratio and the storage heat flux *238*
7.1.4 The CO_2 flux *239*
7.1.5 Fulfilment of eddy covariance assumptions *243*
7.2 OBSERVATIONAL AND METHODOLOGICAL CONSIDERATIONS 245
7.3 RESEARCH IMPLICATIONS 250
7.4 FINAL CONCLUSIONS 252

Bibliography 254

Appendix I.....I

Appendix II.....II

List of Figures

Figure 1.1 Percentage of urban population per country and location of urban agglomerations with at least 500,000 inhabitants, 2014 (United Nations, 2014). 3

Figure 1.2 Global gridded carbon dioxide emissions representing multiyear (1997-2010) data at a spatial resolution of 0.1° (Asefi-Najafabady et al., 2014). 4

Figure 2.1 Daily cycle of the atmospheric boundary layer structure (EZ: Entrainment zone) (Modified from Stull, 1988 in Foken, 2008a). 13

Figure 2.2 Wind speed spectrum near the ground estimated from a study of Van der Hoven (1957) 16

Figure 2.3 Schematic of the TKE spectrum in the atmospheric boundary layer, where E(k) is the scalar energy spectrum illustrating three regions of energy production (A), energy dissipation (C) and the inertial subrange (B) where energy is neither produced or dissipated (Kaimal and Finnigan,1994). 16

Figure 2.4 Example of an EC measurement tower and a Cartesian coordinate system superimposed onto a horizontally homogeneous surface to represent the control volume of interest (Finnigan et al. 2003). 19

Figure 2.5 A conceptual diagram representing 50 and 90% source area footprints for a) downward facing radiation instruments and b) eddy covariance instrumentation. The coloured shadows represent the source areas of the radiation sensor (red) and eddy covariance instruments (orange) (Modified from Oke, 2004). 29

Figure 2.6 Crosswind-integrated footprint for flux measurements of four different cases of stability (strongly convective, forced convective, neutral and stable conditions; measurement height is 50metres, roughness length, z_0, is 0.05 m) obtained by Lagrangian simulation according to Kljun et al. (2002) (Rannik et al., 2012). 31

Figure 3.1 Schematic structure of the ABL, referred to here as the Planetary Boundary Layer (PBL), illustrating the climate scales and vertical sublayers found in urban areas (Oke, 2007). 36

Figure 3.2 The logarithmic wind velocity profile over a dense urban surface , illustrating mean wind speed ū, the height above ground (z), the zero plane displacement height (z_d), the aerodynamic roughness length (z_0), the mean height of the roughness elements (z_H) and the blending height (z_r) (Oke 2007). 38

Figure 3.3 Flow pattern around a sharp-edged building, side view of a) streamlines and flow zones (see text for description of A-D) and b) plan view of streamlines with building oriented normal to the flow (Modified from Oke, 1987:265). 39

Figure 3.4 The flow regimes associated with air flow over building arrays of differing height/width ratios, a) isolated flow regime over low density surface, b) wake interference flow over a medium density surface and c) skimming flow regime over a high density urban surface. Modified from Oke (1988a:105). 40

Figure 3.3.5 Deriving the plan area and frontal area densities using building dimensions of an urban array (Grimmond and Oke, 1999a:1263). 41

Figure 3.6 Local climate zone classification system (Stewart and Oke, 2012). 46

Figure 3.7 A depiction of the sky view factor at the ground surface in a symmetrical street canyon, described by its width (W) and its height (H), ψ Sky is the SVF (Source: www.urban-climate.org). 47

Figure 3.8 Diurnal summer cycles of net radiation (Q*), sensible heat flux (Q_H) and the storage heat flux change (ΔQ_S) for (a) 1-storey (H = 0.2m) and (b) 2-storey arrays. (Source: Pearlmutter et al., 2005). 48

Figure 3.9 (a) Net radiation Q∗ and albedo during a clear winter day with a 20 cm snow cover. Solid lines are measurements over the urban surface (U1); dashed–dotted lines are simultaneously measured rural values (R3). (b) Urban–rural differences in air temperature (ΔT U–R) and absolute humidity (Δa U–R). Temperature and humidity values are an average of U1 and U2 (urban) and R1, R2 and R3 (rural) over the summertime IOP from 10 June to 10 July 2002. Solid lines are measurements over the urban surface (U1); dashed–dotted lines are simultaneously measured rural values (R3). Roof-level temperatures (K) are measured 5 m above z_H; street-level temperatures are from instruments operated inside street canyons at U1 and U2 (2–3 m above ground) (Christen and Vogt, 2004:1406). 50

Figure 3.10 Ensemble hourly averaged radiation flux densities measured over a 40-day period in a Miami suburb in 1995 (Day of year 133-172) in a) cloudless and b) all-sky conditions according to local apparent time (LAT) (Newton et al., 2007). 52

Figure 3.11 Observations of the CNR1 net radiometer (after quality control) at KSK (10/2008–09/2009) and KSS (10/2009–03/2012): net all-wave radiation Q* is the sum of incoming (↓) and outgoing (↑) long-

(L) and short-wave (K) radiation, averages: 15 min(coloured dots), daily (K: daytime, L & Q*: 24 h, black dots) and monthly (white diamonds). Data gap in October 2009 due to instrument maintenance (Kotthaus and Grimmond, 2014a). 53

Figure 3.12 Radiation and clover cover observations from KSK and KSS London, (a) Incoming long-wave radiation according to the fraction of cloud cover, (b) outgoing long-wave radiation normalised by the value observed at sunset: sunset fraction SSF, and (c) the ratio of outgoing and incoming long-wave radiation, also considered to be the night time radiation balance (Kotthaus and Grimmond, 2014a). 55

Figure 3.13 Conceptual representation of the urban (a) energy balance for a balancing volume that reaches from the depth where no exchange with the subsurface is found (zb) to the measurement height on a tower above the urban ecosystem (zt). The terms of the energy balance are Q*: net all-wave radiation, Q_F : anthropogenic heat flux density (electricity, fuel combustion, human metabolism), Q_H : sensible heat flux density, Q_E : latent heat flux density, ΔQ_S : storage heat flux density (ground, buildings, air) (Grimmond and Christen, 2012, modified from Feigenwinter et al., 2012). 60

Figure 3.14 a) Mean Bowen ratio (β) which shows dependency on the number of days after a precipitation event (p), classified as p> 0.1 mm d^{-1} for an urban and suburban location in Oberhausen, Germany (Goldbach and Kuttler, 2013). b) illustrates the frequency distribution (frequency f[%]) of β by the time since last rainfall (hours [h]) for a dense city centre location in London. The solid line represents the median β by time since last rainfall, only β<15 and times up to 48 h after rainfall are shown (Kotthaus and Grimmond, 2014a). 62

Figure 3.15 Daytime Bowen ratio (30min) coloured by number of days since rainfall (exceeding 3 mm) for the study period. Daily rainfall (bars) corresponds to the right-hand axes. Monthly median midday (±2h) (open squares), monthly median daytime (solid squares) and monthly median nighttime (when Q*<0 and K↓<5 W m^{-2})(crosses) Bowen ratios are plotted mid-month (Ward et al., 2013). 63

Figure 3.16 Isoflux diagrams of the daily (x-axis) and annual (y-axis) variations of the radiation balance (Q*), turbulent sensible heat flux density (Q_H) and turbulent latent heat flux (Q_E) at the urban site (URB) and suburban site (SUB) for Oberhausen, Germany. Note the difference in parameter scale (Goldbach and Kuttler, 2013). 64

Figure 3.17 Frequencies of different stability classes for nighttime cases (Hours 22-04) measured simultaneously at five EC sites in Basel, Switzerland between 10 June and 10 July, 2002 (Christen and Vogt, 2004). 66

Figure 3.18 a) An aerial photograph of the measurement location, SMEAR III located 5 km north-east of Helsinki city centre. The topography of the measurement site, relative to sea level, is denoted by blue contour lines. The green contour lines show the particle number flux footprint function when the wind direction is perpendicular to the main road, when the geostrophic windspeed is 10 m s^{-1} and the boundary layer is neutrally stratified. The measurement location is marked by the green star. b) is the footprint function, under the same conditions, as estimated with the analytical model of Horst and Weil (1994; dashed line) and the numerical model (solid line) (Järvi et al., 2009b). 68

Figure 3.19 Median diurnal cycles (lines) and inter-quartile ranges (shading) of the energy fluxes for each month from May 2011 to April 2012. a) represents the storage heat flux estimated using the OHM method (turquoise line) and the energy balance residual (RES)(grey line). b) is the ground heat flux derived from soil heat flux plate measurements from the Swindon measurement site (Modified from Ward et al., 2013). 72

Figure 3.20 Land cover fractions for 30 degree wind sectors within a radius of 500 m around the flux mast in Swindon, UK (Ward et al., 2013). 72

Figure 3.21 The diurnal profile of the anthropogenic heat flux for 6 American cities for summer and winter time, estimated using a top-down, population-based inventory approach (Sailor and Lu, 2004). Note the difference in magnitude on the y-axis. 75

Figure 3.22 The terms of the urban CO_2 budget are - F_C: Net mass-flux of CO_2 between urban surface and atmosphere, ΔS :concentration change of CO_2 in the measurement volume, C: CO_2 emitted by combustion, Re: CO_2 emitted by urban ecosystem respiration (soil, plants, humans), P: CO_2 taken up by photosynthesis of urban vegetation (Grimmond and Christen, 2012, modified from Feigenwinter et al., 2012). 76

Figure 3.23 a)The average diurnal course of CO_2 fluxes for Basel where measurements are recorded within the urban canyon (14.7 m) and above the urban canyon (31 m) (Source: Vogt et al., 2006). b) Mean values of CO_2 fluxes measured in Łódź, Poland from July 2006 to August 2008 calculated for days

of week illustrating a clear reduction in the flux magnitude for Saturday and Sunday (Pawlak et al., 2011). 77

Figure 3.24 Summertime CO_2 fluxes measured in different urban ecosystems as a function of urban density (expressed as plan area fraction of buildings). The text associated with each symbol indicates the city, the year of observations and sometimes the site within the city. Two sites are split-up into ensemble averages for different wind sectors: Es07[p] is a sector containing a large urban park, while Es07[u] is the urban sector of this site. Va08s[r] is a residential sector with only local roads, whereas Va08s[a] is data from all wind sectors that contains busy arterial roads (Modified from Grimmond and Christen, 2012). . 79

Figure 3.25 Carbon fluxes by time of day and time of year for a highly vegetated suburban ecosystem in Baltimore, USA (see Crawford et al., 2011) and a dense urban area in central Basel, Switzerland (based on data from Vogt et al., 2009) (Grimmond and Christen, 2012). 80

Figure 4.1Map of the island of Ireland with the location of the three eddy covariance sites in County Dublin, urban site 1 and 2 refer to Marrowbone Lane and Kevin Street stations respectively. The county of Dublin is divided into four local authorities (see boundary lines of inset figure), urban site 1 and 2 are located in Dublin City while the suburban site is located in South Dublin. 84

Figure 4.2 The C-clamp design of the Campbell Scientific CSAT3 sonic anemometer illustrating the coordinate system with path length of 10 cm for each of the 3 pairs of transducers. Source: Campbell Scientific, 2010. 86

Figure 4.3 a) The Gill Wind Master Pro sonic anemometer illustrating the instrument dimensions and the three onmi-directional support spars, b) is a top view of the three transducers and their relative position to the support spars. Source: Gill Instruments, Lymington, UK. 87

Figure 4.4 a) Schematic representation of the Li7500 open-path infrared gas analyser, and b) a schematic representing the four individual filter windows of the chopper filter wheel and their respective light absorption bands. Source: Burba, 2013. 88

Figure 4.5 Enclosed-path gas analyser illustrating in a) the infrared beam transfer through the sample cell and b) the optical bench of the Li7200 that can be removed for instrument cleaning. Source: Licor.com 90

Figure 4.6 a) Li7200 deployed at urban site 2 illustrating the white insulated inlet tubing and the outlet tubing from the optical bench and b) the inlet filter and insulated inlet tubing. 91

Figure 4.7 Schematic representation of the NR01 net radiometer. 1) skyward facing pyranometer, 2) skyward pyrgeometer, 3) radiation shield, 4) levelling assembly, 5) levelling assembly, 6) location of the instrument temperature sensor (Pt100), 7) surface facing pyrgeometer, 8) levelling assembly and 9) surface facing pyranometer. Source: Hukseflux NR01 manual, version 0816. 92

Figure 4.8 Alignment of the NR01 to supporting structures using a spirit level in the lab before instrument deployment at urban site 2. 93

Figure 4.9 a) The HMP45C temperature and humidity probe manufactured by Vaisala and b) the Gill manufactured radiation shield. Source: Campbell Scientific. 94

Figure 4.10 Tipping bucket mechanism of the ARG100. Rain is tipped into a lower chamber before being channelled out of instrument. The tipping sensitivity of the ARG100 pictured is 0.2 mm per tip. 95

Figure 4.11 Definitions of the tilt angles α, β and γ for the yxz convention. The original axes are x y and z, the final axes are x', y' and z' and the intermediate axes are x_1, y_1 and z_1 (Wilczak et al. 2001:132). 98

Figure 4.12 Determining mean streamline plane for the planar fit method using an ensemble of observations. The z axis is perpendicular to the streamline plane and varies over 30 minute timescales (Finnigan, 2004:29). 98

Figure 4.13 Ogives illustrating the cumulative cospectrum of vertical wind velocity (w) and temperature, CO_2 and H_2O for the suburban and urban site 1 in Dublin. The units of covariance are normalised and plotted from low to high frequencies, f(Hz). 102

Figure 4.14 A comparison of a hypothetical frequency-weighted atmospheric cospectrum (solid line) with one measured by an eddy covariance system (dashed line). There is cospectral attenuation at low and high frequencies, the total flux loss is related to the difference in the under each of the cospectral curves. Here f is the frequency, fx is the frequency at which fCo(f) reaches its maximum value and η and ηx are their respective non-dimensionalised forms (Lee et al., 2004:68). 103

Figure 4.15 a) Latent heat flux estimates, b) sensible heat flux estimates and c) CO flux estimates from urban site 1 calculated by the software packages EddyPro (reference on the x-axis) and EddyUH and TK3.1 (on the y-axis). Note the difference in the magnitude along the x- and y-axis for each flux variable and a, b and c. 113

Figure 5.1 a) Photograph illustrating the location of the EC tower at the suburban location, b) a plan view schematic of the building showing its dimensions in metres and the location of the EC tower and c) a cross section view illustrating the building, tower and EC instrument heights. 126

Figure 5.2 Photograph of the suburban EC station equipped with 1) sonic anemometer (CSAT3), 2) gas analyser (Li7500), 3) Net radiometer (NR01), 4) Solar radiation sensor (CMP6), 5) PAR sensor (SKP215) and 6) the temperature and humidity probe (HMP45C). 127

Figure 5.3 Photographs illustrating the dark asphalt roof surface of the school (a, b and c) and the combination of concrete and asphalt surfaces in the school car park (d). The difference in vegetation can also be seen in a and b illustrating a winter and summer time. Photographs a) and b) refer to area north of the tower, c) is west and d) is the area south-west of the tower. 128

Figure 5.4 Site photographs from the suburban site illustrating in the change in the surface cover of the school yard in the south easterly direction in a) and b), and the north westerly direction in c) and d). The difference in the vegetation between winter and summer months can also be seen from c) and d). 129

Figure 5.5 Map of the source area of the net radiometer (NR01) according to Schmid et al. (1991) when z_M representing the measurement height of the NR01 is 11 m above the ground and the view factor is 95% for a) the original concrete and asphalt school yard surface and b) the Astro or artificial grass surface. 129

Figure 5.6 Site surrounds illustrating a) typical semi-detached dwellings with large, vegetated back gardens, b) tree-lined streets with grass verges, c) light commercial premises constructed of the same building materials as local residential dwellings and d) a typical traffic junction with light traffic activity. 130

Figure 5.7 GIS map illustrating the land cover for a 1 km radius surrounding the suburban EC station (red circle) and trees (green circles). 131

Figure 5.8 Land cover fractions for a 1 km radius of the suburban site for 12 wind sectors..... 132

Figure 5.9 Number of street trees per wind sector for a 500 m radius 132

Figure 5.10 The building height in metres for a 1km radius of the suburban site 133

Figure 5.11 Average building heights for the suburban EC station per 1° wind sector for radiuses equal to 500, 600, 700, 800, 900, 1000m. The plot illustrates very little difference in the average building height for 500-1000m radii. 134

Figure 5.12 a) Zero plane displacement height, b) roughness length, c) plan area density and d) frontal area density for the suburban site per wind direction for a radius of 500, 600, 700, 800, 900, 1000 m. .. 136

Figure 5.13 a)Photograph illustrating the location of the EC tower at marrowbone Lane b) a cross section view schematic of the building illustrating the building, tower and EC instrument heights and c) a plan view schematic showing the building dimensions in metres and the location of the EC tower. 137

Figure 5.14 Marrowbone Lane tower equipped with a 1) sonic anemometer (CSAT3), 2) gas analyser (Li7500), 3) Net radiometer (NR01), 4) solar radiation sensor (CMP6), 5) PAR sensor (SKP215) and 6) a temperature and humidity probe (HMP45C). 138

Figure 5.15 Site photos illustrating the surrounds of the EC site, a) EC mast and north facing direction, b) south east direction , c) north west direction, d) south direction with rain gauge location, e) illustrating the building roof material and the south direction, and f) the south west direction including the aluminium roof of an adjacent warehouse. 139

Figure 5.16 Land use in the surrounds of the EC site comprising of a) 4-5 storey apartment buildings, b) institutional buildings, and c) and d) 1 and 2 storey residential dwellings. 140

Figure 5.17 1 km radius land cover map for urban site 1 illustrating buildings, impervious surfaces, greenspace, canopy cover and street trees. 141

Figure 5.18 Land cover fractions for a 1 km radius of Marrowbone Lane for 12 wind sectors. 142

Figure 5.19 Street tree count for a 1 km radius of Marrowbone Lane for 12 wind sectors. 142

Figure 5.20 The building height in metres for a 1 km radius of the Marrowbone Lane EC station (Please note the scale difference in the legend in comparison to the suburban location and Kevin Street)..... 143

Figure 5.21 Average building heights in metres for Marrowbone Lane EC station per 1° wind sector for radiuses equal to 500, 600, 700, 800, 900, 1000 m. 144

Figure 5.22 a) Zero plane displacement height in metres, b) roughness length in metres, c) plan area fraction and d) frontal area fraction for Marrowbone Lane per 1° wind direction for a radius of 500, 600, 700, 800, 900, and 1000 m. 145

Figure 5.23 a) Photograph illustrating a) the DIT building and immediate surrounds to the north of the EC station b) the roof of Kevin Street DIT illustrating photovoltaic (PV) panels, c) 1) the net radiation sensor (NR01), 2) the mounting plate for the skyward facing PAR sensor, and d) the relative humidity and air temperature probe (HMP45C) mounted to the south point of the lattice tower. 147

Figure 5.24 Land use in the surrounds of the Kevin Street DIT campus comprising of a) terrace housing, b) apartment complexes, c) institutional buildings, and d) public parks. 148

Figure 5.25 Map of a 1 km radius of urban site 2 located on the roof of Kevin Street DIT, illustrating land cover including building footprints, impervious surfaces (including roads, pavements, car parks and courtyards), water bodies, greenspace, canopy cover and street trees. 149

Figure 5.26 Land cover fractions for a 1 km radius of Kevin Street for 12 wind sectors. 150

Figure 5.27 Street tree count for a 1 km radius of Kevin Street for 12 wind sectors. 150

Figure 5.28 The building height in metres for a 1 km radius of the Kevin Street EC station (Please note the scale difference in the legend in comparison to the suburban location and Marrowbone Lane). 151

Figure 5.29 Average building heights in metres for Kevin Street EC station per 1° wind sector for radiuses equal to 500, 600, 700, 800, 900, 1000 m. 152

Figure 5.30 a) Zero plane displacement height in metres, b) roughness length in metres, c) plan area fraction and d) frontal area fraction for Kevin Street per 1° wind direction for a radius of 500, 600, 700, 800, 900, and 1000 m. 153

Figure 5.31 Land cover fractions for each Dublin EC Station 155

Figure 5.32 A Local Climate Zone Map for the Greater Dublin Area derived from LULC and fieldwork (Alexander and Mills, 2014), modified to include the 3 EC sites in Dublin. See legend for LCZs. 157

Figure 6.1 a) monthly rainfall totals recorded at the suburban site and b) Met Éireann's Merrion Square weather station in Dublin (Met Éireann) (Purple colour) indicating percent of 1961-1990 average for years 2010-2011, and 1981-2010 average from January 2012-December 2012 (Turquoise colour). 160

Figure 6.2 Meteorological conditions during the observation period at the suburban site: a) daily mean, minimum and maximum station air temperature, b) mean daily station pressure and c) mean daily station vapour pressure deficit (VPD). 161

Figure 6.3 Windrose illustrating windspeed per wind direction recorded at the suburban site for a) daytime cases and b) nighttime cases. Daytime values are defined as those corresponding to values of incoming shortwave radiation (K↓) greater than 3 W m^{-2}. 162

Figure 6.4 a) Mean daily station air temperature measured at urban site 1 and b) mean daily air temperature difference between urban site 1 and the suburban site. 163

Figure 6.5 Same as Figure 6.1 for a) urban site 1 and b) Merrion Square Met Éireann weather station. Complete monthly rainfall data is not available at urban site 1 for months April 2010 and July 2012 due to the beginning and end dates of the station operation period. 163

Figure 6.6 Same as Figure 6.3 for urban site 1. 164

Figure 6.7 a) Half hourly, b) daily and c) monthly averages for incoming shortwave radiation and d) monthly diurnal cycles of median values observed at the suburban site. There were an insufficient number of data points available for the calculation of the monthly mean for November 2010. Note the scale difference on the y-axis for a, b, c and d. 166

Figure 6.8 Same as Figure 6.7 for reflected shortwave radiation. 166

Figure 6.9 a) Half hourly b) daily, c) monthly averages for surface albedo (α) and d) monthly diurnal cycles of median values observed at the suburban site. Note the scale difference on the y-axis for a, b, c and d. 167

Figure 6.10 a) Half hourly b) daily and c) monthly averages for incoming longwave radiation observed at the suburban site. Note the scale difference on the y-axis for a, b, and c. 169

Figure 6.11 Same as Figure 6.10 but for outgoing longwave radiation observed at the suburban site. ... 169

Figure 6.12 Same as Figure 6.7 but for net all-wave radiation observed at the suburban site. 171

Figure 6.13 Same as Figure 6.7 but for urban site 1 and 2. 172

Figure 6.14 Same as Figure 6.7 for reflected shortwave radiation but for urban site 1 and 2. 172

Figure 6.15 Same as Figure 6.9 but for urban site 1 and 2. 173

Figure 6.16 a) Half hourly b) daily and c) monthly averages for incoming longwave radiation observed at urban sites 1 and 2. Note the scale difference on the y-axis for a, b, and c. 174

Figure 6.17 Same as Figure 6.16 for outgoing longwave radiation observed at urban sites 1 and 2. 174

Figure 6.18 Same as Figure 6.7 for net all-wave radiation observed at urban sites 1 and 2. 175

Figure 6.19 Monthly median diurnal incoming shortwave radiation residual between the suburban site and urban site 1 for months April 2010 to July 2012 for all day time hours. White areas on the plot correspond to observations of K↓ equal to zero W m^{-2}. 176

Figure 6.20 Same as Figure 6.19 for reflected shortwave radiation residual. 177

Figure 6.21 Same as Figure 6.19 for incoming longwave radiation residual for all hours. 178

Figure 6.22 Same as Figure 6.19 for outgoing longwave radiation residual for all hours. 179

Figure 6.23 Same as Figure 6.19 for net all-wave radiation residual for all hours. 180

Figure 6.24 Relative frequency (%) of data quality flags for momentum (τ), sensible heat (Q_H), latent heat (Q_E) and carbon dioxide (F_C) according to Foken et al. (2004) at the suburban site for a) daytime cases and b) nighttime cases. Quality flag classes are shown in the legend. 182

Figure 6.25 Same as Figure 6.24 for urban site 1. 182

Figure 6.26 Same as Figure 6.24 for urban site 2. 183

Figure 6.27 Relative frequency (%) of different atmospheric stabilities (ζ) for total or all hours (T) and night time hours (N) at the suburban site (Sub), urban site 1, (Urb 1) and urban site 2 (Urb 2) for months a) April to September and b) October to March. The stability classes are shown on the legend. 184

Figure 6.28 Relative frequency (%) of different atmospheric stabilities (ζ) throughout the day at the suburban site for months a) April to September and b) October to March. The stability classes are shown on the legend. 185

Figure 6.29 Same as Figure 6.28 for urban site 1. 185

Figure 6.30 Same as Figure 6.28 for urban site 2. 186

Figure 6.31 Flux footprint distance at the suburban site representing the peak flux footprint distance for a) neutral, b) unstable, c) stable and d) very unstable conditions, and the 70% upwind flux footprint distance for e) neutral, f) unstable, g) stable and h) very unstable conditions. The number of cases of each stability condition is given by the number of half hours (n) and the relative frequency (%). Distances are shown in the legend, note inter-site scale differences. 189

Figure 6.32 Same as Figure 6.31 for urban site 1. 190

Figure 6.33 same as Figure 6.31 urban site 2 Distances are shown in the legend, note inter-site scale differences. 191

Figure 6.34 Box plots representing the median, upper quartile and lower quartile, the whisker length represents 1.5, points are determined as outliers if they are larger than $q_3 + w(q_3 - q_1)$ or smaller than $q_1 - w(q_3 - q_1)$, where q_1 and q_3 are the 25th and 75th percentiles, respectively - a) friction velocity(u_*), b) the square root of the drag coefficient ($C_D^{0.5}$) c) the angle of attack and d) histogram of the relative frequency of wind direction binned into 12 classes of 30 degrees; observations refer to those from the suburban site. 194

Figure 6.35 Same as Figure 6.34 for urban site 1. 194

Figure 6.36 Same as Figure 6.34 for urban site 2 (Note scale difference on y-axis d relative to urban site 1 and the suburban site). 195

Figure 6.37 Surface energy budget for 2010 for the suburban location, a) Q*, b) Q_H, c) Q_E and d) the residual of the energy balance equation in addition to the modelled storage heat flux term, $\Delta Q_{S\ OHM}$. Please note scale difference on the y-axis. The black lines represent monthly median diurnal values bounded by upper and lower quartile values in colour. 199

Figure 6.38 Same as Figure 6.37 for 2010 at the urban site 1. 199

Figure 6.39 Same as Figure 6.37 for 2011 at the suburban site. 201

Figure 6.40 Same as Figure 6.37 for 2011 at urban site 1. 201

Figure 6.41 Same as Figure 6.37 for 2012 for at the suburban site. 203

Figure 6.42 Same as Figure 6.37 for 2012 at urban site 1 and 2. Fluxes of Q_E for July 2012 are more variable, data availability in this regard consisted of only 10 days before urban site 1 ceased operation. 203

Figure 6.43 Median diurnal difference in the turbulent latent heat flux between the suburban site and urban site 1 (e.g. $Q_{E\ SUB} - Q_{E\ URB}$) for a) spring, b) summer, c) autumn and d) winter. 205

Figure 6.44 Median diurnal difference in the turbulent sensible heat flux between the suburban site and urban site 1 (e.g. $Q_{H\ SUB} - Q_{H\ URB}$) for a) spring, b) summer, c) autumn and d) winter. 205

Figure 6.45 Seasonal boxplots of daytime ($K\downarrow$ >3 Wm^{-2}) Q_E normalised by incoming radiation ($Q\downarrow$) and wind direction for a) spring, b) summer, c) autumn and d) winter for the suburban site. 207

Figure 6.46 Same as Figure 6.45 for Q_H normalised by incoming radiation ($Q\downarrow$) for the suburban site. . 207

Figure 6.47 Same as Figure 6.45 seasonal Q_E normalised by incoming radiation ($Q\downarrow$) for urban site 1. . 208

Figure 6.48 Same as Figure 6.45 seasonal Q_H normalised by incoming radiation ($Q\downarrow$) for urban site 1. 208

Figure 6.49 Scatter plot showing the relation between the available energy (Q^*- ΔQ_SOHM) and the sum of the turbulent fluxes (Q_E+Q_H) for a) the suburban site and b) urban site 1 between April 2010 and July 2012. Data points refer to monthly median diurnal values where n=1344. 212

Figure 6.50 Monthly median diurnal cycles generated using data from Alexander et al. (in review) for a) the suburban site and b) urban site 1 for a typical climatological year (TCY). 214

Figure 6.51 Energy balance ratio for urban areas according to Offerle et al. (2005b) 215

Figure 6.52 Spring median diurnal CO_2 flux (in black) showing upper and lower quartiles (in blue) observed during weekdays and weekends at urban site 1 and the suburban location. 217

Figure 6.53 Same as Figure 6.50 for summer; with regard to the suburban site summer is separated into two plots to reflect summer months in (June) and out of school term. 218

Figure 6.54 Same as Figure 6.50 for autumn at urban site 1 and the suburban site. 218

Figure 6.55 Same as Figure 6.50 for winter at urban site 1 and the suburban site. 219

Figure 6.56 Seasonal CO_2 flux observed at urban site 1 normalised per wind sector for a) spring, b) summer, c) autumn and d) winter. The magnitude of flux (µmol m^{-2} s^{-1}) is outlined in the legend. The relative frequency of the flux magnitude per wind sector is outline by the dashed circles, e.g. 25, 50 and 75%. 221

Figure 6.57 Same as Figure 6.54 for the suburban site. 223

Figure 6.58 Map illustrating the land cover in a 200m radius of the suburban location. 223

List of Tables

Table 2.1 Sublayers in the atmospheric surface layer over an ideal, flat, land-surface with uniform roughness elements (Modified from Foken,2008a) 13

Table 3.1 Typical roughness properties of homogeneous zones in urban areas (taken from Grimmond and Oke, 1999a:1281) 42

Table 3.2 Radiative properties of typical urban materials and areas 49

Table 4.1 Station names, locations, latitudinal and longitudinal coordinates. 85

Table 4.2 Overview of available EC software and included corrections and quality checks (Updated from Table 4.8 in Foken et al., 2012b) 110

Table 4.3 Comparison of regression analyses for a) the latent heat flux, b) the sensible heat flux and c) the CO_2 flux for the observation campaign dataset where n=4367 half hour values using Eddy Pro as the baseline software 114

Table 4.4 Classification of the data quality by the steady-state test, integral turbulence characteristics and the horizontal orientation of the CSAT3 sonic anemometer by Foken et al. (2004) 119

Table 4.5 Proposal for the combination of the single quality flags into a general data quality according to Foken et al. (2004) 120

Table 4.6 Summary of software processing steps and corrections for each eddy covariance site 124

Table 5.1 Site characteristics for each EC site in Dublin 154

Table 6.1 EC site period of operation and data availability for processing 158

Table 6.2 percentage of turbulent flux data discarded (%) following post-processing procedures for each EC station for each turbulent flux. 181

Table 6.3 Mean values of the drag coefficient derived from eddy covariance measurements and those derived from an empirical expression derived from data in Roth (2000) that is a function of z/z_H. 193

Table 6.4 Empirically derived coefficients used in the objective hysteresis model 197

Table 6.5 Coefficients obtained for each Dublin EC station 197

Table 6.6 Seasonal energy balance flux ratios for the suburban and urban site 1, seasonal values were determined from 33 and 27 months of data the suburban and urban site 1 respectively. 210

Table 6.7 Seasonal and annual means of Q_F (W m^{-2}) modelled using Järvi et al. (2011). 214

Table 7.1 Reproduced and updated from Goldbach and Kutller (2013) outlining urban/suburban energy balance studies of 234

Table 7.2 Mean daily exchange of carbon (C) estimated for each season and estimated net total exchange of C at the suburban site and urban site 1. Missing daily data are gap filled using the equivalent monthly mean daily values. 241

Table 7.3 Table reproduced and modified from Christen (2014) to include seasonal and annual measured mass fluxes of carbon dioxide (F_C), at the suburban site and urban site 1 in Dublin. The locations are sorted by increased annual F_C (kg C m^{-2} $year^{-1}$). In many cases the values are multi-year averages. Positive numbers are net exchange of CO_2 from the surface to the atmosphere (emissions dominate), while negative numbers are cases where uptake dominates and CO_2 is sequestered by the urban biosphere rather than emitted. LCZ refers to the Local Climate Zone classification (Stewart and Oke, 2012) and λb is the plan area fraction of buildings in the tower source area (as reported by the various studies). In most cases, results are for long-term turbulent source areas (all wind directions), with the exception of 'Essen-Grugapark' where a conditional average of only an urbanised sector is shown. 242

List of Equations

Equation 2.1 Reynolds decomposition 17
Equation 2.2 Reynolds postulates 17
Equation 2.3 Covariance of two variables 18
Equation 2.4 Covariance of fluctuating parts of two variables A and B. 18
Equation 2.5 One point conservation equation of any vector quantity (ζ) (Foken et al., 2012). 20
Equation 2.6 Scalar conservation equation (Foken et al., 2012). 21
Equation 2.7 Expanded scalar conservation equation (Foken et al., 2012). 21
Equation 2.8 One point scalar conservation equation (Foken et al., 2012). 21
Equation 2.9 One point scalar conservation equation in the vertical direction (Foken et al., 2012). 22
Equation 2.10 Eddy covariance term for a scalar (Foken et al., 2012). 22
Equation 2.11 The surface energy budget (Oke, 1987). 23
Equation 2.12 Surface radiation balance (Oke, 1987). 23
Equation 2.13 Nighttime net radiation budget (Oke, 1987). 24
Equation 2.14 The components of incoming shortwave (solar) radiation (Oke, 1987) 24
Equation 2.15 Derivation of surface albedo from pyranometer measurements (Oke, 1987). 25
Equation 2.16 Radiation emitted by a body according to Stefan-Boltzmann Law. 25
Equation 2.17 Incoming longwave radiation (Oke, 1987). 25
Equation 2.18 Outgoing longwave radiation (Oke, 1987). 26
Equation 2.19 The turbulent flux of sensible heat (Oke, 1987). 26
Equation 2.20 The turbulent flux of latent heat (Oke, 1987). 26
Equation 2.21 Net storage heat flux (Oke, 1987) 27
Equation 2.22 The circular source area contributing to the radiometer signal at height (z_1) according to Schmid et al. (1991). 28
Equation 2.23 Flux footprint function according to Kormann and Meixner (2001). 30
Equation 2.24 The energy balance ratio (Wilson et al., 2002) 31
Equation 3.1 Frontal area fraction of roughness elements (Grimmond et al., 1999) 40
Equation 3.2 Plan area fraction of roughness elements (Grimmond et al., 1999) 41
Equation 3.3 Energy balance residual (Oke and Cleugh, 1987) 69
Equation 3.4 Objective hysteresis model according to Grimmond et al. (1991). 70
Equation 3.5 The anthropogenic heat flux (Sailor and Lu, 2004) 72
Equation 3.6 Anthropogenic heat estimate based on energy budget closure (Sailor, 2011) 73
Equation 4.1 Velocity of air flow along the transducer axis (u_{pl}) and the speed of sound (c) derived from the sum of the inverse of transit times (Munger et al., 2012). 85
Equation 4.2 Incoming longwave radiation derived from the upward facing pyrgeometer and instrument temperature (Hukseflux, 2007). 93
Equation 4.3 Coordinate rotation matrix transforming measured velocities into the desired coordinate system (Kaimal and Finnigan, 1994). 97
Equation 4.4 Three coordinate rotations performed around the z-axis, new y-axis and new x-axis to give angles α, β and γ (Kaimal and Finnigan, 1994). 97
Equation 4.5 Multiple linear regression performed on wind velocity components for the derivation of regression coefficients to determine instrument offset and the pitch and roll angles for the planar fit coordinate rotation method (Wilczak et al., 2001). 99
Equation 4.6 Determination of planar fit rotations according to Wilczak et al. (2001) 99
Equation 4.7 Transfer function for the vertical flux of a scalar (S) as a function of real frequency (f) according to Moore (1986). 104

Equation 4.8 Flux attenuation of an eddy covariance system according to Moore (1986). 104
Equation 4.9 Corrected vertical flux of a scalar (S) according to Moore (1986). 104
Equation 4.10 Relationship between sonic derived temperature and absolute air temperature considering the crosswind effect according to Liu et al. (2001). 105
Equation.4.11 Sonic temperature along i^{th} transducer path with consideration of the crosswind according to Liu et al. (2001) 105
Equation 4.12 Derivation of mean sonic temperature from sound velocity along each transducer axis considering the crosswind effect according to Liu et al. (2001). 105
Equation.4.13 Derivation of the crosswind velocities specific to the CSAT3 3D sonic anemometer according to Liu et al. (2001). 106
Equation.4.14 Correction from the sonic derived buoyancy flux to the sensible heat flux according to Liu et al. (2001) 106
Equation 4.15 Total trace gas flux including the eddy flux, water vapour flux and heat flux term (Webb et al., 1980) 107
Equation 4.16 Water vapour gas flux including the eddy flux, water vapour flux and heat flux term (Webb et al., 1980) 108
Equation 4.17 Instantaneous mixing ratios of a trace gas and water vapour derived from the Li7200 enclosed-path gas analyser (Foken et al., 2012b) 108
Equation 4.18 Total trace gas fluxes derived using instantaneous mixing ratios for a trace gas (c) and water vapour (q) (Foken et al., 2012b) 108
Equation 4.19 Root-mean squared error (Wilks, 2011) 113
Equation 4.20 Test of integral turbulence characteristics proposed by Foken and Wichura (1996) 119
Equation 4.21 Zero plane displacement height according to Macdonald et al. (1998) 121
Equation 4.22 Roughness length according to Macdonald et al. (1998) 121
Equation 6.1 Atmospheric stability parameter according to Kotthaus and Grimmond (2014a) 183
Equation 6.2 The surface drag coefficient (Roth, 2000) 192
Equation 6.3 The angle of attack (Nakai et al., 2006) 193

Chapter 1 Introduction

1.1 Research background

Although urban areas occupy less than three percent (%) of the planetary landmass, they are the foci of human and economic activity (Mills, 2007). The climates that they generate are distinctive and represent unambiguous evidence of an urban climate effect. This urban climate effect is a consequence of two related properties, land cover (form) and land use (function). The process of urbanisation replaces 'natural' surfaces with manufactured materials that are usually impervious and have distinctive thermal and radiative properties. In addition, the urban surface is both geometrically complex and highly diverse. These properties of form result in the formation of numerous microclimates caused by a number of climate drivers, including access to the sun and shelter from wind (Nunez and Oke, 1977; Oke, 1987). Urban function refers to human or anthropogenic activities that generate waste heat, moisture and materials as a result of transportation, industrial production, energy consumption, and so on. These functions tend to have distinctive spatial and temporal emission patterns. Together, the urban form and function induce differences in the budgets of radiation, heat, mass and momentum between the city and its pre-existing surface (Grimmond and Oke, 1995).

Knowledge of urban climate effects begins with urban based field observations; Luke Howard, in his published work, *The Climate of London* (originally published in three volumes between1818-1833 and later by the International Association on Urban Climate, IAUC (2011)) is recognised as the first investigator to identify the urban heat island (UHI) effect. His analysis involved the examination of air temperature differences observed between 'rural' and 'urban' locations (e.g. ΔT_{u-r}). He attributed the relative warmth of the city to its structure, crowded population and consumption (Mills, 2008). Since then urban climate research encountered challenges concerning the derivation and reporting of urban climate effects. Lowry (1977:129) highlighted the limitations of observation techniques in the field which, similar to Howard, measured the urban climate effect as "differences in values of elements between urban sites and rural or non-urban sites". This method of analyses was largely conducted in the absence of an objective, community-wide framework; as a consequence reporting of urban climate effects could not be contextualised and provided urban climatologists with little explanatory power about the processes giving rise to the distinctive effects. This finding

had implications for subsequent research in the field initiating discussion with regards to more appropriate measurement techniques, and more insightful reporting. In order to learn more about the processes operating at the urban-surface interface, and to move beyond the urban-rural dichotomy, investigators had to rethink about the concept and importance of scale in conducting urban climate observations. Since then the range of temporal and spatial scales over which urban climate effects are observed have been formalised and guidelines for undertaking urban field observations have been established (Oke, 2006; Stewart and Oke, 2012).

Of increasing concern is the interaction of synoptic scale climate events with urban climate effects; under certain conditions the UHI, characterised by high nocturnal air temperatures, can amplify synoptic scale extreme heat events (EHE). The human health impacts of EHEs in cities became increasingly recognised when excess heat-related deaths reached an estimated 70,000 across Europe in 2003 (Robine et al., 2008) and 55,000 in Russia in 2010 (Barriopedro et al., 2011). These impacts are further compounded when considered in unison with two key points:

1) Future climate change projections estimate an increase in the frequency of warm days and nights, in addition to an increase in the duration, intensity and spatial extent of heat waves, particularly in Europe (Hartman et al., 2013). Climate change as a consequence is projected to increase the disparity in extreme temperatures between rural and urban areas leaving urban dwellers relatively more vulnerable (McCarthy et al., 2010)

2) The urban population now accounts for 54% of the total world population of over 6.6 billion. This proportion will increase rapidly in the decades to come as parts of Asia and Africa become progressively less rural and more urban. Globally it is estimated that population growth will add 2.5 billion people to urban areas by 2050, almost 90% of which is expected to occur in Asia and Africa (United Nations, 2014). Projections indicate that cities to experience the greatest population increases in the future are small - to medium – sized cities; by 2030 it is estimated that two thirds of the urban population will reside in these cities whilst megacities will account for approximately one fifth (United Nations, 2014) (Figure 1.1).

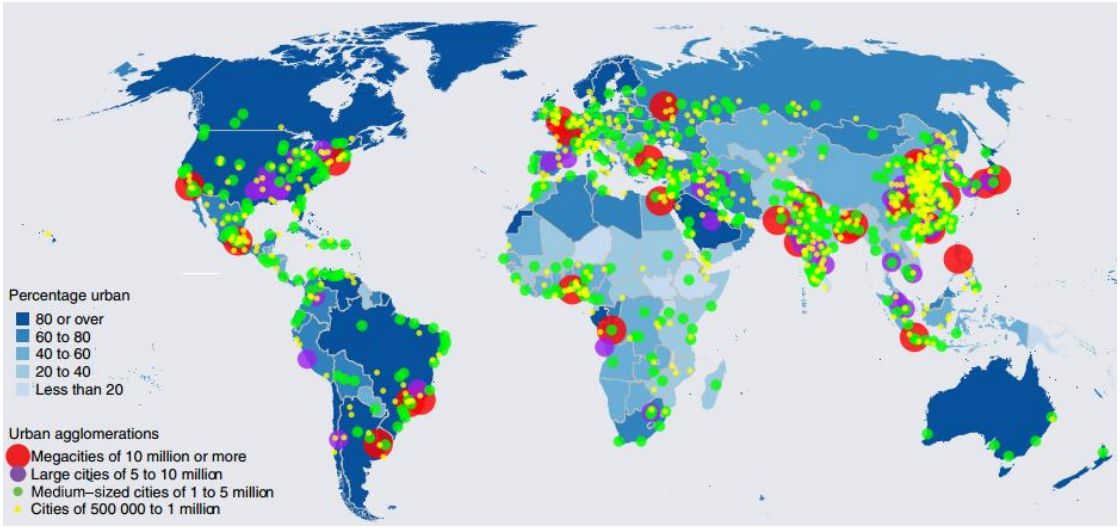

Figure 1.1 Percentage of urban population per country and location of urban agglomerations with at least 500,000 inhabitants, 2014 (United Nations, 2014).

Ultimately an understanding of the processes giving rise to differences in the budgets of radiation, heat, mass and momentum are essential in order to improve our ability to forecast and predict climate extremes and poor air quality events in cities, in addition to improving building and urban design practices; both of which will serve to reduce the deleterious urban climate effects experienced by urban dwellers (Oke, 1987; Oke, 1988a; Mills, 2006). Urban areas comprise of a greater proportion of sealed surfaces leading to the efficient removal of rainfall from the surface, as a result the heat and water budgets are significantly modified in relation to surrounding rural areas (Oke, 1987). Green spaces and water bodies in cities serve to promote evapotranspiration, cool air production and shading, ultimately mitigating summer thermal loads (Spronken-Smith and Oke, 1998). In terms of urban design practices urban climate information will facilitate the development and implementation of evidence-based modifications that can be applied to both existing cities and cities that are in construction; modifications can include for example, orienting street canyons in the direction of prevailing winds allowing for better ventilation (e.g. Ng et al., 2011). Quantifying the effects of such design strategies however is difficult in the absence of urban climate observations.

Of significant importance is the design and development of sustainable urban areas that do not 'lock' cities into untenable greenhouse gas (GHG) emissions trajectories. This is imperative given that urban areas and their inhabitants are key drivers of anthropogenic climate change; they are the main source of anthropogenic carbon dioxide (CO_2) emissions and have been estimated to contribute to between 70-90% of global carbon

emissions (Andres et al., 1997; Svirejeva-Hopkins et al., 2004). Nevertheless urban areas can be regarded as important contributors to global GHG mitigation efforts, particularly given their limited geographical extent (Mills, 2007). Planning authorities, in addition to political systems have jurisdiction at the same scale as the emission of anthropogenic CO_2, thus urban areas represent a unique opportunity to implement geographically-focused mitigation strategies, the efficacy of which can be measured (Velasco and Roth, 2010). In the absence of urban climate observations, particularly those measuring exchanges of CO_2, urban emissions will remain unquantified; instead emissions are typically estimated using fossil fuel inventory methods. Asefi-Najafabady et al. (2014) estimate CO_2 emissions at a spatial resolution of 0.1°x 0.1° combining existing fossil fuel emission data with global power plant emission data; the spatial distribution of emissions shows a clear relationship with the location of the world's cities and the most urbanised countries (Figure 1.1 and Figure 1.2).

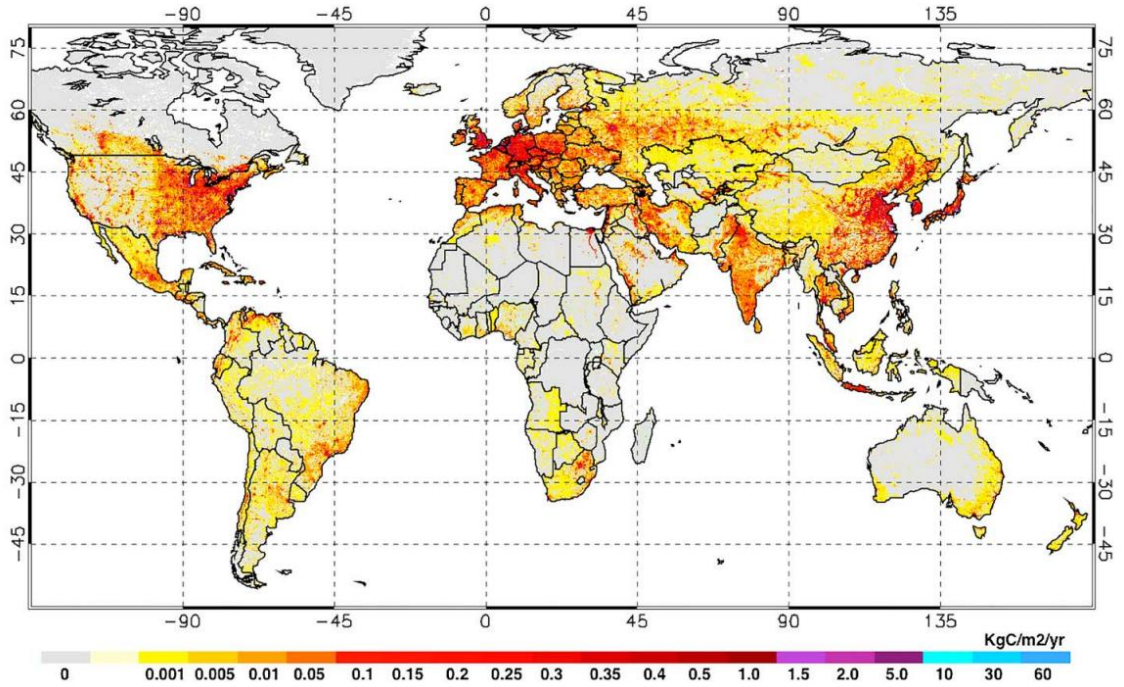

Figure 1.2 Global gridded carbon dioxide emissions representing multiyear (1997-2010) data at a spatial resolution of 0.1° (Asefi-Najafabady et al., 2014).

The traditional inventory approach raises difficulties if the spatial disaggregation of emissions is sought beyond this spatial resolution (Oda and Maksyutov, 2011). City-wide inventories require very detailed spatial and temporal information regarding mobile (e.g. vehicles), area (e.g. residences) and point (e.g. industries) emission sources in addition to natural contributions from urban vegetation and human exhalations (Velasco and Roth, 2010). Very often however data such as this do not exist for cities

or is incomplete and inconsistent, particularly in developing countries (Mills, 2007; Velasco and Roth, 2010). In the absence of this information the precise contribution of cities to regional and global CO_2 emissions remains unquantified; this necessity is compounded given projections associated with climate change and urban population and urbanization growth over the coming century.

1.2 The Eddy Covariance measurement technique

The eddy covariance (EC) technique has been recognised as the only direct measurement method that takes into account all mobile, area and point emission sources in addition to natural sinks and sources, of the environment from which they are representative (Velasco and Roth, 2010; Weissert et al., 2014). EC systems when deployed in urban areas therefore allow for the spatially-integrated surface exchange of CO_2 to be estimated. In brief, this exchange is quantified by measuring the covariance between the fluctuations in vertical wind velocity and CO_2 mixing ratios (Lee et al., 2004). In a similar way surface-atmosphere exchanges of sensible and latent heat can be derived using air temperature data and water vapour (H_2O) mixing ratios. The timing, magnitude and partitioning of energy between these heat fluxes effectively govern the climate experienced at a location (Oke, 1987). Long term, continuous EC measurements have been routinely used in natural or managed ecosystems to investigate CO_2 and H_2O exchange over various timescales (Baldocchi, 2003). Increasingly EC systems are being deployed and operated in urban areas to measure these exchanges and since 1990 the number of urban sites has increased from one to 31 active sites in 2012 (Grimmond and Christen, 2012, http://www.geog.ubc.ca/urbanflux/).

Given the number and diversity of cities internationally (Figure 1.1) the current capacity of the urban international EC network is limited; as a consequence the international published literature states that more direct observations of this kind are required (Piringer et al., 2002; Arnfield, 2003; Grimmond, 2006; Velasco and Roth, 2010; Weissert et al., 2014). EC observations are necessary for developing universal flux and air flow characteristics for urban areas over a range of background climates and urban forms. Where permitted observations should be long term, spanning multiple seasons and years; long term data are necessary in order to sample a range of synoptic conditions for the evaluation and refinement of urban climate and air quality models. Furthermore observational campaigns often derive important empirical parameters, for

example, surface albedo and roughness length, which can be employed to improve model performance (Grimmond, 2006). Arnfield (2003) calls for increased urban EC measurements in central city sites, as oppose to suburbs, where the urban form and function is relatively more complex. Furthermore, the literature calls for the extension of EC observations to cities outside of temperate climates zones, particularly to those in (sub)tropical climates given that these are the cities in which the greatest urban population increases are expected to occur (Roth, 2007).

With the exception of Los Angeles, USA (Grimmond et al., 1996), Basel, Switzerland (Christen and Vogt, 2004), Łódź , Poland (Offerle et al., 2006a and b), Melbourne, Australia (Coutts et al., 2007), Montreal, Canada (Bergeron and Strachan, 2012), London, England (Wood et al., 2010; Helfter et al., 2011; Kotthaus and Grimmond, 2014a) and b), Essen, Germany (Weber and Kordowski, 2010), Oberhausen, Germany (Goldbach and Kuttler, 2013) and Helsinki, Finland (Nordbo et al., 2013), there are few studies worldwide that operate multiple EC sites within the one city. Observations from a range of urban surfaces within a city, experiencing the same synoptic forcing, is critical for deriving empirical relations between the urban form and function and fluxes. This information is critical for the refinement of urban climate models such as 1) the local-scale urban meteorological parameterisation scheme (LUMPS) (Grimmond and Oke, 2002), 2) the surface energy and water balance scheme (SUEWS) (Järvi et al., 2011) and 3) the flux ratio-active index surface exchange (FRAISE) scheme (Loridan and Grimmond, 2012). This is an important factor given the associated financial and logistical cost of undertaking observational campaigns; ultimately where observations are not feasible, cities, particularly those in the developing countries, will rely on model development.

A long term urban-based investigation of radiation, energy and CO_2 exchanges has never been undertaken for Dublin, or any other Irish city. This research therefore presents a novel contribution to the field of climatology on a national scale. Of increasing importance is the need to use measurements, such as those presented in the thesis, to evaluate the impacts of urban policies and development on the urban climate and on emissions of GHGs. Ireland ranks within the highest 15 EU member states in terms of per capita emissions of CO_2 (World Bank, 2015). Given that medium sized cities, such as Dublin, are forecast to undergo the greatest changes between now and

2030, measurements in cities are imperative and could reveal evidence to support increasingly dense, as oppose to sprawling, urban development plans that have been traditionally implemented in Dublin.

1.3 Research aims and objectives

The main research aim is to investigate the long term fluxes of radiation, surface energy and CO_2 across three locations in Dublin. The key purpose of operating multiple concurrent measurement locations within one metropolitan area is significant; it addresses current knowledge gaps and allows for comparisons to be made across the budgets of radiation, surface energy and CO_2 under similar synoptic forcings. Differences can therefore be more readily attributed to site-specific controls such as surface cover and roughness. The objectives of the research are three-fold:

1) To perform an inter-site comparison of the radiation balance over diurnal, seasonal and inter-annual timescales.

2) To perform an inter-site comparison of the turbulent fluxes of sensible and latent heat over diurnal, seasonal and inter-annual timescales.

3) To perform an inter-site comparison of CO_2 fluxes over diurnal and seasonal timescales.

Inter-site comparisons will allow for the partitioning of surface energy to be linked to specific surface properties and roughness. Similarly an inter-site comparison of the CO_2 flux will identify key drivers of the flux across various urban locations in Dublin. A directional analysis of the CO_2 flux will also be undertaken for all seasons and aims to identify the location and strength of local CO_2 sources and sinks. Seasonal and annual estimates of CO_2 will be provided for two of the urban measurement locations in Dublin; the urban locations will be identified as net sources or sinks of carbon according to the annual estimates.

The selected locations for the investigation are important given their spatial representativeness in the Greater Dublin Area (GDA) and include 1) a suburban location located 4-5km from the city-centre, 2) an urban location consisting of residential

dwellings and commercial buildings, and 3) a second urban location that is located in a dense city-centre location comprising of an increased proportion of commercial buildings. Key physical parameters related to the surface cover and roughness are estimated for each location; this urban surface characterisation facilitates a more detailed interpretation of the differences in fluxes of radiation, surface energy and CO_2. Finally distinctive effects on the radiation and surface energy budgets due to extreme synoptic events will be highlighted in the thesis and include those coincident with the extreme cold event that prevailed in November and December 2010 (Met Éireann, 2010).

1.4 Thesis outline

With regard to urban EC measurements experimental design in the urban domain must carefully consider the assumptions of EC theory and scale requirements as applied to homogenous surfaces. **Chapter 2** introduces various scale-related concepts when undertaking EC measurements. Various statements that describe the radiation and energy budget of a surface, in addition to the exchange of CO_2 will outlined in addition to factors governing their exchange. EC measurements require sophisticated instrumentation; the concept of instrument source areas is introduced in unison with numerical approaches developed to model these.

Chapter 3 sets out how traditional scale considerations are applied to urban areas so that EC measurements can be considered to represent vertical exchanges of heat and CO_2 between the urban surface and atmosphere. Definition of the 'surface' to which these exchanges refer has previously posed problems in the urban climate field. A novel conceptual framework according to Stewart and Oke (2012) is introduced; this framework classifies universal urban surfaces according to measurable and physical indicators of the urban form and function. In doing so the scheme addresses limitations associated with traditional 'rural' versus 'urban' reporting of climate variables. The classification scheme can be applied universally to urban surfaces and facilitates the inter-comparison of radiative, energy and mass budget investigations across different cities. The chapter will also review existing literature on urban studies related to air flow characteristics in addition to radiation and energy budgets and the synoptic and surface controls influencing their magnitude and direction. Finally urban CO_2 flux

investigations will be reviewed and key biogenic and anthropogenic drivers of the flux will be identified.

The EC method requires instruments capable of measuring vertical wind velocity, air temperature and atmospheric H_2O and CO_2. **Chapter 4** outlines the instrumentation required for this in addition to auxiliary meteorological instruments required for determining the prevailing synoptic conditions. The data derived from the instruments and their unit of measurement will be outlined, moreover steps regarding data storage, retrieval and conversion will be explained. In order to compute theoretically sound EC fluxes a series of processing steps and corrections must be implemented. Multiple software packages are however available to make these corrections. In the absence of consensus on suitable software for urban use, a software comparison using a sample dataset will be presented using three different software packages. A final software package is selected for processing fluxes at the three EC sites. Once fluxes have been calculated a series of quality control and post-processing procedures are implemented all of which are outlined in Chapter 4.

Much of the assumptions inherent in EC theory rely on its application over homogenous, flat surfaces. Homogeneity requires that the roughness elements, such as trees, should be of similar height and spacing in all directions surrounding the instrumented measurement tower. Furthermore the sources and sinks of heat, moisture and CO_2 should be evenly distributed in the surrounds of the EC instruments. **Chapter 5** describes the three EC sites in terms of their surface cover and roughness elements, which in urban areas comprise of buildings, trees, vehicles and humans. A geographic information system (GIS) containing building footprints, urban vegetation and surface cover will facilitate the directional assessment of the site characteristics, in doing so it will also highlight directions of surface cover heterogeneity. The influence of surface roughness is also important due to its influence on turbulence; as a consequence the surface roughness characteristics are quantified for all wind directions at each EC site.

Chapter 6 presents the results of the research questions presented above. The radiation budget of the EC sites is stated and inter-site differences are investigated. The radiation budget determines the energy available for turbulent exchanges of sensible and latent heat. Differences in the magnitude and direction of these turbulent heat fluxes are

examined in unison with the surface cover characteristics of each site. Furthermore the meteorological conditions prevailing for the observation period are presented and provide explanatory power when attempting to characterise the long term variability of the fluxes. The flux of CO_2 is examined for all four seasons to investigate the relative influence of biogenic and anthropogenic factors. Net annual CO_2 exchange is estimated for suburban and urban EC sites and the results demonstrate the influence of the urban surface on the overall annual CO_2 budget.

Finally **Chapter 7** discusses the main findings of the research. The results are interpreted and explanations for observed findings are presented. The chapter directly addresses the thesis objectives and the results are compared with similar observational studies undertaken in cities and suburbs. In this way the research undertaken for Dublin is contextualised on an international level where it is shown to contribute to knowledge of universal urban flux characteristics. The chapter will also consider the limitations of the research, including the shortcomings of particular methods when applied to the urban surface. Furthermore recommendations for future research will be outlined alongside potential uses for the research findings and datasets presented here.

Chapter 2 Scale and Concepts using Eddy Covariance

An appreciation of scale in the space, frequency and time domains is critical to understanding atmospheric phenomena in the atmospheric boundary layer (ABL), and will serve to illustrate why particular direct measurement methods, such as eddy covariance (EC), are employed when investigating surface-atmosphere exchanges. In the absence of a scale-dependent framework it is difficult to design experiments capable of improving on existing theory or formulating novel theories via field-based observations, scale models and wind tunnel experiments. This chapter introduces the reader to key theoretical concepts and definitions in micrometeorology and provides the background necessary for understanding the subsequent review chapter on urban EC observations (Chapter 3). This chapter will focus on ABL structure and depth over land, ABL airflow, including turbulence, turbulent fluxes and their derivation via one point conservation equations.

2.1 Atmospheric boundary layer structure and depth

The ABL is the shallow layer of the troposphere closest to the Earth's surface. Surface forcings such as evaporation and transpiration, heat transfer, pollutant emission, frictional drag, and terrain induced flow modification serve to influence this shallow zone where responses to forcings are observed in the ABL over timescales of less than one hour (Oke, 1987; Stull, 1988; Garrat, 1994; Kaimal and Finnigan, 1994; Foken, 2008a). Investigations seeking to understand these surface forcings are imperative given that it is within the ABL where humans reside, where crops are grown and where commerce takes place (Stull, 1988).

The ABL height varies from between 0.5 and 2 kilometres (km) depending on the time of day, atmospheric stability and the underlying surface (Oke, 1987; Stull, 1988; Kaimal and Finnigan, 1994; Foken, 2008a). Following sunrise, in response to heating of the Earth's surface a well-mixed turbulent layer is formed, known as the mixing layer (ML) (Figure 2.1). Strong convective turbulence in the ML blends out almost all variation in the vertical mean profiles of temperature and humidity (Kaimal and Finnigan, 1994). The ML extends by entraining stable and less turbulent air from the entrainment zone (EZ) above and typically reaches a maximum height in the late afternoon. The EZ demarcates the boundary between the ABL and the free atmosphere above, the latter of

which is characterised as a relatively more stable layer that experiences intermittent turbulence due to convective clouds (Stull, 1988; Foken, 2008). Prior to sunset, in response to cooling of the surface and of the immediate overlying atmosphere, the nocturnal stable boundary layer (NBL), also known as the Stable Boundary Layer (SBL), begins to develop from the surface upwards (Figure 2.1). The NBL grows to a fraction of the ML depth (approximately 100 metres (m) or less), the air aloft remains warmer than the volume in the NBL and possesses weakening characteristics of the day's ML (the residual layer, RL). The warm air above the cooler air gives rise to a capping inversion (Figure 2.1) (Stull, 1988; Oke, 1987; Kaimal and Finnigan, 1994; Foken, 2008a). During cloud free conditions vigorous thermal mixing and strong convective cells will develop shortly after sunrise whereby the ML breaks up the NBL and RL. In cloudy conditions with less direct solar radiation and weaker thermal mixing, the ML may not penetrate the RL giving rise to a stratified ABL (Stull, 1988; Foken, 2008a).

There is further distinction of the ABL structure into vertical layers based on the dominant mechanisms of exchange and whether they are influenced by atmospheric stability. The following outline is representative of exchange over an ideal, flat, land-surface with uniform roughness elements, such as blades of grass. The Ekman-layer, commonly referred to in the literature as the Outer or Upper layer (Garratt, 1994; Foken, 2008a) extends to the top of the ABL making up 90 percent (%) of the ABL volume. Airflow within this layer is affected by the Earth's rotation. The dominant transport mechanism in the Ekmann-layer is via turbulence where fluxes are not constant and generally decrease with height. In short this is due to the vertical mixing of more moisture laden air parcels from close to the surface with relatively drier air parcels entrained from the EZ. The vertical extent of the Ekmann-layer is stability dependent ranging from one to two kilometres during stable and unstable conditions respectively (Stull, 1988; Foken, 2008a).

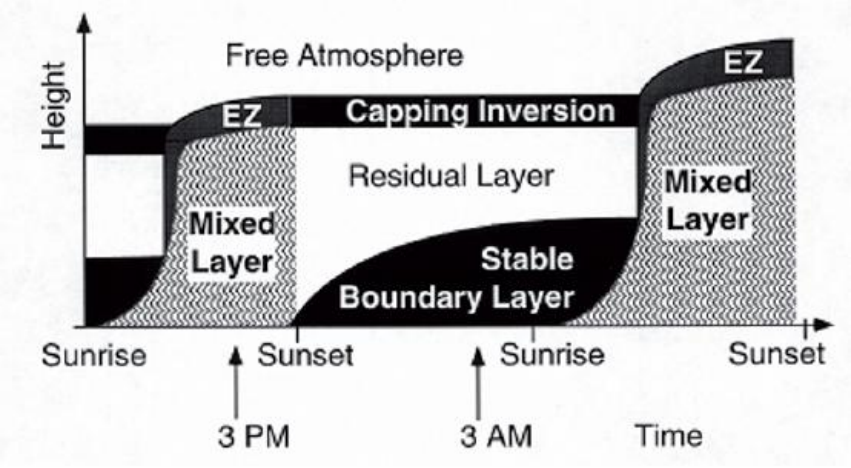

Figure 2.1 Daily cycle of the atmospheric boundary layer structure (EZ: Entrainment zone) (Modified from Stull, 1988 in Foken, 2008a).

The remaining 10% of the ABL volume is referred to as the surface layer (SL) or Prandtl-layer which lies below the Ekman-layer, comprising of four sub-layers (Table 2.1) (Foken, 2008). Over flat terrain, with shallow homogenous roughness elements the SL can extend to between 20-50m during unstable conditions and only a few metres during stably stratified conditions (Foken, 2008a). Turbulence is the dominant exchange mechanism in the two upper most sub-layers (i.e. the turbulent layer and dynamical sublayer). A viscous layer of one centimetre thickness (cm) serves as a buffer layer between the turbulent, fluid atmosphere and the rigid surface, as a result it shares mixed mechanisms of exchange via turbulence and molecular diffusion. Millimetres above the surface, at the laminar boundary layer, energy transfer with the atmosphere is exclusively via molecular diffusion and is three orders of magnitude less efficient than turbulent exchange (Kaimal and Finnigan,1994; Foken, 2008a).

Table 2.1 Sublayers in the atmospheric surface layer over an ideal, flat, land-surface with uniform roughness elements (Modified from Foken,2008a)

Height in metres (m)	Sublayer	Exchange	Stability dependent
20-50	Turbulent layer	Turbulent	Yes
1	Dynamical sublayer		No
0.01	Viscous sublayer	Molecular/Turbulent	No
0.001	Laminar boundary layer	Molecular	No

2.2 Airflow in the Atmospheric Boundary Layer

The ABL is characterised by turbulent mixing however airflow in general in the ABL can be considered as comprising of three transport mechanisms, namely, mean wind, turbulence and waves, the latter two can be thought of as being superimposed on the mean wind (Stull, 1988; Kaimal and Finnigan, 1994; Foken, 2008a). Although waves occur in the ABL they are less frequent and are generated as the local mean wind flows over surface obstacles (Stull, 1988).

With regard to mean wind let us consider a right-handed Cartesian coordinate axis where the X and Y axes correspond to horizontal wind in the u and v directions, where u is rotated parallel to the mean wind direction, v is perpendicular or normal to this and w represents vertical wind in the ABL. Vertical mean wind is considered negligible in the ABL whilst the horizontal mean wind component, known as advection, is the dominant mechanism for transporting momentum, mass constituents and energy in the horizontal direction (Stull, 1988; Kaimal and Finnigan, 1994; Arya, 2001). Advection in the ABL typically ranges from 2 to 10 metres per second (m s^{-1}). In micrometeorology the expression for mean wind speed as a function of height above the surface is the wind profile (Sutton, 1953). ABL wind speeds are generally slowest close to the local surface due to frictional drag, increasing with height above the surface to produce a logarithmic wind profile (Stull, 1988; Kaimal and Finnigan, 1994; Ayra, 2001; Foken, 2008a).

Turbulence occurs along a continuum whereby space scales relate to wave lengths ranging from kilometres to millimetres, frequencies correspond to the number of cycles of a signal per hour and the time scale associated with each cycle ranges from milliseconds to hours (Figure 2.2) (Oke, 1987; Stull, 1988; Kaimal and Finnigan, 1994; Arya, 2001; Foken, 2008a). Turbulent flow can be described as a superposition of different sized eddies combined to form coherent patterns of velocity, vorticity and pressure (Kaimal and Finnigan, 1994). They serve as the dominant vertical transfer mechanism, transporting momentum, energy and mass constituents such as water vapour (H_2O) and carbon dioxide (CO_2) from one location to another in the vertical direction.

Figure 2.2 illustrates a representation of the wind speed spectrum close to the ground; the y-axis illustrates the portion of turbulent kinetic energy (TKE) an eddy of particular length contributes to the total spectrum, where TKE simply represents the kinetic energy contained by eddies in turbulent flow. The first peak represents large wavelengths corresponding to high energy synoptic scale phenomena such as the passage of fronts and weather systems (Stull, 1988). The smaller secondary peak (circa 10 Hours in Figure 2.2) corresponds to the increase of windspeed during the day and subsequent decrease during the night time. The right hand side (RHS) of the spectrum refers to lower energy perturbations in the wind speed due to relatively smaller scale turbulent motions. Here small eddies in terms of length have shorter time periods and greater frequency (i.e. 0.001 time period and 1000 cycles per hour), but are less intense and consequently have a lower TKE. Eddies of longer length and longer time periods are consequently less frequent per hour (i.e. between 0.1 and 0.01 hours corresponding to timescales of between 10 minutes and 10 seconds respectively) but contain much greater intensity represented as the peak on the RHS of Figure 2.2.

The distribution of energy at turbulent scales is further illustrated in Figure 2.3 and can be divided into three distinct regions; a) the energy containing range where turbulence is generated by shear and buoyancy forces and where energy production peaks, b) the dissipation range where energy contained in the smallest sized eddies is dissipated into heat by molecular viscosity and drops to zero, and c) the inertial range where TKE is neither produced or dissipated, instead energy is transferred through a cascade into smaller and smaller eddies (Stull, 1988; Kaimal and Fininigan, 1994). In the inertial subrange energy decreases with increasing frequency according to Kolmogorov's Law (slope equal to -5/3) (Kaimal and Finnigan, 1994) (Figure 2.3).

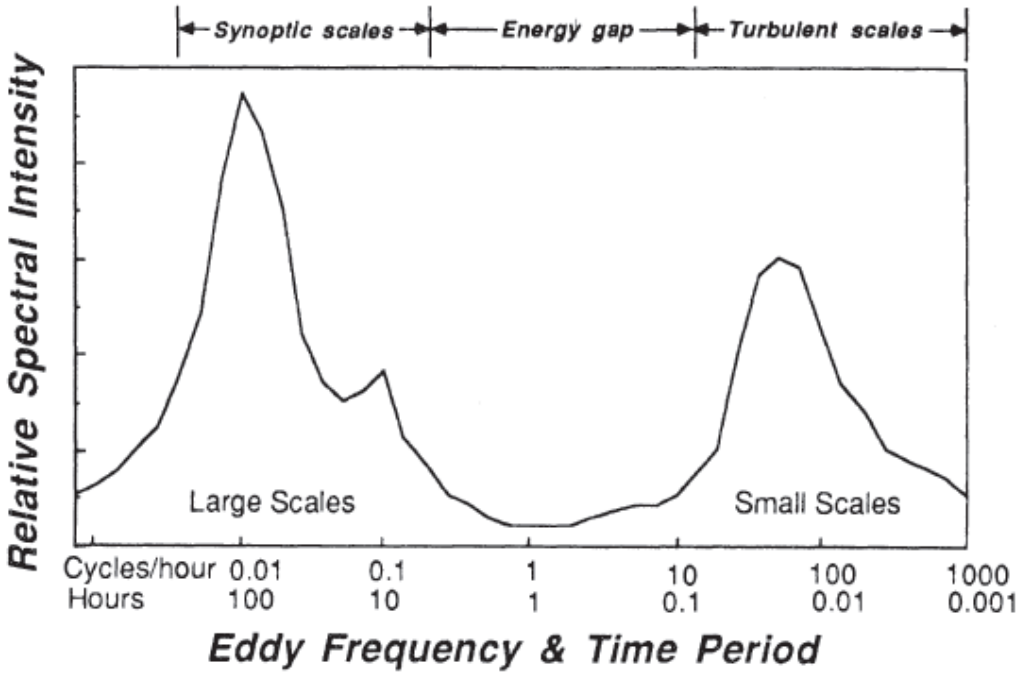

Figure 2.2 Wind speed spectrum near the ground estimated from a study of Van der Hoven (1957) (Stull, 1988:32).

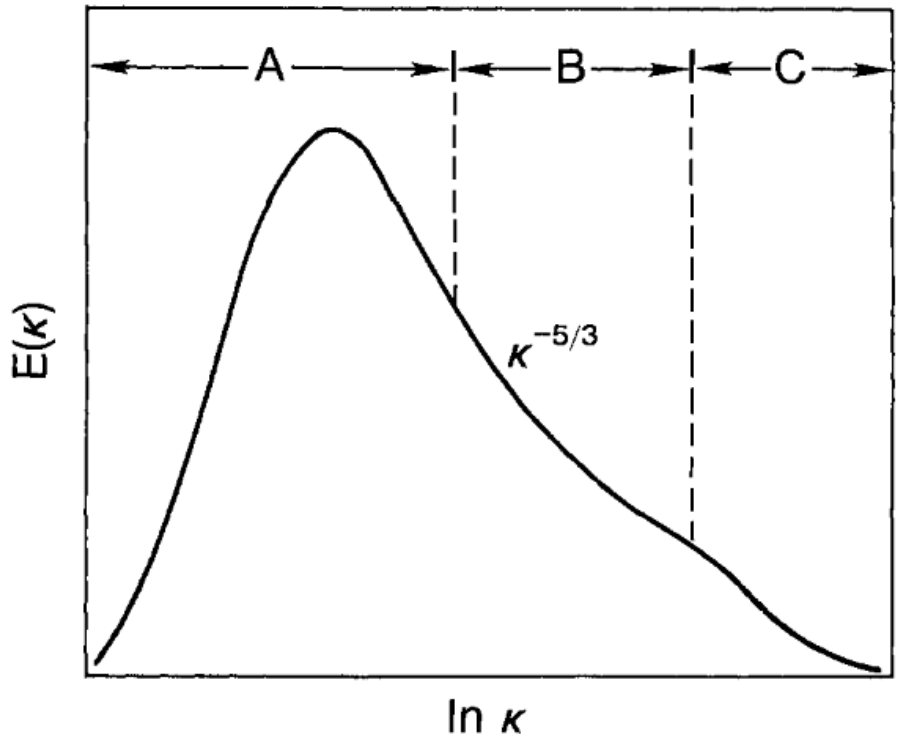

Figure 2.3 Schematic of the TKE spectrum in the atmospheric boundary layer, where E(k) is the scalar energy spectrum illustrating three regions of energy production (A), energy dissipation (C) and the inertial subrange (B) where energy is neither produced or dissipated (Kaimal and Finnigan,1994).

When investigating ABL turbulence it is useful to consider Taylor's Hypothesis which assumes that an eddy of any diameter advected past a measurement sensor is 'frozen', in

other words the properties of the eddy are unchanged (Stull, 1988). Application of Taylor's hypothesis therefore allows micrometeorologists to study turbulence measurements from instruments at a single point in space. To do so consider the horizontal wind speed within a continuous record; this varies over a finite range of values. Selection of a finite period allows for the calculation of a mean wind speed and the subsequent separation of the time series into mean and fluctuating parts. The turbulent part of this time series can be considered as the positive and negative departures from the mean where smaller (larger) departures indicate small (large) turbulent intensities. This separation of a time series into its mean and fluctuating part is known as Reynolds averaging and can be represented as:

$$u = \overline{U} + u'$$

Equation 2.1 Reynolds decomposition

Where *u* is the recorded wind speed, $\overline{U}$ denotes the time averaged mean wind speed and *u'* is the fluctuating part of the signal representing gusts or eddies. In order for Reynolds decomposition to be valid a series of Reynolds postulates, or averaging rules need to be applied to the turbulent value (Stull, 1988; Kaimal and Finnigan, 1994; Foken, 2008a; Foken et al., 2012a):

$$\overline{\zeta'} = 0 \quad Term\ I$$

$$\overline{\zeta\xi} = \overline{\zeta}\ \overline{\xi} + \overline{\zeta'\xi'} \quad Term\ II$$

$$\overline{\overline{\zeta}\xi} = \overline{\zeta}\overline{\xi} \quad Term\ III$$

$$\overline{a\zeta} = a\overline{\zeta} \quad Term\ IV$$

$$\overline{\zeta + \xi} = \overline{\zeta} + \overline{\xi} \quad Term\ V$$

Equation 2.2 Reynolds postulates

Where ζ and ξ refer to vector and scalar quantities and *a* is a constant. In physical terms when the fluctuation is positive the instantaneous gust or eddy is greater than the average wind speed and vice versa for negative fluctuations. The second of Reynolds postulates (Term II in Equation 2.2) is important in subsequent equations as it separates out the mean and fluctuations of two variables to form the basis of the EC method. The covariance between any two variables A and B is given as

$$covar(A,B) = \frac{1}{N}\sum_{i=0}^{N-1}(A_i - \bar{A}).(B_i - \bar{B})$$

Equation 2.3 Covariance of two variables

Using the turbulent part of variables A and B derived via Reynolds decomposition the covariance of a' and b' for a time series is expressed as

$$covar(A.B) = \frac{1}{N}\sum_{i=0}^{N-1} a_i^{'}\, b_i^{'}$$
$$= \overline{a'b'}$$

Equation 2.4 Covariance of fluctuating parts of two variables A and B.

This forms the eddy covariance term, when the vertical wind velocity fluctuation is expressed alongside the fluctuation of another vector or scalar quantity. They will be derived later and are known as fluxes describing how much of a quantity moves through a unit area per unit time.

As already stated, turbulence is three dimensional whereby turbulent motions will very likely produce simultaneous fluctuations in the velocities of wind in the *v* and *w* directions, where the same relationship described in Equation 2.1 can be applied to *v* and *w* wind speed (Stull, 1988). Turbulence or eddies will be set into motion by two key forces, 1) buoyancy forces and 2) shear or mechanical forces. Buoyancy force is due to the vertical gradient of temperature in the atmosphere. It explains the propensity of a parcel to move vertically in the ABL as a result of its temperature relative to the surrounding air. If a parcel of air is warmer it will tend to rise (the buoyancy force is said to be positive within the parcel), conversely if the parcel is cooler it will tend to sink (the buoyancy force is negative).

Turbulence produced due to mechanical forces, such as frictional drag which is caused by the fluid atmosphere moving across a rigid surface, and by vertical wind shear caused by changes in wind speed and direction close to the surface (Foken, 2008a). If the state of the atmosphere is conducive to, or amplifies vertical motion via these two forces it is said to be unstable and if it inhibits such motion it is said to be in a stable state (Oke, 1987; Stull,1988; Ayra, 2001; Foken, 2008a). When evaluating turbulence (co)spectra the wavelength at the spectral peak (λ_m) is important in that it is representative of the size of the eddies containing the most energy. The location of λ_m is

stability dependent; during stable conditions the spectrum is shifted towards higher frequencies (and consequently smaller eddies), on the other hand during unstable conditions eddies of different sizes are contributing to the total energy spectrum, as a result the λ_m is typically shifted towards lower frequencies (and larger sized eddies).

2.3 Turbulent fluxes and their derivation

The ABL receives much of its heat and all of its water via buoyant and mechanical turbulent processes (Stull, 1988). In order to estimate for example the vertical exchange of water vapour (H_2O) between the surface and atmosphere using single point measurements from suitable EC instrumentation we must first define a volume of interest over which the exchange takes place. Consider the control volume illustrated in Figure 2.4 whereby measurements of vertical wind velocity and humidity are taken using EC instrumentation mounted on a tower at some height (h) above the ground. A Cartesian coordinate frame is applied to the volume where the *z* direction corresponds to the vertical plane (Figure 2.4). Measurements obtained will also measure exchanges over horizontal planes *x* and *y*, corresponding to wind in the *u* and *v* directions respectively, and where $\bar{u}$ is the prevailing wind direction. *S* denotes the strength of the source or sink term of momentum, heat, moisture or CO_2 within the volume (Figure 2.4). A homogeneous area in this regard is one where the spacing, type and height of the roughness elements within and outside of the volume are uniform in all directions and the terrain is flat (e.g. Figure 2.4).

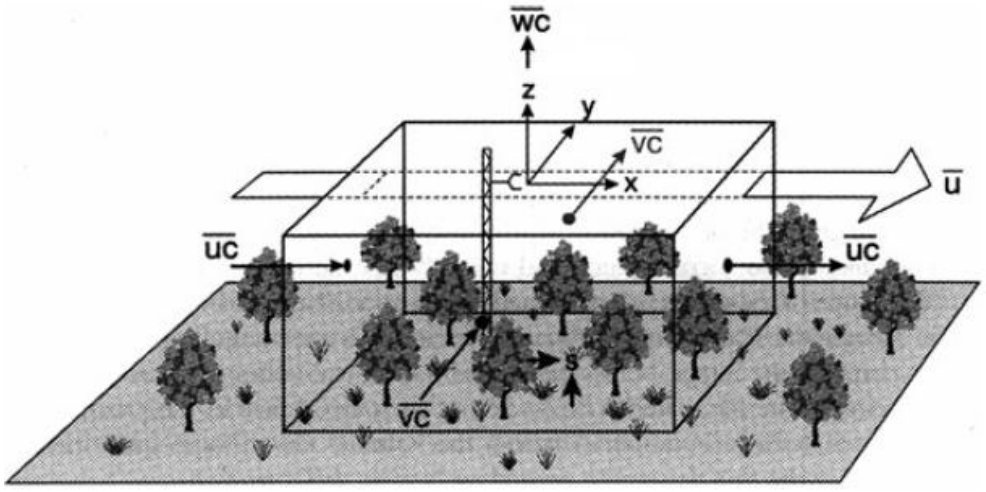

Figure 2.4 Example of an EC measurement tower and a Cartesian coordinate system superimposed onto a horizontally homogeneous surface to represent the control volume of interest (Finnigan et al. 2003).

These conditions are essential when undertaking EC measurements as it requires that horizontal gradients in temperature, humidity and momentum are negligible, and hence advective exchange across the volume will also be negligible.

According to the one point conservation equation, measured fluxes in the SL are constant with height; when integrated over a horizontal plane (2l x 2l, where l is the length of the volume in Figure 2.4) solve to produce the net vertical transport of either momentum or any scalar quantity between the surface and overlying atmosphere. As mentioned earlier atmospheric phenomena occur along a continuum and as such the conservation equations apply, where energy can neither be created nor destroyed, only converted from one state to another across an infinitesimal volume of air (or Figure 2.4 in our example), mathematically stated as:

$$\underbrace{\frac{\partial \rho_d \zeta}{\partial t}}_{\text{I}} + \underbrace{\underset{\nabla}{\rightarrow}\left(\underset{u}{\rightarrow} \rho_d \zeta\right)}_{\text{II}} + \underbrace{K_\zeta \Delta(\rho_d \zeta)}_{\text{III}} = \underbrace{S_\zeta}_{\text{IV}}$$

Equation 2.5 One point conservation equation of any vector quantity (ζ) (Foken et al., 2012).

Where ρ_d is the density of dry air, ζ represents any vector, $\underset{u}{\rightarrow}$ is the wind velocity vector, ∇ represents Laplacian operators, $\left(\frac{\partial^2}{\partial x^2} + \frac{\partial^2}{\partial y^2} + \frac{\partial^2}{\partial z^2}\right)$, Δ represents divergence $\left(\frac{\partial}{\partial x}, \frac{\partial}{\partial y}, \frac{\partial}{\partial z}\right)$, K_ζ is the molecular diffusivity of the quantity ζ and S_ζ represents the strength of the source or sink of the quantity within the volume. The rate of change of ζ represented by term I will be due to its atmospheric transport (II), to molecular diffusion (III) or due to its production by a source or absorption by a sink in the volume (IV). Transport via molecular diffusion (term III Equation 2.5) is confined to the lowest sub layers of the SL (Table 2.1) and can therefore be neglected where the measurement height is sufficiently above the roughness elements. If Equation 2.5 refers to a vector then it is the equivalent of the momentum conservation equation in that direction (where the 3 directions, *u*, *v* and *w* constitute the Navier Stokes equations). Consider the example of scalar conservation in the SL where X_s refers to the mixing ratio (the ratio of the constituent to that of dry air) of one atmospheric component such as water vapour

(H_2O) or carbon dioxide (CO_2) then Equation 2.5 can now be expressed as the scalar conservation equation:

$$\frac{\partial \rho_d X_s}{\partial t} + \vec{\nabla}\left(\vec{u}\rho_d X_s\right) = S_s$$

Equation 2.6 Scalar conservation equation (Foken et al., 2012).

The term representing transport via molecular diffusion (term III in Equation 2.5) has been removed however the term describing atmospheric transport (term II Equation 2.5) must be expanded to include the *u*, *v* and *w* directions in the SL. Furthermore the application of Reynolds averaging requires that a time-averaging operator is applied (i.e. a finite time period is necessary for the calculation of the mean and fluctuating part) so Equation 2.6 is now expressed as

$$\underbrace{\frac{\partial \rho_d X_s}{\partial t}}_{\text{I}} + \underbrace{\frac{\partial \rho_d u X_s}{\partial x} + \frac{\partial \rho_d v X_s}{\partial y} + \frac{\partial \rho_d w X_s}{\partial z}}_{\text{II}} = \underbrace{S_S}_{\text{III}}$$

Equation 2.7 Expanded scalar conservation equation (Foken et al., 2012).

Where term I represents the time-averaged component, term II is expanded in *u*, *v* and *w* directions and term III represents the strength of the scalar source/sink. Application of Reynolds decomposition also requires Term II of Equation 2.7 to be expanded to represent the mean and fluctuating contributions and is expressed as

$$\underbrace{\overline{\rho_d}\frac{\overline{\partial X_s}}{\partial t}}_{\text{I}} + \underbrace{\overline{\rho_d}\overline{u}\frac{\partial \overline{X_s}}{\partial x} + \overline{\rho_d}\overline{v}\frac{\partial \overline{X_s}}{\partial y} + \overline{\rho_d}\overline{w}\frac{\partial \overline{X_s}}{\partial z}}_{\text{II}} + \underbrace{\frac{\partial \overline{\rho_d}\,\overline{u'X'_s}}{\partial x} + \frac{\partial \overline{\rho_d}\overline{v'X'_s}}{\partial y} + \frac{\partial \overline{\rho_d}\overline{w'X'_s}}{\partial z}}_{\text{III}} = \underbrace{\bar{S}_s}_{\text{IV}}$$

Equation 2.8 One point scalar conservation equation (Foken et al., 2012).

Where Term I refers to the time derivative, term II refers to mean wind components, term III refers to the turbulent fluctuation components and IV is the source/sink term.

A number of considerations regarding the siting of the measurement tower were outlined earlier. An assumption of horizontal homogeneity allows us to consider the advective terms in Equation 2.8 associated with the *u* and *v* directions as having a negligible effect on the conservation of a scalar in the vertical direction. Furthermore, as the vertical mean wind is negligible (i.e. no divergence/convergence) turbulence is the dominant vertical transport mechanism in the SL. Finally let us assume steady state conditions where the time derivative (term I) is also nullified leaving

$$\frac{\partial \overline{\rho_d} \overline{w'X'_s}}{\partial z} = \bar{S}_s$$

Equation 2.9 One point scalar conservation equation in the vertical direction (Foken et al., 2012).

Where the vertical gradient of eddy covariance is equal to the strength of the source or sink in the volume (Figure 2.4) and where the eddy flux term is

$$\overline{\rho_d} \overline{w'X'_s} = \bar{S}_s$$

Equation 2.10 Eddy covariance term for a scalar (Foken et al., 2012).

Equation 2.10 then represents the vertical flux of a scalar through a horizontal plane above the surface roughness elements.

Finally where EC towers are deployed above non-flat terrain coordinate rotation is required to align the measured wind velocities (*u*, *v* and *w*) with the coordinate system (*x*, *y*, *z*) in which the mass balance equation is solved in the EC method. This step is required because alignment of the vertical sonic axis normal to the underlying surface is very difficult, especially if the topography is not flat terrain. If coordinate rotation is not implemented the streamwise or mean horizontal wind velocity ($\bar{u}$) will contaminate the vertical velocity measurements (*w*) and the subsequent vertical flux of a scalar (e.g.$\overline{w'Xs'}$) (Kaimal and Finnigan, 1994). Coordinate rotation methods will be discussed in greater in Section 4.2.2.

The equations outlined describe how vertical exchanges of momentum, scalars (i.e. H_2O or CO_2) and energy (i.e. sensible and latent heat, described later) can be estimated from EC measurements. These vertical exchanges will be explained and expressed in the following section in the context of the surface energy balance (SEB).

2.4 The surface energy balance

The energy budget is a statement of the principle of the conservation of energy. Applied to a surface it describes the magnitude and types of surface-air energy exchanges that give rise to distinctive near-surface climates, and is stated as follows,

$$Q^* = Q_H + Q_E + \Delta Q_S + \Delta Q_A$$

Equation 2.11 The surface energy budget (Oke, 1987).

Where net radiation (Q^*) is partitioned into the vertical exchange of sensible and latent heat (Q_H+Q_E) via turbulence, the heat storage change (ΔQ_S) via conduction and the horizontal transport of energy or advection (ΔQ_A). Each term is expressed as a flux density, the flow of energy per unit surface area. As outlined earlier when these terms are measured over a homogenous surface then there is no horizontal transfer in the system and $\Delta Q_A \approx 0$. In these circumstances, the only concern is the height at which the remaining terms are measured. Ideally, the observation platform should be located within a constant flux layer where each of the energy budget terms is nearly invariant with height. This layer represents the level at which the atmospheric properties have come into equilibrium with the surface below. It is located above the height of the roughness elements, which may be blades of grass on a prairie, trees in a forest, or buildings in an urban environment.

2.5 The radiation budget

The radiation budget determines the principal input into the surface energy balance (SEB) equation and is comprised of both incoming (↓) and outgoing (↑) short- (K) and longwave (L) radiation,

$$Q^* = K\downarrow - K\uparrow + L\downarrow - L\uparrow$$

Equation 2.12 Surface radiation balance (Oke, 1987).

Where K and L represent shortwave and longwave components, * denotes a net flux (where no distinction is made between direct and diffuse radiation for K*) and positive (negative) values equate to energy being received (lost) by the surface (Offerle et al., 2003). The radiative flux density is defined as the amount of radiant energy received at or emitted by a unit area of the surface per unit time, expressed as Watts per square metre (W m^{-2}).

Shortwave (or solar) radiation is emitted by the Sun; it occupies a wavelength range between 0.01 and 3 micrometres (μm) and has a peak wavelength at approximately 0.5 μm within the spectrum of visible radiation. Incident shortwave radiation (K↓) at a surface is a function of day of year and time of day, which govern the altitude of the sun in the sky. In Ireland maximum K↓ (approx. 990 W m^{-2}) will occur on a flat surface at noon under a clear sky during the summer solstice. At noon on a clear winter day, the magnitude of K↓ will be a great deal less (approx. 390 W m^{-2}). Time of year also controls the length of day, whereas during the summer solstice the day-length in Dublin is 17 hours, at the time of the winter solstice, it is just 7.5 hours. At nighttime solar radiation is absent so that:

$$Q* = L\downarrow - L\uparrow = L*$$

Equation 2.13 Nighttime net radiation budget (Oke, 1987).

The amount of K↓ received by the surface will be reduced in comparison to K↓ incident at the top of the atmosphere because of depletion in passing through the atmosphere, and reflection caused by clouds (Oke, 1987). The cloud type, height and size are particularly influential, for example low, stratus clouds serve to significantly reduce K↓ at the surface in comparison to small cumuli clouds (Ayra, 2001; Foken, 2008a). Atmospheric turbidity is also responsible for depleting K↓ and is defined as any condition of the atmosphere that reduces its transparency to shortwave radiation. Reduced transparency will be primarily as a result of the presence of particulates, such as pollen, dust, smoke and haze (Oke, 1987; Ayra, 2001). Particles such as aerosols serve to reflect part of the direct beam radiation and scatter the remaining part; large solid particles will reflect more solar radiation than they scatter (Oke, 1987; Ayra, 2001). K↓ comprises of diffuse (D) and direct beam (S) radiation and is expressed as

$$K\downarrow = D + S$$

Equation 2.14 The components of incoming shortwave (solar) radiation (Oke, 1987)

Where D represents shortwave radiation that is reflected, scattered and back-scattered between the surface and atmosphere, and S consists of shortwave radiation incident on a surface that has not yet been absorbed or diffused (Oke, 1987). In general diffuse radiation dominates during cloudy conditions, increasing with water vapour haze and when the sun is near the horizon (i.e. at sunrise and sunset). At these solar elevations

more radiation is scattered due to the increased path length through the atmosphere (Oke, 1987).

At the surface, reflection of shortwave radiation (K↑) will depend on the magnitude of K↓ and surface albedo (α). Albedo is defined as the fraction of total incoming shortwave radiation incident upon the surface that is reflected back to the atmosphere via direct outgoing shortwave radiation and is expressed as,

$$\alpha = \frac{K\downarrow}{K\uparrow}$$

Equation 2.15 Derivation of surface albedo from pyranometer measurements (Oke, 1987).

Albedo varies with surface cover and common values are provided in Oke (1987).

Longwave (or terrestrial radiation) is emitted by all objects according to the Stefan-Boltzmann Law which states that any body that has a temperature greater than absolute zero (Kelvin) emits radiation according to the following equation,

$$R = \sigma T^4$$

Equation 2.16 Radiation emitted by a body according to Stefan-Boltzmann Law.

Where R is the radiation emitted by the body, σ is the Stefan-Boltzmann constant (5.67 X 10^{-8} W m^{-2} K^{-4}) and T is the surface temperature of the body in Kelvin. The majority of longwave radiation occupies a range between 4 and 40 μm and has a peak wavelength at approximately 10 μm. The magnitude of emitted radiation is a function of both temperature and emissivity (ε). For a surface, incoming longwave radiation (L↓) is derived from the overlying atmosphere,

$$L\downarrow = \varepsilon_a \sigma T_a^4$$

Equation 2.17 Incoming longwave radiation (Oke, 1987).

Where T_a is air temperature (in Kelvin, K) and ε_a is atmospheric emissivity, which is substantially a function of atmospheric water content. Outgoing longwave radiation (L↑) is comprised of that which is emitted and reflected L↓,

$$L\uparrow = \varepsilon_s \sigma T_s^4 + (1 - \varepsilon_s) L\downarrow$$

Equation 2.18 Outgoing longwave radiation (Oke, 1987).

where the subscript (s) refers to the surface. Emissivity is defined as the ratio of the energy flux emitted by the surface at a given wavelength and temperature to that emitted by a blackbody at the same wavelength and temperature (Ayra, 2001). A black body, or full radiator, is defined as a body emitting the maximum possible radiation per unit area for a given temperature. Natural surfaces and materials, such a forest canopies, are not perfect blackbodies but can be considered as grey bodies with emissivities typically greater than 0.9, and can approach values close to unity when surface moisture increases. As a result reflection of longwave radiation is small, typically less than 0.1 (Oke, 1987).

Over the course of a day, each of the radiation terms inscribes a distinctive pattern. In the absence of cloud, K↓ increases from sunrise to noon and declines until sunset and K↑ displays a similar pattern and at night both are zero. By comparison the longwave terms show little diurnal variation and typically L↑ exceeds L↓. Net radiation (Q*) is then negative at night and positive during the daytime.

2.6 Surface heat fluxes

As previously described vertical heat exchanges with the atmosphere occur as turbulent motions which transfer sensible and latent heat. These occur as a consequence of vertical gradients of air temperature and humidity. The nature of these exchanges can be represented simply as,

$$Q_H = C_a(\overline{w'T'})$$

Equation 2.19 The turbulent flux of sensible heat (Oke, 1987).

$$Q_E = L_V(\overline{w'\rho_v'})$$

Equation 2.20 The turbulent flux of latent heat (Oke, 1987).

Where C_a is the heat capacity of air and L_V is the latent heat of vapourisation (L_V), which may be treated as constant near the surface. The terms in the parenthesis represent the covariance of vertical velocity (w) and air temperature (T) and of w and

absolute humidity (ρ_V). The over bar represents an average and the primes represent fluctuations (positive and negative) from that average.

The final term in the SEB (Equation 2.11) is net storage heat flux, which refers to the change in energy stored in the volume under study. A small proportion of this heat is stored in the atmosphere and is revealed as changes in the vertical air temperature and humidity profiles that result from surface-air exchanges. The remainder however is stored in the solid substrate, the layer below the surface. The lower boundary of the volume under study extends to a depth (D) where no diurnal temperature change occurs so that,

$$\Delta Q_S = DC_s \frac{\Delta T}{\Delta t}$$

Equation 2.21 Net storage heat flux (Oke, 1987)

Where C_s is the heat capacity (J m^{-3} K^{-1}) of the substrate and $\Delta T/\Delta t$ is the change in temperature with time (K s^{-1}).

When the terms of the SEB (Q*, Q_H, Q_E and ΔQ_S) are plotted over the course of a day each flux exhibits characteristic patterns that illustrate the nature of the exchanges. The net radiation curve is negative overnight and positive during the day, which corresponds to daytime radiative heating (associated with the receipt of shortwave radiation) and night-time radiative cooling. At night this cooling is driven by heat drawn out of storage and by heat transfer from the overlying atmosphere. During the daytime, the opposite occurs as the surplus energy at the surface is used to heat the atmosphere and the substrate. However, the patterns are not symmetrical about noon. When the sun rises and Q* becomes positive, most of this energy is initially transferred into the substrate. As the atmosphere near the surface is very stable there is little turbulent activity (Figure 2.1). As the surface continues to warm the near-surface air temperature gradient increases, vertical motion becomes more vigorous and Q_H and Q_E begin to dominate exchanges. By the afternoon, ΔQ_S typically becomes negative (heat drawn out of storage), even though Q* is still positive. Q_H and Q_E remain positive even after sunset, when Q* again becomes negative. Over shorter timescales, the surface energy balance for example can differ from unity. The energy storage as a result may be positive or negative. Sign convention in this regard deems positive (negative) as an addition (a loss) of energy to the volume.

2.7 Measurement source areas

The concept of an instrument footprint and their use in EC investigations describes the probable source areas of measurements from radiation budget and SEB campaigns. When the underlying surface is not homogenous for an adequate upwind distance from the EC system (e.g. for all wind directions and stable conditions), inconsistencies in the source areas of the radiation and EC instruments may arise (Equation 2.11). Traditionally the field of view (FOV) of a sensor is known as the footprint, and represents the influence of the surface on the measurements recorded at the sensor height (Grimmond, 2006; Oke, 2007; Rannik et al., 2012). The footprint itself will be determined by the following factors: the variable being measured, the instrument used to measure the variable, the location of the instrument and its height above ground level, and the roughness of the underlying surface. Additionally, in the case of turbulent variables, the meteorological conditions (e.g. atmospheric stability) influence the extent and direction of the footprint (Grimmond, 2006; Rannik et al., 2012).

2.7.1 *The radiation source area*

With regard to radiation measurements the FOV of a downward facing pyranometer (shortwave) or a pyrgeometer (longwave), parallel to the ground, is a circular area expressed as

$$r = Z_1 \left(\frac{1}{F} - 1\right)^{0.5}$$

Equation 2.22 The circular source area contributing to the radiometer signal at height (z_1) according to Schmid et al. (1991).

Where r is the radius of the circular source area, Z_1 is the measurement height of the radiometer, and F is the view factor (i.e. 50, 75, or 90%) (Schmid et al., 1991).In mathematical terms the area of influence goes to infinity, hence one must define the percentage level for the view factor (Schmid, 1994). The source area is symmetrical, centred on the instrument location and increases with height above ground level (Figure 2.5a).

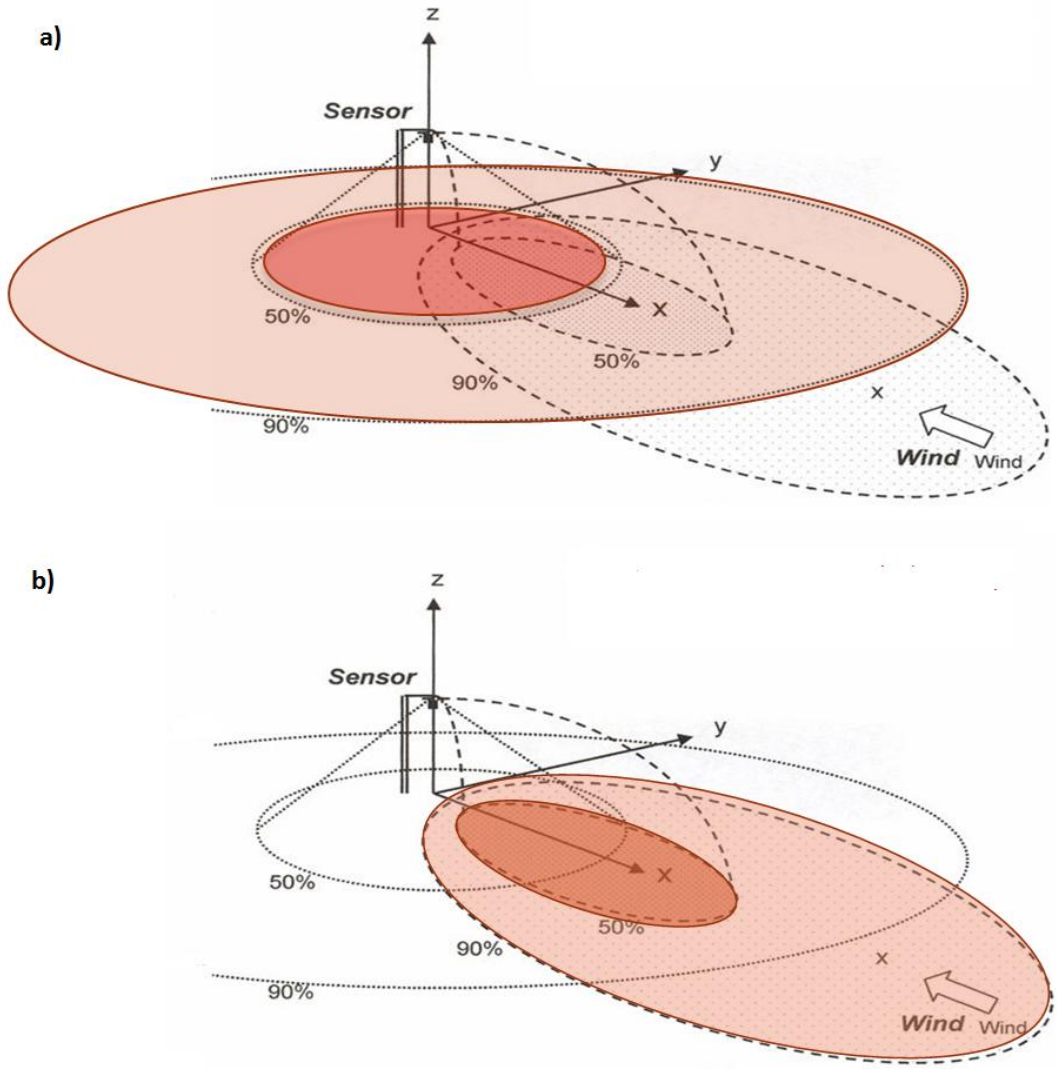

Figure 2.5 A conceptual diagram representing 50 and 90% source area footprints for a) downward facing radiation instruments and b) eddy covariance instrumentation. The coloured shadows represent the source areas of the radiation sensor (red) and eddy covariance instruments (orange) (Modified from Oke, 2004).

2.7.2 *The turbulent flux footprint*

Determining the footprint of the turbulent fluxes (e.g. Q_E, Q_H and CO_2 flux) is naturally more complex and is commonly calculated as a function of atmospheric stability, wind speed and direction, lateral diffusion, the roughness characteristics of the surface and the height of the instruments above the ground (Rannik et al., 2012). A conceptual representation of the turbulent flux is illustrated in Figure 2.5b where it is evident that the extent of the radiation footprint does not reach the ellipse-shaped turbulent footprint. Where inconsistencies in the source areas occur, the likelihood of energy balance non-closure, discussed next, may increase particularly when their surface characteristics are different (Grimmond, 2006).

Several theoretical approaches have been employed to derive the turbulent flux footprint function and include 1) analytical models, 2) Lagrangian stochastic particle dispersion models, 3) large eddy simulations (LES) and 4) ensemble-averaged closure models (a comprehensive review of each is provided in Vesala et al., (2008) and Rannik et al., (2012). Analytical models include for example, those developed by Schmid (1994;1997) (Flux Source Area Model, FSAM), Hiesh et al. (2000) and Kormann and Meixner (2001), all of which have been frequently employed in rural and urban studies to provide a 2-dimensional probable source area location (see for example, Moriwaki and Kanda, 2004; Velasco et al., 2005; Crawford et al., 2011; Liu et al., 2012; Nordbo et al., 2013; Kotthaus and Grimmond, 2014b). The functions assume conditions of horizontal homogeneity and stationarity where the vertical turbulent flux, $F(0, 0, z_m)$ measured at a height above ground level (z_m) is related to the surface flux $F(x,y,0)$ upwind of the measurement point by

$$F\ (0,0,z_m) = \int_{-\infty}^{\infty}\int_{0}^{\infty} F(x,y,0)\phi(x,y,z_m)dx\ dy,$$

Equation 2.23 Flux footprint function according to Kormann and Meixner (2001).

Where the x-axis is normal to the average horizontal wind direction and the flux footprint $\varphi(x,y,z)$ describes the flux portion seen at $(0,0,z_m)$ resulting from a point source at the surface $(x,y,0)$ (Kormann and Meixner, 2001). For any given time interval the peak or maxima of the flux footprint function will vary according to stability conditions. In strongly convective conditions turbulence serves to transport a scalar vertically and the peak flux is yielded a short distance upwind of the sensor location (Figure 2.6). With increasing stability however the upward motion is relatively reduced and the source area increases in distance from the sensor location (Figure 2.6). The location of the peak flux during increasing stability becomes more skewed, increasing to a few dozen times the measurement height. During stable conditions it is commonly reported that EC fluxes underestimate surface-atmosphere exchanges (see review by Aubinet et al., 2012). During these conditions the surface can become decoupled from the EC measurement above; the exchange measured over a time interval is therefore not representative of the surface exchange. For example turbulence may be too low for the transportation of CO_2 released overnight from plant respiration to the height of the measurement system. This introduces uncertainty into flux estimates and as a result application of turbulence

criteria to nighttime fluxes has been suggested to avoid flux underestimation (Goulden et al., 1996).

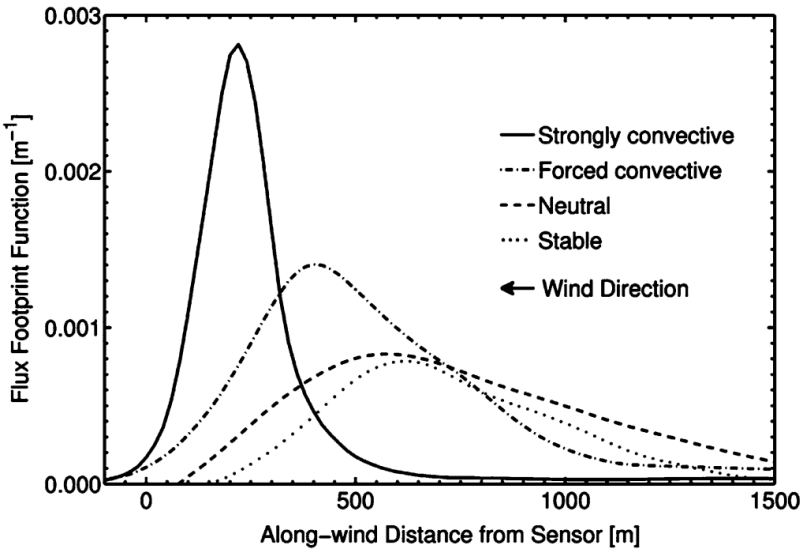

Figure 2.6 Crosswind-integrated footprint for flux measurements of four different cases of stability (strongly convective, forced convective, neutral and stable conditions; measurement height is 50metres, roughness length, z_0, is 0.05 m) obtained by Lagrangian simulation according to Kljun et al. (2002) (Rannik et al., 2012).

2.8 Energy balance closure

Closure of the energy balance is calculated as the energy balance ratio (EBR);

$$EBR = \frac{\sum(Q_E + Q_H)}{\sum(Q^* - \Delta Q_S)}$$

Equation 2.24 The energy balance ratio (Wilson et al., 2002)

Where $Q_E + Q_H$ represents the sum of the turbulent heat fluxes measured by the EC system, and $Q^* - \Delta Q_S$ represents the available energy derived from net radiation observations minus the storage (or ground) heat flux. Theoretically SEB closure is achieved over horizontally homogenous surfaces where the surface cover and roughness characteristics in any upwind distance from the EC tower is uniform. Typically experiments report non-closure of the surface energy balance where the available energy is found to be larger than the turbulent heat fluxes over a range of ecosystems (Aubinet et al., 1999; Wilson et al., 2002; Stoy et al., 2013). Traditionally numerous reasons were provided for non-closure of the surface energy balance including 1) measurement errors associated with EC and radiation fluxes, 2) advection effects during low turbulent conditions, 3) different sampling scales between the net radiation,

turbulent heat fluxes and the ground heat flux and 4) land surface heterogeneity upwind of the measurement tower.

Instrumental improvements in both EC systems and radiation sensors, coupled with more stringent EC data quality screening has meant that potential errors associated with measurement and processing techniques are significantly reduced (Foken et al., 2012b). Furthermore low turbulent conditions, identified using indicators of turbulence intensity such a friction velocity (u_* typically <0.1 m s^{-1}), are found to highlight periods of potential horizontal transfer in the system (e.g. $\Delta Q_A \neq 0$). Energy balance closure as a consequence has been reported as close to unity for high values of u_* over boreal (Sánchez et al., 2010) and subalpine forests (Turnipseed et al., 2002). Careful consideration of scale and the appropriate siting of sensors has also been shown to achieve energy balance closure however these field experiments refer to extremely homogenous surfaces such as deserts (Heusinkveld et al., 2004) and bush land (Mauder et al., 2007a). Broadly speaking however upwind surface heterogeneities give rise to EBRs of between 0.63 and 0.86 (see Foken, 2008b).

2.9 Discussion

This chapter outlined the key scale and theoretical requirements for EC systems in addition to the energy balance and flux footprint concepts required for the correct interpretation of EC flux estimates. Application of Taylor's frozen hypothesis, and the conservation equations allow micrometeorologists to estimate ecosystem exchanges over several timescales, ranging from less than an hour to a year. Combining observations of the turbulent fluxes of latent and sensible heat with net radiation and storage heat flux observations allow for the SEB to be investigated. Each flux exhibits characteristic patterns and are governed by the availability of Q* which is negative overnight and positive during the day. The non-turbulent storage heat flux is a key component of the SEB increasing soon after sunrise to represent heat transfer via conduction to the soil substrate.

Uncertainty in flux estimates are introduced when EC systems are deployed over non-ideal surfaces comprising of non-uniform roughness elements. The use of flux footprints allow for the assessment of EC flux estimates in relation to the ecosystem of interest. Where the flux footprint is not representative of the ecosystem of interest it can

be removed from subsequent analysis and annual sums. Over largely homogeneous surfaces energy balance closure has been achieved however available energy via Q* - ΔQ_S is generally larger than the combined turbulent heat fluxes.

The following chapter will extend the treatment of 1) airflow in the ABL, 2) the SEB and CO_2 flux, and 3) the flux footprint to include investigations undertaken in an urban context. The storage heat flux, typically treated over a plane surface is extended to include a more complex 3-dimensional surface. Furthermore the timing, magnitude and partitioning of the SEB components are altered in relation to natural or managed ecosystems due to the three dimensional structure of the urban surface and the influence of anthropogenic sources of heat and moisture.

Chapter 3 Literature Review

The previous chapter outlined the underlying theory and concepts in relation to EC systems. Central to the method is the appreciation of scale in both the vertical and horizontal directions. Uncertainty is introduced to the fluxes as a surface deviates from the 'idealised' homogeneous surface to which eddy covariance theory relates (See Figure 2.4). However as Baldocchi (2003) argues, fluxes from non-ideal surfaces, like urban surfaces, have value and provide us with a greater understanding of the controls on land atmosphere exchanges of energy, water and carbon dioxide. Careful consideration of spatial scales in the horizontal and vertical direction must be maintained when undertaking EC measurements if we wish to transfer the underlying EC theory and concepts to the urban surface. Section 3.1 will outline the vertical scales of the ABL over the urban surface in addition to the main characteristics of airflow therein. The development of guiding principles for climatological measurement techniques in urban areas (Oke, 2004), coupled with the establishment of the Local Climate Zone (LCZ) classification scheme (Stewart and Oke, 2009) has allowed for investigations over 'non' ideal, urban surfaces to be achieved and subsequent theory to be developed. This framework will be outlined in Section 3.2.

This chapter will also outline and describe the key controls, surface, synoptic and latitudinal, that affect the radiation budget and surface energy balance (SEB) of the urban surface. Section 3.3 will outline how the budget differs from natural or vegetated canopies and under different synoptic conditions. In a similar style literature concerning the components of the urban SEB will be discussed in Section 3.4 in relation to the surface and synoptic factors that drive changes in the partitioning of turbulent heat fluxes. Conditions of non-closure of the SEB will be explored in section 3.5 with reference to urban flux footprints. Particular attention will also be paid to the advantages and limitations of using flux footprints in urban areas that have been developed for ideal, homogenous terrain. The fluxes of storage heat and anthropogenic heat will be addressed in Sections 3.6 and 3.7 in terms of the difficulties in directly measuring these terms and methods to parameterize and model them. CO_2 flux investigations have increased dramatically in urban areas over the last decade and Section 3.8 will summarise international findings and the key controls reported in the published literature.

3.1 The atmospheric boundary layer over urban surfaces

As air flow encounters the urban surface it experiences a change in surface characteristics from the rural surface due to urban modification (Oke, 1987). The physical presence of the city through its form and function serves to alter vertical gradients of temperature, momentum, moisture and pollutants in what is referred to as the urban boundary layer (UBL) in comparison to its rural counterpart. Observational investigations should therefore begin at the scale that alters these gradients. As Nunez and Oke outline the city is complex in terms of its structure however "there are some representative urban surface units whose basic form is repeated throughout the urban area" (1977:11). These basic units largely consist of vertical and horizontal facets arranged so that they form 3-dimensional structures known as urban canyons (Nunez and Oke, 1977). This urban surface unit is repeated worldwide and provides the basis for the study of modern urban climatology.

3.1.1 *Vertical scales of the UBL*

The existence of an urban boundary layer (UBL) is analogous to the ABL structure in 2 main ways, 1) the UBL comprises of a SL and ML; within the SL fluxes are strongly characterised by the underlying surface, while the mixing layer contains a composite signal of multiple urban neighbourhoods and 2) the SL is disaggregated into sublayers according to behaviour of the mean wind and vertical fluxes of energy mass and momentum. The atmosphere extending from the ground to the roof tops is referred to as the urban canopy layer (UCL) (Figure 3.1c). Within the UCL vertical gradients in temperature, moisture and pollutants will be strongly dependent on individual roughness elements, such as a building's access to solar radiation (shading versus sunlit streets), the presence of water at the surface, and heat and pollutant emissions from vehicles (Roth, 2000). Conducting observations within the street canyon allows investigators to study micro-scale climate effects (Figure 3.1c). Each surface has its own microclimate the scale of which varies from less than one metre to hundreds of metres (Oke, 2007). For example, observations of air temperatures conducted at or below the height of the street canyon in the UCL reveal differences of several degrees over small spatial scales as a result of solar shading or solar trapping within the canyon.

The roughness sublayer (RSL) includes the UCL and extends above the top of the roughness elements to at least one to two times their height or spacing where the

influence of the roughness elements is mixed up by turbulence (Rotach, 1999) (Figure 3.1b and c). The vertical extent of the RSL can also be stability dependent, typically higher for unstable stratification (e.g. Garratt, 1980). Wake diffusion and the heterogeneity of sources and sinks of momentum and scalars in the RSL lead to a non-uniform turbulence field and local-advection is common (Roth, 2000). Ultimately within this layer airflow is highly irregular and is still strongly affected by the nature of individual roughness elements (Rotach, 1999; Grimmond, 2006; Oke, 2007).

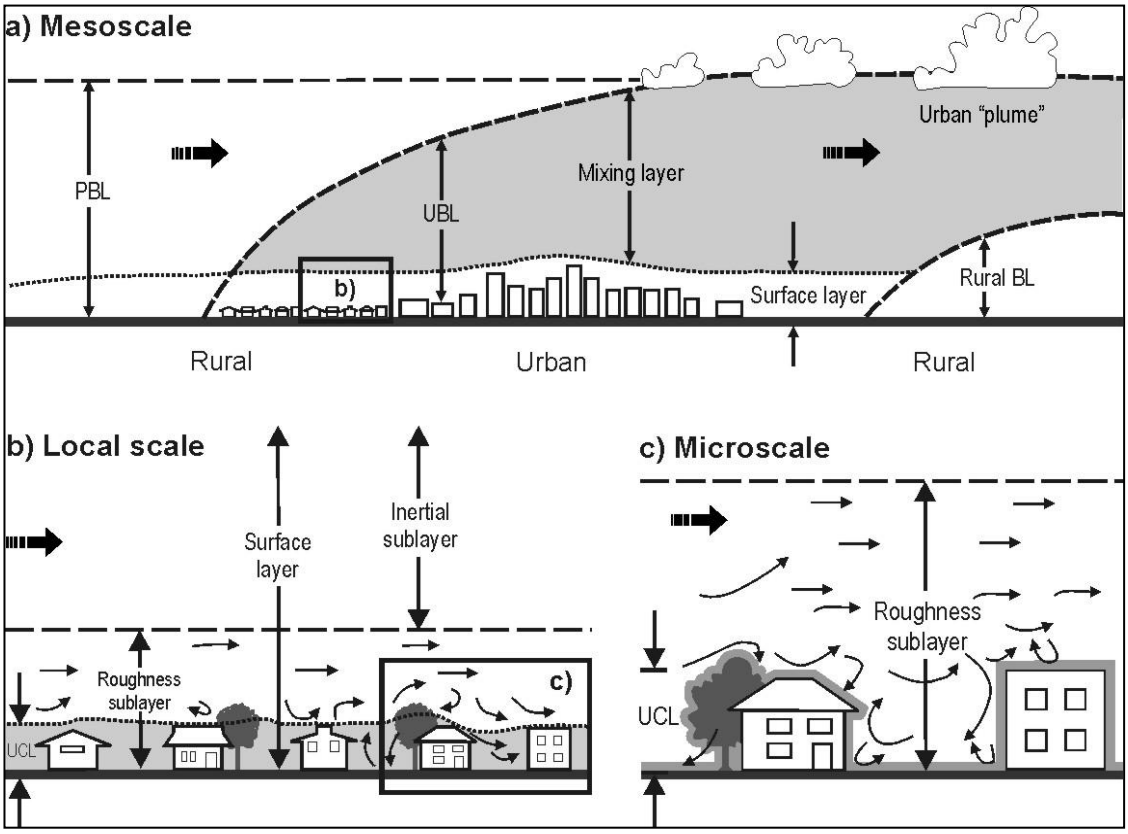

Figure 3.1 Schematic structure of the ABL, referred to here as the Planetary Boundary Layer (PBL), illustrating the climate scales and vertical sublayers found in urban areas (Oke, 2007).

Experimental studies have shown that constant fluxes can be observed in the UBL according to scaling factors above the local roughness elements. This is found to be 1.5-2 times the average height of the roughness elements (z_H), within the constant flux layer (CFL) or inertial sublayer (ISL) (Rotach, 1995; Rotach et al., 2005; Oke, 2007) (Figure 3.1b). Within the ISL observations will correspond to a spatially-integrated local-scale signal where fluxes are almost constant with height (Grimmond, 2006). The focus of urban EC observations has therefore been in the ISL permitting the application of integrated one point conservation equations over the urban surface (e.g. Christen and Vogt, 2004; Offerle et al., 2006a; Vogt et al., 2006; Piringer et al., 2007). The vertical extent of the ISL is determined by the development of internal boundary layers

(outlined in section 3.1.2) which are influenced by meso-scale land use changes in the upwind surface.

Above the ISL is the ML (Figure 3.1a) where turbulent properties are most likely independent of the underlying surface roughness, however relatively few observations exist at this height due to the height restrictions of measurement towers (Roth, 2000). Conducting measurements in the ML will yield measurements more representative of the whole city (e.g. Wood et al., 2010). Data from multiple stations are required however for a thorough and complete depiction of the meso-scale city climate (Oke, 2007).

3.1.2 *Airflow within the UBL*

Although an understanding of the vertical layers of the UBL is important, an appreciation of surface change in the horizontal direction is fundamental in order to make assumptions regarding horizontal homogeneity for urban EC applications. Furthermore an appreciation of change in the horizontal direction will explain the existence and development of internal boundary layers (IBLs). IBLs develop as air comes into contact with new surfaces that possess different thermal and surface properties, for example roughness elements of differing heights and density (Rotach, 1999). If for example, air travelling over a flat homogeneous surface comes into contact with an urban surface the air will be churned up via mechanical forces in response to the change in roughness. The effect of this will reduce the mean wind speed at the ground and hence the wind profile.

Airflow over an urban surface experiences greater surface drag due to the presence of increasingly rough urban structures. In a homogenous environment, such as a grassland, the surface itself serves as the dominant momentum sink. At increasing urban densities however the airflow cannot penetrate inter-element air spaces as efficiently and the roughness elements (e.g. buildings) become the dominant energy sink (Grimmond and Oke, 1999a). This means that the logarithmic profile assumed over flat homogenous surfaces is effectively displaced vertically in the urban situation to the mean height of the momentum sink, a height close to the top of the roughness elements known as the zero-plane displacement height (z_d) (Figure 3.2). z_0, the roughness length is the height at which the wind velocity approaches zero in the logarithmic profile (Figure 3.2).

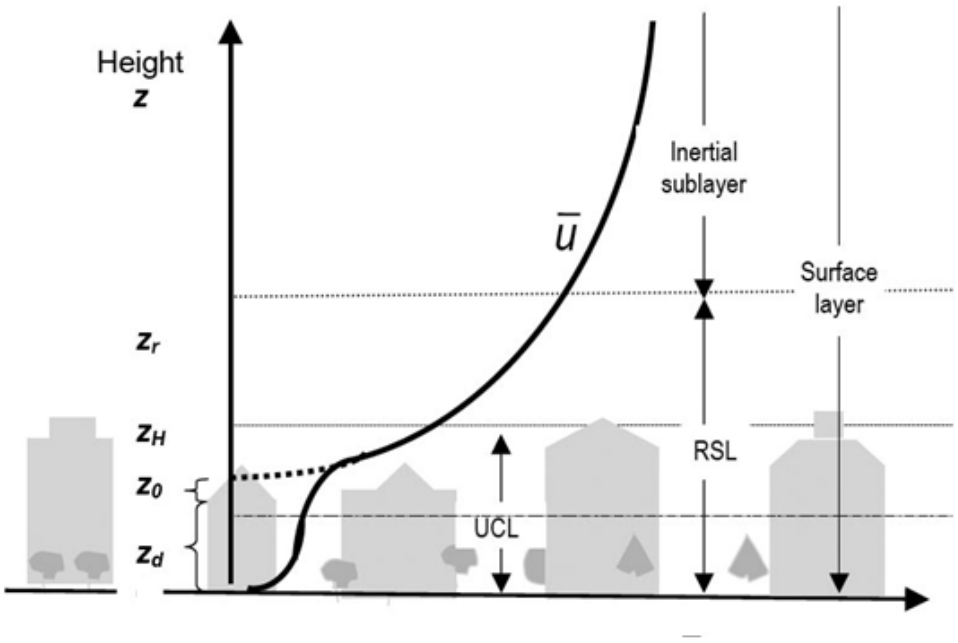

Figure 3.2 The logarithmic wind velocity profile over a dense urban surface , illustrating mean wind speed ū, the height above ground (z), the zero plane displacement height (z_d), the aerodynamic roughness length (z_0), the mean height of the roughness elements (z_H) and the blending height (z_r) (Oke 2007).

Wind tunnel studies revealed 4 main flow zones surrounding a sharp-edged building; A - undisturbed, B – displacement, C – cavity and D – wake (Figure 3.3a). As the mean flow approaches the impermeable building air is either deflected over the top, down the front or around the sides of the building giving rise to differential pressures on the windward building surface. Greatest pressure is exerted in the upper middle part of the windward side where the wind is effectively stopped, creating a stagnation point (Oke, 1987; Munger et al., 2012).

Pressure on the windward side decreases away from this stagnation point and wind flow accelerates around the sides (horse shoe vortex in Figure 3.3b) and over the top of the building (displacement zone) (Figure 3.3a and b). As the flow encounters the sharp edges of the building sides and roof it separates from the building surface to create low pressure zones in the immediate vicinity of the building sides and roof. Air subsequently moves from high to low pressure giving rise to reverse flows and a cavity eddy circulation zone at the leeward side of the building (Figure 3.3a C). The mean wind speed is typically reduced in the wake zone however residual turbulence here continues to facilitate momentum transport at a greater rate than in the undisturbed zone on the windward side of the building (Oke, 1987;1988). As the density of a building

array increases so too does the roughness of a surface, however at increasing densities where the buildings are closely packed the effective drag is reduced due to sheltering effects. In these situations the main flow (in a normal direction to the buildings) reported from wind tunnel experiments is reported to detach from the surface below to form a skimming flow where building height to street width (H/W) ratios are greater than 0.65 (Hussain and Lee, 1980) (Figure 3.4c). In the same investigation at low densities (H/W<0.3) the flow is characterised as isolated where buildings are spaced far apart so that their flow regimes do not interact, and finally at medium densities (H/W<6.5) the flow is typically described as wake interference flow. In this situation the buildings are spaced close enough to reinforce each other's wake effects, in other words, the leeward eddy interacts with the displaced flow at the windward side of the next building (Oke, 1987;1988) (Figure 3.4b).

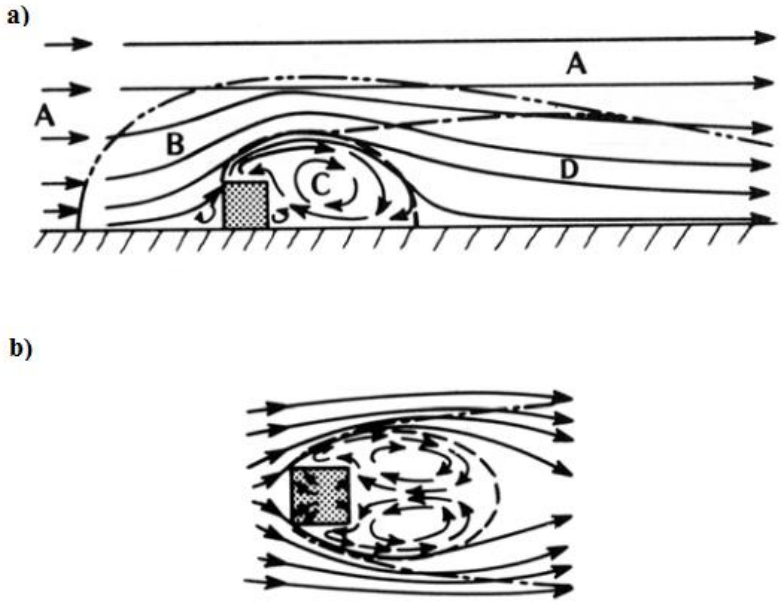

Figure 3.3 Flow pattern around a sharp-edged building, side view of a) streamlines and flow zones (see text for description of A-D) and b) plan view of streamlines with building oriented normal to the flow (Modified from Oke, 1987:265).

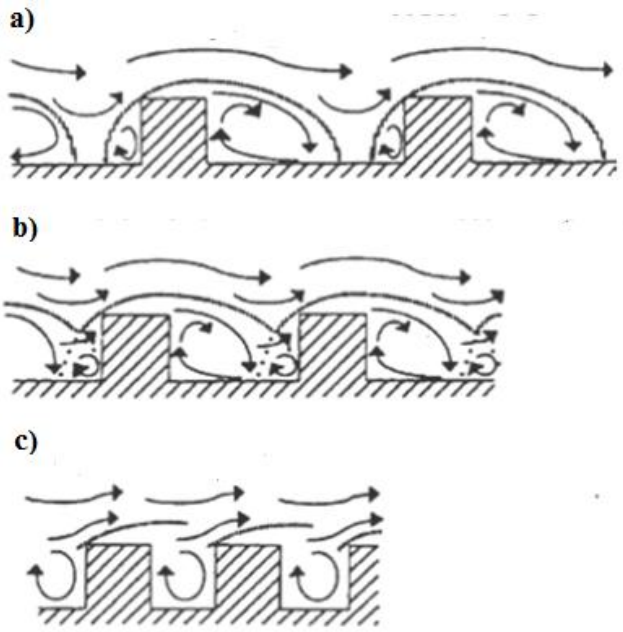

Figure 3.4 The flow regimes associated with air flow over building arrays of differing height/width ratios, a) isolated flow regime over low density surface, b) wake interference flow over a medium density surface and c) skimming flow regime over a high density urban surface. Modified from Oke (1988a:105).

Deriving surface roughness parameters such as z_d and z_0 for an urban surface is required when attempting to characterise the flow regime as isolated, wake interference or skimming. Two methods exist to determine these aerodynamic properties, namely micrometeorological (using anemometers) and morphometric (geometric). Micrometeorological methods require wind profile field observations from either 1) slow response windspeed sensors at 3-4 different heights or 2) a fast response 3D sonic anemometer (allowing for the determination of friction velocity, u_*). Careful siting of the instrumented tower is required, in addition to stratification of the datasets because variations in the wind direction may represent upwind areas of differing roughness and hence differing wind fields (Grimmond et al., 1998).

Morphometric methods on the other hand require more readily available datasets in the urban domain; information on the geometry and spacing of the roughness elements. When input into geographic information systems (GIS) building footprint data is employed to derive variables such as 1) the frontal area density (λ_f) expressed as

$$\lambda_f = \frac{A_f}{A_d}$$

Equation 3.1 Frontal area fraction of roughness elements (Grimmond et al., 1999)

and 2) the plan area density (λ_p) expressed as,

$$\lambda_p = \frac{A_p}{A_d}$$

Equation 3.2 Plan area fraction of roughness elements (Grimmond et al., 1999)

Where A_d is the lot area of roughness elements (calculated as the total surface area divided by the number of roughness elements), A_f is the frontal area of roughness elements, A_p is the plan area of roughness elements, λ_f is the frontal area fraction of roughness elements, and λ_p is the plan area fraction of roughness elements. The plan area density is used to describe how dense an urban surface is, typically λ_p ranges from 0.05-0.4 for low density surface, 0.3-0.5 for medium density surfaces and 0.5-0.8 for high density surfaces (Grimmond and Oke, 1999a) (Figure 3.3.5).

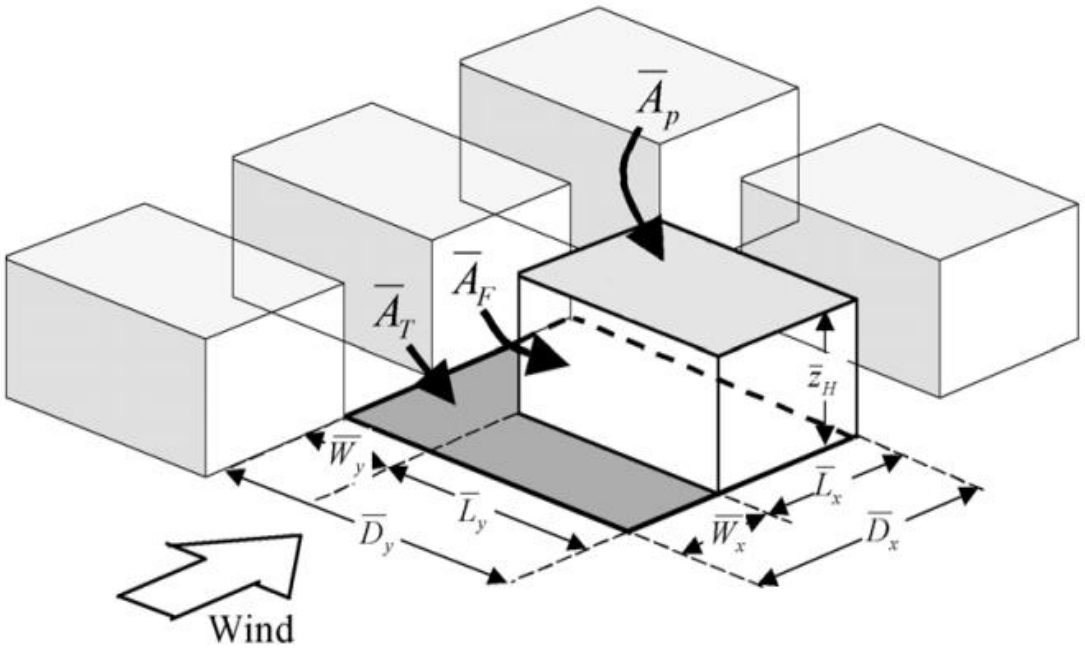

Figure 3.3.5 Deriving the plan area and frontal area densities using building dimensions of an urban array (Grimmond and Oke, 1999a:1263).

A comparison of values for z_d and z_0 for 11 sites in seven North American cities using common morphometric methods was undertaken by Grimmond and Oke (1999a) and included 1) simple height-based, rule-of-thumb methods where z_d is estimated as 0.7 z_H and z_0 is estimated as 0.1 z_H, 2) methods that use height and plan area density, and 3) methods that use height, plan area density and frontal area density (see Grimmond and Oke, 1999a for a complete set of equations). The results of the comparison show that almost all morphometric methods produce reasonable values for z_d and z_0 and unlike the

original method proposed by Lettau (1969), methods by Macdonald et al. (1998) successfully predict declining roughness at large densities (i.e. skimming flow) (Grimmond and Oke, 1999a). Typical values presented by Grimmond and Oke (1999a) for roughness and aerodynamic properties in urban areas are presented below in Table 3.1.

Table 3.1 Typical roughness properties of homogeneous zones in urban areas (taken from Grimmond and Oke, 1999a:1281)

Urban surface form	$\overline{z_H}$ (metres)	$\overline{z_d}$(metres)	$\overline{z_0}$(metres)
Low height and density Residential- one or two storey single houses, gardens, small trees. Mixed houses and small shops. Warehouse, light industrial, few trees.	5-8	2-4	0.3-0.8
Medium height and density Residential- two and three storey large or closely spaced, semi-detached and row houses, large trees. Less than five storey blocks of flats with open surroundings. Mixed houses with shops, light industry, churches, schools.	7-14	3.5-8.0	0.7-1.5
Tall and high density Residential- closely spaced<six storey rows and block buildings or major facilities (factory, university, etc.), town centre.	11-20	7-15	0.8-1.5
High-rise Urban core or suburban nodes with multi-storey tower blocks in dense urban surroundings. Major institutional complexes.	>20	>12	>2.0

Morphometric methods are reported as advantageous in that they are cost effective, require widely available building footprint data, and are capable of calculating z_d and z_0 for all wind directions in comparison to micrometeorological methods which may not yield sufficient data for all wind directions. One year long datasets from slow and fast response sensors pertaining to Chicago and Los Angeles were not sufficient to determine roughness parameters for all wind sectors (Grimmond et al., 1998). That said however anemometric methods allow for the determination of z_d and z_0 during leaf on and leaf off periods for urban areas where the porosity of trees in winter is increased leading to smaller values of z_d (<5%) and z_0 (<13-18%) (Grimmond et al., 1998).

3.1.3 *Turbulence characteristics in the UBL*

In addition to changes in the wind profile, roughness elements at the urban surface considerably alter the turbulence field in relation to homogenous rural surfaces due to a number of factors. Wake effects serve to reduce the mean wind velocity between roughness elements; however the roughness elements and form drag induce enhanced mechanical turbulence. This leads to higher turbulence intensities and efficient vertical mixing and diffusion of momentum, heat, moisture or any other scalar quantity (Roth, 2000; Feigenwinter et al., 2012). The size of the eddies responsible for this efficient mixing is related to the dimensions of the wake-shedding roughness element, smaller elements contributing less to the vertical transport of momentum, heat and moisture.

High turbulent intensities are also generated at the top of the UCL due to an intense shear layer where mean kinetic energy is converted into turbulent kinetic energy. Shear stress over dense urban surfaces is greatest at the top of the UCL, decreasing to zero below the canopy due to the roughness elements serving as the dominant momentum sink. Coherent structures, such as sweeps and ejections, may also exist in the turbulent field due to a regularity of the building structures and are efficient in transporting heat (Feigenwinter et al., 2012) (Figure 3.6). Sweep motions are characterised by high-velocity fluid moving downwards towards the surface (where $u'>0$ and $w'<0$) and ejections are characterised by low-velocity fluid moving from within the UCL upwards (where $u'<0$ and $w'>0$) (Oikawa and Meng, 1995).

The extreme heterogeneity of the urban surface in terms of momentum and scalar sources and sinks leads to dissimilarities in the vertical transport of energy and mass. The physical presence of a building modifies the radiative, thermal, moisture and aerodynamic properties of the surrounding surface. Radiative effects (described in more detail in Section 3.3) serve to create sunlit and shaded surfaces in the vicinity of the building giving rise to localised areas of surface heating and cooling. Precipitation is unevenly distributed at the surface due to sheltering and interception effects by the building (Oke, 1987). Air flow is significantly modified around and above buildings giving rise to areas of higher and lower turbulent intensities. Gradients at the surface arise as result of these heterogeneities and local advection is very likely (Feigenwinter et al., 2012). Enhanced mechanical turbulence due to roughness elements, coupled with

nocturnal heat release due to urban heat island (UHI) effects, both serve to reduce atmospheric stability and increase boundary-layer heights in comparison to rural surfaces. The existence of the stable NBL is therefore reduced and very often the urban atmosphere remains unstable throughout the nighttime (discussed in greater detail in Section 3.5) (e.g. Christen and Vogt, 2004).

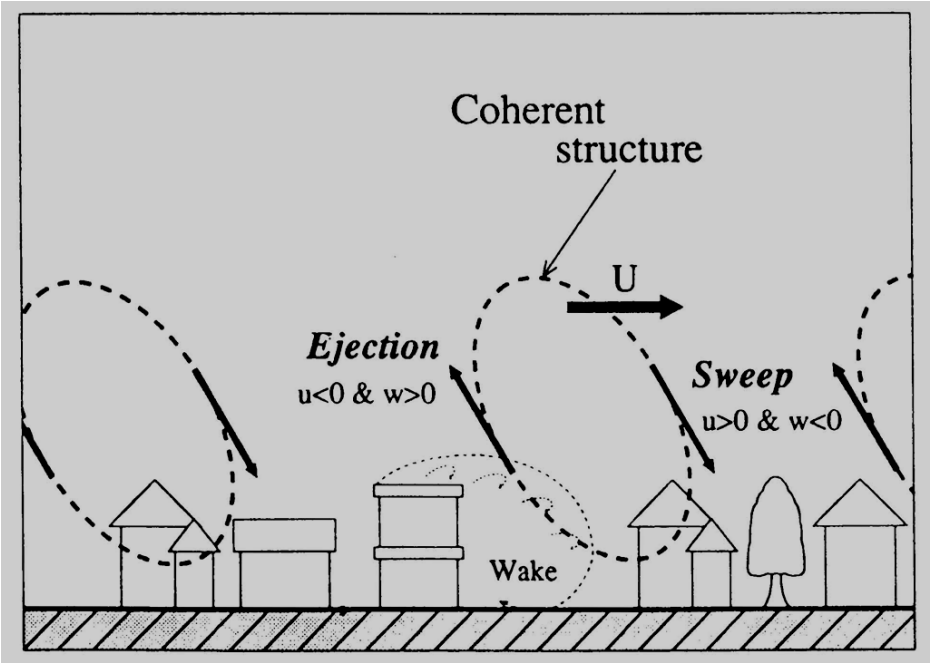

Figure 3.6 Schematic representation of coherent structures; sweeps and ejections in and above the UCL, here U represents the mean air flow direction (Oikawa, 1993).

3.2 Implementing a conceptual framework for urban based observational studies

The properties of the air, at some distance upwind of the change in surface characteristics (i.e. the fetch), will eventually become blended vertically by turbulence. When EC instruments are located at a sufficient fetch from a surface change and are of sufficient height above street-level, measurements represent a spatially-integrated flux of multiple micro-climate effects distinctive to the local-scale environment of interest (Grimmond 2006; Oke 2007). Hence it can be argued that conducting measurements at the horizontal boundary of distinctive surface changes does not ensure representative measurements of one single landscape and deems data interpretation more difficult for the investigator because the air has not yet come into an equilibrium state with the underlying surface. Rather, in order to measure the neighbourhood- or local- scale EC fluxes, referring to scales of one kilometre to several kilometres, observations must be

conducted sufficiently within a distinctive urban subtype, for example a suburb of a given density with largely homogeneous properties.

Under these specifications EC observations yielded in the ISL should represent a spatially blended average representative of the local-scale underlying surface. That said however the representative siting of EC towers, to facilitate meaningful, measurable inter-site comparison, is difficult in the absence of a well-defined conceptual framework representing distinctive local-scale urban surface subtypes (Stewart, 2011). Data from observational campaigns had been criticised as representing idiosyncrasies of individual observational sites, limiting the comparability of urban climate observations across cities with similar background climates. In response to criticisms field researchers increasingly partook in collaborative studies enabling the collection and synthesis of climate data from distinctive urban subtypes and from within single cities (Christen and Vogt 2004; Grimmond et al. 2004; Rotach et al. 2005; Vogt et al. 2006).

Standardisation in terms of site selection criteria was ultimately established in a publication commissioned by the World Meteorological Organisation (WMO) (Oke, 2007) that provided urban climatologists with recommendations and a framework in which to conduct urban climate observations. Subsequently Stewart and Oke (2009) called into question the heuristic value of the traditional rural-urban classification and presented a classification system that disaggregates the universal landscape into distinctive local climate zones (LCZs). This scheme takes into account all non-vegetated, vegetated and urban landscapes (Figure 3.6). In this way the landscape is treated in terms of measurable indicators that serve to modify the wind, thermal and moisture gradients in the UBL.

The classification scheme requires that observational programmes present quantitative station metadata along with their reported findings. Scientists compare their station metadata to the LCZs and select the most appropriate fit with the templates provided by Stewart and Oke (2012). Metadata includes measured indicators such as average building and tree height, sky view factor (SVF), the canyon-aspect ratio or H/W ratio, surface roughness, impervious, pervious and building surface fractions, surface albedo and photographs to illustrate predominant land use in the local neighbourhood (Stewart and Oke, 2012). It serves as a framework within which to site meteorological

instruments and is intended to increase the applicability, and comparison, of observational studies to the wider urban climate community. Transparency in this regard also allows anomalies to be investigated and tested with the overall intention of developing distinctive theory pertaining to each local climate zone.

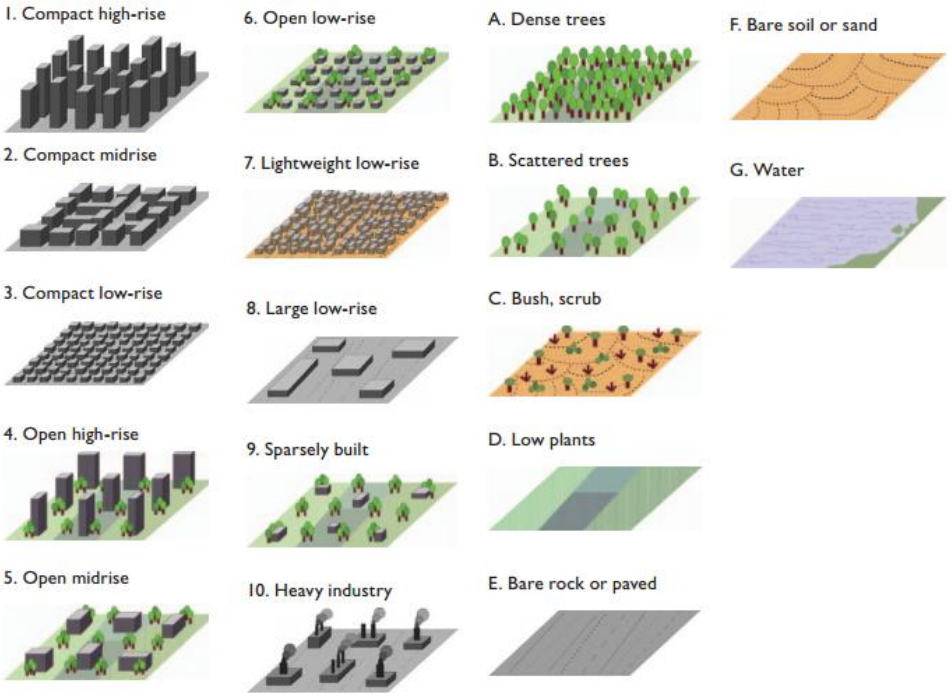

Figure 3.6 Local climate zone classification system (Stewart and Oke, 2012).

3.3 The radiation budget of the urban surface

The following section outlines urban effects on the radiation budget. The magnitude and portioning of the radiation budget components are altered in distinctive ways in comparison to the those pertaining to a natural surface largely due to the properties of the urban atmosphere (altering incoming radiative fluxes) and the urban surface (altering outgoing, or emitted radiative fluxes). Direct measurements of radiation budget components are largely from mid-latitude developed cities (e.g. Grimmond and Oke, 1995; Stanhill and Kalma, 1995; Offerle et al., 2003; Christen and Vogt, 2004; Moriwaki and Kanda, 2004; Bergeron and Strachan, 2012; Kotthaus and Grimmond, 2014a). There have been some exceptions to the above which include investigations carried out in lower latitudes with relatively more consistent day lengths throughout the year (e.g. Grimmond and Oke, 1995; Jauregui and Kuyando, 1999; Offerle et al., 2005a; Jonsson et al., 2006; Newton et al., 2007; Ferreira et al., 2013).

3.3.1 *Urban geometry and its effects on the radiation budget*

Terjung and Louie (1973) and Nunez and Oke (1977) in unison with later findings reported by Harman et al. (2004) demonstrate a strong link between radiative energy exchanges and the geometry of the urban canyon. They argue that knowledge of 1) the H/W ratio and 2) the SVF will aid in the evaluation of the urban radiation budget. The sky view factor defined by Svensson (2004:201) is "the ratio between radiation received by the planar surface and the entire hemispheric radiating environment". It can be described as a measure of the openness of the sky to radiative transport (Figure 3.7). The SVF at ground level of densely built-up, urban areas will generally be made up of a greater proportion of buildings and trees, at the expense of the relatively colder sky, which serves as a radiative sink (Oke, 1979). Greater obstruction equates to greater amounts of outgoing radiation (K↑ and L↑) being intercepted and re-radiated within the relatively warmer urban canyon (Svensson, 2004).

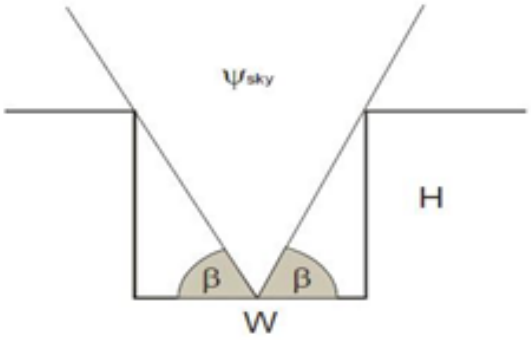

Figure 3.7 A depiction of the sky view factor at the ground surface in a symmetrical street canyon, described by its width (W) and its height (H), ψ Sky is the SVF (Source: www.urban-climate.org).

The H/W ratio, inherently linked to the SVF, also exercises an important influence over the net radiation budget - increasing it increases the total surface area, relative to a flat surface and hence the number of facets between which radiative exchange and reflections can take place (Harman et al., 2004). This surface area enlargement is the main cause of radiation budget modification in urban areas. H/W ratios for suburban locations typically range from 0.2-0.4 where radiative exchange is largely between the sky and road surface; conversely for dense city-centres with H/W ratios closer to 1, radiative exchange occurs between adjacent wall facets, roads and the sky (Harmann et al., 2004). Multiple reflections of radiation should therefore not be neglected when evaluating the Q* of an urban area (Terjung and Louie 1973; Harman et al., 2004).

Pearlmutter et al. (2005) employed an open-air scale model of a building-street canyon surface array to investigate the SEB of 2 urban configurations, a 1-storey and 2-storey scale model. The 2-storey array model revealed a higher peak in net all-wave radiation (Q*), and also a greater daytime total (when Q* >0) of between 15-20% in comparison to the 1-storey surface The authors attribute the difference in Q* to increased radiative trapping by the 2-storey model, in addition to a lower mean surface albedo. The lower albedo pertaining to the 2-storey array is due to the increased building height, inhibiting the propagation of K↑ to the sky.

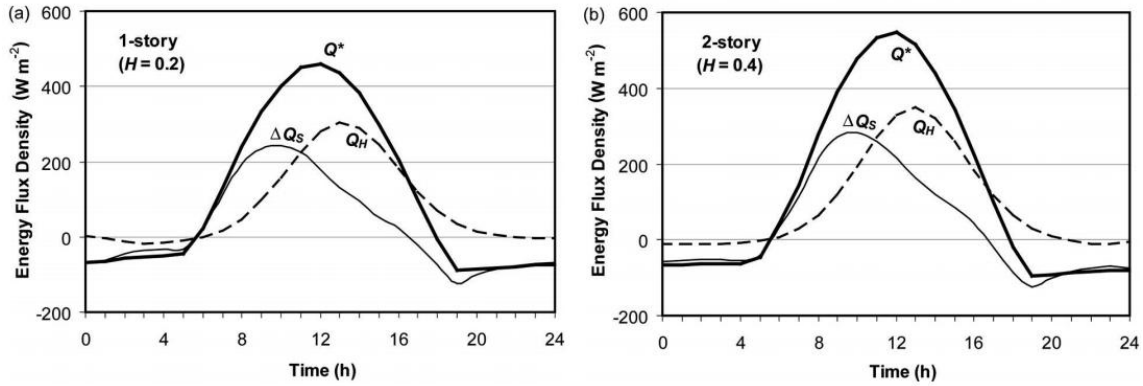

Figure 3.8 Diurnal summer cycles of net radiation (Q*), sensible heat flux (Q_H) and the storage heat flux change (ΔQ_S) for (a) 1-storey (H = 0.2m) and (b) 2-storey arrays. (Source: Pearlmutter et al., 2005).

3.3.2 *Albedo and reflected shortwave radiation in urban areas*

Building materials commonly sourced in urban environments include asphalt, concrete, slate and ceramic tiles, brick, stone, corrugated iron, and glass, each of which possess a unique value for albedo and emissivity (typical values are presented in Table 3.2). Albedo is typically reported as being smaller in urban areas relative to rural areas, with a minimum in the middle of the day coincident with higher sun elevation angles (Ferreira et al., 2012). Albedo typically ranges from 0.10 to 0.27 in urban mid latitude cities that are snow free and are on average 0.15 (Table 3.2) (Oke 1987; Offerle et al., 2003). Kondo et al. (2001) report however that albedo values will be higher when the building height is small, open spaces are wide and when building height is relatively uniform.

Christen and Vogt (2004) report bulk surface albedo of around 0.1 for the 2 urban sites and 0.32 for an urban site where the total source area of the downward facing pyranometer is from a light-coloured concrete car park. This trend was also observed in Melbourne, Australia, where higher albedos at the urban location (0.19 versus 0.15 at a

suburban location) are attributed to light-coloured concrete and corrugated iron used as rooftop materials in the surrounds on the measurement station. Łódź, Poland reported an even lower bulk albedo of 0.08 which was similar to that reported in Marseille (Lemonsu et al., 2004) suggesting that dense European cities may be better absorbers of K↓ than less dense North American city surfaces with typically wider canyons (Christen and Vogt, 2004).

Table 3.2 Radiative properties of typical urban materials and areas

Surface	Albedo(α)	Emissivity (ε)
1.*Roads*		
Asphalt	0.05-0.20	0.95
2.*Walls*		
Concrete	0.10-0.35	0.71-0.90
Brick	0.20-0.40	0.90-0.92
Stone	0.20-0.35	0.85-0.95
Wood		0.90
3.*Roofs*		
Tar and gravel	0.08-0.18	0.92
Tile	0.10-0.35	0.90
Slate	0.10	0.90
Thatch	0.15-0.20	
Corrugated iron	0.10-0.16	0.13-0.28
4.*Windows*		
Clear glass		
Zenith angle less than 40°	0.08	0.87-0.94
Zenith angle 40 to 80°	0.09-0.52	0.87-0.92
5.*Paints*		
White, whitewash	0.50-0.90	0.85-0.95
Red, brown, green	0.20-0.35	0.85-0.95
Black	0.02-0.15	0.90-0.98
6.*Urban areas**		
Range	0.10-0.27	0.85-0.96
Average	0.15	~0.95

*** Based on mid-latitude cities in snow-free conditions. Table reproduced from Oke (1987:281).**

Seasonal variations in K↑ and albedo are inherently linked to 1) latitude and the solar azimuth angle governing K↓ 2) snow cover effects and 3) vegetation effects. Albedo can increase in the presence of snow cover, a phenomenon observed in Chicago (0.23 versus 0.16 normally), Łódź (0.09 versus 0.07 normally) and Montreal (0.13-0.44 for an urban site in March and December respectively). Intra-city investigations in Basel,

Switzerland and Montreal, Canada revealed albedo values of 0.7-0.85 for their rural locations where snow cover was not disturbed or removed. For suburban and urban locations with snow-free walls, shading effects, faster snow melt, and snow removal by city councils/departments albedo values were 0.15 and 0.17 in Basel (Christen and Vogt, 2004) and 0.3 and 0.44 in Montreal (Bergeron and Strachan, 2012). Figure 3.9a illustrates Q* and albedo for a clear-sky winter day for the rural (R3) and urban site (U1) in Basel. Q* at solar noon was approximately 190 versus 10 W m^{-2} at U1 and R3 respectively when the corresponding albedo values were 0.1 and 0.7 respectively. As previously mentioned, albedo displays a minimum during the day coincident with higher solar elevation angles, increasing at low solar elevations during sunrise and sunset due to increased reflectance of horizontal surfaces at less than or equal to solar elevation angles of 20 degrees (Figure 3.9a).

Vegetation in general has a higher albedo than constructed surfaces; see Oke (1987) for typical values pertaining to natural surfaces. The albedo of urban locations with a high proportion of vegetated surface will therefore have higher albedos that may vary seasonally when the trees are in leaf and when they are in decay. In winter, neighbourhoods with tall and dense vegetation may induce shading of snow covered areas serving to decrease the bulk albedo property of the location in winter time, a phenomenon observed in Montreal (Bergeron and Strachan, 2012).

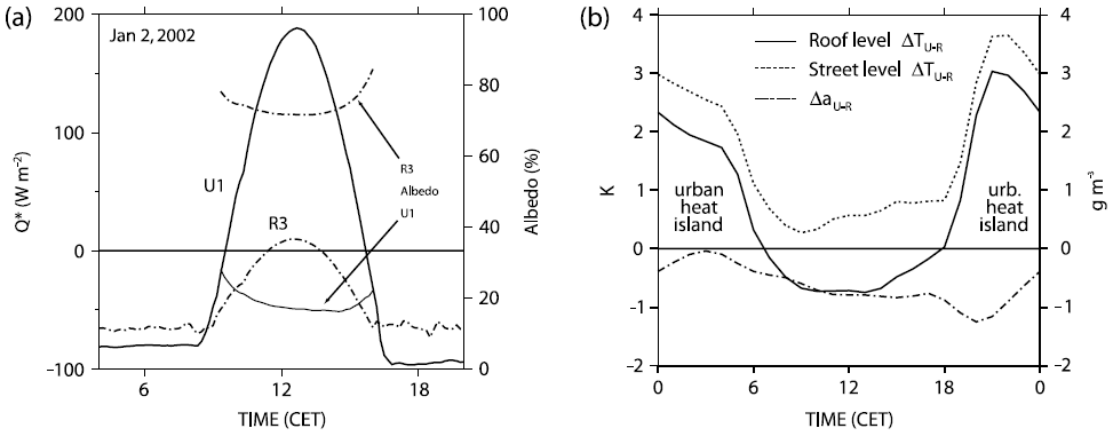

Figure 3.9 (a) Net radiation Q∗ and albedo during a clear winter day with a 20 cm snow cover. Solid lines are measurements over the urban surface (U1); dashed–dotted lines are simultaneously measured rural values (R3). (b) Urban–rural differences in air temperature (ΔT U–R) and absolute humidity (Δa U–R). Temperature and humidity values are an average of U1 and U2 (urban) and R1, R2 and R3 (rural) over the summertime IOP from 10 June to 10 July 2002. Solid lines are measurements over the urban surface (U1); dashed–dotted lines are simultaneously measured rural values (R3). Roof-level temperatures (K) are measured 5 m above z_H; street-level temperatures are from instruments operated inside street canyons at U1 and U2 (2–3 m above ground) (Christen and Vogt, 2004:1406).

In general seasonal variations in albedo are largely attributed to vegetation effects in St Louis, Hartford and Basel (White et al., 1978; Brest, 1987; Christen and Vogt, 2004) and to geometric and snow effects in Chicago, Łódź and Montreal (Offerle et al., 2003; Offerle et al., 2006a; Bergeron and Strachan, 2012).

3.3.3 *Incoming shortwave radiation in urban areas*

The actual amount of K↓ received at a horizontal surface per unit area strongly depends on latitude, time of year and time of day. Furthermore for an urban area turbidity is influenced primarily by various man-made sources of aerosols, as oppose to rural or ocean boundary layers where turbidity is more influenced by pollen and sea spray respectively (Ayra, 2001).

In contrast to previous findings from large or mega cities K↓ in Basel, Switzerland and Oberhausen, Germany was observed to be a similar magnitude across the urban and rural sites (Christen and Vogt, 2004, Goldbach and Kuttler, 2013). Stanhill and Kalma (1995) detected significant decreases in K↓ for Hong Kong (-33%) between measurements over a 35 year period. This decrease was attributed to increased aerosol loading as a result of a doubling of population and a seven-fold increase in energy use over the study campaign (Stanhill and Kalma, 1995). Jauregui and Luyando (1999) report decreases of K↓ (-21.6%) at the surface for a rural and urban site in Mexico City, where attenuation is due to increased absorption and reflection by a smog layer. Similarly in Cairo, Egypt, the ensemble-average difference in K↓ at solar noon between Cairo University (urban location) and the rural location was -62 W m^{-2} and was attributed to increased pollution in the city (Frey et al., 2011). Basel and Oberhausen, by comparison, are considered to be a mid-sized city where aerosol concentrations were not as influential in attenuating K↓ at the urban location. Christen and Vogt (2004) also attribute the spatially conservative nature of K↓ with the close proximity of the conjoining urban and rural areas in Basel.

According to Grimmond and Oke (1995) meteorological conditions may also affect the transmission of K↓. During an inter-city observational campaign, it is suggested that previous precipitation events in the city of Chicago served to cleanse the atmosphere of dust and pollutants, thus increasing the receipt of K↓ at the surface on a clear-sky day in comparison to cities such as Los Angeles, Sacramento and Tucson under clear skies.

Ferreira et al. (2012) attributed maximum receipt of K↓ in São Paulo, Brazil to below normal values for relative humidity and precipitation, indicative of clear sky conditions. Gorbarenko and Abakumova (2011) also report cloudiness as a key factor in reducing K↓ and hence Q*, and the effect is clearly demonstrated for Miami by Newton et al. (2007) (Figure 3.10). K↓ at solar noon is reduced from approximately 900 to 600 W m^{-2} at solar noon and Q* is reduced proportionally from 700 to 400 W m^{-2} (Newton et al., 2007) during cloudless and all-sky conditions.

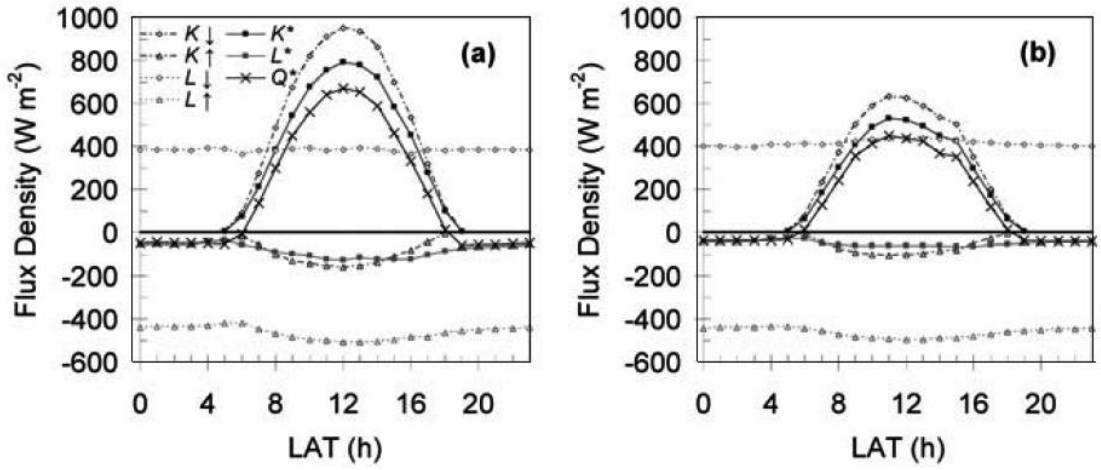

Figure 3.10 Ensemble hourly averaged radiation flux densities measured over a 40-day period in a Miami suburb in 1995 (Day of year 133-172) in a) cloudless and b) all-sky conditions according to local apparent time (LAT) (Newton et al., 2007).

Long term measurements from the Meteorological Observatory of Moscow State University (Gorbarenko and Abakumova, 2011) and Tokyo (Moriwaki and Kanda, 2004) exhibit very large seasonal differences in the receipt of K↓ due to differences in the solar azimuth angle, for example, in Tokyo K↓ was 900 versus 500 W m^{-2} at solar noon between July and December respectively. Observations in a dense city centre location in London, England, a similar latitude to Dublin, reveal significant seasonal variation in each of the radiation budget components (Figure 3.11) (Kotthaus and Grimmond, 2014a). K↓, which influences Q*, is significantly reduced in the winter months leading to a simultaneous reduction in the magnitude of K↑ (Figure 3.11). Maximum receipt of K↓ occurs close to the summer solstice (June 21st) each year of the three year observational campaign.

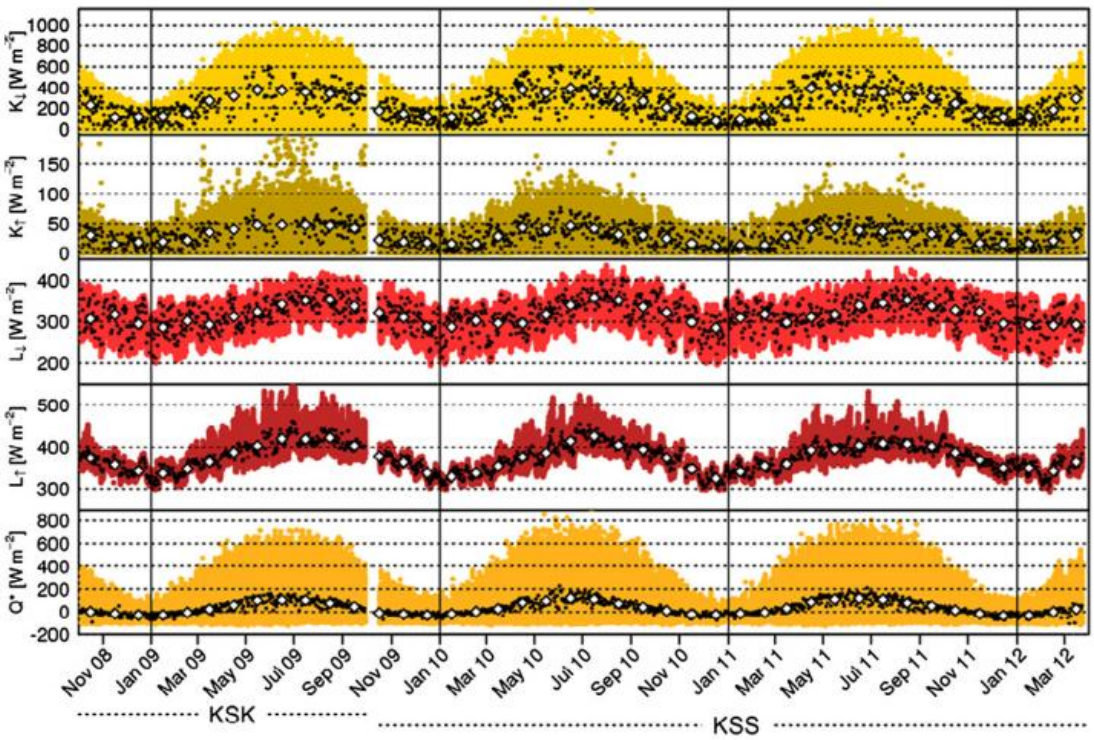

Figure 3.11 Observations of the CNR1 net radiometer (after quality control) at KSK (10/2008–09/2009) and KSS (10/2009–03/2012): net all-wave radiation Q* is the sum of incoming (↓) and outgoing (↑) long- (L) and short-wave (K) radiation, averages: 15 min(coloured dots), daily (K: daytime, L & Q*: 24 h, black dots) and monthly (white diamonds). Data gap in October 2009 due to instrument maintenance (Kotthaus and Grimmond, 2014a).

3.3.4 *Incoming and outgoing longwave radiation in urban areas*

L↓ is generally found to be higher in urban areas (Oke 1978; Landsberg, 1981; Oke, 1997; Arnfield, 2003), this is explained by the enhanced atmospheric emissivity brought about by the presence of greenhouse gases and aerosols and the relative warmth of the UBL (Tapper, 1984; Nunez et al., 2000; Jonsson et al., 2006; Ferreira et al., 2012). Moisture will also serve to enhance L↓ however in general UBLs will be relatively drier than their rural counterparts (Aida and Yaji, 1979; Christen and Vogt, 2004; Jonsson et al., 2006). Inter-city observations in Göteberg, Sweden, Oberhausen, Germany, and Christchurch, New Zealand, revealed higher values of L↓ at the urban locations (11 W m^{-2} or 3.6% for Göteberg, ±9 W m^{-2} or ±2% for Oberhausen, and +7% for Christchurch) on average in comparison to their rural and suburban counterparts (Tapper, 1984; Nunez et al., 2000; Goldbach and Kuttler, 2013). Conversely Basel reported higher L↓ values at rural sites throughout the day however differences were said to be on the order of instrumental errors (Christen and Vogt, 2004). The close proximity of urban and rural sites in Basel, coupled with the fact it is not a heavily polluted city may help to explain

the spatial conservativeness of L↓. Interestingly Jonsson et al. (2006) report that L↓ in 3 tropical locations did not vary dramatically from mid-latitude investigations.

L↑ on the other hand is primarily a function of L↓ and surface emissivity (ε) and will determine the surface temperature of an urban location and influence its air temperature. The typical surface emissivities of urban areas range from 0.92-0.95 (Vogt and Oke, 2003). Unlike the shortwave radiation components however a comparatively small contribution of L↑ is driven by L↓ (Oke, 1987). The urban surface, in terms of surface effective emissivity, shows little seasonal exchange in comparison to rural surfaces which will vegetate and de-vegetate annually in response to changing thermal and moisture regimes (Ferreira et al., 2012). Exceptions to this are relatively well-vegetated urban areas or areas that experience a rainy season where the urban surface remains wet for prolonged periods.

In relation to Basel, the difference between L↑ from the urban and rural sites ($\Delta L\uparrow_{U-R}$) is greatest in the evening following sunset. Differences reported in Basel reached -20 W m^{-2} during the nighttime decreasing to -10 W m^{-2} in the early morning. $\Delta L\uparrow_{U-R}$ occurs due to differing rates of cooling, rural surfaces comprised of vegetated surfaces heat up and cool down more rapidly in comparison to urban manmade surfaces which display a lag effect, giving rise to the nocturnal urban heat island (UHI) and a daytime urban cool island (Figure 3.19b). Basel also reveals evidence of an urban 'dry' island' when absolute humidity is examined, on average the moisture content of the UBL is reduced at the urban sites by 10% in relation to R1, R2 and R3 (Christen and Vogt, 2004). L↑ also reported higher values in summer time, due to increased surface temperatures, a trend also evident in London where maximum L↑ reached 500 versus 300 W m^{-2} in July and January respectively (Figure 3.12). Inter-city comparisons of L↑ in Oberhausen revealed greater differences between the urban and suburban station than L↓, the maximum difference was 32 W m^{-2} (9%) increasing to 58 W m^{-2} during clear-sky and calm conditions (16%) (Goldbach and Kuttler, 2013).

Kotthaus and Grimmond (2014a) investigate the relationship between longwave radiation components and ceilometer-derived cloud cover percentages for nighttime conditions. L↓ is significantly greater in magnitude during overcast conditions (on average 340 W m^{-2}) in comparison to cloud-free conditions (approximately 260 W m^{-2})

(Figure 3.12a). Furthermore L↑ between sunset and sunrise decreases by a smaller magnitude and at a slower rate during overcast conditions in comparison to clear-sky conditions (Figure 3.12b). Finally the night time radiation balance pertaining to central London is illustrated in Figure 3.12c, and shows that during overcast sky conditions the ratio of L↓ to L↑ is almost in equilibrium (i.e. values are close to 1). Under clear-sky night conditions however, the behaviour changes significantly and almost 35% more energy leaves the system as L↑ than is received by L↓ (Kotthaus and Grimmond, 2014a).

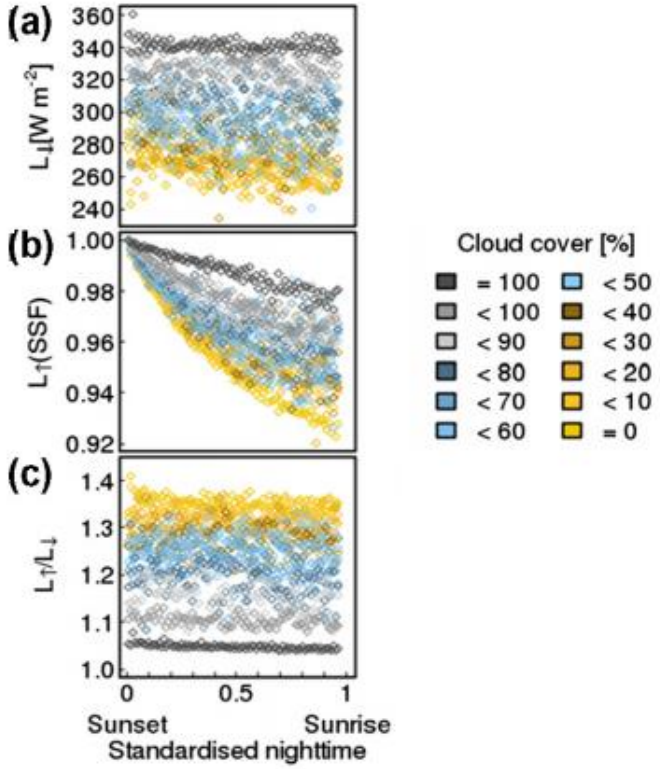

Figure 3.12 Radiation and clover cover observations from KSK and KSS London, (a) Incoming long-wave radiation according to the fraction of cloud cover, (b) outgoing long-wave radiation normalised by the value observed at sunset: sunset fraction SSF, and (c) the ratio of outgoing and incoming long-wave radiation, also considered to be the night time radiation balance (Kotthaus and Grimmond, 2014a).

3.3.5 *Net all-wave radiation in urban areas*

The magnitude of Q* at any given time defines the amount of energy at the surface-atmosphere interface available for heating the atmosphere, evaporating water, and heating the substrate (Oke,1987; Stull, 1988). During the METROMEX experiment in St Louis, White et al. (1978) were among the first researchers to identify K↑ and L↑ as the key components responsible for the difference in the rural and urban radiation budgets. The amount of energy absorbed and retained is ultimately governed by the

nature of the urban surface. On the other hand K↓ and L↓ are similar in magnitude at any given time over conjoining urban and rural areas, particularly in the absence of a heavily polluted atmosphere. Seasonal differences in the components of the radiation budget will largely depend on the latitude of the urban area, with more pronounced seasonal changes at mid-high latitudes in comparison to low latitude cities. Values pertaining to the suburb of Swindon, east of London (latitude 51°35'4.6''N) report seasonal differences in median diurnal Q* of 80 W m^{-2} in December compared to 470 W m^{-2} in June (Ward et al., 2013). These findings are similar to those pertaining to the Central London investigation at King's College London, where daily maximum values of Q* range from 150 W m^{-2} to 700 W m^{-2} in summer (Kotthaus and Grimmond, 2014a).

Also evident in the literature is more pronounced nocturnal radiative cooling, indicated by negative Q* magnitudes, during spring-autumn months in comparison to winter months (e.g. Christen and Vogt, 2004; Offerle et al., 2005a; Ward et al., 2013). During this time the urban fabric stores more heat due to increased day length and higher surface temperatures. This heat released throughout the nighttime leads to increased energy loss by the urban surface and induces the widely reported phenomenon of the nocturnal UHI (Figure 3.9a and b) (for review see Oke, (1995) and Taha, (1997)).

Typical urban surfaces serve to increase reflections and emissions of radiation due to their geometry; they are made of darker surfaces and are characterised by an albedo and emissivity smaller than their rural surface counterparts. Findings suggest a spatially conservative behaviour in relation to Q* across urban and rural surfaces in the same city (e.g. Christen and Vogt, 2004; Offerle et al., 2006a; Coutts et al., 2007; Goldbach and Kuttler, 2013). Although the magnitude of Q* differs only slightly, the individual components can display significant differences for different surface types. In general in urban areas, K↓ and K↑ are systematically smaller than their rural counterparts due to the presence of atmospheric aerosols and a reduced surface albedo respectively. On the other hand L↓ and L↑ are typically greater in urban areas due to higher UBL and surface temperatures respectively. The overall effect of which is a 'built-in negative feedback' where gains in K* in rural locations are matched by large L* losses, and vice versa for urban locations (Oke, 1987:23).

When comparing conjoined urban and rural radiation budgets the differences in Q* over the course of the day are minimal despite large differences in the individual components (e.g. Oke, 1987; Schmid et al 1990; Parlow, 2003; Christen and Vogt, 2004; Offerle et al., 2006a; Goldbach and Kuttler, 2013). That said however there have been some exceptions to this. The first refers to two nearby suburbs of Los Angeles, one with higher (30%) and lower (10%) tree and scrub cover. Q* for the more vegetated neighbourhood was 19% greater and was attributed to a lower albedo and lower surface temperature, leading to a reduced loss of energy overall (Grimmond et al., 1996). The second case is reported for Montreal, again where differences in albedo induced significant differences in Q* across conjoining suburban and urban sites (i.e. 20-30 W m^{-2} greater at the suburban station relative to urban station with lighter concrete surfaces) (Bergeron and Strachan, 2012). Finally, Coutts et al. (2007) and Frey et al. (2011) report reduced Q* at their low density sites which they attribute to an absence of radiative trapping relative to their urban locations.

3.4 The energy budget of the urban surface

Unlike SEB investigations in natural or managed ecosystems, the principal aim of urban EC measurements is seldom to quantify annual sums of Net Surface Exchange (NSE) or Net Ecosystem Exchange (NEE) of water vapour or CO_2, although comparisons across urban and forest ecosystems do exist (Järvi et al., 2009). More often the aim of urban SEB studies is to investigate controls, such as land cover on the partitioning of turbulent fluxes and to evaluate their effect on the local climate. Controls on the SEB will naturally extend to external forcings, including synoptic conditions, and as seen from the previous section, to factors like latitude which govern solar inputs. Greater use of EC instruments in urban areas has also been achieved for the development and validation of weather prediction and atmospheric dispersion models (the latter of which concerns fluxes of CO_2 and aerosol particulates).

Table 3.3 Examples of recent, large campaign-style urban climate studies (Table reproduced from Grimmond, 2006:6)

Location	Study	Characteristics	Reference for study	When
Basel, Switzerland	Basel urban boundary layer experiment (BUBBLE), SARAH	ES, AP, S1, S2, S3, S4, RS2, RS3	Rotach et al. (2005)	2001-02
Marseille, France	ESCOMPTE/CLU-UBL	AP, S1, S2, S3, S4, S5, RS1, RS2, RS3	Cros et al. (2004) Mestayer et al. (2005)	2001
Mexico City, Mexico	IMADA-AVER Boundary Layer Experiment	NP, ES, AP, RS3, S4, S5	Doran et al. (1998)	1997
Nashville, USA	Southern Oxidant study	AP S4, S5, RS1, RS3	Cowling et al. (1998;2000) Meagher et al.(1998)	1995,1999
Oklahoma City, USA	Joint Urban 2003	NP, AP, S1, S2, S4, RS1, RS3	Allwine (2004)	2003
Paris, France	Atmospheric Pollution over Paris Area (ESQUIF) field campaign	NP, AP, S3, S4, S5, RS1, RS3	Menut et al. (2000)	1998-99
Phoenix, USA	1998 Ozone Field study	NP, ES, AP	Fast et al. (2000) Gaffney et al. (2002)	1998
Phoenix, USA	CAP-LTER	NP, ES, S1, S1, S3, S4, S5	Brazel et al. (2000)	1998
Phoenix, USA	2001 Phoenix Sunrise Experiment	ES, AP, S1, S5, RS1,RS3	Doran et al. (2003)	2001
Salt Lake City, USA	VTMX/Urban 2000	AP, S1, S2, S4, S5, RS1, RS3	Allwine et al. (2002) Doran et al. (2002)	2000
Vancouver, Canada	Pacific '93	ES AP S4, S5,, RS1, RS3	Steyn et al. (1997)	1993

NP - Network Present, ES - Earlier studies in the city, AP - Air Pollution a focus

S1 - Indoor or building or canyon scale, S2 - Neighbourhood or local scale, S3 - multi neighbourhoods, S4 - urban area, S5 - Region

RS1 - aircraft, RS2 - satellite, RS3 - lidar and/or sodar and/or radar

More recently large campaign-style urban climate investigations, such as the Basel UrBan Boundary Layer Experiment (BUBBLE) (See Table 3.3 reproduced from Grimmond (2006)) encouraged interaction between field scientists and numerical modellers (Rotach et al., 2005; Christen and Vogt, 2004). This interaction allowed for progress to be made in terms of the relevant scales and heights for which field observations were necessary for initialising and validating urban climate models (Grimmond, 2006). However, a key limitation identified from such large scale projects was the lack of longevity in terms of observations. Long term observations are necessary in order for a wider range of synoptic conditions to be measured for model evaluation (Piringer et al., 2002; Grimmond, 2006).

The SEB of an urban surface is typically investigated in the context of a volume budget, the upper boundary of which is above the roughness elements at a height (z_t) within the ISL (Figure 3.13). The horizontal extent of the volume is usually taken to be the building height to fetch ratio, the maximum bounds of which is regarded as 1:100 in urban areas (Oke, 2004). The lower boundary of the volume (z_b), defined by Feigenwinter et al. (2012:385), is the depth in the subsurface where "annual substrate temperature variations approach zero" (Figure 3.13). Within the volume Q* and the two turbulent fluxes of latent and sensible heat (Q_E and Q_H) are directly measured at a height above Z_t. The remaining fluxes of anthropogenic heat (Q_F) and the change in heat storage (ΔQ_S) are usually estimated using inventory approaches, numerical techniques or parameterizations, and will be discussed separately in Sections 3.6 and 3.7.

The urban SEB will be modified due to 1) the geometry of the surface which influences Q*, 2) the discontinuous nature of the surface characteristics (i.e. surface albedo, surface emissivity, the presence of vegetation and impervious surfaces), 3) the height and spacing of roughness elements and 4) anthropogenic injections of heat from combustion processes, space heating and cooling, and human metabolism (Schmid et al., 1990; Feigenwinter et al., 2012). The urban form, described by factors 1, 2 and 3 results in differences in the partitioning of Q_E and Q_H across neighbourhoods in the same city. While the urban function will typically influence the timing and magnitude of anthropogenic injections of heat (Grimmond and Christen, 2012).

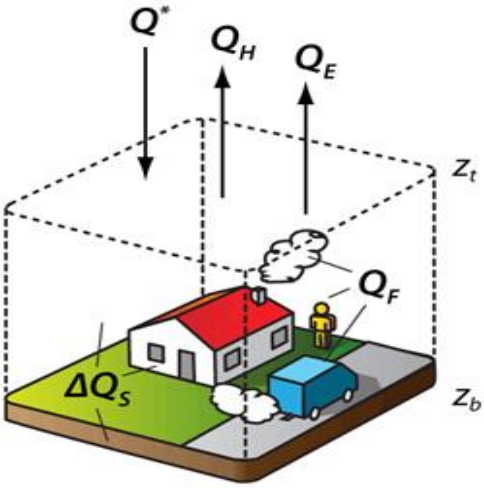

$$Q^* + Q_F = Q_H + Q_E + \Delta Q_S$$

Figure 3.13 Conceptual representation of the urban (a) energy balance for a balancing volume that reaches from the depth where no exchange with the subsurface is found (zb) to the measurement height on a tower above the urban ecosystem (zt). The terms of the energy balance are Q*: net all-wave radiation, Q_F : anthropogenic heat flux density (electricity, fuel combustion, human metabolism), Q_H : sensible heat flux density, Q_E : latent heat flux density, ΔQ_S : storage heat flux density (ground, buildings, air) (Grimmond and Christen, 2012, modified from Feigenwinter et al., 2012).

3.4.1 *Diurnal trends in the turbulent fluxes of latent and sensible heat*

The turbulent fluxes of Q_H and Q_E increase shortly after sunrise reaching a peak around local solar noon, slightly after the radiative fluxes. This lag effect is attributed to the channelling of energy into the urban substrate at the expense of the atmosphere early in the morning (Offerle et al., 2005a). During the summer months Q_H is typically the dominant energy sink, with the greatest flux densities, followed by ΔQ_S and Q_E (Spronken-Smith, 2002; Christen and Vogt, 2004; Offerle et al., 2005a; Newton et al., 2007; Coutts et al., 2007; Ward et al., 2013). Nevertheless ΔQ_S is often reported to approach the magnitude of Q_H, particularly during dry periods with little precipitation (Grimmond and Oke, 1995; Coutts et al., 2007; Newton et al., 2007).

A hysteresis pattern is commonly reported from these experiments between Q_H and Q* (e.g. Grimmond and Oke, 1995; Newton et al., 2007) where fluxes of Q_H are not symmetrical around solar noon. Instead ΔQ_S is the dominant flux early in the morning, where stable stratification of the atmosphere favours heat transfer via conduction, which is channelled to the substrate. Gradually as surface heating creates vertical gradients in the temperature profile, heat transfer via convection is encouraged leading to increases

in Q_H relative to ΔQ_S. Similarly where water is present at the surface, convection will transfer latent heat into the overlying atmosphere, reaching a peak around solar noon (Grimmond and Oke, 1995; Oke, 1987).

Due to the difference in the flux magnitude of Q_E and Q_H across seasons and between cities, when making comparisons it is more useful to investigate the behaviour of flux ratios, such as Q_H/Q_E (i.e. the Bowen Ratio), Q_H/Q^*, Q_E/Q^* and $\Delta Q_S/Q^*$. The Q_E/Q^* quotient is reported in several cities as higher in the early morning before decreasing and remaining relatively constant throughout the day. Early morning peaks are attributed to evaporation of dew and overnight irrigation (Grimmond and Oke, 1995; Spronken-Smith, 2002). Q_H/Q^* accounts for a large portion of Q* (i.e. 0.45 throughout the day in Christchurch) and becomes increasingly significant at nighttime. $\Delta Q_S/Q^*$ is also reported as significant, increasing soon after sunrise, before becoming negative in the late afternoon. A double peak is also evident in the diurnal cycle of ΔQ_S, the first peak generally occurs 1-2 hours prior to that of Q_H, whilst the second occurs as previously shaded facets and surfaces become exposed at lower solar elevations encouraging heat transfer via conduction (Spronken-Smith, 2002; Christen and Vogt, 2004).

3.4.2 *The Bowen ratio*

The Bowen ratio ($\beta=Q_H/Q_E$) is used to describe the partitioning of Q* between the turbulent heat fluxes. It is an important indicator for urban climatology in that it succinctly describes whether energy is predominantly channelled into latent heat (resulting in the evaporation of water at the surface) or sensible heat (sensed as an increase in air temperature). Given the nature of its calculation and dependence on Q*, the Bowen ratio will vary on a diurnal basis; in early morning, following sunrise, Q_H will be dominant, however following solar noon Q_E increases at the expense of Q_H hence altering the magnitude of β (e.g. Christen and Vogt, 2004). Kotthaus and Grimmond (2014a) evaluate the dependency of β according to the time of day for a dense city centre, reporting β equal to 11 during the nighttime when Q_H is dominant and Q_E is almost negligible. Following this ratios begin to decrease, reaching a minima of approximately 5 during the late afternoon (16:00 hours UTC) and from 18:00 hours onwards β increases again throughout the night (Kotthaus and Grimmond, 2014a).

β is inherently dependent on moisture availability at the surface and will display a relationship with precipitation events. Some studies investigate this relationship using the number of days (or hours) after a precipitation event as an indicator (e.g. Goldbach and Kuttler, 2013; Kotthaus and Grimmond, 2014a; Ward et al., 2013). The relationship is typically characterised by increasing β with increasing days since rainfall, as reported for urban and suburban sites in Oberhausen, Germany (Goldbach and Kuttler, 2013) (Figure 3.14a). Energy is channelled into the atmosphere via Q_H at the expense of the Q_E. This relationship is more pronounced in the urban location where mean β reach values similar to median values in the London (Kotthaus and Grimmond, 2014a) (Figure 3.14a and b). Similar to Oberhausen, the lowest magnitude of β (e.g. β=1-3) is reported in the immediate hours preceding a rainfall event (0-6 hours) in London. At this time water settling on the surrounding surfaces (i.e. roof tops, concrete paving and roads) is evaporated, serving to increase the partitioning into Q_E.

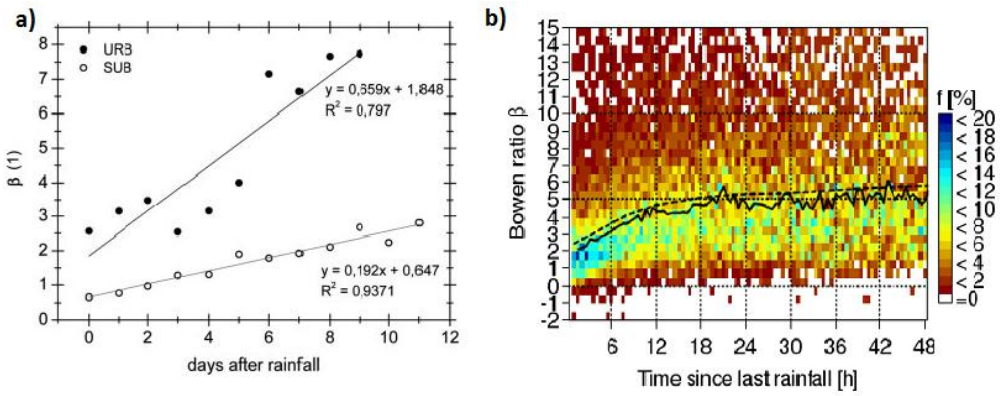

Figure 3.14 a) Mean Bowen ratio (β) which shows dependency on the number of days after a precipitation event (p), classified as p> 0.1 mm d^{-1} for an urban and suburban location in Oberhausen, Germany (Goldbach and Kuttler, 2013). b) illustrates the frequency distribution (frequency f[%]) of β by the time since last rainfall (hours [h]) for a dense city centre location in London. The solid line represents the median β by time since last rainfall, only β<15 and times up to 48 h after rainfall are shown (Kotthaus and Grimmond, 2014a).

Over the course of the year the Bowen ratio is also found to vary in accordance with wet and dry periods, for example the highest Bowen ratios in suburban Swindon occurred during the driest conditions of the observational campaign (May 2011, the end of July 2011 and mid-October, 2011) (Ward et al., 2013) (Figure 3.15). On the other hand Bowen ratios decreased in unison with wetter periods indicated by high precipitation events, particularly during December 2011 and January 2012 where daily rainfall often exceed 3mm per day.

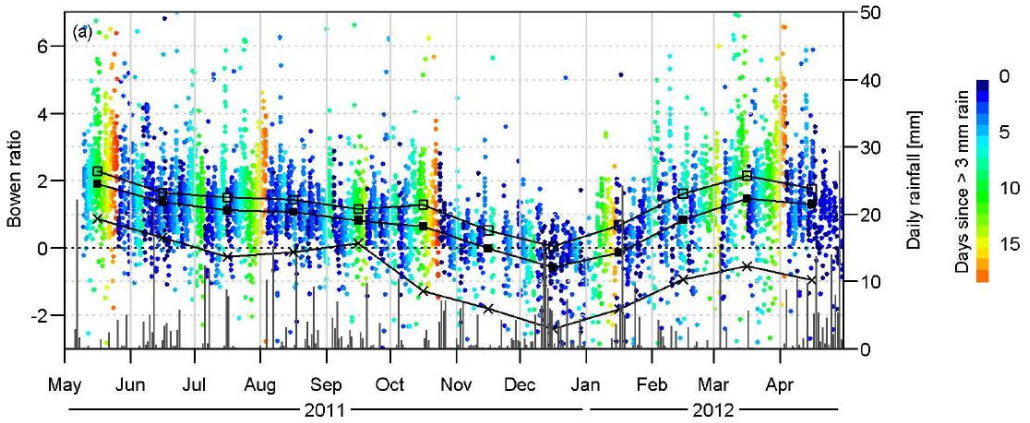

Figure 3.15 Daytime Bowen ratio (30min) coloured by number of days since rainfall (exceeding 3 mm) for the study period. Daily rainfall (bars) corresponds to the right-hand axes. Monthly median midday (±2h) (open squares), monthly median daytime (solid squares) and monthly median nighttime (when Q*<0 and K↓<5 W m^{-2})(crosses) Bowen ratios are plotted mid-month (Ward et al., 2013).

Ultimately the Bowen ratio is significantly altered in comparison to natural ecosystems where the turbulent heat fluxes are of similar magnitude, or where Q_E is greater than Q_H (Oke, 1987). The trend in urban locations is that of a greater Bowen ratio, that typically increase with increased impervious surface fraction and with dry conditions (Arnfield, 2003).

3.4.3 *Seasonal trends in Q* and the turbulent heat fluxes*

Seasonal fluxes pertaining to Q*, Q_H and Q_E are investigated for conjoined urban and suburban locations in Oberhausen with surface vegetated fractions of 18 and 58% respectively (Goldbach and Kuttler, 2013). Fluxes of Q* are slightly reduced for the urban location, largely due to increased nocturnal losses at nighttime, particularly in spring. Interestingly the maximum values for Q_H were reported for April 2011 for the urban and suburban locations, where conditions were characterised by a blocking high pressure system which gave rise to prolonged clear sky conditions. Conversely, synoptic conditions during the summer months of July and August 2010 were generally dominated by cyclonic conditions, with relatively lower solar inputs and higher precipitation. In April, the authors argue that because of low precipitation, coupled with the fact that the trees were not yet in leaf, fluxes of Q_E were minimal particularly in the urban location (Figure 3.16) (Goldbach and Kuttler, 2013). During cyclonic conditions in August and September of 2010 fluxes of Q_E where significantly increased, particularly in the suburban location where a greater vegetated fraction increases the extent for evaporation to occur relative to the impervious urban surface which serves to drain water away from the surface (Goldbach and Kuttler, 2013) (Figure 3.16). In this

case the urban location exhibited a relatively drier and warmer climate than that of the nearby suburban location (Figure 3.16).

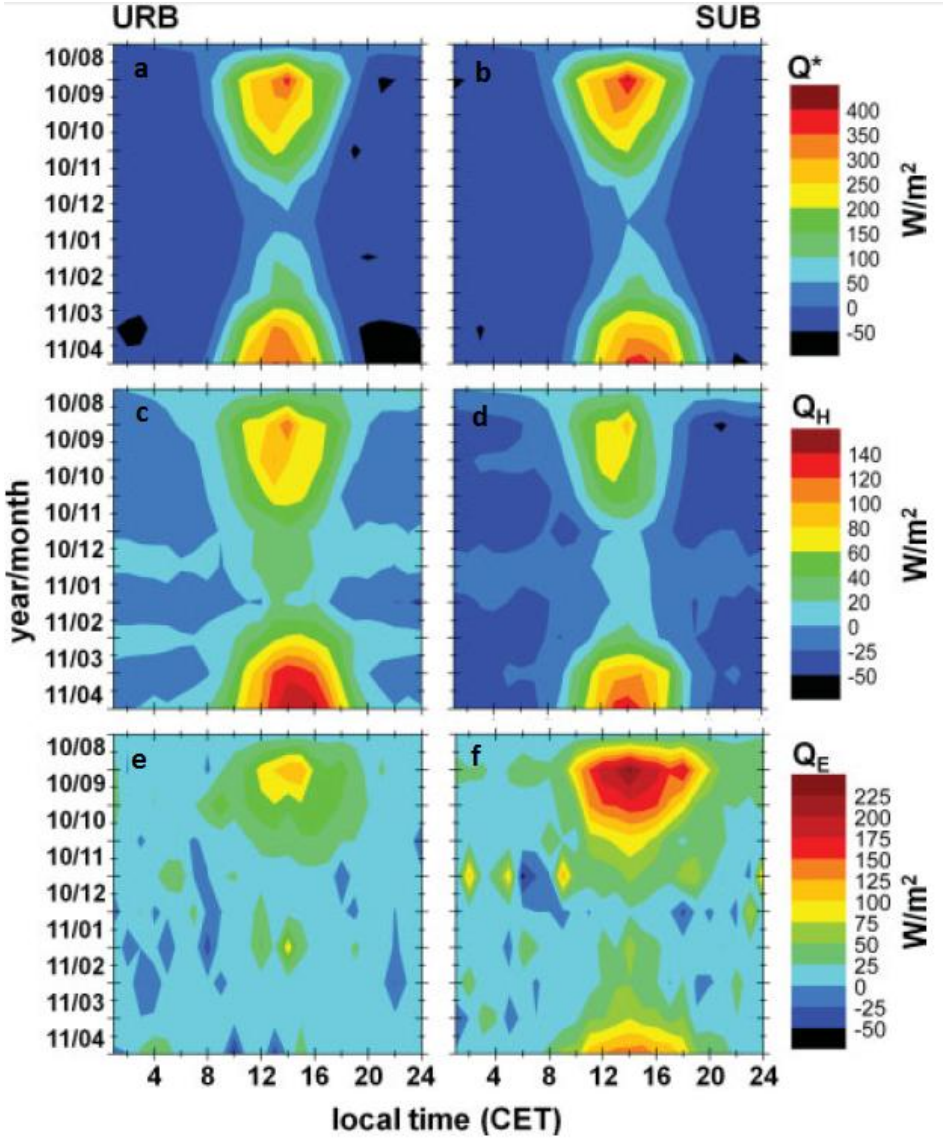

Figure 3.16 Isoflux diagrams of the daily (x-axis) and annual (y-axis) variations of the radiation balance (Q*), turbulent sensible heat flux density (Q_H) and turbulent latent heat flux (Q_E) at the urban site (URB) and suburban site (SUB) for Oberhausen, Germany. Note the difference in parameter scale (Goldbach and Kuttler, 2013).

3.5 Measurement sources areas in the urban domain

This section explores the sources of error that leads to non-closure of the SEB equation. Typically non-closure of the energy balance in urban areas results from radiation and EC instruments measuring different areas comprised of different surface characteristics (Oke, 2007). This assertion gives weight to the guiding principles outlined by Oke (2007) regarding the most appropriate siting of micrometeorological instrumentation in urban areas. The surface characteristics within the horizontal boundaries of the SEB study volume (Figure 3.13) should be uniform in all directions of the EC tower and

should extend longer than the instrument footprint so as to yield a spatially-averaged, representative signal of the LCZ. Non-closure of the SEB is therefore more pronounced when the surrounding surface is heterogeneous (Oke, 2007). Ensuring sufficient fetch in all directions of the EC tower for all stability conditions will also reduce the contribution of sources and sinks due to advection from warmer, cooler or wetter surfaces upwind (Grimmond, 2006; Oke, 2007).

Atmospheric conditions conducive to non-closure of the SEB, such as an increasingly stratified NBL, are not as frequent in urban areas (Aubinet et al., 2012). Satisfying fetch requirements is more difficult in an urban setting owing to the heterogeneous nature of the urban form and function; however the influence of the surface roughness on turbulence acts to reduce uncertainty and measurement error in comparison to natural, homogenous environments. As previously mentioned, the release of heat from the urban fabric, increased surface roughness and anthropogenic heat sources serve to enhance turbulence throughout the night. Coupled with free convection, the urban area, due to bluff obstacles will also induce forced convection enhancing the unstable stratification of the UBL. Unstable conditions at night are commonly reported in urban areas, with only a small fraction of observations representing a stable NBL (e.g. Liu et al., 2012; Nordbo et al., 2013; Kotthaus and Grimmond, 2014a). In relation to the Basel observation campaign, the nighttime stability conditions from the five EC sites are compared in Figure 3.17. The relative percentage of stable conditions is reduced with increasing urban density, from rural (approximately 70%) to dense urban (approximately 10%) (Christen and Vogt, 2004).

The overall effect of the increasing instability of the UBL means that urban EC measurements are more likely to satisfy the fundamental assumption of EC method; well-developed turbulent conditions. The traditional development of a stable NBL over a rural surface encourages intermittent turbulence and lower turbulence intensities. These factors fail to satisfy the theoretical assumptions of EC but also underestimate the total flux influencing closure of the nighttime SEB (Aubinet et al., 2012).

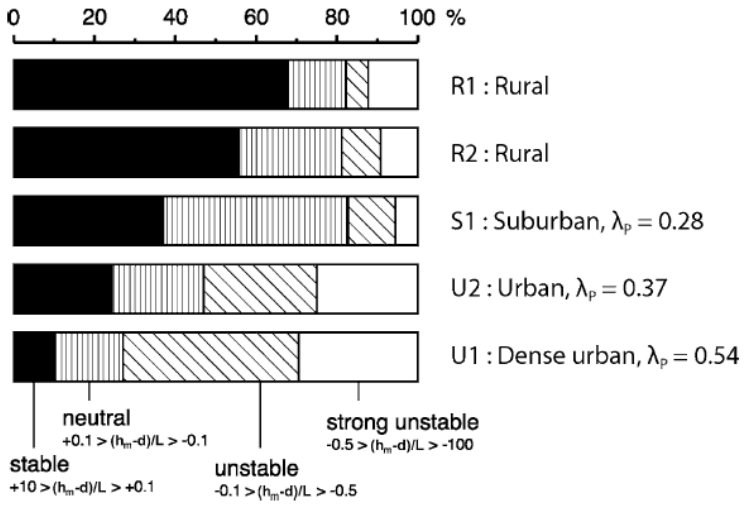

Figure 3.17 Frequencies of different stability classes for nighttime cases (Hours 22-04) measured simultaneously at five EC sites in Basel, Switzerland between 10 June and 10 July, 2002 (Christen and Vogt, 2004).

3.5.1 *Radiation and flux source areas*

The potential inconsistencies between the radiation and EC instrument footprints that result in measurement discrepancies in the SEB were outlined in Section 2.5. In urban areas the radiation sensor will 'see' vertical facets in addition to horizontal surfaces. As a consequence Offerle et al. (2003) and Roberts (2010) suggest deploying radiation sensors high enough above the roughness elements so that a representative portion of typical surface units (i.e. walls, roofs, trees, gardens and roads) are sampled. Kotthaus and Grimmond (2014b) investigate the effect of forward scattering, highly reflective surfaces in the FOV of a downward facing pyranometer on observations of K↑. Outliers identified in the spatial distribution of K↑ are linked to roof windows, where values of K↑ and α increase compared to the surrounding roof area comprised of concrete and slate. The authors report that contribution from specular reflections from reflective surfaces is greatest for sensors deployed at relatively low heights above the roof level. Kotthaus and Grimmond (2014b) therefore recommend deploying radiation sensors above EC instruments where possible in the urban environment, or deploying multiple sensors in various locations surrounding the EC instrumentation to ensure improved spatial coverage. Furthermore care must be taken to ensure that obstacles, such as tall trees or buildings, do not obstruct the FOV of the upward facing pyranometers and pyregeometers (Oke, 2007).

A simple way to evaluate non-closure of the SEB in urban areas is to estimate the probable flux footprint and examine conditions (stable/unstable) and wind directions that may lead to inconsistencies in the footprint of the radiation and EC instrumentation. Similar to natural ecosystems, the flux footprint allows the relative contribution of surface sources and sinks to be estimated (Schmid, 1994; Schmid, 2002; Grimmond, 2006). In this way the spatial representativeness of the measured fluxes can be evaluated in relation to the LCZ of interest, and locations of bias, leading to non-closure, can be identified (Schmid, 1994; Grimmond, 2006).

Current attempts to incorporate the 3-dimensional nature of the urban surface into flux footprint models remain limited, while analytical models generally only include individual bulk values for z_H and z_0 in their calculations. These parameters will most likely vary for different wind directions in an urban setting and will hence affect the location of the peak flux footprint. Given the inherent assumptions of the analytical models (i.e. horizontal homogeneity) Rannik et al. (2012) and Järvi et al. (2009b) suggest that their application in urban areas should only be used as an indicator of the footprint in the absence of a 3-dimensional structure. To illustrate their limitations Järvi et al. (2009b) employ an analytical model (after Horst and Weil, 1994) in addition to the numerical model, SCADIS (Sogachev and Sedletski, 2005), for an urban area of Helsinki, Finland. Land use surrounding the SMEAR III measurement site outside of central Helsinki was classified into nine different types including soil, car parks, roads and trees according to two height classes, and buildings according to 4 height classes. The results of the flux footprint function comparison highlighted the relative simplicity in the analytical model illustrated by the smooth line, and smooth peak indicating the local maxima (Figure 3.18b). The flux footprint derived from the numerical model revealed 1) a shift in the location of footprint maximum due to the topography and 2) two local maxima occurring 200 and 400 m upwind of the measurement site (Figure 3.18 a and b).

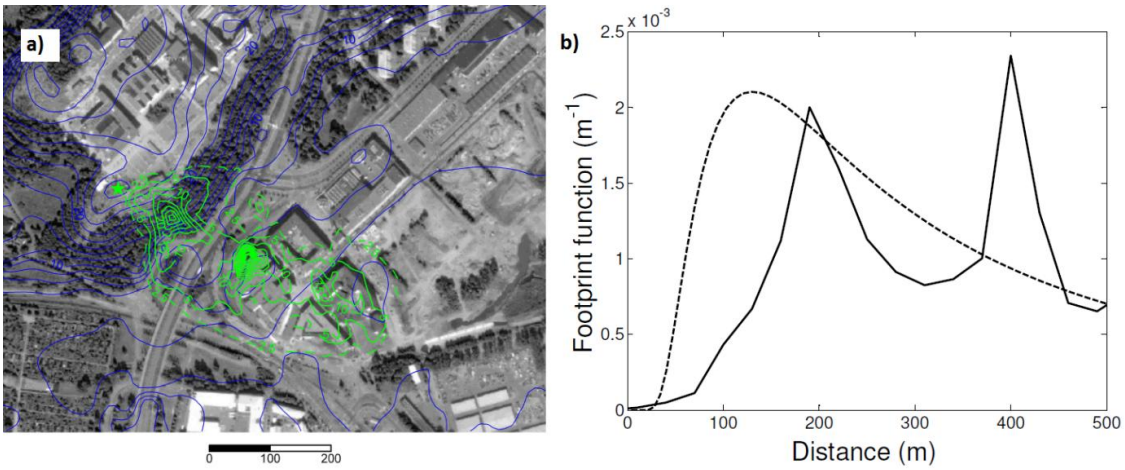

Figure 3.18 a) An aerial photograph of the measurement location, SMEAR III located 5 km north-east of Helsinki city centre. The topography of the measurement site, relative to sea level, is denoted by blue contour lines. The green contour lines show the particle number flux footprint function when the wind direction is perpendicular to the main road, when the geostrophic windspeed is 10 m s^{-1} and the boundary layer is neutrally stratified. The measurement location is marked by the green star. b) is the footprint function, under the same conditions, as estimated with the analytical model of Horst and Weil (1994; dashed line) and the numerical model (solid line) (Järvi et al., 2009b).

The investigation highlights the sensitivity of the turbulent flux to topography, wind direction and the 3-dimensional structure of the urban surface and therefore the limitations of any 2-dimensional (2-D) model, assuming horizontal homogeneity. The use of analytical models in urban EC investigations can be attributed to 1) their relative ease of use (very often incorporated into commonly used EC software, such as EddyPro, EddyUH and TK3.1), 2) their reduced computing demand and cost in comparison to sophisticated and expensive LES methods, and 3) the scarcity of alternative 3-dimensional methods. At present a model is in development by the University of Helsinki that will be incorporated into their EddyUH software package (Olli Peltola, personal communication). This model requires 2 datasets, the first, a digitised map of buildings, classified into different height classes, and secondly a land cover map, classified into surface cover fractions for buildings, vegetation, roads and water. For each calculation period (i.e. 30 minutes) land cover fractions and values for z_H, z_d and z_0 are calculated according to the wind direction in addition to a flux footprint according Kormann and Meixner (2001). In this way the 2-D flux footprint model ingests wind direction-dependent roughness parameters for the calculation of the flux footprint for each interval. The footprint can then be evaluated in unison with the land cover fractions for each interval. This approach allows for the geostatistical interpretation of the footprint and the development of more robust footprint climatologies for each wind direction under an array of stability conditions.

3.6 The storage heat flux

The storage heat flux, ΔQ_S, represents the change in the heat storage of the subsurface ground materials (ΔQ_{Sg}), the buildings (ΔQ_{Sb}), the vegetation (ΔQ_{Sv}) and the indoor and outdoor air (ΔQ_{Sa}) (Feigenwinter et al., 2012). From the earliest investigations the term was found to be a substantial component of the energy balance of the urban canyon, and one that could not be ignored (Nunez and Oke, 1977). It serves to "slow the response of the surface to changes in radiative and atmospheric forcing, and thus dampens the amplitude of the turbulent fluxes" particularly following sunrise where heat is preferentially channelled into the substrate (Offerle et al., 2005a:1405).

Due to the impracticality of measuring each of the components of the heat storage change term individually, ΔQ_s must be estimated by indirect methods. Ferreira et al. (2013) outline the most common methods which include; 1) the energy balance residual (Oke and Cleugh, 1987), 2) numerical modelling (Masson, 2000; Martilli et al.,2002; Oleson et al., 2008; Grimmond et al., 2010), 3) the thermal mass scheme (Oke et al., 1981) and 4) the parameterization method (Grimmond et al., 1991). The most accurate of the above methods is considered to be the energy balance residual method, and the most successfully applied parameterization method is the objective hysteresis model (OHM) (Ferreira et al., 2013) both of which will be discussed in the following sections.

3.6.1 *Methods to estimate the storage heat flux: Residual of the SEB*

Direct measurement of ΔQ_S is largely deemed as impractical due to the heterogeneity of the suburban and urban surface (Oke and Grimmond, 1995; Arnfield, 2003; Roberts et al., 2006; Feigenwinter et al., 2012). The term is more generally determined as the residual in the surface energy balance equation (Oke and Cleugh, 1987),

$$\Delta Q_S \approx (Q^* + Q_F) - (Q_H + Q_E)$$

Equation 3.3 Energy balance residual (Oke and Cleugh, 1987)

In this formulation ΔQ_S includes any measurement errors and observational inaccuracies associated with the terms on the RHS and it is impossible to isolate accumulated errors from other flux calculations from the value calculated for ΔQ_S therefore caution must be taken when interpreting the flux (Oke and Grimmond, 1995; Spronken-Smith, 2002; Pearlmutter et al., 2005). In order to address the uncertainty surrounding the storage change signal, Grimmond and Oke (1995) directly measure the

soil heat flux at four suburban sites. Using heat flux plates, the results of the soil heat flux provided "a check on the behaviour of ΔQ_S" (Grimmond and Oke, 1995:885). In unison with findings for ΔQ_S discussed above, the SEB for four cities, Chicago, Los Angeles, Sacramento, and Tucson, revealed a positive net storage heat flux, indicative of a net heat gain by the surface volume (Grimmond and Oke, 1995). The magnitude of ΔQ_S is constrained by Q* and as a consequence it is very often considered as an upper threshold of the estimate.

3.6.2 *Methods to estimate the storage heat flux: Modelling techniques*

Given that the heat storage flux, calculated as the residual (ΔQ_{SRES}) of atmospheric, measured variables, it will inherently contain errors associated with these. In order to have confidence in the representativeness and plausibility of the SEB results which contain ΔQ_{SRES}, the Objective Hysteresis Model (OHM), developed by Grimmond et al. (1991), can be employed to generate modelled values for heat storage (ΔQ_{SOHM}) over a measurement campaign. Application of the OHM requires detailed information regarding the fractional cover of surfaces surrounding the measurement location including greenspace, rooftop and impervious (i.e. concrete and asphalt). Each of these surface types have empirically derived coefficients which describe their

1. Direct proportionality to Q* (a_1)
2. Timing in relation to Q*(which accounts for hysteresis) (a_2)
3. Value of ΔQ_s when Q* equals zero (a_3)

The coefficients are derived from previous studies undertaken for urban surfaces and will be outlined in Chapter 6. The modelled values are a function of Q* however they are independent of the measured turbulent heat fluxes (Q_E and Q_H) and hence are a useful tool for evaluating ΔQ_{SRES} where,

$$\Delta\, Q_{S\,OHM} = \sum_{i=1}^{n} \left[a_{1i} Q* + a_{2i} \frac{\Delta Q*}{\Delta t} + a_{3i} \right]$$

Equation 3.4 Objective hysteresis model according to Grimmond et al. (1991).

Where *i* refers to each of the *n* surface types that are found in a radius area surrounding the observation platform where Q* is measured and the terms a_1, a_2 and a_3 are coefficients described above that are obtained from previous studies. While this does

not address the errors associated with inconsistent source areas, it does provide some confidence in the calculated ΔQ_{SRES} term and indirectly in the turbulent flux terms. The average values of coefficients a_1, a_2 and a_3 are used here in conjunction with surface cover statistics to calculate site specific model coefficients.

Residual values, although not measured themselves, are regarded as the upper threshold reference values and as the closest to potential correct values given that they are the result of high-grade scientific measurement campaigns (Roberts et al., 2006). Typically ΔQ_{SOHM} values are compared with ΔQ_{SRES} to evaluate the SEB and energy balance closure (Roth and Oke, 1994; Grimmond and Oke, 1999b; Keogh et al., 2012; Ferreira et al., 2013; Ward et al., 2013). In relation to São Paulo, Brazil, estimates of ΔQ_S employing the OHM method are in good agreement with the residual estimate for the rising and declining limb. Greater divergence occurs between the hours 10:00 to 13:00 whereby the OHM method consistently underestimates the residual value by approximately 40 W m^{-2}.

With regard to the Swindon case (Ward et al., 2013), soil heat flux measurements, representing the ground heat flux, Q_G were available throughout the campaign, against which the OHM estimates could be cross-checked. In general ΔQ_{SOHM} and ΔQ_{SRES} are almost equal in the summer months, indicating the energy balance closure is close to 100% (Figure 3.19a). This is most likely a result of good site selection where the surface cover fractions in all wind directions surrounding the EC tower are almost identical (Figure 3.20). In winter however, the energy balance is over-closed by about 20% according to ΔQ_{SOHM} estimates. The ΔQ_{SOHM} is more negative for all hours when compared to ΔQ_{SRES} and the authors suggest that the OHM is incapable of replicating the same trend as ΔQ_{SRES} and Q_G, which reveal a decreasing nocturnal flux from summer to winter (Figure 3.19b). The difference in ΔQ_{SOHM} and ΔQ_{SRES} in winter is attributed to the use of the negative coefficient a_3 which seems to be too large during winter however other estimations of the term, taking into account of seasonal change, do not exist (Ward et al., 2013).

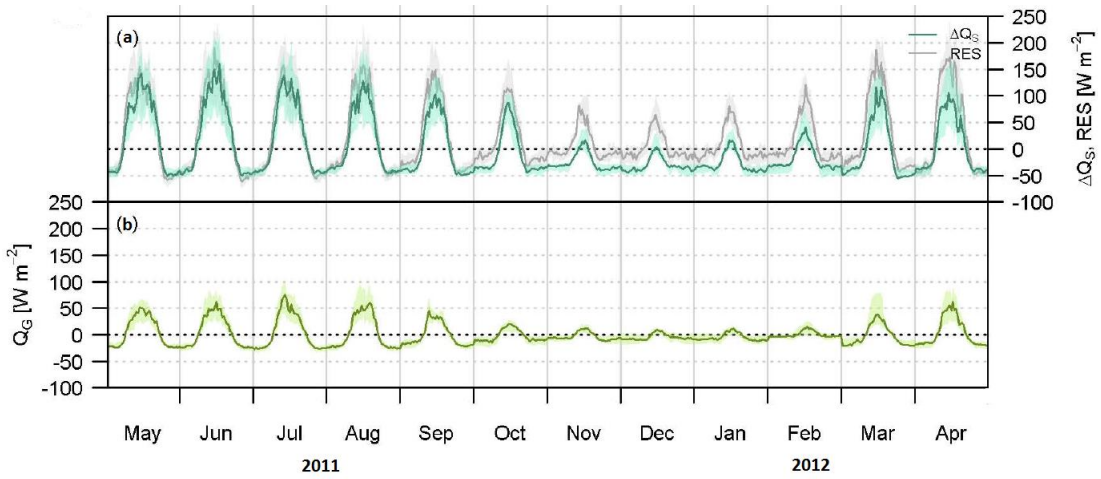

Figure 3.19 Median diurnal cycles (lines) and inter-quartile ranges (shading) of the energy fluxes for each month from May 2011 to April 2012. a) represents the storage heat flux estimated using the OHM method (turquoise line) and the energy balance residual (RES)(grey line). b) is the ground heat flux derived from soil heat flux plate measurements from the Swindon measurement site (Modified from Ward et al., 2013).

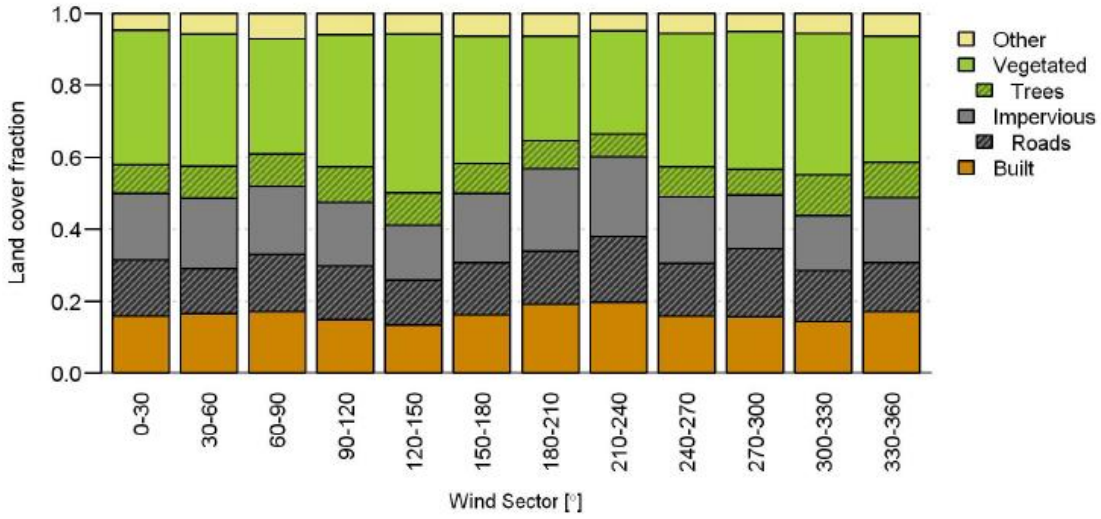

Figure 3.20 Land cover fractions for 30 degree wind sectors within a radius of 500 m around the flux mast in Swindon, UK (Ward et al., 2013).

3.7 The anthropogenic heat flux

Typical sources of anthropogenic heat are illustrated in Figure 3.13 and largely comprise of heat from vehicles, stationary sources such as houses and human metabolism. Traditionally in order to estimate the magnitude of Q_F for a location, the term is disaggregated into these components and is expressed as

$$Q_F = Q_{FV} + Q_{FB} + Q_{FM}$$

Equation 3.5 The anthropogenic heat flux (Sailor and Lu, 2004)

Where Q_{FV} denotes heat from vehicles, Q_{FB} is heat from houses and other buildings and Q_{FM} represents human and animal metabolism.

Methods to estimate Q_F include 1) energy-budget-based estimates, 2) inventory based approaches, and 3) those using building energy models which inevitably must be coupled with emissions estimates from transportation and industry sectors (Sailor, 2011). Estimates based on the energy budget closure requires EC data for a targeted neighbourhood and is expressed as

$$Q_F = Q_{H+} Q_E + \Delta Q_S - Q^*$$

Equation 3.6 Anthropogenic heat estimate based on energy budget closure (Sailor, 2011)

When parameterization methods are employed to estimate ΔQ_S, such as the OHM, Q_F can then be calculated as the energy balance residual. This method, given the resolution of the measured variables, allows for the estimation of Q_F on short timescales. In the absence of the heat storage estimates, which can be assumed to be negligible over 24 hour periods, Q_F can be interpreted as the residual of the daily energy balance (Offerle et al., 2005b). The limitations of this method echo those associated with the derivation of ΔQ_{SRES}, in that estimates will inherently contain instrumental errors associated firstly, with the turbulent heat fluxes and secondly, with the potential mismatch of instrumental source areas. Furthermore Q_F derived from the EC measurements cannot easily be disaggregated into the individual components of Equation 3.5 and is very often reported as a single value representative of all possible sources within the volume (e.g. Offerle et al., 2005b).

Q_F, estimated using residual methods in Łódź, Poland, reported an inverse relationship with air temperature, with average winter time values of 32 W m^{-2} (representing on average 60% of available energy from October to March) and summer time values of -3 W m^{-2}. Unrealistic summer time values, as the authors argue, indicate an underestimation of the turbulent fluxes or an overestimation of Q*, however no definitive causal factor was identified (Offerle et al., 2005b).

Inventory based approaches require a number of datasets to estimate the individual components, including those representing traffic counts (ideally to include hourly values

and fleet information), human population and building energy use (including the contribution of heating fuels from natural gas, kerosene, fuel oil and LPG) (Arnfield, 2003; Sailor and Lu, 2004; Offerle et al., 2005b). Heat emitted as a result of human metabolism (Q_{FM}) can largely be assumed to occur indoors (>50%) and typically accounts for between 1 and 3% of Q_F in a city, therefore it is not surprising that it is often ignored (Sailor and Lu, 2004; Sailor, 2011). A top-down inventory-based method was employed in 6 American cities, Atlanta, Chicago, Los Angeles, Philadelphia, Salt Lake City, and San Francisco. The largest winter time values estimated for Q_F are reported for Chicago, San Francisco and Philadelphia (70-75 W m^{-2}) (Figure 3.21). In summer time Q_F is generally the same magnitude or less than winter time values (30-60 W m^{-2}) although Atlanta and Salt Lake City report reduced values for all seasons, which the authors attribute with a substantially lower population density (Sailor and Lu, 2004). Large seasonal differences in the estimated Q_F term was attributed to significant heating loads in colder climates where heating fuels accounted for 51, 52 and 57% of the flux for Philadelphia, Salt Lake City and Chicago respectively. Diurnal peaks for all cities occur simultaneously and represent the morning and evening rush hours, suggesting that traffic, and heat from vehicles is significant, accounting for between 47 to 62% of the total summer time flux (Sailor and Lu, 2004).

The inventory approach can prove problematic when coupled with EC investigations due to the potential inconsistency of data resolution in both space and time for variables such as heat emissions from buildings (Sailor, 2011). However the incorporation of these emissions into numerical models has been achieved and complements both inventory and residual approaches. The Town Energy Balance (TEB) developed by Masson (2000) was one of the first simple attempts to estimate Q_F from buildings, however it ignored the building's internal heating and cooling loads and the effect of radiation through windows (typically accounting for 20-40% of the external surface area of buildings) (Sailor, 2011). More recent attempts account for these factors, and much of the work has been carried out for Tokyo, Japan. Ohashi et al. (2007) investigated the summer time anthropogenic heat flux and reported increased air temperatures of 1 to 2 °C as a result of air-conditioning heat rejection from buildings. Building energy models also allow for the aggregation of building effects on Q_F over a neighbourhood scale where the building stock is similar, and where several building prototypes can be defined and modelled (see for example Hsieh et al., 2007).

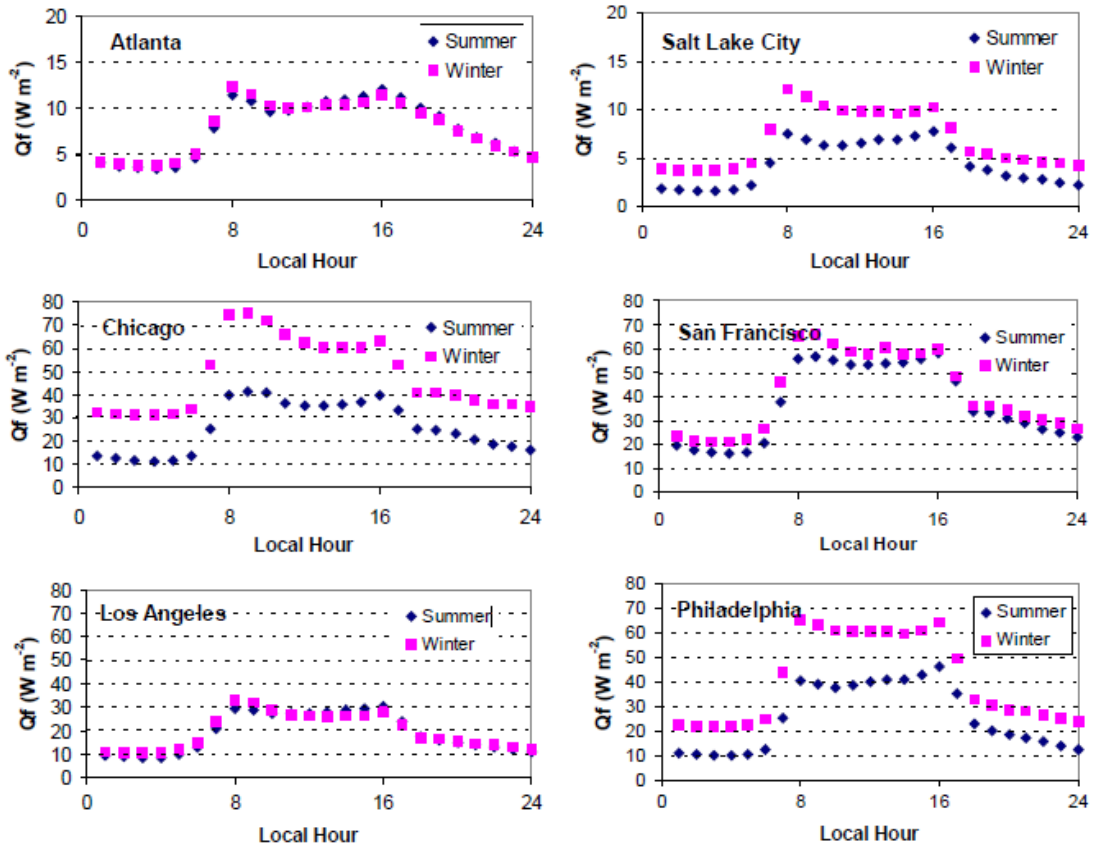

Figure 3.21 The diurnal profile of the anthropogenic heat flux for 6 American cities for summer and winter time, estimated using a top-down, population-based inventory approach (Sailor and Lu, 2004). Note the difference in magnitude on the y-axis.

Ultimately a combination of methods is required to estimate Q_F in order to be representative of the local scale climate. The residual method requires EC measurements, the inventory method is data intensive and the resolution of available data may not allow for diurnal profiles of Q_F to be calculated, and finally building energy model estimates need to be combined with estimates of heat emissions from vehicles and human metabolism.

3.8 The CO_2 flux in urban domain

The first EC campaign measuring CO_2 fluxes was in Chicago, 1995 (Grimmond et al., 2002) and up until 2002 the longest EC investigation of CO_2 fluxes, spanned 1 year (Soegaard and Møller-Jensen, 2003) consequently the quantification of annual NEE for CO_2 for an urban ecosystem was not possible. Rather, short term datasets of CO_2 fluxes were widely used to develop and validate pollution dispersion models, and have also been reported in the literature as evaluating emissions inventories (Velasco et al., 2009). More recently EC investigations are concerned with quantifying the CO_2 source

strength of urban areas, and investigations have also been extended to investigate fluxes of atmospheric aerosols (Järvi et al., 2009) and methane (CH_4) (Gioli et al., 2012).

Similar to the SEB techniques, the study volume approach is applied where sources of CO_2 include those from combustion processes related to vehicles and buildings (C), and respiration processes by soil, humans and vegetation (R_e), while CO_2 sinks include photosynthesis by urban vegetation. Changes in concentrations within the volume (ΔS) will occur due to the change in carbon storage capacity of vegetation each year (Feigenwinter et al., 2012) (Figure 3.22).

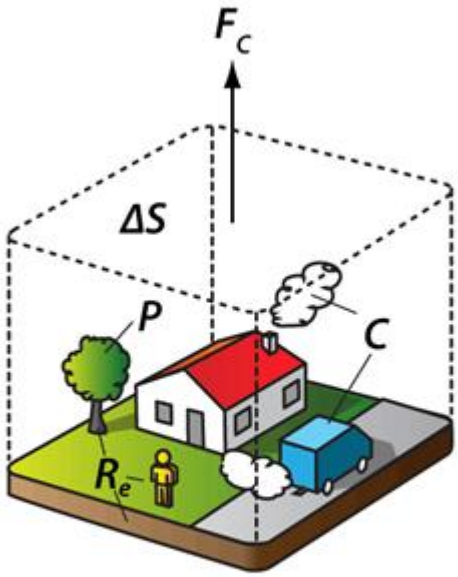

$$F_C + \Delta S = C + R_e - P$$

Figure 3.22 The terms of the urban CO_2 budget are - F_C: Net mass-flux of CO_2 between urban surface and atmosphere, ΔS :concentration change of CO_2 in the measurement volume, C: CO_2 emitted by combustion, Re: CO_2 emitted by urban ecosystem respiration (soil, plants, humans), P: CO_2 taken up by photosynthesis of urban vegetation (Grimmond and Christen, 2012, modified from Feigenwinter et al., 2012).

3.8.1 *The temporal variability of the CO_2 flux*

The diurnal fluxes of CO_2 are largely influenced by the urban form and function. Of the international studies undertaken in the urban environment a clear diurnal cycle in fluxes is evident within the literature which correlates with traffic volume (Nemitz et al., 2002; Soegaard and Moller-Jensen, 2003; Moriwaki and Kanda, 2004; Velasco et al., 2005; Vogt et al., 2006). As illustrated in Figure 3.23 fluxes increase during the morning coincident with increased surface layer mixing and traffic volume. Peaks around the

evening rush hour are also evident before fluxes begin to gradually decrease throughout the night. Experiments in Basel included the mounting of EC instrumentation at 2 heights above ground level, allowing for the vertical profile of fluxes and concentrations to be investigated.

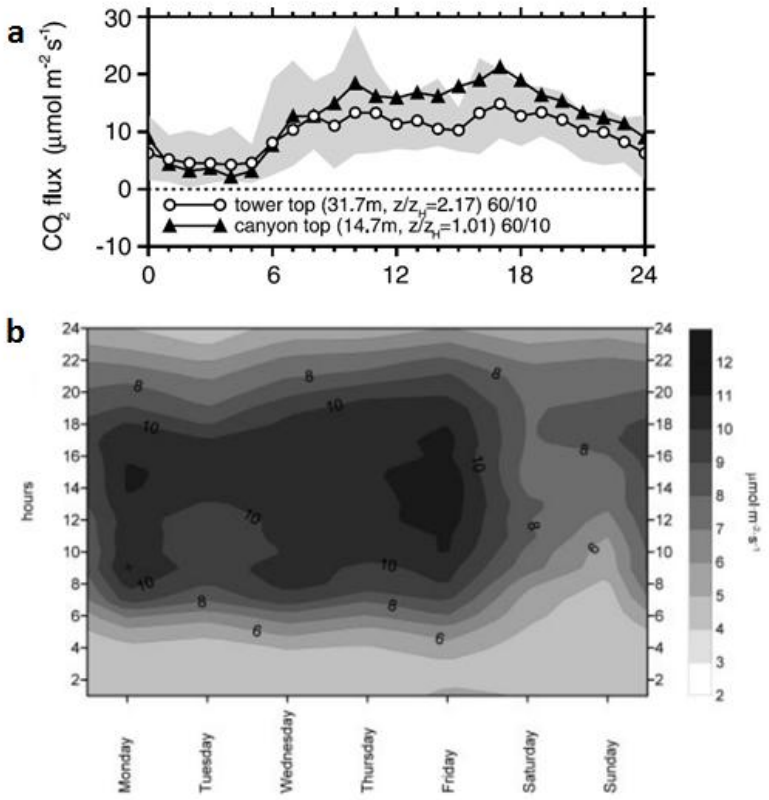

Figure 3.23 a)The average diurnal course of CO_2 fluxes for Basel where measurements are recorded within the urban canyon (14.7 m) and above the urban canyon (31 m) (Source: Vogt et al., 2006). b) Mean values of CO_2 fluxes measured in Łódź, Poland from July 2006 to August 2008 calculated for days of week illustrating a clear reduction in the flux magnitude for Saturday and Sunday (Pawlak et al., 2011).

A more variable trend in fluxes throughout the day is evident from Figure 3.23a at the canyon top (14 metres above ground level, agl hereafter) relative to the tower top (31 m agl). This trend indicated a relatively well-mixed layer at the tower top, assumed to be within the ISL and representative of the neighbourhood scale, relative to the canyon top, which represents the RSL (Figure 3.23a) (Vogt et al., 2006). CO_2 fluxes in urban environments are generally smaller in magnitude at nighttime in comparison to daytime fluxes and can be largely attributed to reduced anthropogenic activity (Velasco and Roth, 2010) (Figure 3.23a and b). With regard to winter months, nighttime fluxes are largely governed by space heating (e.g. building emissions) (Moriwaki and Kanda, 2004; Matese et al., 2009; Crawford et al., 2011).

A ‘weekend effect’ is also commonly reported in the literature and is represented by reduced CO_2 fluxes on Saturdays and Sundays due to reduced vehicular emissions (Figure 3.23b) (Coutts et al., 2007; Velasco et al., 2009; Pawlak et al., 2011). Where traffic flow does not vary throughout the year, changes in seasonal emissions are attributed to fossil fuel use for space heating and cooling, particularly in densely built areas with little vegetation (i.e. Tokyo, Japan, Moriwaki and Kanda, 2004).

A unique opportunity to investigate the CO_2 flux magnitude with and without traffic-related constraints was accomplished in Beijing, China during the 2008 summer Olympic Games. The flux of 0.40 mg m^{-2} s^{-1} measured for September 2008 was approximately 0.17 mg m^{-2} s^{-1} lower than the flux measured during the previous September, with no traffic constraints (Song and Wang, 2012). Despite these constraints however, Beijing reported annual CO_2 fluxes that were 40, 57 and 75% greater than those reported for residential suburbs of Tokyo, Melbourne, Montreal, and 38 and 48% greater when compared to the urban centres of Copenhagen, and Łódź respectively (Song and Wang, 2012). Given that Beijing is considered a mega city, the authors compared annual fluxes to a developing megacity of a similar magnitude, Mexico City, and report that CO_2 fluxes for Beijing were 40% greater. The authors suggest that this substantial difference is attributed to CO_2 sources from space heating requirements relative to Mexico City (Song and Wang, 2012; Velasco et al., 2009).

The urban function, specifically relating to space heating and vehicular traffic, has been identified as a key control of the magnitude and timing of the CO_2 flux, however the urban form is central to determining the ability of an urban ecosystem to serve as a source or sink of CO_2. A clear positive relationship is illustrated in Figure 3.24 between increased summer time flux magnitudes and increased plan area fraction of buildings in the surrounds of EC towers. In less dense neighbourhoods, biogenic effects serve to balance anthropogenic effects in summer time, for example in Baltimore (Crawford et al., 2011), Essen (Kordowski and Kuttler, 2010) and Montreal (Bergeron and Strachan, 2012).

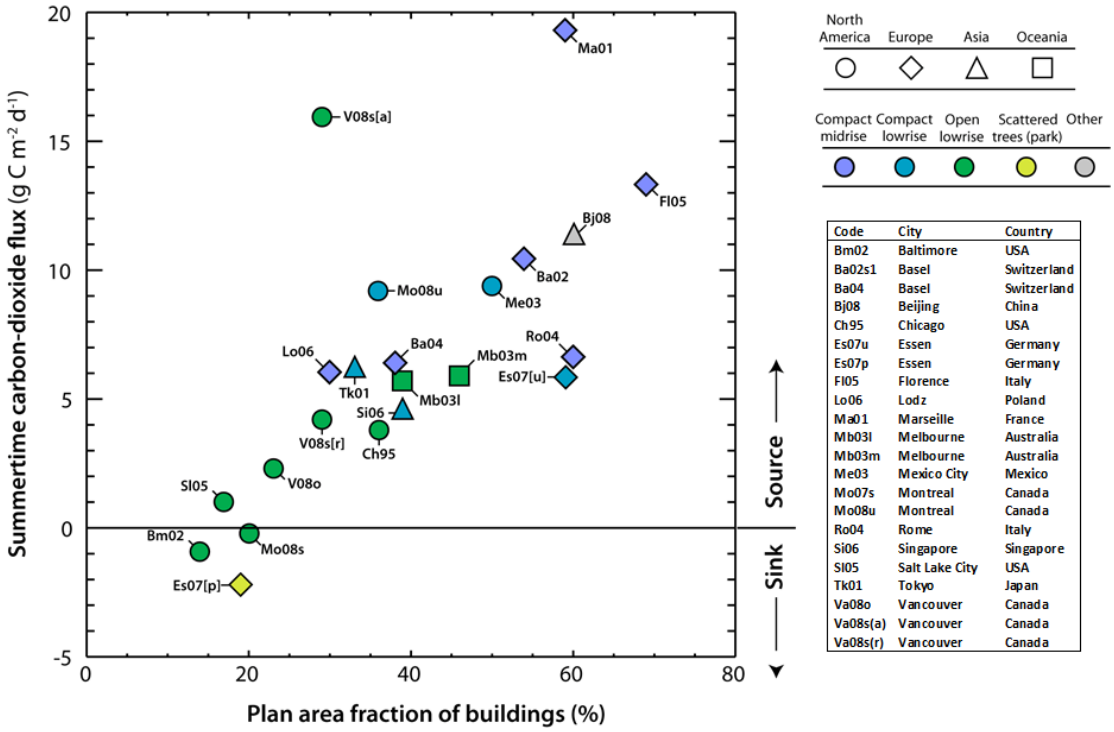

Code	City	Country
Bm02	Baltimore	USA
Ba02s1	Basel	Switzerland
Ba04	Basel	Switzerland
Bj08	Beijing	China
Ch95	Chicago	USA
Es07u	Essen	Germany
Es07p	Essen	Germany
Fl05	Florence	Italy
Lo06	Lodz	Poland
Ma01	Marseille	France
Mb03l	Melbourne	Australia
Mb03m	Melbourne	Australia
Me03	Mexico City	Mexico
Mo07s	Montreal	Canada
Mo08u	Montreal	Canada
Ro04	Rome	Italy
Si06	Singapore	Singapore
Sl05	Salt Lake City	USA
Tk01	Tokyo	Japan
Va08o	Vancouver	Canada
Va08s(a)	Vancouver	Canada
Va08s(r)	Vancouver	Canada

Figure 3.24 Summertime CO_2 fluxes measured in different urban ecosystems as a function of urban density (expressed as plan area fraction of buildings). The text associated with each symbol indicates the city, the year of observations and sometimes the site within the city. Two sites are split-up into ensemble averages for different wind sectors: Es07[p] is a sector containing a large urban park, while Es07[u] is the urban sector of this site. Va08s[r] is a residential sector with only local roads, whereas Va08s[a] is data from all wind sectors that contains busy arterial roads (Modified from Grimmond and Christen, 2012).

Unlike non-urban ecosystems overnight respiration of vegetation exercises a small influence on diurnal CO_2 fluxes however Crawford et al. (2011) present findings that indicate a large overnight flux in summertime as a result of vegetation respiration from a well-vegetated suburb of Baltimore (Figure 3.25a). Despite serving as a strong sink during the daytime in the summer months, plant respiration and anthropogenic effects lead to the ecosystem serving as a source of CO_2 over the course of the year (Figure 3.25a). This is similar to results published for Salt Lake Valley where contributions from nighttime fluxes during the summer time were also high (Ramamurthy and Pardyjak, 2011). Although both studies were conducted in heavily vegetated areas (tree and grass cover of 67.4 and 49% for Baltimore and Salt Lake Valley respectively), this was not sufficient to offset local emissions from anthropogenic activity on an annual basis (Crawford et al., 2011; Ramamurthy and Pardyjak, 2011).

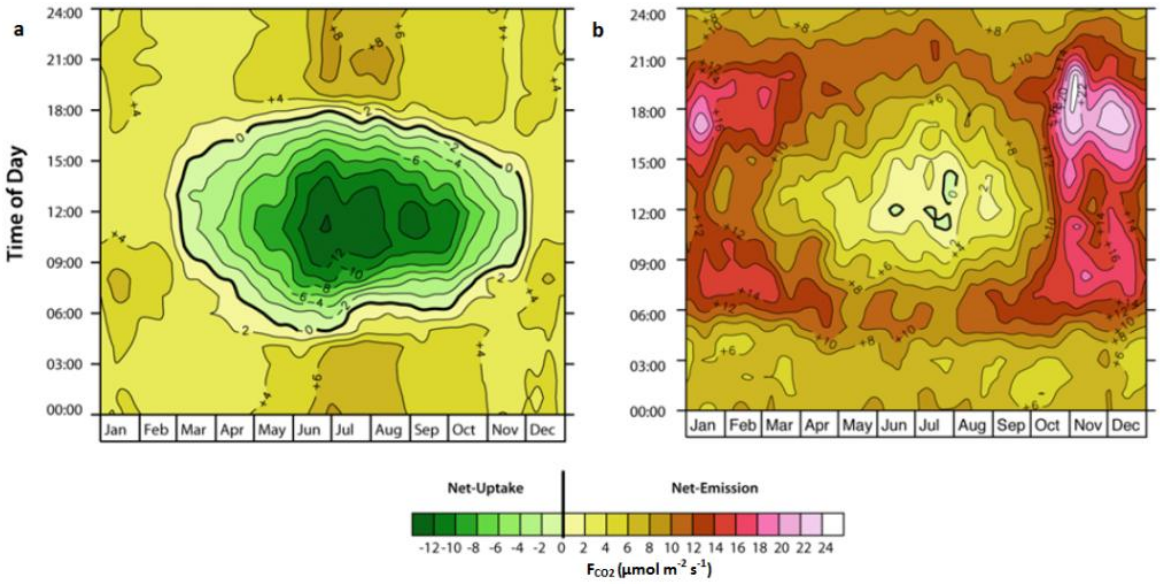

Figure 3.25 Carbon fluxes by time of day and time of year for a highly vegetated suburban ecosystem in Baltimore, USA (see Crawford et al., 2011) and a dense urban area in central Basel, Switzerland (based on data from Vogt et al., 2009) (Grimmond and Christen, 2012).

Figure 3.25b illustrates more typical annual CO_2 fluxes, in that the urban area of Basel is almost exclusively a source of CO_2 throughout the year, with the exception of periods in the summer time around solar noon where photosynthesis from the small vegetated fraction is strongest. Similar findings are reported for a two-year study in Łódź; fluxes were positive in all seasons and the city was reported as a substantial net source of CO_2 (Pawlak et al., 2011). This is in unison with results yielded for Copenhagen (Soegaard and Møller-Jensen, 2003), Seoul (Park et al., 2013), Swindon (Ward et al., 2013), London (Helter et al., 2010), Melbourne (Coutts et al., 2007), and Tokyo (Moriwaki and Kanda, 2004) whereby anthropogenic emissions to the atmosphere from all industrial, mobile and minor commercial and residential sources outweighed the potential benefits of the existence of carbon sinks within or close to the city.

3.9 Discussion

This chapter outlined how the urban geometry serves to alter the mean and turbulent wind fields giving rise to complex flow patterns within the RSL. The best characterisation of the RSL is non-uniformity of fluxes with height (Rotach, 1999; 2001), where the heterogeneous distribution of sources and sinks result in dissimilarities in the transport of energy and mass. When EC measurements are yielded from 1) sufficiently within a LCZ, where sufficient height/fetch ratios of 1:25, 1:5 are satisfied

and 2) from within the ISL, the fluxes are largely constant with height and representative of the local neighbourhood scale.

Concurrent EC studies in conjoining urban, suburban and rural sites have yielded insightful information about the timing, magnitude and partitioning of radiation and turbulent heat flux densities under similar synoptic forcings. In summary the radiation budget displays a spatially conservative nature, reductions in K* are generally offset by increases in L* when compared to rural locations. The surface albedo is reduced in urban areas however cases of high surface reflectivity have been found for surfaces such as roof windows, light coloured concrete and corrugated sheeting. ΔQ_S is found to be a considerable component of the urban SEB, often reaching the magnitude of Q_H. Of the turbulent heat fluxes, Q_H dominates and is reflected by large Bowen ratios frequently exceeding 8-9. Q_E is considerably reduced in relation to its rural counterparts, and a distinct positive relationship with vegetation surface fraction is found internationally. The urban form is efficient in removing water from the surface in addition to channelling heat into its substrate.

The CO_2 flux, having received much attention since the first study in Chicago by Grimmond et al. (2002), is found to be almost exclusively positive, indicating that the urban surface is a constant source of CO_2. Only in very-well vegetated suburban and park locations, like that found in Baltimore, is the role of urban trees and vegetation found to offset the CO_2 source for certain times of the year. The building surface fraction, vehicular traffic and space heating and cooling are significant controls on the diurnal and seasonal behaviour of the CO_2 flux and densely populated mega cities, like Beijing, report the highest fluxes.

ΔQ_S and Q_F remain key areas for investigation and require detailed information about the urban form and function. One way to treat uncertainty with regard to the residual storage flux term is to generate this term independently via the OHM and empirically derived land cover fractions. Use of flux footprint models has also been employed in urban studies to assess SEB closure and to indicate locations unrepresentative of the LCZ.

In this review the controls on radiation and turbulent heat surface-atmosphere exchanges in an urban setting have been discussed. As Baldocchi (2003:488) states "confidence in long-term carbon flux measurements will come using multiple constraints to interpret the annual sums". In an urban setting this translates into the evaluation of fluxes in unison with site specific databases containing detailed spatial and temporal information regarding the sources and sinks of CO_2 in the study volume. Urban investigators will be relatively well served in this regard, given that information regarding the urban land cover is generally well-documented (Grimmond, 2006; Grimmond et al., 2012; Feigenwinter et al., 2012). Long-term measurements covering several years remain relatively scarce, and even where they do exist, problems due to instrument maintenance, poor site access, micro-scale sources, advection, flow distortion, and unsuitable meteorological conditions (i.e. rainfall in the case in open-path gas analysers) will serve to deteriorate the data and induce bias towards dry conditions (Grimmond, 2006; Ward et al., 2013). Anomalous data points or events in the dataset may however yield useful information about the site characteristics, as demonstrated by Kotthaus and Grimmond (2012). Transparency in the literature in this regard will only serve to educate new or early EC investigators in the requirements, limitations and difficulties of operating urban EC sites.

Ultimately analysis of urban flux databases as a single entity is limited; instead EC data from a single tower should be evaluated using a suite of stratified conditions. Flux climatologies can be developed using footprint estimates for different wind directions corresponding to different surface cover fractions and anthropogenic influences, stability conditions, and synoptic conditions. In a stratified form, long-term EC datasets will also prove extremely useful for the validation of urban climate models where initial conditions for a wide range of external synoptic forcings are required. Emphasis in this regard should also be placed on EC measurements from different local climate zones within the same city where the influence of surface forcings on the SEB can be investigated under the same climate conditions.

Chapter 4 Methodology

This chapter will outline the instruments, data and processing techniques required to generate EC fluxes with specific reference to the EC sites in Dublin. Explanation of the instrumentation and their theory of operation will be presented in addition to their deployment and orientation requirements. The data derived from the instruments and their unit of measurement will be outlined, moreover steps regarding data storage, retrieval and conversion will be explained. In order to compute theoretically sound EC fluxes a series of processing steps and corrections must be implemented. The majority of these are as a consequence of the physical EC system itself and the limitations of the instruments to measure the true turbulent and scalar signals.

A number of EC software are freely available to calculate fluxes of sensible and latent heat and the CO_2 flux, a brief overview of these will be presented before the final EC software selection is made. Within the EC software a series of decisions must be made by the user and this chapter will outline the options for each processing step. A time averaging period over which to compute the flux must be selected, the ogive method, implemented here, has been developed to determine the most appropriate averaging period. Different methods to calculate the covariance over the averaging period also exist and will be outlined. Signal frequency loss due to instrument response times, path length averaging and separation of the sonic and gas analyser sensors will be discussed and methods to determine site specific transfer functions to account for these losses will be presented. Conversion of the sonic derived buoyancy flux to the sensible heat flux is required; furthermore changes in air density over an averaging period will lead to apparent flux over that time. The Webb Pearman and Leuning (WPL) correction according to Webb et al. (1980) will be implemented to account for these density change-related effects.

Once the necessary corrections have been performed a series of quality flagging and control procedures are carried out. This is a fundamental part of the data post processing in that it determines whether the EC flux for each averaging period satisfies the theoretical assumptions of the EC method, most notably conditions of steady-state and well-developed turbulence. Post processing also requires the examination of instrument diagnostics and meteorological variables to ensure correct operation of the instruments

and identify periods of reduced measurement accuracy. The derivation of an analytical flux footprint, computed within EC software will be discussed in unison with methods employed to determine surface roughness properties and land cover fractions for the surrounds of each of the EC sites.

4.1 Instruments

EC theory relies on measurements of wind velocity in the x, y and z directions in addition to gas analyser measurements when surface energy balance and CO_2 fluxes are to be investigated. A suite of instrumentation is therefore required, the placement of which should follow the scale considerations and published guidelines discussed in earlier chapters. This section will individually outline the instruments deployed at the three EC sites in Dublin in addition to their theory of operation (Table 4.1). The three stations will be referred to as the suburban site, urban site 1 and urban site 2 and are illustrated in Figure 4.1. The suburban site and urban site 1 have been in operation since April 2010 (Urban site 1 ceased operation in July 2012) while urban site 2 commenced observations in July 2012. Key differences in the suite of instrumentation deployed at each site relate to the infrared gas analysers and sonic anemometers and are outlined in Table 4.1.

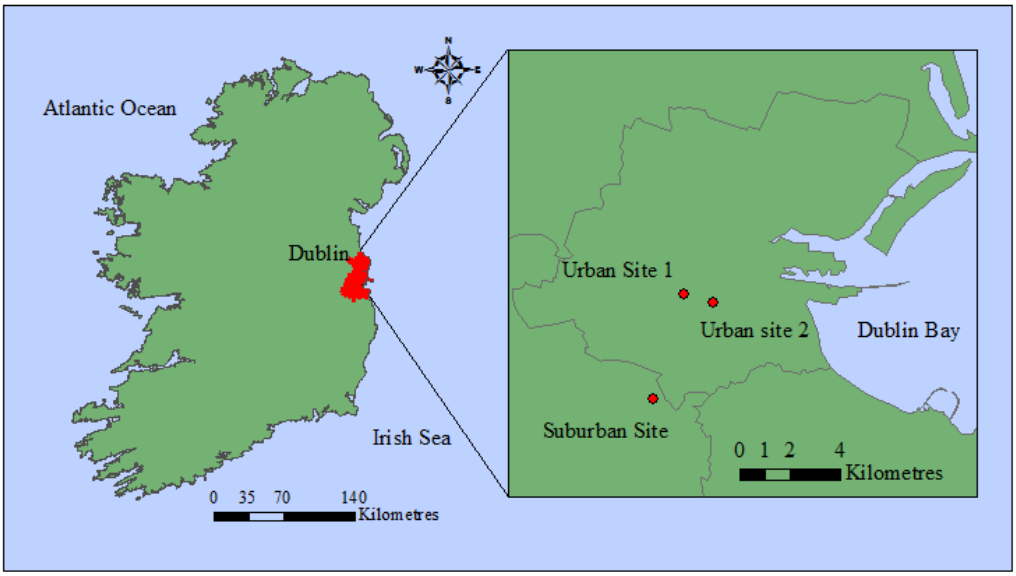

Figure 4.1Map of the island of Ireland with the location of the three eddy covariance sites in County Dublin, urban site 1 and 2 refer to Marrowbone Lane and Kevin Street stations respectively. The county of Dublin is divided into four local authorities (see boundary lines of inset figure), urban site 1 and 2 are located in Dublin City while the suburban site is located in South Dublin.

Table 4.1 Station names, locations, latitudinal and longitudinal coordinates.

Station Name	Station Location	Latitude/ Longitude	Sonic anemometer	Infrared gas analyser
Suburban site (SUB)	St Pius X, Templeogue, Dublin	53°18'10"N 6°18'17"W	CSAT3, Campbell Scientific	Li7500, Licor Biosciences
Urban site 2 (URB2)	Kevin Street DIT, Dublin City Centre	53°20'10"N 6°16'03"W	Wind Master Pro, Gill	Li7200, Licor Biosciences
Urban site 1 (URB1)	Marrowbone Lane, Dublin City Centre	53°20'22"N 6°17'06"W	CSAT3 Campbell Scientific	Li7500, Licor Biosciences

4.1.1 *Sonic anemometers (CSAT3 and WindMaster Pro)*

The sonic anemometer deployed at the suburban site and urban site 1 is model CSAT3 manufactured by Campbell Scientific (Table 4.1). The CSAT3 is a three-dimensional anemometer where sonic pulses are transmitted between three pairs of transducers, the time of flight between each pair is used to calculate the wind velocity and speed of sound along the three non-orthogonal axes (Campbell Scientific, 2014),

$$u_{pl} = \frac{d_{pl}}{2}\left\{\frac{1}{T_{1,2}} - \frac{1}{T_{2,1}}\right\}$$

$$c = \frac{d_{pl}}{2}\left\{\frac{1}{T_{1,2}} + \frac{1}{T_{2,1}}\right\}$$

Equation 4.1 Velocity of air flow along the transducer axis (u_{pl}) and the speed of sound (c) derived from the sum of the inverse of transit times (Munger et al., 2012).

Where u_{pl} is the wind velocity along the transducer axis, d_{pl} is the known distance between the two transducer heads or the path length and $T_{1,2}$ and $T_{2,1}$ are the transit times from transducer one to two, and transducer two to one respectively. Trigonometric axis transformations applied to the measurements give wind speed along orthogonal axes u_x, u_y and u_z (Munger et al., 2012). These transformations are applied by the instrument firmware during signal processing. The CSAT3 has a c-clamp structure, as oppose to omni-directional support spars, designed to minimise flow distortion on wind speed measurements (Figure 4.2). Its geometry comprising of non-orthogonal, angled, transducer configurations is also optimal in that it 1) reduces self-shadowing effects for winds aligned with the direction of one of the transducer axes and 2) serves to wick

water droplets off the transducer following a rainfall event. This allows for a relatively faster return period to valid sonic measurements (Munger et al., 2012) (Figure 4.2).

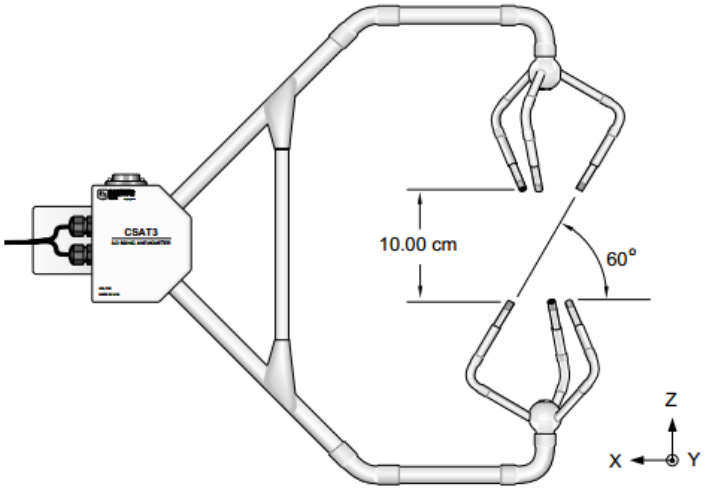

Figure 4.2 The C-clamp design of the Campbell Scientific CSAT3 sonic anemometer illustrating the coordinate system with path length of 10 cm for each of the 3 pairs of transducers. Source: Campbell Scientific, 2010.

At urban site 2 the Wind Master Pro sonic, manufactured by Gill, is used to measure wind velocity (Table 4.1). The three pairs of transducers have similar non-orthogonal geometry to the CSAT and the instrument operates in the same way. The structure of the supporting spars is different from the c-clamp structure. Three omni-directional support spars surround the transducers and the instrument is mounted on top of a cylindrical support structure (see Figure 4.3). A north alignment notch located at the instrument base should be aligned with true north. In situations where this orientation of the spars is unsuitable due to the prevailing wind direction of an EC site, the north-offset must be entered into the instrument software to ensure correct wind directions are reported. Typically it is ideal to orient the instrument so that the support spars do not conflict with the prevailing wind direction. Both the CSAT3 and Wind Master Pro have measurement rates greater than 20 Hz and have programmable output rates that are typically set to 10 or 20 Hz.

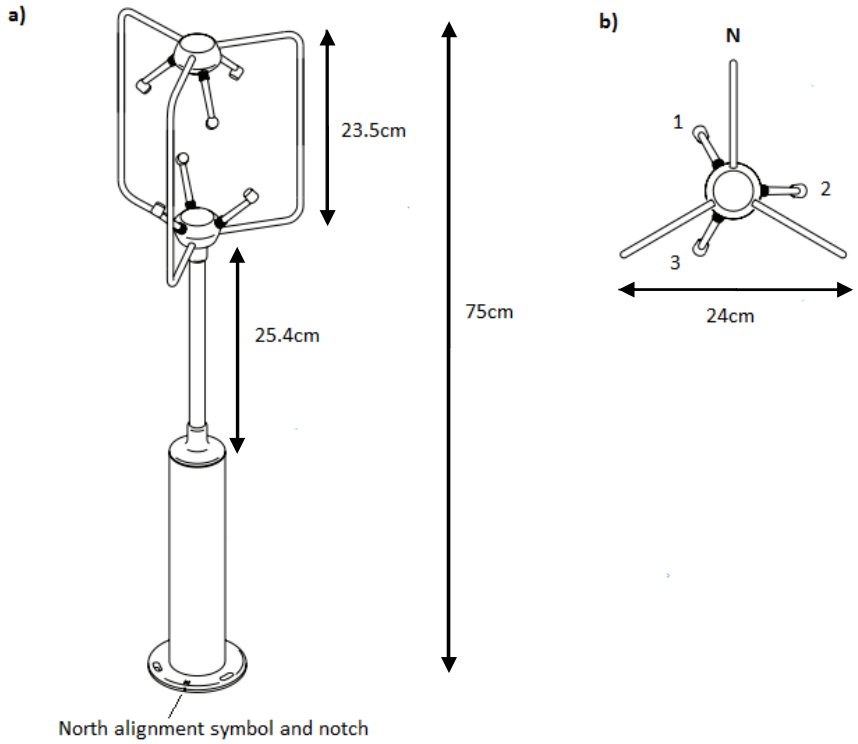

Figure 4.3 a) The Gill Wind Master Pro sonic anemometer illustrating the instrument dimensions and the three onmi-directional support spars, b) is a top view of the three transducers and their relative position to the support spars. Source: Gill Instruments, Lymington, UK.

4.1.2 *Open-path infrared gas analyser (Li7500)*

Mass densities of CO_2 and H_2O are measured using non-dispersive infrared gas analysers. The Li7500 is one such model developed by Licor biosciences and is a widely used gas analyser in EC studies (Figure 4.4). This instrument is deployed at the suburban site and urban site 1. The operation of the instrument relies on a source of infrared light. A beam passes through a sample cell to a detector, as the beam is transmitted it passes through a filter window known as a chopper wheel (Figure 4.4). The chopper wheel consists of four individual filter windows and rotates at hundreds of Hz (Burba, 2013) (Figure 4.4b). At time one the beam passes through the CO_2 filter window where the light absorption band is centred on 4.26µm, at this instant the light transmitted in the CO_2 absorption band is measured by the detector. At time two the beam passes through a reference filter window, a non absorbing window for either CO_2 of H_2O. At this instant the no-CO_2 reference is measured. The density of CO_2 is measured as the ratio of light transmitted in the CO_2 sample band to the light measured in the no-CO_2 reference band. The remaining two filter windows of the chopper wheel

contain a H_2O filter window where the light absorption band is centred at 2.59 µm and another reference filter window. Similar to above, at time three the beam is transmitted through the H_2O filter to measure light absorption and at time four the reference no-H_2O is measured. As the chopper wheel rotates at hundreds of Hz, the measurements are averaged to 10 Hz and logged via the data logger.

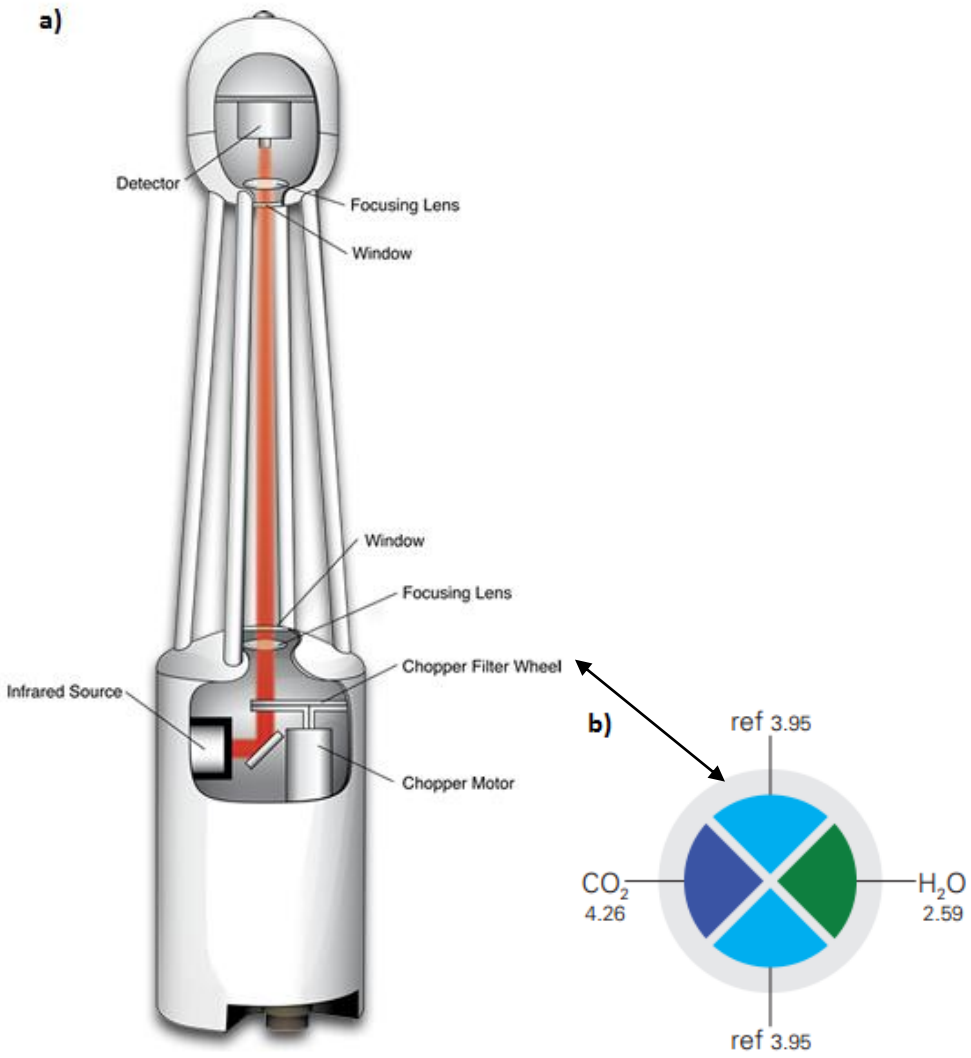

Figure 4.4 a) Schematic representation of the Li7500 open-path infrared gas analyser, and b) a schematic representing the four individual filter windows of the chopper filter wheel and their respective light absorption bands. Source: Burba, 2013.

Diagnostics from the chopper motor and chopper filter wheel are provided at a 30 minute resolution. In addition the automatic gain control (AGC) values, provided as a diagnostic variable, can approach 100% during and after rainfall events because the sample cell is effectively open (Figure 4.4). Precipitation falling through the sample cell will affect the transmission of the infrared beam, generally indicated by AGC values above 50 and approaching 100 (Licor Li7500 manual). The Li7500 gas analysers are

mounted at 15 degrees from vertical so as to prevent water droplets from settling on the lower optical window after a rainfall event.

4.1.3 *Enclosed-path infrared gas analyser (Li7200)*

Data gaps will occur due to data loss during and after precipitation events for the aforementioned reasons. To address the limitations of an open-path infrared gas analyser (IRGA) Licor developed an enclosed-path gas analyser (Li7200); this instrument is deployed at urban site 2. The sample cell is enclosed by a removable optical bench and the air is sampled via an intake tube (Figure 4.5). Similar to the Li7500, the Li7200 operates as a single beam gas analyser with a rotating chopper wheel consisting of the same four filter windows. In order to modulate the air flow in the intake tube and to ensure the continuous measurement of new air samples a flow module is required (Li7550). As mentioned earlier an open path IRGA measures mass densities of CO_2 and H_2O as oppose to mixing ratios. An open sample cell is subject to temperature, pressure and humidity fluctuations. As a result density corrections must be applied to open path IRGA density measurements. The enclosed path IRGA allows fast measurements of temperature and pressure to be measured within the sample cell synchronously with H_2O and CO_2. Temperature, pressure and water vapour content measurements allow for the conversion of density measurements to dry mole fraction per volume measurements which eliminates the necessity for density corrections in EC processing software (See section 4.4.4).

Logistical requirements for the deployment of a Li7200 include air sample inlet and outlet tubing. In order to avoid heating of the black inlet tube, a white insulated cover can be installed (Figure 4.6). An intake filter may also be required at the end of the inlet tube to reduce the build-up of fine particles within the sample cell and to avoid erosion of the inner walls of the inlet tube by these particles. Comparison of datasets and instrument response times were carried by Mammarella et al. (2009) using the same inlet tubing. Significant differences in the response times and hence signal loss were reported between the data when the tubing was first deployed in 2002 and 4 years later in 2006. The increased signal loss in the 2006 dataset was attributed to the relative dirtiness of the inlet tube. Examination of the optical window and inlet filter during cleaning will typically indicate the amount of fine particulates in the inlet tubing and whether replacement of the tubing is required.

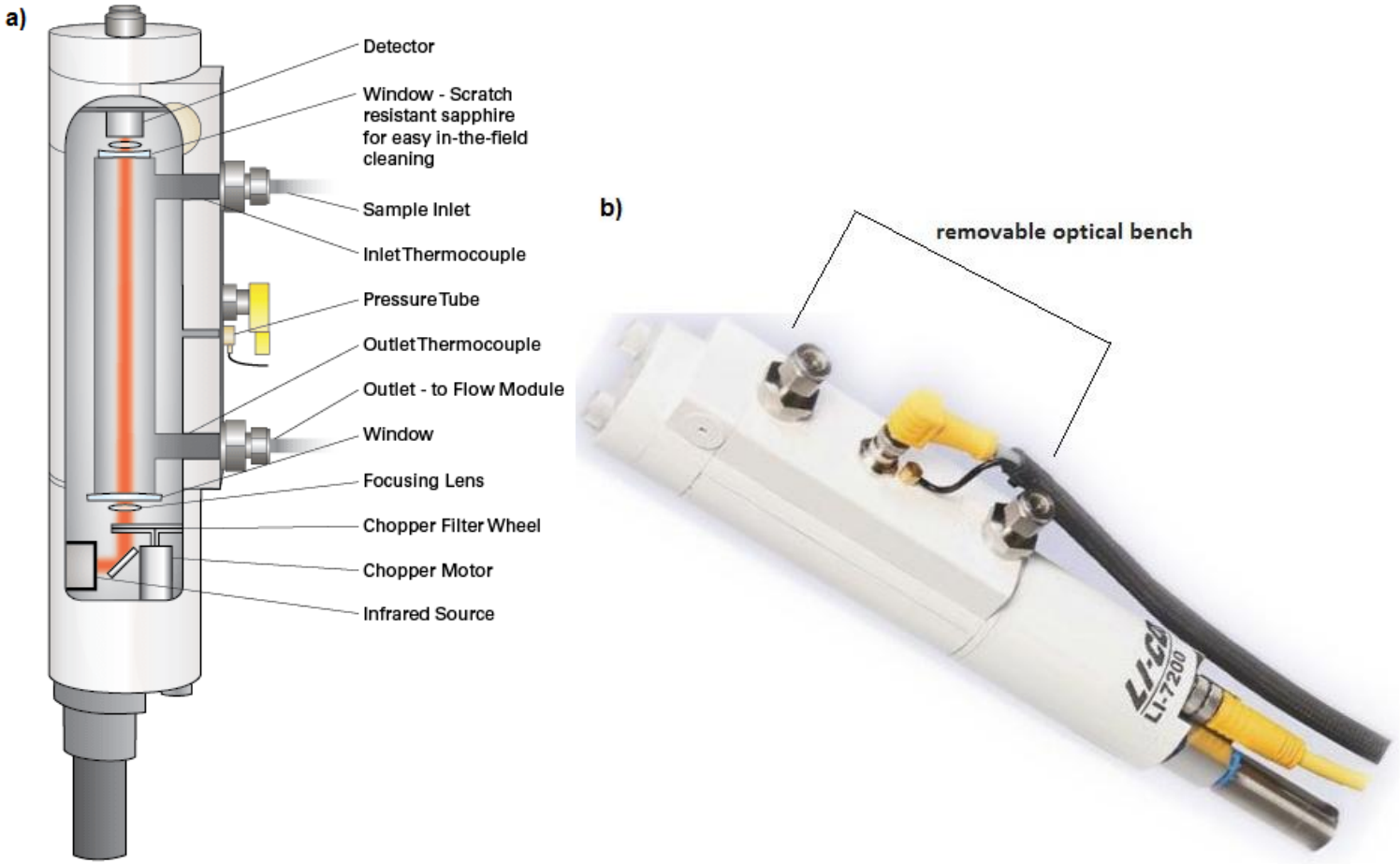

Figure 4.5 Enclosed-path gas analyser illustrating in a) the infrared beam transfer through the sample cell and b) the optical bench of the Li7200 that can be removed for instrument cleaning. Source: Licor.com

Figure 4.6 a) Li7200 deployed at urban site 2 illustrating the white insulated inlet tubing and the outlet tubing from the optical bench and b) the inlet filter and insulated inlet tubing.

4.1.4 *Auxiliary meteorological instruments (NR01, HMP45C, FW, SK215, ARG100)*

In order to investigate surface energy balance fluxes, shortwave and longwave radiation components must be measured alongside wind speed and gas concentration measurements. A four component net radiometer is deployed at each EC site. The net radiometer (model NR01) is manufactured by Hukseflux and comprises of two pryanometers, measuring incoming and reflected shortwave radiaiton and two pyregeometers measuring terrestrial incoming and surface emitted radiation (Figure 4.7).

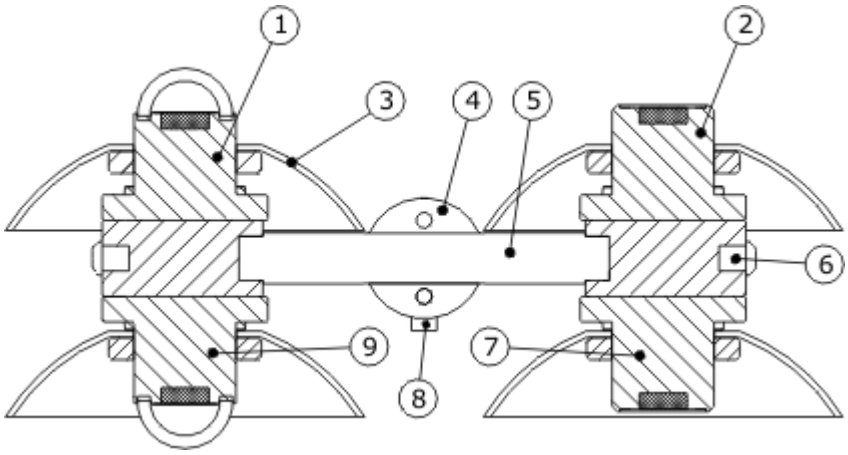

Figure 4.7 Schematic representation of the NR01 net radiometer. 1) skyward facing pyranometer, 2) skyward pyrgeometer, 3) radiation shield, 4) levelling assembly, 5) levelling assembly, 6) location of the instrument temperature sensor (Pt100), 7) surface facing pyrgeometer, 8) levelling assembly and 9) surface facing pyranometer. Source: Hukseflux NR01 manual, version 0816.

Positioning of the net radiometer should be as close in the vertical direction to the EC instruments whilst avoiding shading effects from the EC instruments, tower and support structures. In order for the pyranometers to attain correct directional and spectral characteristics of solar radiation it contains a thermopile sensor coated in black (see dark shaded rectangles in Figure 4.7). The sky – and surface – facing pyranometers are capable of absorbing solar radiation from 300 to 50000 nanometers (nm). The glass dome limits the spectral response of the sensor from 300 to 2800 nm, cutting off a negligible part of the total solar spectrum.

The absorbed radiation is then converted to heat and a proportional voltage output signal is generated by the thermopile sensor and recorded by the data logger. The glass dome also shields the thermopile sensor from convection (Huskeflux NR01 manual). Pyrgeometers operate in a similar way to pyranometers however thermopile sensors absorb all solar and longwave radiation. As a result a silicon window is required to block the solar part of the spectrum, limiting the spectral response to longer wavelengths between 4500 to 50000 nm. The silicon window is also used to shield the thermopile sensor from convective effects. The absorbed radiation by the thermopile sensor is again converted to heat where a proportional voltage output signal is generated by the thermopile and recorded by the data logger. The longwave radiative flux components, $L\downarrow$ and $L\uparrow$ require the inclusion of an instrument temperature measurement (number 6 in Figure 4.7) in their calculation given that the instrument itself will emit radiation according to the Stefan-Boltzmann Law,

$$L\downarrow = \left(U_{pyrgeo,up}\ /E_{pyrgeo,up}\right) + 5.67.10^{-8}\left(T_{pyrgeo}\right)^{4}$$

Equation 4.2 Incoming longwave radiation derived from the upward facing pyrgeometer and instrument temperature (Hukseflux, 2007).

Where U_{pyrgeo} denotes the voltage output of the upward facing pyrgeometer, E_{pyrgeo} refers to the sensivity of the upward facing pyrgeometer and T_{pyrgeo} is the temperature of the pyrgeometer.

Due to the directional or cosine response of beam radiation to the surface, e.g. full response at local solar noon when the sun is normal to the surface and zero response when the sun is at the horizon, the alignment of the instrument should accurately represent the local surface. Careful levelling of the instrument to support structures is therefore required. Initial levelling of the NR01 relative to support structures was carried out in a lab environment before deployment. Once the support structure was mounted to the tower final adjustments were made to ensure correct alignment was maintained (Figure 4.8). Additional radiation sensors measuring solar radiation and photosynthetic active radiation (PAR) are mounted on an additional supporting structure at the suburban site and urban site 1. The CMP 6 solar pyranometer manufactured by Kipp and Zonen has a spectral range of 285 to 2800 nm and a 180° field of view. Similar to the NR01 pyranometer it has a glass dome and generates a voltage output signal proportional to the radiation absorbed by the thermopile sensor.

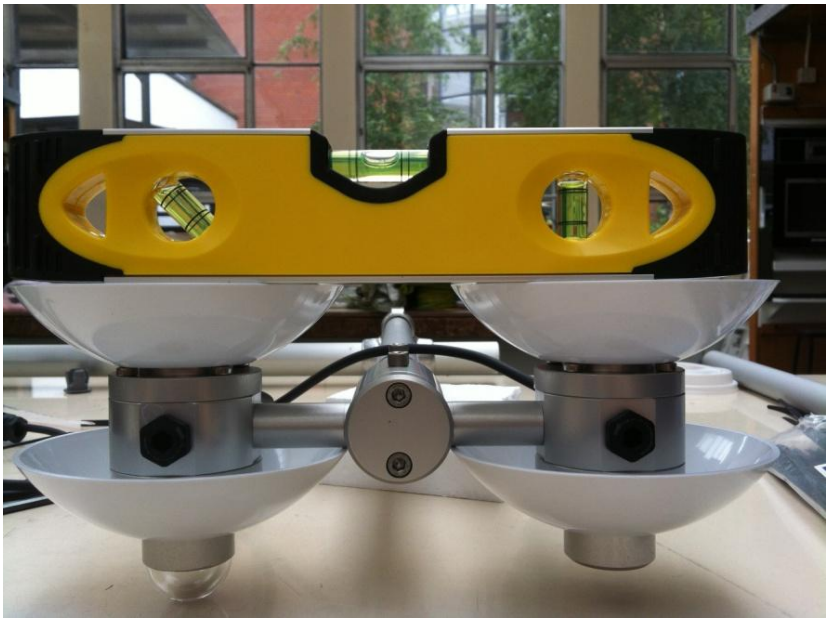

Figure 4.8 Alignment of the NR01 to supporting structures using a spirit level in the lab before instrument deployment at urban site 2.

The SKP 215 Quantum PAR sensor manufactured by Skye measures radiation between 400-700 nm, the part of the solar spectrum used by plants for photosynthesis (Skye SKP215 manual). The SKP 215 sensor detector is a silicon photocell that converts the energy of light into a voltage output signal. The magnitude of PAR indicates the level of absorption of photons or light by the chlorophyll contained in plant cells. Shorter wavelengths (e.g. 400 nm) will have greater energy content and hence the rate of photosynthetic activity will be increased (Pearcy, 1989).

Fast ambient air temperature and humidity measurements are made using a temperature and humidity probe manufactured by Vaisala Inc (Figure 4.9a). The probe is housed in a 10 plate Gill radiation shield (Figure 4.9b). The air temperature is measured using a platinum resistant thermometer (PRT). The principle of measurement of a PRT is the variation in the resistance of a platinum wire as a function of temperature (Price, 1959). Electrical resistance is measured in units of ohms where the HMP45C consists of a 1000 ohm PRT, a resistance of 1000 ohms at 0°C and a measurment range of -40 to +60 ° C (Campbell Scientific, 2009).

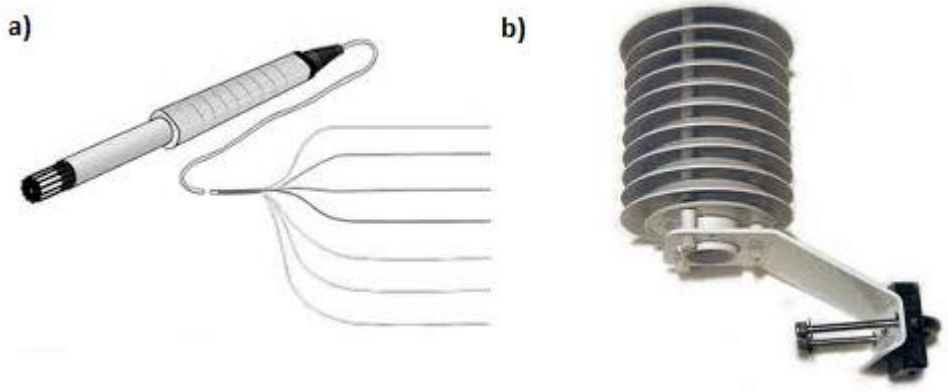

Figure 4.9 a) The HMP45C temperature and humidity probe manufactured by Vaisala and b) the Gill manufactured radiation shield. Source: Campbell Scientific.

Humidity is measured using Vaisala's HUMICAP which is a synthetic polymer sensor where a thin-film polymer is located between 2 conductive electrodes. The polymer layer absorbs or releases water vapour in response to relative humidity increases or decreases respectively (Vaisala Inc.). As the properties of the polymer layer change so too does the capacitance of the sensor, these changes are then converted to relative humidity changes.

Finally an aerodynamic rain gauge, manufactured by Waterra (model ARG100) is deployed alongside the EC instruments at each of the measurement sites. The ARG100 instrument employs the commonly applied tipping-bucket principle. The inlet funnel allows rain to collect at the base of a tipping mechanism (Figure 4.10), the sensitivity of which is typically set to 0.2 mm. Once rainfall reaches 0.2 mm the mechanism tips the water into a lower chamber where it is subsequently channelled out of the bucket. The tip is registered as the instrument output, where each tip equates to 0.2 mm. The ARG100 is capable of measuring rainfall of up to 500 mm per hour (ARG100 manual).

Figure 4.10 Tipping bucket mechanism of the ARG100. Rain is tipped into a lower chamber before being channelled out of instrument. The tipping sensitivity of the ARG100 pictured is 0.2 mm per tip.

4.2 Data processing

Data retrieval and storage methods are outlined in Appendix I in addition to information on the raw data collected and their units of measurement. This section will outline the series of data processing steps necessary for the calculation of fully corrected fluxes that satisfy the underlying assumptions inherent in the EC method. Data processing decisions must be made with regard to data despiking, detrending, coordinate rotation and spectral correction methods.

4.2.1 *Despiking the raw 10 Hz dataset*

Despiking is the only procedure that will alter the raw time series for subsequent processing, as a result careful application of the despiking algorithm is required and must account for plausible variations in the time series (Rebmann et al., 2012). Spikes in the raw time series can be detected due to their magnitude, duration and abruptness of occurrence. Spikes are often as a result of a number of factors including instrumental problems, electrical noise and water contamination from precipitation such as ice, snow and rain (Rebmann et al., 2012). Precipitation settling on the transducers of the sonic anemometer or measurement lenses of open-path gas analysers correspond to and are identified by large departures (either positive or negative) from the mean of the chosen time interval and are flagged as a spike.

Typically a despiking is applied to a time series of 18000 data points (equivalent to 30 minute data file of 10 Hz data) which is divided into smaller windows of length T = 3000 data points (e.g. Vickers and Mahrt, 1997). The mean and standard deviation for each window is calculated, if individual data points lie outside of ±3.5 standard deviations they are considered to be spikes. 4 consecutive spikes are not determined as spikes and the signal is considered to be physical. The window moves by 1500 data points and repeats the algorithm until the complete 18000 data points have been treated. Following one complete iteration of the algorithm, the standard deviation multiplication factor increases by 0.1 so that data points now lying outside of ±3.4 standard deviations are now considered spikes. The algorithm is iterated up to 20 times until no more spikes are detected, data points identified as spikes are replaced using linear interpolation.

4.2.2 *Coordinate rotation*

Coordinate rotation is the mathematical way to align the sonic sensor output (wind velocities *u*, *v* and *w*) with the coordinate system (*x*, *y*, *z*) in which the mass balance equation is solved in the EC method. This step is required because alignment of the vertical sonic axis normal to the underlying surface is very difficult, especially if the topography is not flat terrain. If coordinate rotation is not implemented the streamwise or mean horizontal wind velocity ($\bar{u}$) will contaminate the vertical velocity measurements (*w*) and the subsequent vertical flux of a scalar (e.g.$\overline{w'Xs'}$) (Kaimal and Finnigan, 1994). It is possible to transform measured wind velocities (index m in Equation 4.3) from the sonic coordinate system to that of the control volume by matrix multiplication with a rotation matrix A,

$$\begin{bmatrix} u_m \\ v_m \\ w_m \end{bmatrix} = \boldsymbol{A} \begin{bmatrix} u \\ v \\ w \end{bmatrix}$$

Equation 4.3 Coordinate rotation matrix transforming measured velocities into the desired coordinate system (Kaimal and Finnigan, 1994).

Where *A* is a 3x3 matrix of the direction cosines between the measured and desired coordinate systems. In a three dimensional coordinate system the full transformation is divided into three separate rotations (R) around the three principal axes *x*, *y* and *z*,

$$R_{01} = \begin{pmatrix} cos\alpha & sin\alpha & 0 \\ -sin\alpha & cos\alpha & 0 \\ 0 & 0 & 1 \end{pmatrix}, R_{12} = \begin{pmatrix} cos\beta & 0 & sin\beta \\ 0 & 1 & 0 \\ -sin\beta & 0 & cos\beta \end{pmatrix}, R_{23} = \begin{pmatrix} 1 & 0 & 0 \\ 0 & cos\gamma & sin\gamma \\ 0 & -sin\gamma & cos\gamma \end{pmatrix}$$

Equation 4.4 Three coordinate rotations performed around the z-axis, new y-axis and new x-axis to give angles α, β and γ (Kaimal and Finnigan, 1994).

For application to anemometer tilts, the first, second and third rotations are performed around 1) the original y-axis to give the pitch angle (α), 2) the new or intermediate x-axis to give the roll angle (β) and 3) the new z-axis to give the yaw angle (γ) (Figure 4.11). Theoretically each rotation is performed in a positive, clockwise direction looking down the axis of rotation, from the original to the transformed coordinate system (Wilczak et al., 2001) (Figure 4.11). A 1D rotation forces the coordinates so that ū is directed towards the mean horizontal wind speed, thus the mean lateral wind velocity ($\bar{v}$) equals 0. 2D rotation includes 1D rotation and also rotates such that the mean vertical velocity ($\bar{w}$) equals zero.

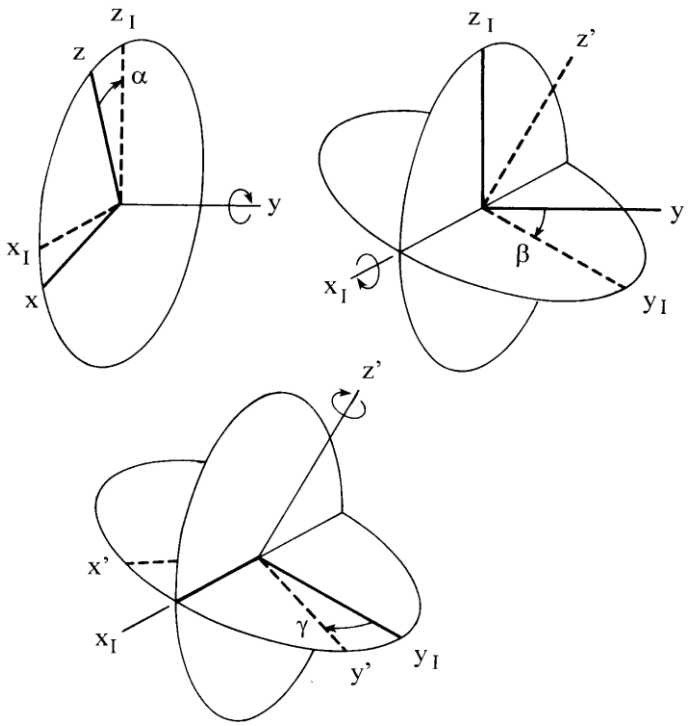

Figure 4.11 Definitions of the tilt angles α, β and γ for the yxz convention. The original axes are x y and z, the final axes are x', y' and z' and the intermediate axes are x_1, y_1 and z_1 (Wilczak et al. 2001:132).

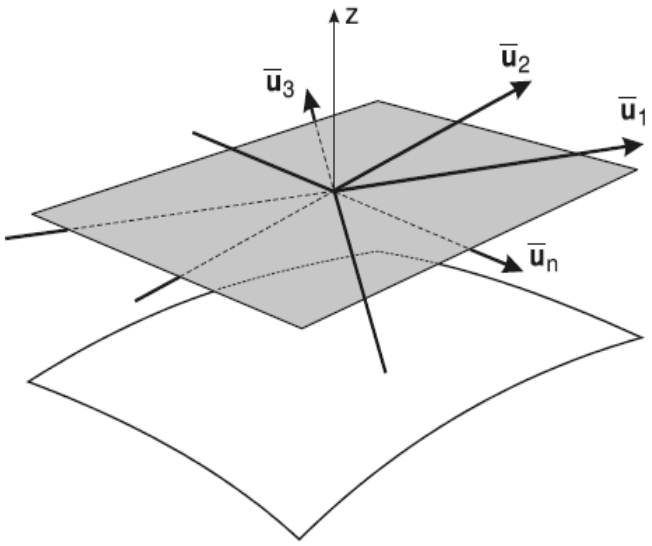

Figure 4.12 Determining mean streamline plane for the planar fit method using an ensemble of observations. The z axis is perpendicular to the streamline plane and varies over 30 minute timescales (Finnigan, 2004:29).

The planar fit (PF) method introduced by Wilczak et al. (2001) is a similar form of rotation in that the z-axis is normal to the streamline; however the streamline is determined by performing a linear regression using an ensemble of observations made over weeks or months (Figure 4.12),

$$\overline{w}_m = b_0 + b_1\overline{u}_m + b_2\overline{v}_m$$

Equation 4.5 Multiple linear regression performed on wind velocity components for the derivation of regression coefficients to determine instrument offset and the pitch and roll angles for the planar fit coordinate rotation method (Wilczak et al., 2001).

Where b_0, b_1 and b_2 are regression coefficients and $\overline{u}_m$, $\overline{v}_m$ and $\overline{w}_m$ are the measured velocity components of the sonic coordinate system for a 30 minute interval. b_0 is the instrument offset in the vertical wind velocity measurement and is subtracted from w_m, while the coefficients b_1 and b_2 are used to determine the aforementioned pitch and roll angles for each 30 minute averaging interval (Wilczak et al., 2001),

$$sin\alpha_{PF} = \frac{-b_1}{\sqrt{b_1^2 + b_2^2 + 1}}, cos\alpha_{PF} = \frac{\sqrt{b_2^2 + 1}}{\sqrt{b_1^2 + b_2^2 + 1}}$$

$$sin\beta_{PF} = \frac{b_2}{\sqrt{1 + b_2^2}}, cos\beta_{PF} = \frac{1}{\sqrt{1 + b_2^2}}$$

$$\gamma_{PF} = tan^{-1}\left(\frac{\overline{v_2}}{\overline{u_2}}\right)$$

Equation 4.6 Determination of planar fit rotations according to Wilczak et al. (2001)

The pitch and roll angles are applied before the yaw rotation, which is finally applied with a varying angle for each interval. Applying this fitted plane is only valid for periods when the alignment of the sonic anemometer has not been altered and for periods where a sufficient amount of data points have been sampled.

4.2.3 *Correction for time lags*

The raw time series of the sonic and the gas analyser (whether open-, enclosed- or closed-path) must be aligned in time so that the software can estimate the largest covariance in the 30 minute interval. Typically this type of a covariance maximization time lag should be employed simply because the lag time between instruments will change depending on the wind direction. In this case if the sonic measured the eddy first the sonic time series will be lagged to match that of the gas analyser (open-path). Alternatively if the wind changes direction, the gas analyser may measure the eddy first and hence its time series will be lagged to match that of the sonic's.

With regard to enclosed- and closed-path gas analysers further consideration must be given to the time lag determination due to sorption effects of H_2O on the air inlet tube walls (Nordbo et al., 2012). Typically as relative humidity increases from 0.4 (40%) to 1

(100%) the lag window centre and corresponding window width are increased for the time lag determination for H_2O. A separate time lag is also determined for CO_2 because it is a passive gas which does not experience sorption effects with the tube walls. In most cases a covariance maximization time lag is suitable for open-path sensors, especially if the vertical and lateral separation of the sonic and gas analyser sensors is small (e.g, <10-20 cm).

4.2.4 *Detrending*

The purpose of averaging, de-trending and filtering is to separate the active turbulent transport treated as an eddy flux from slower, deterministic atmospheric motions such as advection (Finnigan et al., 2003; Moncrieff et al., 2004). Typically there are three options for determining the mean and fluctuating part of the signal, the most widely used of which is block averaging (BA) (Finnigan et al., 2003). BA divides the raw time series into consecutive segments of length T (e.g. 30 minutes), averages over this period and removes the mean from the instantaneous raw time series to define turbulent fluctuations. The second method is linear detrending (LD) which calculates the line of best fit or the linear trend for length T and subtracts that to calculate the turbulent fluctuations. LD in relation to BA reports reduced fluxes but is found to perform well under rapidly changing conditions, for example, transition times in the morning and evening and when there is suspected instrumental drift (Rebmann et al., 2012). The third method for mean removal is a running mean approach (RM) where the mean is calculated for a filter window of length t, for example 300 seconds, which is then subtracted to give the fluctuating part of the signal for t.

The average covariance over the period T is determined according to the averaging operator, BA, LD or RM. The covariance for BA is the average of each instantaneous fluctuation following mean removal in period T. The covariance calculated for LD is the average of the instantaneous fluctuations following the removal of the line of best fit. And finally the average covariance for RM is the average of the instantaneous fluctuations calculated for each filter window, t, within the full length period T.

4.2.5 *Ogive analysis*

The ogive method refers to an approach for determining the most appropriate averaging period (T) for calculating covariances. The user tests whether the covariance reaches its maximum value within the selected averaging time. Ogive plots are used to illustrate the

cumulative contribution of eddies of all frequencies measured by the EC system to the total covariance or flux. The plots contain the same information as the cospectrum, where the line represents the integral under the spectral density curve between the highest frequency recorded and the frequency of interest. The period at which the ogive reaches asymptote, or a constant value, indicates that the maximum covariance was reached and that there is no additional flux beyond that period (Moncrieff et al., 2004; Foken et al., 2012b). The ogive method is useful as it allows the user to determine whether their selected interval is long enough to sample low frequency contributions to the turbulent transport. Selecting an averaging period that is too short will cut off the low frequency, energy containing, turbulent motions that make a significant contribution to the total flux (Kaimal and Finnigan, 1994; Moncrieff et al., 2004; Foken et al., 2012b).

Figure 4.13 illustrates ogives for two separate EC systems in Dublin, the suburban site and urban site 1. In relation to Figure 4.13 the ogive has reached asymptote and converged for all variables at the suburban and the urban site 1 indicating that there is no additional flux beyond the 30 minute averaging interval (Figure 4.13a and b). In Figure 4.13 c and d the ogives do not converge for all variables at the suburban site and the urban site 1 respectively; this indicates that there is more flux beyond the selected 30 minute averaging interval and that the total flux at this height was not captured by the EC systems. The practical application of evaluating ogives for each cospectrum (temperature, CO_2 and H_2O) for each averaging interval is difficult. As a consequence Foken et al. (2012b) suggest evaluating whether ogives converge for selected time series for unstable, stable and transition periods in the morning and evening and applying the correct averaging periods according to your findings. Ogive analysis was performed for each EC station for the above mentioned periods, where convergence of the ogives did not occur, it was found that convergence could only be achieved by reprocessing the dataset according to a dynamic averaging period which is currently not possible in any of the available software. Furthermore convergence of the ogives may be impossible if steady-state conditions were not observed over the course of the averaging interval.

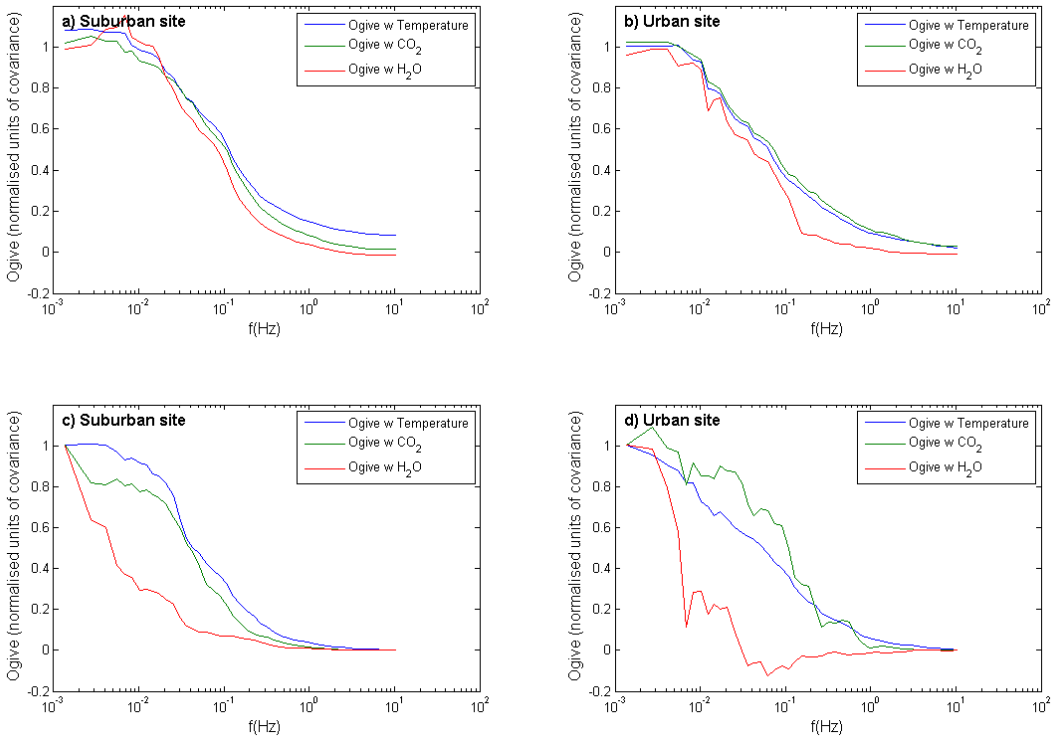

Figure 4.13 Ogives illustrating the cumulative cospectrum of vertical wind velocity (w) and temperature, CO_2 and H_2O for the suburban and urban site 1 in Dublin. The units of covariance are normalised and plotted from low to high frequencies, f(Hz).

4.3 EC corrections

Processing of the EC raw data involves 1) conversion of instrument voltage outputs to units, 2) despiking of the data and replacement of spikes using linear interpolation, 3) correcting for lag effects introduced by the raw time series of the sonic and gas analyser, 4) converting the sonic measurements into the coordinate frame of the control volume using the planar fit method, 5) selecting the most appropriate time averaging interval for the calculation of the flux using the ogive, 6) defining block averaging as the mean removal method for determination of turbulent fluctuations and finally 7) calculating the half hourly flux according to the mean removal method. Due to the limitations of the physical EC system, in addition to the need to separate fluctuations due to density changes from those associated with eddy flux a number of corrections must be applied to the calculated fluxes. Following the application of these corrections the fluxes will be tested for conditions of stationarity and well-developed turbulence so that the quality of the fluxes in relation to EC assumptions can be examined.

4.3.1 *Spectral corrections*

An EC system will underestimate the high frequency turbulent and scalar signal due to (1) the response mismatch between the anemometer and gas analyser, (2) the physical

separation of the sensors, and (3) path averaging occurring along the path length of the sonic and the gas analyser. The response time of an instrument is the time in milliseconds below which the instrument can resolve the turbulent or scalar signal. At a given time there may be more than 1 eddy passing the sensor path, the sensors as a result observe an average of the properties of the eddies in the path length. Combined these 3 effects serve to dampen the high frequency contribution to the total calculated flux. The low frequency signal representing large eddies is also underestimated, however this is as a result of the EC method as oppose to the particular setup of an EC site. Low frequency attenuation occurs due to trend removal and the necessity to average the flux over a finite period (i.e. 30 minute interval) (Massman and Clement, 2004; Foken et al., 2012b). The flux-averaging period may not be sufficient to adequately represent low frequency transport however performing ogive analysis to determine the most suitable averaging period will reduce low frequency losses.

All EC systems are limited in terms of their ability to adequately resolve turbulent flow, due to their design and setup they serve as filters attenuating the high frequency signal (Figure 4.14) (Kaimal and Finnigan, 1994 Massman and Clement, 2004; Foken et al., 2012). The relationship between the true and measured covariance (i.e. solid line and dashed line respectively in Figure 4.14) is the flux attenuation (F_a) and is simply taken to be the difference in the area under the two cospectral curves in Figure 4.14.

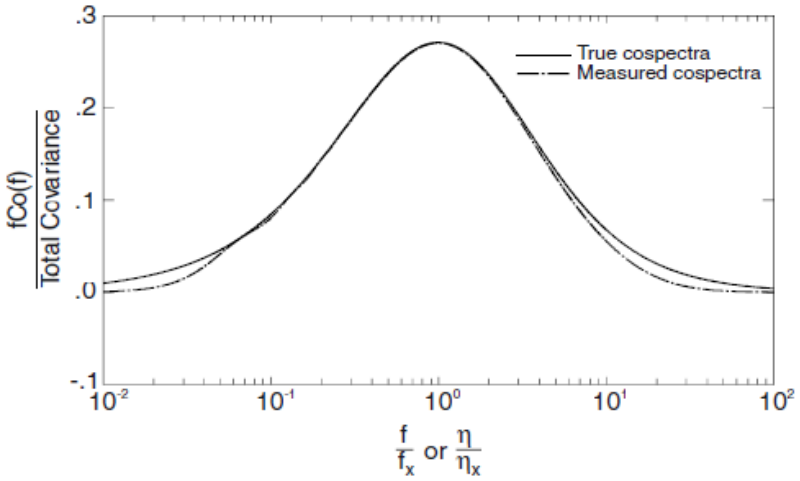

Figure 4.14 A comparison of a hypothetical frequency-weighted atmospheric cospectrum (solid line) with one measured by an eddy covariance system (dashed line). There is cospectral attenuation at low and high frequencies, the total flux loss is related to the difference in the under each of the cospectral curves. Here f is the frequency, fx is the frequency at which fCo(f) reaches its maximum value and η and ηx are their respective non-dimensionalised forms (Lee et al., 2004:68).

Previous attempts at minimizing and recovering instrument-related attenuation involved developing transfer functions (TFs) that would describe how instrument design, path averaging and sensor separation affect high frequency signals. The method, proposed by Moore (1986) and further developed by Moncrieff et al. (1997), attempts to mathematically describe these cumulative effects on spectral losses pertaining to an EC system. The total transfer function, TF_{ws}, representing an EC system for the vertical flux of a scalar S may be described as a function of real frequency (f),

$$TF_{ws}(f) = G_w(f).G_s(f).T_{ss}(f).\sqrt{T_{pw}(f)}.\sqrt{T_{ps}(f)}.\sqrt{T_{ta}(f)}$$

Equation 4.7 Transfer function for the vertical flux of a scalar (S) as a function of real frequency (f) according to Moore (1986).

Where $G_w(f)$ and $G_s(f)$ describe high frequency loss by the sonic and gas analyser sensors, $T_{ss}(f)$ represents the high-cut filtering due to the separation of sensors, T_{pw} and T_{ps} represent the path averaging effects along the sonic and gas analyser optical paths and in closed-path cases T_{ta} describes the fluctuation attenuation (F_a) due to air transport in the inlet tubes of the analyser. F_a for a given EC system is then estimated by integrating a model co-spectrum $C_{ws}(f)$ multiplied by the TF_{ws},

$$F_a = \frac{\overline{w's'_{measured}}}{\overline{w's'_{true}}} = \frac{\int_0^\infty TF_{ws}(f)C_{ws}(f)df}{\int_0^\infty C_{ws}(f)df}$$

Equation 4.8 Flux attenuation of an eddy covariance system according to Moore (1986).

Where w' and s' are fluctuations of vertical wind velocity and a scalar concentration, C_{ws} is the frequency-weighted model co-spectrum that is normalized by the covariance and multiplied by natural frequency (f). F_a will range in value from 0-1, where a value of 0.8 equates to correcting for 20% of the measured flux. The corrected co-spectrum is then calculated as;

$$\overline{w's'}_{corr} = \frac{\overline{w's'_{measured}}}{F_a}$$

Equation 4.9 Corrected vertical flux of a scalar (S) according to Moore (1986).

4.3.2 *Sonic corrections*

Wind normal or perpendicular to the sonic path length axis contaminates the wind speed measurements, as a result it is necessary to perform a crosswind correction. The correction, originally proposed by Schotanus et al. (1983) for 1D sonics was later modified by Liu et al. (2001) to provide instrument-specific coefficients for 3D sonics. Taking into account the crosswind along a transducer pair the relationship between sonic temperature and absolute air temperature for one measurement path can be obtained as follows

$$T_{si} = T_i(1 + 0.5q) - \frac{V_{ni}^2}{\gamma_d R_d}$$

Equation 4.10 Relationship between sonic derived temperature and absolute air temperature considering the crosswind effect according to Liu et al. (2001).

Where the subscript i indicates the i^{th} pair of transducers; T_i is the air temperature; q is the specific humidity; V_{ni} is the wind component normal to the i^{th} pair of transducers, R_d is the gas constant for dry air (R_d =287.04 J K^{-1} kg^{-1}); γ_d =1.4 and $\gamma_d R_d \approx 403$ m^2 s^{-2} K^{-1}; T_{si} is the sonic temperature for the i^{th} path length without considering the effects of crosswind,

$$T_{si} = \frac{c_i^2}{\gamma_d R_d}$$

Equation.4.11 Sonic temperature along *i*th transducer path with consideration of the crosswind according to Liu et al. (2001)

where c_i is the speed of sound derived from the i^{th} path length. In relation to 3D sonic anemometers, measurements from the three path lengths are combined to derive the mean sonic temperature

$$T_s = T(1 + 0.5q) - \frac{1}{3}\left(\frac{V_{n1}^2}{403} + \frac{V_{n2}^2}{403} + \frac{V_{n3}^2}{403}\right)$$

Equation 4.12 Derivation of mean sonic temperature from sound velocity along each transducer axis considering the crosswind effect according to Liu et al. (2001).

Where $T_s = (c_1^2 + c_2^2 + c_3^2)/(1209)$ is the value of the mean sonic temperature. In order to derive the crosswind velocities Liu et al. (2001) deems the mean vertical wind velocity to be negligible and is ignored, crosswind velocity in the x, y and z axes is therefore derived using the *u* and *v* measured horizontal wind velocities,

$$V_{n1}^2 = \frac{3}{4}u^2 + v^2$$

$$V_{n2}^2 = \frac{15}{16}u^2 + \frac{13}{16}v^2 + \frac{\sqrt{3}}{8}uv$$

$$V_{n3}^2 = \frac{15}{16}u^2 + \frac{13}{16}v^2 - \frac{\sqrt{3}}{8}uv$$

Equation.4.13 Derivation of the crosswind velocities specific to the CSAT3 3D sonic anemometer according to Liu et al. (2001).

Where u and v are the wind velocity magnitudes of the x-axis and y-axis defined by the right-handed co-ordinate system of the CSAT3. This cross-wind correction is applied in the internal firmware of the CSAT3 and applying it later in EC data processing software would be redundant and may cause errors in the data (Campbell Scientific, 2014; Mauder and Foken, TK3 manual, 2011). T_s differs from T because it does not take into account the dependence of c on vapour pressure, as a result it is generally not regarded as an accurate representation of absolute air temperature. That said however T_s can be cross-checked with fast response absolute air temperature measurements from thermocouples or platinum resistant thermometers (PRTs) located alongside the sonic anemometer and gas analyser. Often the temperature error between the temperature measurements are constant and therefore do not affect the variances and covariances for flux computation (Munger et al., 2012).

In order to calculate the sensible heat flux in situations where measurements of absolute air temperature are not available, T_s is decomposed into a mean and fluctuating part and is used to derive the buoyancy flux, $\overline{w'T_s'}$. The original correction was proposed by Schotanus et al. (1983) for 1D sonics and was modified by Liu et al. (2001) to account for 3 path lengths and the effect of crosswind to give,

$$(\overline{w'T'c}) = \overline{w'T_s'} - 0.5\overline{w'q'}\overline{T} + \frac{2\overline{T}}{c^2}(\overline{w'u'}\overline{u}A + \overline{w'v'}\overline{v}B)$$

Equation.4.14 Correction from the sonic derived buoyancy flux to the sensible heat flux according to Liu et al. (2001)

Where $\overline{w'T'c}$ is the corrected sensible heat flux; *A*= (3/4+15/16+15/16)/3 and *B*= (1+13/16+13/16)/3.

4.3.3 *Open-path IRGA surface heating correction*

Burba et al. (2008) carried out an experiment to measure the surface temperature of the Li7500 open-path IRGA in relation to ambient air temperature. It was found that in very cold climates during the non-growing season the instrument surface was warmer than ambient air temperature during the daytime. This relative heating serves to increase natural convection surrounding the measurement path of the open-path IRGA leading to an overestimation of the flux, and an apparent ecosystem uptake of CO_2. The effect on annual CO_2 budgets from an urban area in Helsinki was 450 g C m^{-2} $year^{-1}$ (or 17% of emissions) (Järvi et al., 2009). However the overestimation is most pronounced in very cold climates, therefore the correction was not implemented for Dublin which has a temperate maritime climate.

4.3.4 *WPL correction*

The Webb, Pearman and Leuning (WPL) correction, proposed by Webb et al. (1980) accounts for the effects of density fluctuations (e.g. temperature and humidity) on fluctuations of trace gas concentrations (e.g. CO_2). Open-path gas analysers used in EC systems measure mass densities or molar concentrations that are not conserved during air compression or expansion, evaporation or water vapour diffusion (Burba et al., 2012; Foken et al., 2012b; Leuning, 2004). The WPL correction is required to account for these fluctuations because they are not responsible for the net transport of a trace gas, hence including them would lead to incorrect EC fluxes as reported by Ham and Heilman (2003). In this situation raw uncorrected fluxes are compared with WPL corrected fluxes for CO_2 from an EC system deployed in a car park for a total of seven days in July 2002. Warming of the car park's asphalt surface indicated a large apparent uptake of CO_2 by the ecosystem in the raw uncorrected fluxes when in fact there was a slight positive flux of CO_2 throughout the day according to the WPL corrected fluxes (Ham and Heilman, 2003).

Density fluctuations concurrent with the eddy flux are accounted for as follows:

$$\underbrace{\overline{F_{c,WPL}}}_{\substack{\text{Open-path}\\ \text{total trace gas flux}}} = \underbrace{\overline{w'\rho_c'}}_{\text{Eddy flux}} + \underbrace{\mu(\overline{\rho_c}/\overline{\rho_d})\,\overline{w'\rho_q'}}_{\substack{\text{Water vapour flux term}\\ \text{(water dilution effects)}}} + \underbrace{(1+\mu\sigma)(\overline{\rho_c}/\,\overline{T})\overline{w'\,T'}}_{\substack{\text{Heat flux term}\\ \text{(Thermal expansion effects)}}}$$

Equation 4.15 Total trace gas flux including the eddy flux, water vapour flux and heat flux term (Webb et al., 1980)

Where $\mu = m_d/m_q$ is the ratio of molar masses of dry air and water vapour, and $\sigma = \overline{\rho_q}/\overline{\rho_d}$ is the ratio of the densities of water vapour and dry air. The corresponding eddy flux of water vapour is

$$\underbrace{\overline{F_{q,WPL}}}_{\text{Total trace gas flux}} = \underbrace{\overline{w'\rho_q'}}_{\text{Eddy flux}} + \underbrace{\mu\left(\overline{\rho_q}/\overline{\rho_d}\right)\overline{w'\rho_q'}}_{\substack{\text{Water vapour flux term} \\ \text{(Water dilution effects)}}} + \underbrace{(1+\mu\sigma)\left(\overline{\rho_q}/\bar{T}\right)\overline{w'T'}}_{\substack{\text{Heat flux term} \\ \text{(Thermal expansion effects)}}}$$

Equation 4.16 Water vapour gas flux including the eddy flux, water vapour flux and heat flux term (Webb et al., 1980)

In the case of open-path IRGAs the correction applied assumes that the EC fluxes are measured using perfect instruments. We have seen from previous sections however that EC instruments attenuate the total flux; hence application of the WPL correction is implemented after spectral corrections have been performed.

With regard to the enclosed-path gas analyser deployed at urban site 2, the Li7200 is capable of outputting instantaneous mixing ratios or dry mole fraction using the mass densities in unison with temperature and pressure measurements that are made in the analyser at the same frequency. As a consequence instantaneous temperature- and pressure- related fluctuations associated with thermal expansion and dilution of the sampled air are already accounted for and the WPL correction is not necessary (Leuning, 2004; Nakai et al., 2011) as follows,

$$X_c' = \frac{\rho_c'/m_d}{p_i'/(R\,T_i') - \rho_q'/m_q}, \qquad X_q' = \frac{\rho_q'/m_d}{p_i'/(R\,T_i') - \rho_q'/m_q},$$

Equation 4.17 Instantaneous mixing ratios of a trace gas and water vapour derived from the Li7200 enclosed-path gas analyser (Foken et al., 2012b)

Where X_c' and X_v' are the instantaneous mixing ratios of a trace gas (c) and water vapour (q) respectively; p_i and T_i are pressure and absolute temperature measured in the gas analyser. The corresponding fluxes of a trace gas and water vapour at some height above the surface are subsequently calculated as,

$$\overline{F_{c,WPL}} = \overline{\rho_d}\,\overline{w'X_c'}, \qquad \overline{F_{q,WPL}} = \overline{\rho_d}\,\overline{w'X_q'},$$

Equation 4.18 Total trace gas fluxes derived using instantaneous mixing ratios for a trace gas (c) and water vapour (q) (Foken et al., 2012b)

This section has demonstrated the complex set of data processing steps and flux corrections necessary to ensure the validity of the final flux estimates. Spikes will inevitably occur in the data and careful implementation of despiking algorithms is necessary to ensure that the raw dataset is not unduly modified due to despiking and replacement of spikes using linear interpolation. It has also been shown that different corrections are necessary depending on the suite of instrumentation deployed at the EC site, particularly regarding the gas analyser and the application of spectral corrections and the WPL correction.

4.4 Software comparison

There are several EC software freely available that implement the above processing steps and corrections, the most popular of which are presented in Table 4.2. The table is taken from Foken et al. (2012b) and has been modified to include two novel software, 1) EddyUH, developed by the Department of Physics in the University of Helsinki, and 2) EddyPro developed by Licor biosciences. Both of these software provide the user with relatively more flexibility in terms of accepted instruments, coordinate rotation methods, spectral correction methods and data quality control (Table 4.2). EddyPro at the time of its launch by Licor Biosciences was largely based on The Eddy Covariance Community software (ECO_2S) but in later versions it has implemented increasingly novel algorithms (e.g. in-situ spectral corrections according to Fratini et al. (2012)).

Within the urban EC community there is no definitive consensus with regard to software suitable for post processing urban datasets. In the absence of strict guidelines urban EC scientists are typically advised to 1) apply the data processing chain implemented for non-urbanized ecosystems, 2) assess and evaluate potential flow distortion caused by surrounding roughness elements and 3) gain a thorough understanding of the source area characteristics via detailed data sets containing building footprints, building heights, land cover (Feigenwinter et al., 2012). In general the available literature urges EC scientists to employ established software, like those outlined in Table 4.2 when calculating fluxes, and discourages the production and use of ‘in-house’ scripts to calculate fluxes arguing that their use limits the degree to which EC flux estimates can be readily compared (Fratini and Mauder, 2014).

Table 4.2 Overview of available EC software and included corrections and quality checks (Updated from Table 4.8 in Foken et al., 2012b)

Software	**TK3**	**Alteddy**	**ECPack**	**EddySoft**	**EdiRE**	**Eth-flux**	**TUDD**	**S+ packages**	**ECO_2S[a]**	**EddyPro**	**EddyUH**
	Univ. of Bayreuth	Alterra	Univ. of Wageningen	Max-Planck Institute Jena	Univ. Of Edinburgh	Technical University Zürich	Technical University Dresden	NCAR/EOL	IMECC-EU Univ. of Tuscia	Licor Biosciences	Univ. of Helsinki
Data sampling	CSAT3, USA-1, HS, R2,R3,ATI K, NUW, Young; 6262,7200, 7500,KH20 ,ADC OP-2	R2, R3, WMPro, CSAT3,USA-1; 6262,7500,7000, KH20,TGA100A, Los Gatos DLT100	R2,R3,Young; 6262,7000,7500, ADC OP-2	R2,R3,Young; 6262,7000,7500, ADC OP-2	Any	CSAT3,R2,R3,H S;6262,7000,750 0,FM-100,Monitor Labs, Scintrex, LMA3,Los Gatos, FMA and FGGA, Aerodyne QCL	R2,R3,HS,US A-1;6262,7000	CSAT; KH20,7500, other sensors possible	R2,R3, WMPro; CSAT3, USA-1; 6262,7500,7000 ,7550(7200/770 0)	R2,R3, WMPro, CSAT3, Young, USA-1; 6262,7500,7000,7 550 (7200/7700), other sensors possible	R2,R3,HS, CSAT3, USA-1; 6262,7500,7000, 7550(7200/7700) , TDL, Los Gatos, Picaroo,TSI CPC, LOZ-3, Aerodyne QCL
Data preparation	Test plausibility, spikes, block average, time lag const/auto	Test plausibility, spikes, block average; optional detrending (filter) time lag const.	Test plausibility, spikes, optional detrending (linear); time lag const.	Test plausibility, spikes, block average; optional detrending; time lag const/auto	Test plausibility, spikes, optional detrending (linear/filter) ; block average; time lag const/auto	Test plausibility, spikes, block average, optional detrending; time lag const/auto	Test plausibility; block average, time lag for closed path sensor	Test/replace spikes; block average; time lag; (all in NIDAS software)	Test plausibility, spikes, block average; optional detrending and running mean; time lag const/auto/RH dependent	Test plausibility, spikes, block average, linear detrending and running mean; time lag const/auto/RH dependent	Test plausibility, spikes, block average, linear detrending and running mean; time lag const/auto/RH dependent
Coordinate rotation	Planar fit/2D rotation, head-correction	2D rotation; Nakai et al. (2006)	Planar fit/2D/3D rotation	Planar fit/2D/3D rotation	Planar fit/2D/3D rotation	2D/3D rotation	3D rotation	Planar fit	Planar fit/2D/3D rotation;head correction for Gill sonics (Nakai et al. 2006)	Planar fit (sector-wise), 2D/3D rotation, Van Dijk et al. (2004), Nakai et al. (2006), Nakai and Shimoyama (2012)	Planar fit (sector-wise), 1D/2D/3D rotation
Buoyancy flux to sensible heat flux	Schotanus et al.(1983)/Li u et al. (2001)	Schotanus et al.(1983)	Schotanus et al.(1983)	Schotanus et al.(1983)/Liu et al. (2001)	Schotanus et al.(1983)/Li u et al. (2001)	-	Schotanus et al.(1983)/Liu et al. (2001)	Schotanus et al.(1983)	VanDijk et al. (2004)/Liu et al. (2001)	Schotanus et al.(1983)/Liu et al. (2001)	Schotanus et al.(1983)/Liu et al. (2001)

Table 4.2 (continued)

Software	TK3	Alteddy	ECPack	EddySoft	EdiRE	Eth-flux	TUDD	S+ packages	ECO_2S[a]	EddyPro	EddyUH
	Univ. of Bayreuth	Alterra	Univ. of Wageningen	Max-Planck Institute Jena	Univ. Of Edinburgh	Technical University Zürich	Technical University Dresden	NCAR/EOL	IMECC-EU Univ. of Tuscia	Licor Biosciences	Univ. of Helsinki
High-frequency loss	Moore (1986)	Moore (1986)/ Eugster and Senn (1995)	Moore (1986)	Eugster and Senn (1995)	Moore (1986)/ Eugster and Senn (1995)	Eugster and Senn (1995)	Moore (1986)/ Eugster and Senn (1995)	Horst and Lenschow (2009)	Moncreiff et al.,(1997),Horst (1997), Ibrom et al. (2007); Horst and Lenschow (2009)	Moncreiff et al.,(1997),Horst (1997), Ibrom et al.(2007),Horst and Lenschow (2009), Fratini et al. (2012)	Moncreiff et al.,(1997), Aubinet et al. (2000), Mammarella et al. (2009)
WPL correction	Webb et al. (1980)	Webb et al. (1980),Burba et al. (2008)	Webb et al. (1980)	Webb et al. (1980)	Webb et al. (1980)	Webb et al. (1980)	Webb et al. (1980)	Webb et al. (1980)	Webb et al. (1980),Burba et al. (2008), Ibrom et al (2007)	Webb et al. (1980),Burba et al. (2012), Ibrom et al (2007)	Webb et al. (1980), Ibrom et al. (2007)
Quality control	Test steady state, integral turbulence characteristics: Foken and Wichura (1996); Footprint Kormann and Meixner (2001), Ogive	Uncertainty factor	Statistical error: van Dijk et al. (2003)	Test steady state, integral turbulence characteristics : Foken and Wichura(1996) ;Footprint	Test steady state, integral turbulence characteristics : Foken and Wichura (1996), Vickers and Mahrt (1997); Footprint	Test steady state,integral turbulence characteristics : Foken and Wichura (1996);	Nighttime critical u*	Manual; use redundant sensors	Test steady state, integral turbulence characteristics : Foken and Wichura (1996); Vickers and Mahrt (1997); Footprint; Schuepp et al. (1990); Kljun et al. (2004)	Test steady state, integral turbulence characteristics: Foken and Wichura (1996); Vickers and Mahrt (1997); Footprint; Kljun et al. (2004); Kormann and Meixner (2001);Hsieh et al. (2000), Ogive	Test steady state, integral turbulence characteristics: Foken and Wichura (1996); Vickers and Mahrt (1997); Footprint; Kormann and Meixner (2001), Ogive

In the absence of a consensus regarding a specific software suitable for the urban domain, coupled with the increasing number of software available, a comparison using a subset of data was undertaken prior to the calculation of fluxes for all 3 EC sites. This investigation sought to determine whether there was a difference in the flux estimates of Q_E, Q_H and F_C utilising a uniform dataset and data processing scheme in 3 different EC software packages. The 3 EC software packages included EddyPro version 4.2.1 (EP) and EddyUH version 1.3 (UH) and TK3 version 3.1 (TK3). A uniform dataset from urban site 1, spanning 91 days (April 7 to July 7 2010) was employed in EP, UH and TK3 resulting in 4367 half hourly flux estimates from each software for comparison.

The quality of the match between EP, UH and TK3 was quantified by deriving linear regressions (slope, intercept and r^2) of the scatter plots of individual fluxes (where n is 4367). In this case EP was selected to represent the independent variable and UH and TK3 represent the response variables (y). The selection of EP was based on its thorough validation against six other EC package, furthermore EP has been used extensively according to Licor Biosciences who report 3800 software downloads in 155 countries worldwide (Licor, 2015). That said, given that no software is capable of calculating the true flux and ultimately just a measured flux, the choice of an 'independent' variable is somewhat trivial.

The regression analyses was performed in Matlab version R2013b using the in-built regstats function that performs a multi-linear regression of the responses in y on the predictors in x (Mathsworks, 2015). The scatter plots for the fluxes of Q_E, Q_H and F_C are presented in Figure 4.15 and the statistics for the regression analyses are presented in Table 4.3. The slopes of the regression lines differ by less than 3.5% from 1 for Q_E, and by less than 2% for Q_H and F_C. The intercepts of the regression lines are <0.5 W m^{-2} for Q_E, <0.25 W m^{-2} for Q_H, and finally <0.1 μmol s^{-1} m^{-2} for F_C. To compare the regression results of UH and TK3, intercepts are almost identical for Q_H and F_C, differing by around 0.2 W m^{-2} for Q_E (Table 4.3). r^2 values demonstrate that all or almost all variation (i.e. r squared equal to 1) in UH and TK3 output is explained by the EP reference datasets (Table 4.3). These results are very similar to findings reported in Fratini and Mauder (2014) between output from EP and TK3.

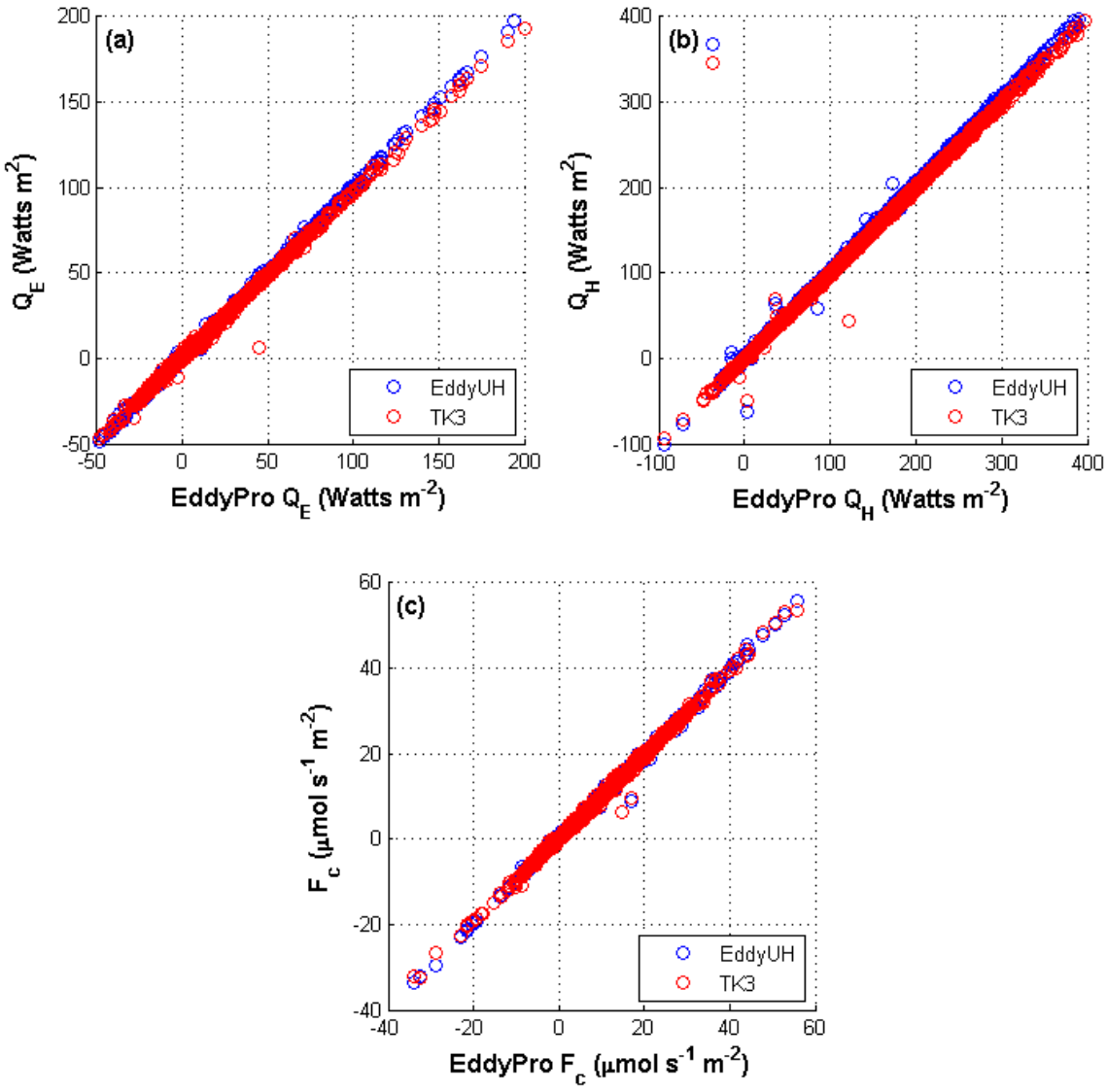

Figure 4.15 a) Latent heat flux estimates, b) sensible heat flux estimates and c) CO flux estimates from urban site 1 calculated by the software packages EddyPro (reference on the x-axis) and EddyUH and TK3.1 (on the y-axis). Note the difference in the magnitude along the x- and y-axis for each flux variable and a, b and c.

The mean squared error (MSE) and root-mean squared error (RMSE) are often calculated to measure the accuracy of field forecasts against observations. The RMSE is defined as,

$$RMSE = \sqrt{\frac{1}{M}\sum_{m=1}^{M}(y_m - o_m)^2}$$

Equation 4.19 Root-mean squared error (Wilks, 2011)

Where M represents the data points and the RMSE is computed for each pair of observed and forecast data points ($y_m - o_m$). A perfect forecast is indicated as a RMSE of zero, and larger RMSE indicating decreasing accuracy, (or agreement) of the forecast. In this investigation the RMSE was calculated using EP as the 'observed' data points (o_m) and the UH and TK3 as the 'forecast' data points (y_m). The average RMSE was calculated using 4367 half hourly flux estimates for each flux and are presented in Table 4.3. The RMSE from EP was smallest for UH, 0.65 W m^{-2} on average for Q_E increasing to 1.2 W m^{-2} for TK3. In terms of Q_H, the RMSE were larger due to the relatively large flux magnitudes (illustrated in Figure 4.15b) and are similar for both UH and TK3. Again for F_C the RMSE are similar for UH and TK3 and are reduced relative to the reduced size of the F_C (Figure 4.15c).

Table 4.3 Comparison of regression analyses for a) the latent heat flux, b) the sensible heat flux and c) the CO_2 flux for the observation campaign dataset where n=4367 half hour values using Eddy Pro as the baseline software

Software	Slope	Intercept (Watts m^{-2})	r^2	RMSE (Watts m^{-2})
a) Q_E				
UH	1.01	0.06	1.00	0.65
TK3	0.96	0.30	0.99	1.2
b) Q_H				
UH	1.02	0.24	0.99	6.88
TK3	0.99	0.25	0.99	6.48
	Slope	**Intercept (µmol s^{-1} m^{-2})**	**r^2**	**RMSE (µmol s^{-1} m^{-2})**
c) F_C				
UH	0.99	0.08	0.99	0.25
TK3	0.98	0.09	0.99	0.33

This investigation concluded that very similar results can be achieved in EP, UH and TK3 when a uniform raw dataset and uniform data processing steps are implemented. Overall the results of the regression analyses showed very good agreement for all fluxes with some variability during unstable conditions (data not shown). The results are consistent with output from Fratini and Mauder (2014) and provide EC scientists with increased confidence in the output of previous published software comparisons that were performed over shorter timescales (ranging from 5 days to one month) (Mauder et al., 2008; Mauder and Fratini, 2014).

In terms of software constraints TK3 did not have the option to perform a sector-wise planar fit rotation which is necessary for urban sites with relatively complex surrounds. A sector-wise method could only be employed if the raw data was first disaggregated into selected wind sectors and processed separately. The required raw data file formats for ingestion into TK3 are relatively restrictive allowing for 3 specific input options 1) CR23X 2) TOA5 and 3) Labview. Furthermore the output options were reduced in comparison to EP and UH. The software does however incorporate a novel and computationally efficient method for spike detection that employs the Median Absolute Deviation (MAD) (outlined in Mauder et al., 2013) as oppose to traditional mean statistics (Vickers and Mahrt, 1997).

UH is a relatively novel software with a smaller user-base than both EP and TK3, as a result there were several bugs identified throughout the processing steps. The manual documentation accompanying UH is less thorough compared to TK3 and EP where applied corrections are not adequately outlined in the text. As a result communication with the software developers was required on several occasions to clarify processing techniques and to report bugs. In saying that there were more options for raw data file formats than TK3 and the user can easily plot raw data using the UH plotting tools. This tool is particularly helpful to users and allows for 1) a first look at the raw data and 2) the identification of hard spikes indicating instrumental problems for example.

EP was selected for processing raw data pertaining to each of the Dublin EC sites for the entire observation campaign. Greater flexibility in terms of de-spiking methods, coordinate rotation options, and spectral correction methods are provided in EP which are required the urban domain, particularly when enclosed- and closed- path gas analysers are deployed. Furthermore Licor have dedicated software developers that address user-defined problems (e.g. software bugs) and requests for new data analysis and reporting tools. Open online user discussion forums and updated user manuals are presented alongside EP software, both of which serve to educate the user on the most scientifically appropriate use of EP for their specific settings.

4.5 Data processing for Dublin eddy covariance sites

The following section summarises the specific processing steps carried out in EP version 4.1 that were employed to compute final fluxes across the 3 EC sites in Dublin for the entire observational campaign. EP requires the user to create a metadata file for each EC site within a graphical user interface. Site specific information must be provided relating to the instrument models, their height and separations, surface roughness properties, and the site's geographical coordinates and altitude. Within the EP metadata window, the column order of raw 10 Hz files must be outlined in addition to the variables' units of measurement. For Dublin meteorological datasets containing variables such as relative humidity, air temperature, net radiation and pressure were also provided for processing. Once all of the necessary information was entered the site-specific metadata file was created for each EC site; these files could be edited in situations where instruments have been reoriented.

The Vickers and Mahrt (1997) despiking approach was applied to the raw data time series for Dublin. Within EP the user is free to decide the number of standard deviations and the number of permitted consecutive spikes for each variable in the raw time series. In the case of Dublin EC raw datasets, if a 30 minute interval containing a total of 18000 data points has more than 180 spikes, 1% of the total data points, the program will assign the corresponding flux value as a missing value (-999).

With regard to coordinate rotation, a sector-wise planar-fit was performed for all sites. This involves performing the linear regression and fitting a tilted plane for user-defined number of wind direction sectors. It is important to once again ensure that an adequate number of data points are sampled from each of the wind sectors to ensure a representative plane. A sector-wise PF was selected for coordinate rotation of datasets pertaining to each EC site in Dublin. A total of 12 wind sectors were selected for plane fitting, each 30 degrees wide. Where there were less than 100 time intervals for a particular wind direction over a 3 month period a fitted plane was not calculated and the 2D rotation was applied to the data instead. Finally intervals reporting low wind speeds ($u<1$ m s^{-1}), with reduced turbulent intensity were rejected from the plane fitting regression. The decision to use 30° sectors for the planar fit was largely based on the nature of the surrounds of the EC sites. Using too few sectors for the determination of the fitted planes would not reflect the variation of the urban form surrounding the EC

towers. Use of the planar fit coordinate rotation method also requires long term datasets to determine the fitted plane. A 3 month dataset was chosen to maximise the possibility of sampling from all wind sectors whilst maintaining the timely processing of datasets for the three EC sites.

In order to determine the correct lag time, a maximum cross-covariance function is applied to the time series of the vertical wind velocity and scalar which locates their maximum covariance within a time window. The covariance maximisation method was employed for the EC sites with open path IRGAs, namely urban site 1 and the suburban site (Table 4.1) This method is suitable for EC sites where there is small vertical and lateral separations between the sonic and gas analyser measurement paths (e.g. < 20 cm). With regard to the enclosed path IRGA deployed at urban site 2, EP can determine a site-specific time lag which varies according to relative humidity. Ambient relative humidity affects the determination of the EC system lag time for closed- and enclosed-path analysers due to the sorption effects of H_2O on the air inlet tube walls (Nordbo et al., 2012). Within EP it was possible to calculate a varying time lag according to a user-specified number of RH classes. Typically as relative humidity increases from 0.4 (40%) to 1 (100%) the lag window centre and corresponding window width are increased for the time lag determination. A separate time lag was also determined for CO_2 because it is a passive gas which does not experience sorption effects with the tube walls.

The detrending method selected for each of the EC sites in Dublin was the block average method where length T was 30 minutes (note: justification for the averaging interval, T, is presented in the next section). This method of mean removal obeys the Reynold's averaging conditions outlined in Chapter 2; furthermore it attenuates the low frequency, energy containing, part of a turbulent signal to the least degree (Rebmann et al., 2012). Spectral correction methods for OP IFGA sites employed the fully analytical method by Moncrieff et al. (1997) which corrects for spectral losses induced by the EC system. Similar to the time lag determination, treatment of the spectral corrections is more complex for urban site 2 (Li7200 enclosed path IFGA) due to adsorption/desorption effects on the tube walls. EP users can select one of two in-situ methods developed by Ibrom et al. (2007) or Fratini et al. (2012) to derive correction factors for the H_2O flux. As previously mentioned the attenuating adsorption/desorption

effects on the H_2O flux is dependent on relative humidity (Foken et al., 2012b; Nordbo et al., 2012). Consequently spectral correction methods rely on an in-situ assessment made over weeks or months to determine robust relationships between lag times and ambient relative humidity. Within EP the user can define the number of classes in which to divide relative humidity for the frequency response calculation. An in-situ assessment according to methods outlined in Ibrom et al. (2007) deemed suitable for use in rough terrain, was employed for data pertaining to urban site 2 where the Li7200 enclosed IRGA is deployed (See Table 4.6 for a summary).

4.6 Data quality flagging

The same quality flagging procedure according to Foken et al. (2004) was implemented in EP for the 3 EC sites. The flagging scheme employs 2 main steps to test for stationarity and well-developed turbulence within the averaging period according to Foken and Wichura (1996). Flags of different magnitudes are assigned to each data point for each flux (e.g. Q_H, Q_E and F_C) based on the outcome of the tests. The magnitude of the flag is an indication of the quality of the flux estimate, flags range from 1 to 9, 1 representing best quality flux and 9 representing the worst quality flux. The flagging procedure provides adequate information via the designation of flags from 1-9 and is considered more suitable for use in the urban domain in comparison to methods proposed during a CarboEurope workshop on EC quality assurance and quality control in Spoleto Italy in 2004. The latter method proposes a 3-flag procedure, 0 representing good quality date, 1 representing data suitable for long term budgets and 2 bad quality data that should be discarded from subsequent analysis.

With regard to the flagging procedure by Foken et al. (2004) the stationarity test requires that the individual mean and fluctuation of a variable for 6 subintervals of 5 minutes each are within 30% of the overall 30 minute mean and fluctuation (Foken and Wichura 1996). If the mean or fluctuating part of the individual 5 minute data series is outside of this range then the stationarity requirements are not fulfilled and the half hourly value is flagged according to the magnitude of deviation (%) from the overall 30 minute statistics (Foken et al., 2004) (Table 4.4).

To test for fully developed turbulence, measured integral turbulence characteristics (ITC) are calculated for each 30 minute interval. ITCs describe simple flux-variance

similarity whereby the ratio of the standard deviation of a turbulent parameter (i.e σ_u) and its turbulent flux (u^*) is nearly constant and a function of stability (Arya, 2001; Kaimal and Finnigan, 1994; Stull, 1988). The measured ITCs for turbulent and scalar fluxes are compared with modelled ITCs (e.g. Foken et al., 1991,1997; Thomas and Foken, 2002) for the interval time and when the half hourly test parameter is less than or equal to 30%, well-developed turbulence throughout the 30 minute interval can be assumed (Foken and Wichura, 1996),

$$ITC_\sigma = \left| \frac{\left(\frac{\sigma_x}{x^*}\right)_{model} - \left(\frac{\sigma_x}{x^*}\right)_{measurement}}{\left(\frac{\sigma_x}{x^*}\right)_{model}} \right|$$

Equation 4.20 Test of integral turbulence characteristics proposed by Foken and Wichura (1996)

where ITC_σ is the test parameter, σ_x is the standard deviation of a turbulent or scalar parameter and x^* is the associated flux. Similar to above, the magnitude of the quality flag will be determined based on the deviation of the test parameter from modelled parameters (Table 4.4). The two individual flagging systems are then combined to form an 'overall' quality flag system whereby data of class 9 should be excluded from further data analysis (Foken et al. 2004) (Table 4.5).

Table 4.4 Classification of the data quality by the steady-state test, integral turbulence characteristics and the horizontal orientation of the CSAT3 sonic anemometer by Foken et al. (2004)

Steady-state test		**Integral turbulence characteristics**		**Horizontal orientation of the sonic anemometer**	
Class	**Range**	**Class**	**Range**	**Class**	**Range**
1	0-15%	1	0-15%	1	±0-30°
2	16-30%	2	16-30%	2	±31-60°
3	31-50%	3	31-50%	3	±60-100°
4	51-75%	4	51-75%	4	±101-150°
5	76-100%	5	76-100%	5	±101-150°
6	101-250%	6	101-250%	6	±151-170°
7	251-500%	7	251-500%	7	±151-170°
8	501-1000%	8	501-1000%	8	±151-170°
9	>1000%	9	>1000%	9	>±171°

Table 4.5 Proposal for the combination of the single quality flags into a general data quality according to Foken et al. (2004)

Flag of the general data quality	Steady state test	Integral turbulence characteristics	Horizontal orientation of the sonic anemometer
1	1	1-2	1-5
2	2	1-2	1-5
3	1-2	3-4	1-5
4	3-4	1-2	1-5
5	1-4	3-5	1-5
6	5	<=5	1-5
7	<=6	<=6	<=8
8	<=8	<=8	<=8
	<=8	6-8	<=8
9	One flag equal to 9		

4.7 Post-processing and data quality control

Mauder et al. (2013) suggest using on-site diagnostic variables to determine periods in the data when instruments may not be capable of accurate measurements. The estimated fluxes for each EC site were cross referenced with instrument-derived diagnostic variables, precipitation events and quality flags. Although the CSAT3 and Wind Master Pro employed here have advantages over those with orthogonal heads in that their orientation wicks water off the transducer heads, in general all sonic anemometers will fail during heavy rainfall and icy conditions (Munger et al. 2012). The signal from the transducers is dampened during such conditions and hence reliable measurements of wind velocities and the speed of sound are not possible. Warnings are provided by the sonics and are reported individually as the number of low amplitude, high amplitude, poor signal and temperature warnings.

The Li7500 reports warnings associated with the chopper motor and wheel. Furthermore the automatic gain control (AGC) variable can be used as an indicator for optical window purity. Typically AGC values for Li7500 models are between 50-60% at the time of factory deployment and should be recorded to represent the instrument-specific clean window baseline (Licor Li7500 manual). An increase from initial values can indicate an accumulation of dirt and/or precipitation on the optical windows and as the value approaches 100%, the optical path should be cleaned (Licor Li7500 manual). Initial AGC values recorded by the Li7500 at urban site 1 and the suburban site were 50%; values greater than 50 as a result represent periods when the lenses was relatively unclean, wet or dirty. With regard to the Li7200 AGC values are typically around 30 at

the time of factory deployment and when AGC values reach 90 the optical window is completely blocked (Licor Li7200 manual). Half hourly CSAT warnings and AGC values are reported for Dublin datasets and were used during data quality control to determine periods with reduced instrument accuracy. In addition periods corresponding to rainfall events (> 0.2 mm measured by the ARG100) and quality flags of class 7 or greater according to Foken et al. (2004) were discarded from the final flux dataset.

4.8 Surface roughness and flux footprint calculations

Profile measurements were not available at the time of processing to allow for the determination of roughness parameters using anemometric methods. Given that information on the spatial distribution of roughness elements and heights were available, the zero-plane displacement height (z_d) and aerodynamic roughness length (z_0) were calculated according to morphometric methods proposed by Macdonald et al. (1998). Building footprint datasets were employed in ArcGIS to determine a 1km radius centred on the EC station. These datasets displayed buildings according to different height classes and were subsequently exported from ArcGIS in .tif image format for ingestion into Matlab version R2013b where datasets were used to calculate the frontal area fraction and plan area fraction (see Equation 3.1and Equation 3.2). In unison with the building height data, the plan area fraction was employed to calculate z_d according to MacDonald et al. (1998),

$$z_d = z_H\left(1 + \alpha^{-\lambda_p}(\lambda_p - 1)\right)$$

Equation 4.21 Zero plane displacement height according to Macdonald et al. (1998)

Where α is an empirical coefficient equal to 4.43, obtained from evaluation of wind tunnel data. α in this calculation of the zero plane displacement height corresponds to wind tunnel data from a staggered building array as opposed to a square, or grid-like array. As will be shown in the following chapter staggered arrays were found to best represent the orientation of buildings at each of the Dublin EC sites. The roughness length, $z_{0,}$ is calculated using z_H and $z_{d,}$

$$z_0 = z_H\left(1 - \frac{z_d}{z_H}\right) exp\left(-\left(0.5\beta\frac{C_D}{k^2}(1 - z_d/z_H)\,\lambda_f\right)^{-0.5}\right)$$

Equation 4.22 Roughness length according to Macdonald et al. (1998)

Where C_D is the drag coefficient (constant value of 1.2) and k is the Von Karman constant (equal to 0.4) and β (equal to 0.55) is an empirical coefficient that corrects C_D for sheltering effects (Macdonald et al., 1998). For each of the EC sites calculations were made according to Nordbo et al. (2013) for a circular area with a varying radius ranging from 500 to 1000 m with a 100 m resolution. Given that the only information provided for the calculation of λ_p, λ_f, z_H, z_d and z_0 are building footprints, these calculated parameters do not consider the presence of roughness elements such as trees and cars. The frontal area fractions of the buildings were calculated for the EC site surrounds based on four inflow sectors, north, south, east and west; the program employed to calculated these parameters is computationally demanding and increasing the number of inflow categories was not deemed feasible. For each inflow direction only the walls of buildings facing the direction were accounted for, where λ_f was calculated using corresponding values for the individual building heights. Average values pertaining to λ_p, λ_f, z_H, z_d and z_0 were calculated for 1 and 30° arcs of radii 500, 600, 700, 800, 900 and 1000 m.

The analytical footprint model according to Kormann and Meixner (2001) was employed to derive the probable source area of the measured fluxes for different wind directions. It was selected because it is a numerically robust model that is also sufficiently fast to be applied within EddyPro to determine an approximate footprint for every 30 minute interval. The footprint model uses surface roughness parameters (z_d and z_0), the measurement height, the Monin-Obukhov length (L) and mean windspeed to determine the upwind footprint distance. Within EddyPro it is not possible to use dynamical surface roughness parameters according to the wind direction; instead average values for z_d and z_0 are employed. This is a limitation of the software given that both parameters can vary depending on the wind direction as shown in Chapter 5. Nevertheless the estimated flux footprint can be examined in conjunction with calculated surface roughness parameters and land cover maps to evaluate wind directions that vary significantly from average values employed in the software.

4.9 Discussion

This chapter outlined and explained the suite of instrumentation necessary to compute EC fluxes of latent and sensible heat and of CO_2. Placement of the instruments in relation to each other and in relation to the tower and surrounding roughness elements

should carefully consider published guidelines. In addition, where the surface energy balance and energy balance closure is investigated it is necessary to 1) observe net radiation and 2) estimate the heat storage flux for the EC site. Various diagnostic and meteorological variables are also required, firstly for data quality control and secondly to understand the flux magnitude for varying meteorological conditions and wind directions.

A software comparison, the first of its kind for the urban domain, was presented in Section 4.4 and concluded that very similar results can be achieved in EP, UH and TK3 when a uniform raw dataset and uniform data processing steps are implemented. For urban EC scientists, processing of raw data using established software packages is the first part in a series of steps to ensure theoretically sound flux estimates. A suite of post-processing and data quality flagging procedures are also required to identify good quality flux estimates and to identify conditions when the theoretical assumptions of EC theory are not met (See Table 4.6 below for a summary of all processing steps and corrections applied to each of the Dublin EC sites). The methods proposed by Foken et al. (2004) (e.g. flags from 1 to 9) were selected for data quality flagging and are considered more informative for the investigator in comparison to other published data quality flagging procedures (e.g. flags 0, 1 and 2 in Mauder and Foken, (2004)).

Finally urban EC investigators will also have to evaluate 1) the surrounding surface roughness characteristics and their ability to distort the air flow surround the measurement towers and 2) the surrounding surface cover characteristics and their effect on the flux footprint. Methods to determine the probable flux footprint and the surface roughness characteristics of the EC sites have been outlined, the latter of which requires data on the spatial distribution and height of the roughness elements. Spatial datasets representing each EC site will be presented in the following chapter; the surface cover and roughness characteristics of the three EC sites will be described in detail. Differences in these characteristics ultimately influence the timing, magnitude and partitioning of the estimated turbulent fluxes giving rise to distinctive local-scale climates

Table 4.6 Summary of software processing steps and corrections for each eddy covariance site

Step	Method	EC Site	Published
Data preparation	Despiking	SUB, URB1, URB2	Vickers and Mahrt (1997)
Coordinate rotation	Sector-wise planar fit	SUB, URB1, URB2	Wilczak et al. (2001)
Time lag correction	Covariance maximization	SUB, URB1	Eddy Pro version 4.1
	Automatic time lag optimisation	URB2	Eddy Pro version 4.1
Detrending	Block average	SUB, URB1, URB2	Finnigan et al. (2003)
Buoyancy to sensible heat flux	Performed via internal firmware of sonics	SUB, URB1, URB2	Schotanus et al. (1983); Liu et al. (2001)
Ogive analysis		SUB, URB1, URB2	Moncrieff et al. (2004)
High frequency loss	Fully analytic	SUB, URB1	Moncrieff et al. (1997)
	In-situ assessment	URB2	Ibrom et al. (2007)
WPL correction	Correction for the effects of density fluctuations	SUB, URB1	Webb et al. (1980)
		URB2	Burba et al. (2012)
Quality control	Stationarity and ITCs	SUB, URB1, URB2	Foken and Wichura (1996)
	Data quality flagging (Flags 1-9)	SUB, URB1, URB2	Foken et al. (2004)
	Footprint estimation	SUB, URB1, URB2	Kormann and Meixner (2001)
Data post-processing	Removal of data points corresponding to rainfall events and instrumental problems (e.g. AGC values)	SUB, URB1	Mauder et al. (2013)
	Removal of data points corresponding to instrumental problems (e.g. AGC values)	URB2	Mauder et al. (2013)
Surface roughness	Morphometric methods	SUB, URB1, URB2	Macdonald et al., (1998); Nordbo et al. (2013)
Estimation of net heat storage flux	Energy balance residual method	SUB, URB1, URB2	Oke and Cleugh (1987)
	Objective hysteresis model	SUB, URB1, URB2	Grimmond et al. (1991)

Chapter 5 Surface cover and roughness properties

This chapter will provide a detailed description of the three EC stations located in Dublin. Maps, photographs and schematics will be presented to illustrate the geography of the surrounds of the stations with regard to their physical and functional characteristics. Furthermore the surface roughness properties for each EC site will be presented according to methods proposed by Nordbo et al. (2013). Spatial datasets relating to building footprints were provided by Dublin City Council and derived from the Ordnance Survey of Ireland (OSI). With regard to canopy cover and street trees, data was provided by Dr Tine Ningal of University College Dublin (UCD). Canopy cover is yielded from aerial imagery, while street tree data was collected as part of a tree inventory of Dublin City (see Ningal et al., 2010). Datasets describing the extent of greenspace were unavailable for the suburban site and were digitized using Google Earth imagery. The building footprints, canopy cover, street trees, and greenspace datasets were combined into a GIS to derive surface cover fractions for each EC site. The residual planar surface area within a 1 km radius of each EC site is finally assumed to represent the impervious surface fraction (e.g. comprising of roads, pavements, courtyards, car parks and storage yards). Furthermore land cover fractions for 30° wind sectors were derived within the GIS to distinguish typical surface cover fractions and identify sectors of potential bias.

As noted in the previous chapter the calculation of surface roughness parameters according to Nordbo et al. (2013) requires building footprint data for its calculation and hence is directionally dependent. This method does not incorporate roughness elements such as trees, vehicles and road signs. As a consequence the calculated roughness properties, particularly in the direction of urban parks which are typically tree-lined, do not account for these roughness elements. Therefore it is likely that the roughness characteristics in these wind sectors, described in detail later, are underestimated; methods to include tree data from these locations however were not available.

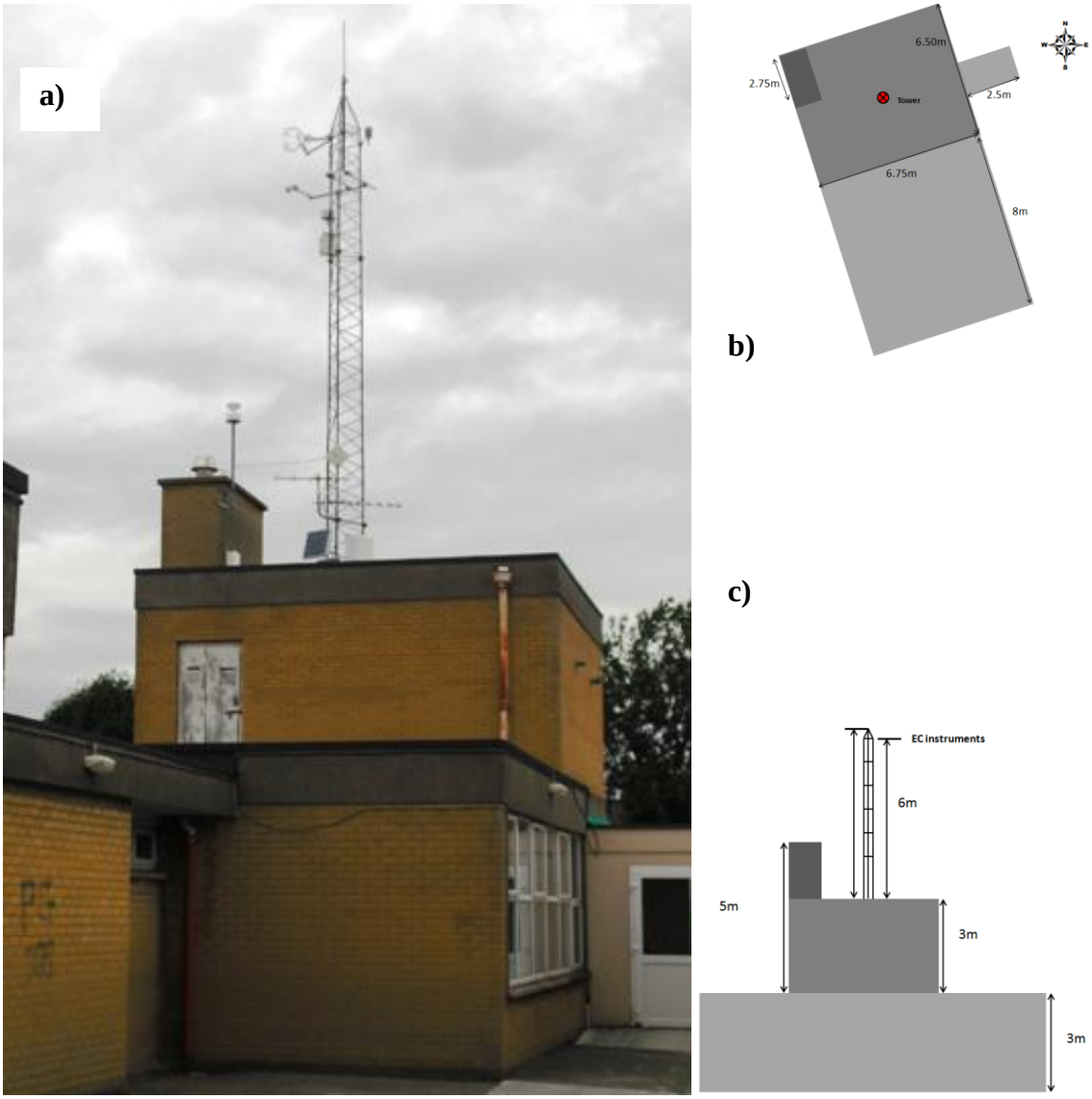

Figure 5.1 a) Photograph illustrating the location of the EC tower at the suburban location, b) a plan view schematic of the building showing its dimensions in metres and the location of the EC tower and c) a cross section view illustrating the building, tower and EC instrument heights.

5.1 Suburban Site – St Pius X

The suburban site is located on the grounds of St Pius X Girls National School in Templeogue, South Dublin. The EC station began operation in September 2009 however initially the instruments were deployed too close to the roof surface, within the RSL. The instruments were raised to 12 m, within the ISL in April 2010. The EC instruments are mounted on a 6 metre lattice tower on the roof (Figure 5.1a). The EC instruments, e.g. the sonic anemometer and the gas analyser are located at the top of the tower on a 0.2 m horizontal boom at a height of 12 m above the ground (agl) (Figure 5.1c). The sonic anemometer is orientated at an azimuth of 240 ° (that is, toward the

south west), corresponding to the prevailing wind direction recorded at Dublin Airport between 1942 and 2010 (Met Éireann, 2014).

The gas analyser is mounted alongside the sonic anemometer to ensure the measurement paths of both instruments are as close as possible. The gas analyser is tilted 30° from a vertical position to allow rain droplets to roll off and the horizontal separation of the instrument measurement paths is 10 cm. Because the instruments are located on the same horizontal structure the vertical separation of the measurement paths is less than 5cm.The net radiometer, solar radiometer and the PAR sensor are located one metre below the EC instruments (11 m agl) and are facing south to reduce shading effects of the mounting structures on the measurements (Figure 5.2). The temperature and humidity sensor (HMP45C) is located at the north east end of the lattice tower at 12m agl, approximately 80cm from the EC instruments (Figure 5.2). The precipitation gauge (ARG100) is located on a support structure to the west of the lattice tower at 9m agl and the dataloggers, CR3000 and CR1000 are housed at the base of the lattice tower in a Campbell Scientific storage box. Power supply is provided via the school and communication from within the school network to the datalogger is made via the Campbell Scientific NL115 Ethernet Module.

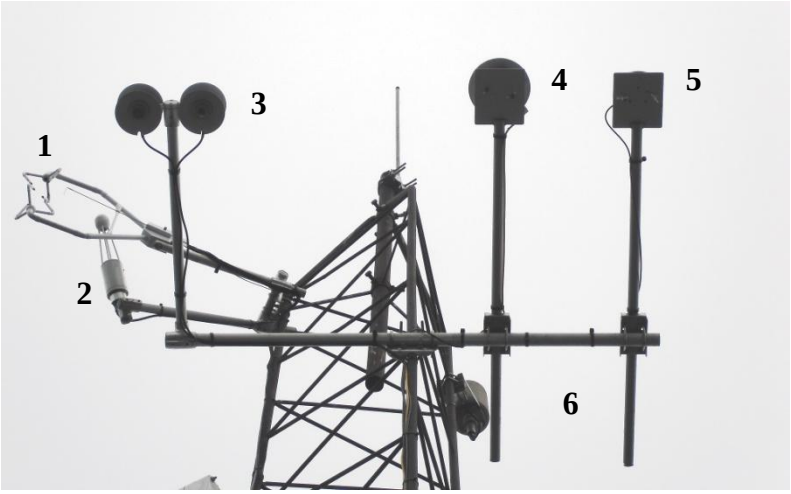

Figure 5.2 Photograph of the suburban EC station equipped with 1) sonic anemometer (CSAT3), 2) gas analyser (Li7500), 3) Net radiometer (NR01), 4) Solar radiation sensor (CMP6), 5) PAR sensor (SKP215) and 6) the temperature and humidity probe (HMP45C).

5.1.1 *Site surrounds and surface cover of the suburban site*

The St Pius X Girls School building is mostly one storey tall apart from a small section that has a second floor; this is where the support tower and instruments are located

(Figure 5.3a). The roof is flat and comprises of dark asphalt with plastic roof windows (Figure 5.3a, b and c). The car park and schoolyard is a combination of concrete and asphalt surfaces. The school building materials comprise of brick with the exception of a relatively new building located to the south west of the EC tower (Figure 5.3d). This building has a pitched, dark tile roof and roughcast or pebbledash walls. A substantial portion of the asphalt schoolyard surface was replaced with astro-turf material between July 2012 and July 2013 (Figure 5.4a, b, c and d). The radiation source area at the suburban site was calculated according to Schmid et al. (1991). When the measurement height (z_m) is 11 m the radius of the 95% source area is approximately 48 m. As outlined in Chapter 3 the source area is invariant with time once the orientation or height of the instrument remains unchanged. In the suburban case the underlying surface changed, and although the new astro surface is artificial, its radiative and thermal properties will affect the local surface albedo. The change in the suburban radiation source area is illustrated in Figure 5.5 and is discussed in the following chapter.

Figure 5.3 Photographs illustrating the dark asphalt roof surface of the school (a, b and c) and the combination of concrete and asphalt surfaces in the school car park (d). The difference in vegetation can also be seen in a and b illustrating a winter and summer time. Photographs a) and b) refer to area north of the tower, c) is west and d) is the area south-west of the tower.

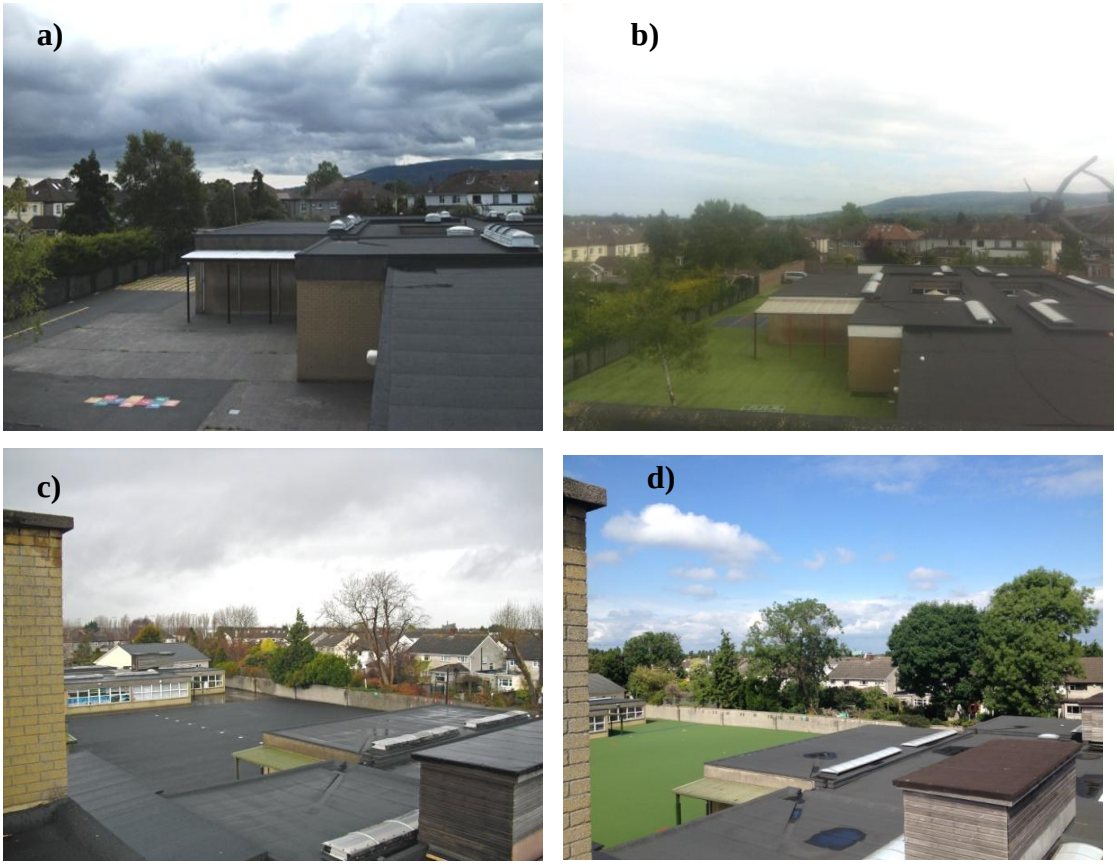

Figure 5.4 Site photographs from the suburban site illustrating in the change in the surface cover of the school yard in the south easterly direction in a) and b), and the north westerly direction in c) and d). The difference in the vegetation between winter and summer months can also be seen from c) and d).

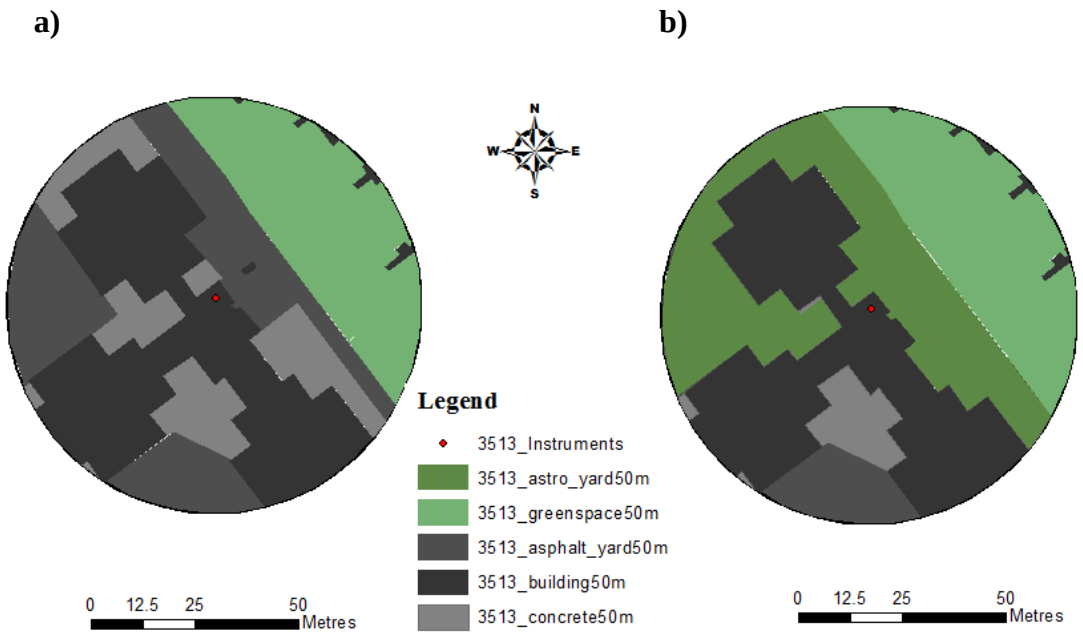

Figure 5.5 Map of the source area of the net radiometer (NR01) according to Schmid et al. (1991) when z_M representing the measurement height of the NR01 is 11 m above the ground and the view factor is 95% for a) the original concrete and asphalt school yard surface and b) the Astro or artificial grass surface.

Beyond the school grounds the land use is almost exclusively residential, comprising of two storey detached and semi-detached dwellings predominantly built between 1942-1960 (CSO, 2011). The houses are on average 8 metres in height with pitched, slate, roofs (Figure 5.6a). Gardens are large, typically 3 times the building footprint consisting of grass, trees and shrubbery. Tree species are typically deciduous (e.g. Hornbeam, Chinese and Japanese Cherry Blossom, Lime, Ash, Rowan and Sycamore) and shed their leaves in the winter months (Figure 5.3a and b, Figure 5.4c and d, and Figure 5.6b). Apart from the houses there are other institutional buildings: sports clubs and secondary schools lie to the east, south east and west of the site and a church is located 300m to the north east of the EC station (this is the tallest building within a 1km radius). Light commercial buildings within a 1 km radius of the site consist of small supermarkets and local shops that are located directly south of the school grounds and are very similar to the surrounding housing stock (Figure 5.6c). Furthermore 800m to the south east of the site is a large supermarket with adjacent car parks. Vehicular traffic in the surrounds of the EC station is moderate during morning and evening commute times and school opening and closing times, otherwise traffic activity is light.

Figure 5.6 Site surrounds illustrating a) typical semi-detached dwellings with large, vegetated back gardens, b) tree-lined streets with grass verges, c) light commercial premises constructed of the same building materials as local residential dwellings and d) a typical traffic junction with light traffic activity.

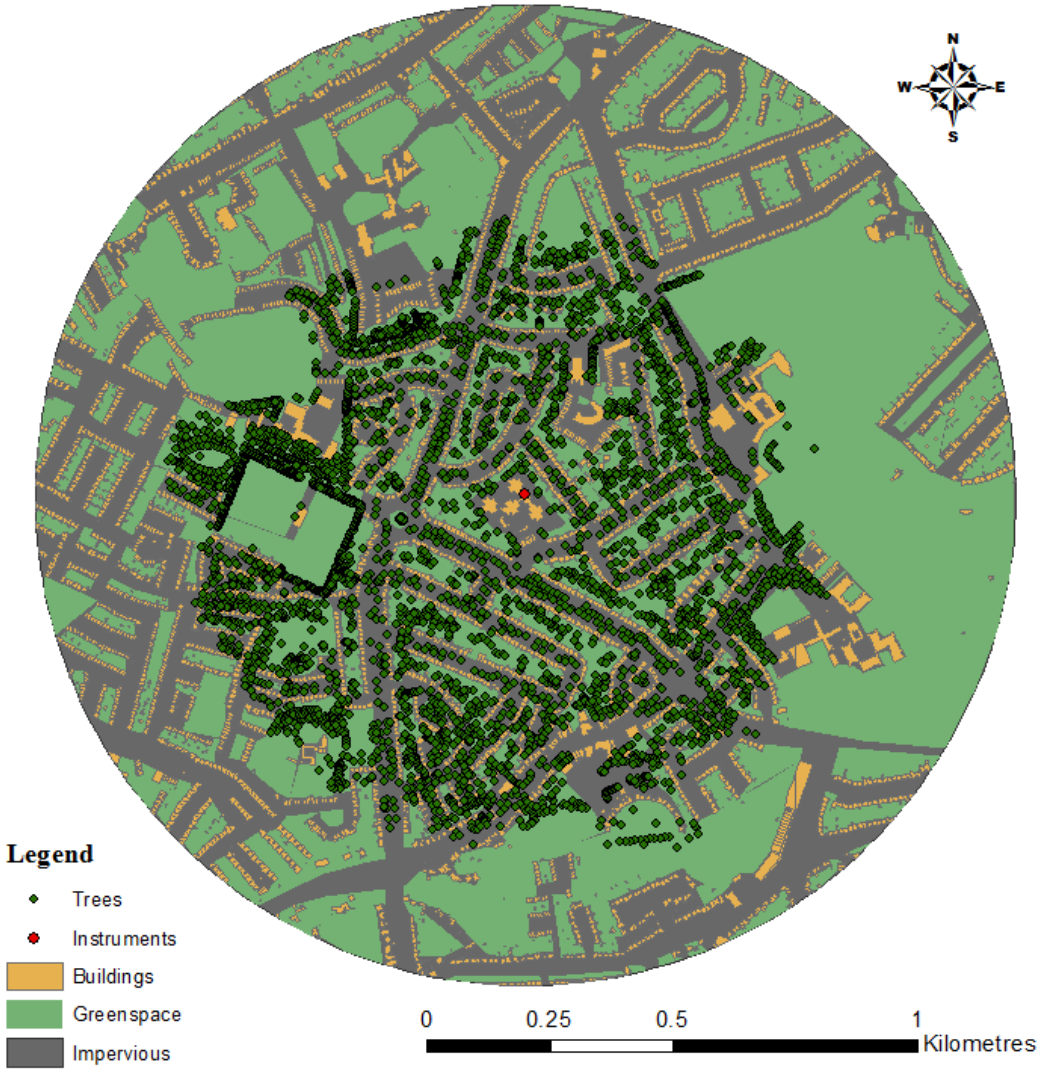

Figure 5.7 GIS map illustrating the land cover for a 1 km radius surrounding the suburban EC station (red circle) and trees (green circles).

The total built surface fraction for a 1km radius of the suburban EC site is 16% with a further 34% comprising of impervious surfaces, however this fraction is likely to be larger than reality because it includes front gardens and grass verges along the roads. The total vegetated fraction of the surrounds is 50% owing to the large gardens, large urban parks and sports grounds in the vicinity of the EC site (Figure 5.7). The proportion of surface cover types differs slightly depending on the direction relative to the EC station (Figure 5.8). The built surface fraction is relatively consistent for all directions, typically between 10-15%; the largest impervious surface cover direction (150-180°) corresponds to the direction of a large supermarket and adjacent car park, and a large road junction to the south east (Figure 5.7 and Figure 5.8).

To the east (600 m) there are extensive playing fields and a large park; this wind sector is the most vegetated (>85%) (Figure 5.8). The vegetated fraction outlined here

corresponds to grassland only, tree data was only available for approximately a 700 metre radius however it does account for the majority of mature, deciduous streets located in private gardens, school grounds and public parks.

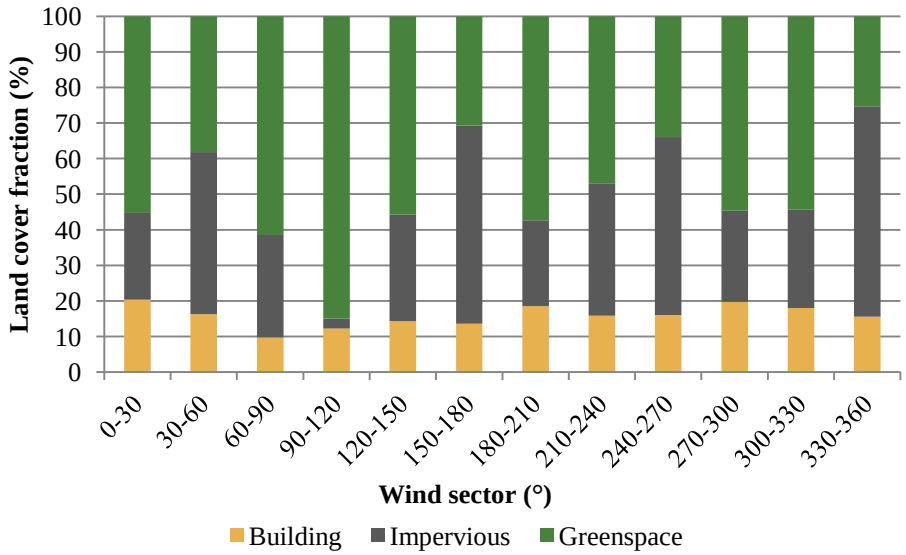

Figure 5.8 Land cover fractions for a 1 km radius of the suburban site for 12 wind sectors

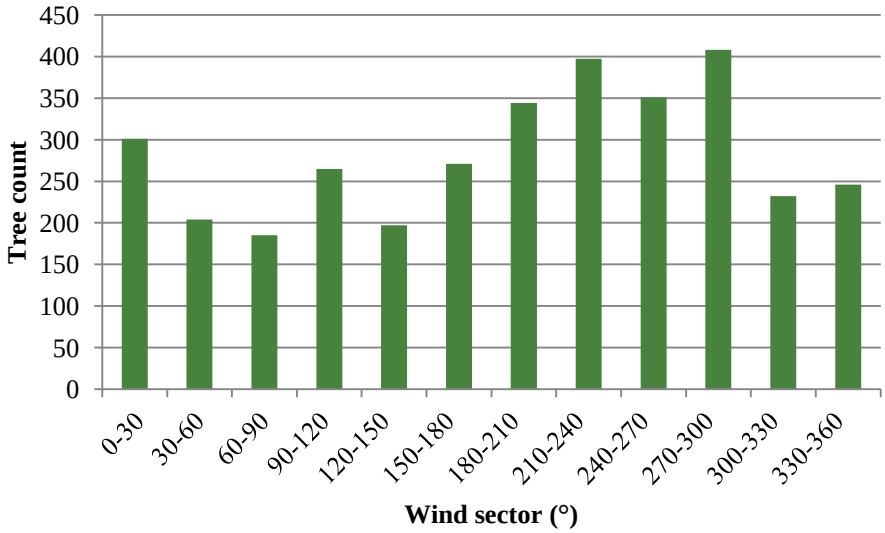

Figure 5.9 Number of street trees per wind sector for a 500 m radius

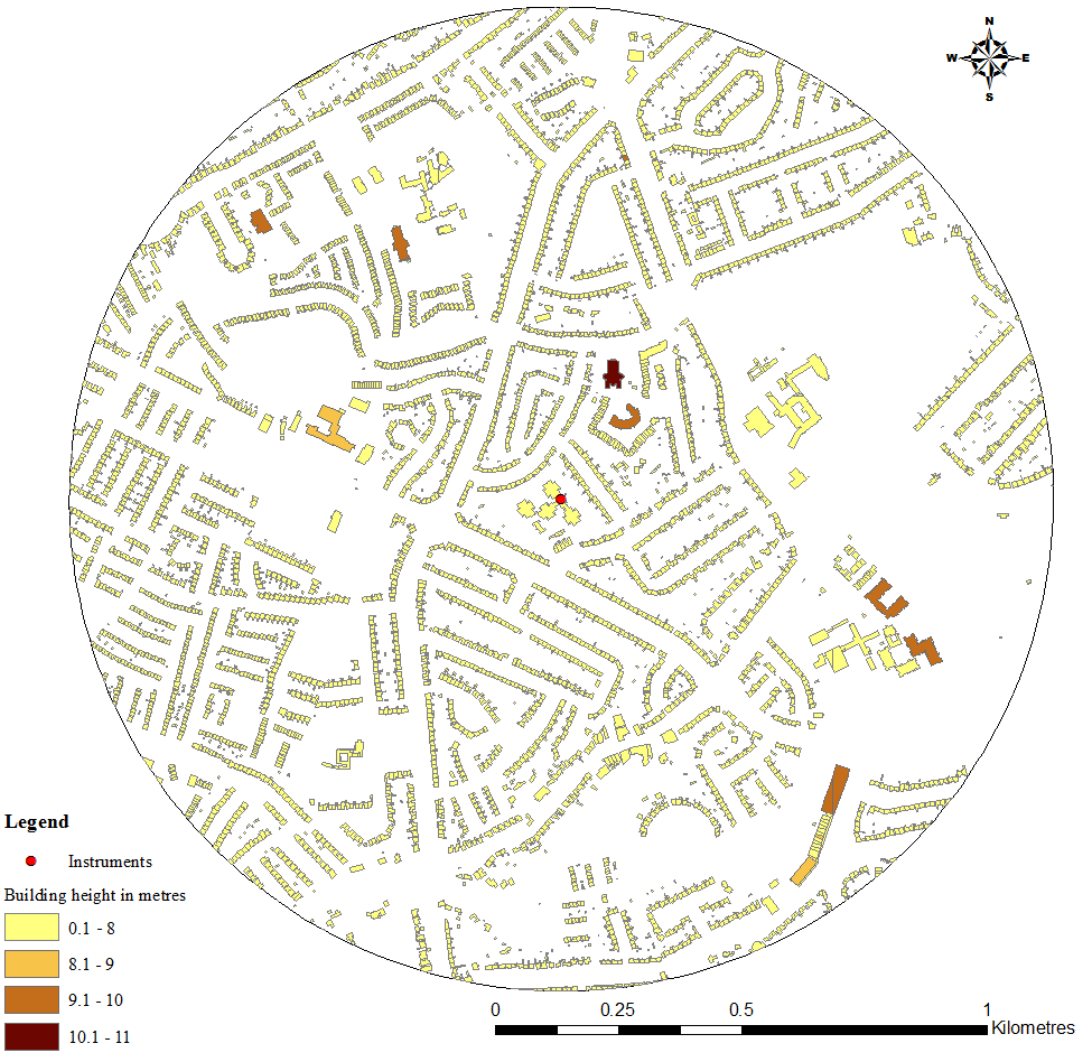

Figure 5.10 The building height in metres for a 1km radius of the suburban site

5.1.2 *Surface roughness properties of the suburban site*

The H/W ratio was previously described as influencing the radiation budget and the airflow regime of a neighbourhood. Small H/W ratios (<0.3) are typically described as having isolated flow regimes, while large H/W ratios (>6.5) may experience skimming flow where the airflow cannot penetrate the street canyon due to the high density of the neighbourhood (see Section 3.1.2). At this site, street widths are typically 25-35 m including the paved road, pavements, grass verges and private gardens in front of houses. The road widths are generally 8-10 m for cul-de-sacs and greater than 10m for larger regional roads. The height to width ratio (H/W) for the suburban location, taking 8 m as the average building height and 30 m as the average street width, is 0.26.

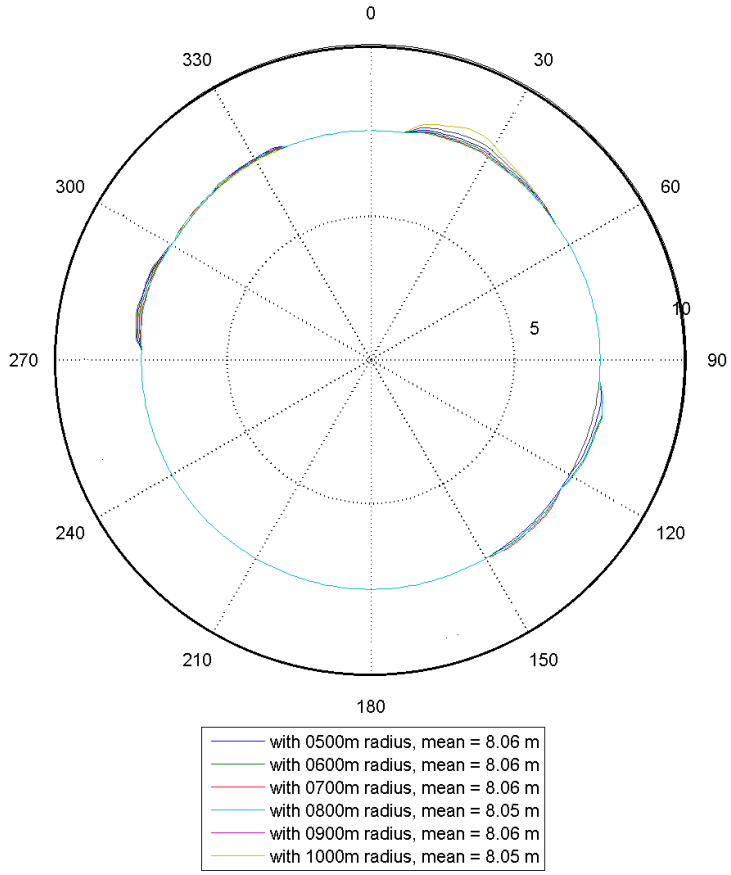

Figure 5.11 Average building heights for the suburban EC station per 1° wind sector for radiuses equal to 500, 600, 700, 800, 900, 1000m. The plot illustrates very little difference in the average building height for 500-1000m radii.

The average building height for 2 storey buildings in the suburban neighbourhood is 8 metres, exceptions to this were identified from aerial imagery and observations made during site visits (Figure 5.10). This step was necessary for the derivation of surface roughness parameters described in Section 4.8 above. Figure 5.11 illustrates the average building height calculated for each 1 degree wind sector for radii of 500, 600, 700, 800, 900 and 1000 m. In general the building height for each wind sector and radius is 8m, exceptions to this correspond to wind sectors containing taller buildings, such as the church (11 m) to the north east and the large supermarket (10 m) to the south east (Figure 5.10).

Figure 5.12 shows maps of the zero plane displacement (z_d), roughness length (z_0), plan area density (λ_p) and frontal area density (λ_f) based on direction around the EC station. The suburban location is as a low density neighbourhood with an average plan area fraction (λ_p) of 0.14 (according to Grimmond and Oke (1999a), λ_p values for such neighbourhoods lie between 0.05-0.4). The flow regime as a result may be described as

isolated flow, especially given that the H/W is less than 0.3. Wake interference flow may occur for the narrow wind sectors where λ_p is about 0.2 (Figure 5.12c). The zero plane displacement height (z_d) is relatively consistent for most wind direction sectors, typically ranging from between 2.4-3 m. There are exceptions where z_d is smaller, between 1-2m; these cases coincide with wind sectors and radiuses containing large greenspace fractions (see Figure 5.7 and Figure 5.10). Greenspace in this regard is treated as grass with a z_d=0 and z_0=0, hence lowering the displacement height in comparison to more densely built wind sectors. Channelling effects will likely occur for these wind directions where airflow, due to the lack of large and tall roughness elements, can penetrate deeper into the UCL. Figure 5.12b shows z_0 values which are consistent with international findings from similar neighbourhood types (Ward et al., 2013; Nordbo et al., 2013); z_0 is largest for wind sectors with large frontal area densities (Figure 5.12b and d). In general z_0 for the suburban site is 0.57m however for wind sectors with the greatest frontal area density and small greenspace fraction (e.g. 150, 240 and 300°), the corresponding value for z_0 reaches 0.75m.

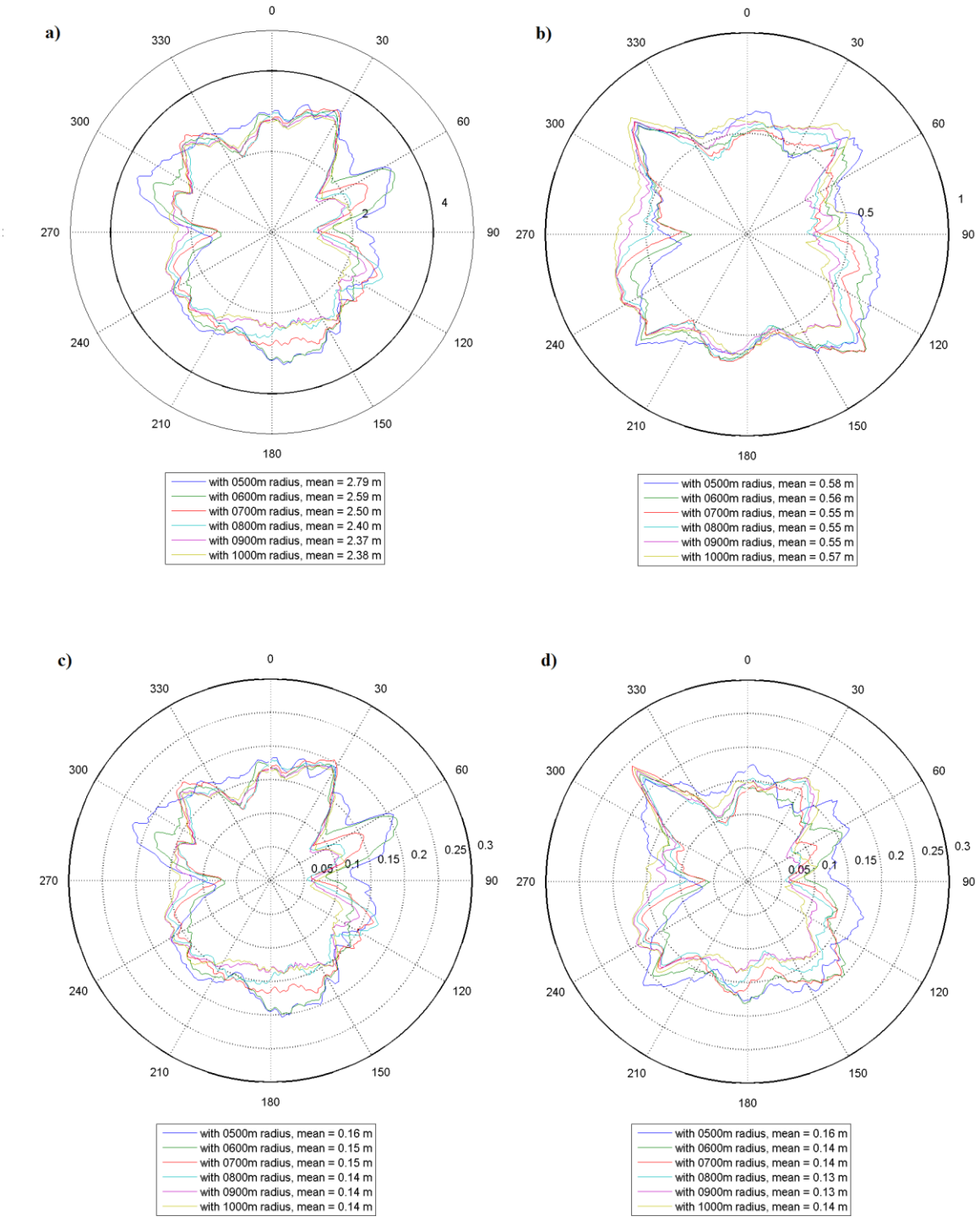

Figure 5.12 a) Zero plane displacement height, b) roughness length, c) plan area density and d) frontal area density for the suburban site per wind direction for a radius of 500, 600, 700, 800, 900, 1000 m.

5.2 Urban Site 1 – Marrowbone Lane

Marrowbone Lane is located approximately 4 km north east of the suburban site and 4 km west of Dublin Bay (Figure 4.1). The EC instruments are located on a mast on the roof of Dublin City Council (DCC) offices located on Marrowbone Lane. The building

is 3 storeys (9 m in height) with an additional storey (11 m) on the north east corner of the building (Figure 5.13a, b and c). The offices were built circa 1960; the roof material is concrete and the walls are constructed of bricks with glazed surfaces (see Figure 5.13). The mast structure is 15 m and the EC instruments are mounted on a horizontal boom at a height of 18 m agl and are orientated at an azimuth of 240° (Figure 5.14). The net radiometer, global radiation sensor (CMP6) and PAR sensor (SKP215) are mounted 1 metre below the EC instruments (17 m agl) so as to reduce flow distortion effects on the sonic anemometer measurements. They are orientated in a southerly direction to minimize shading effects from the tower structure and instruments above. The HMP45C is also located at 17 m agl and is housed in a radiation shield (Figure 5.14).

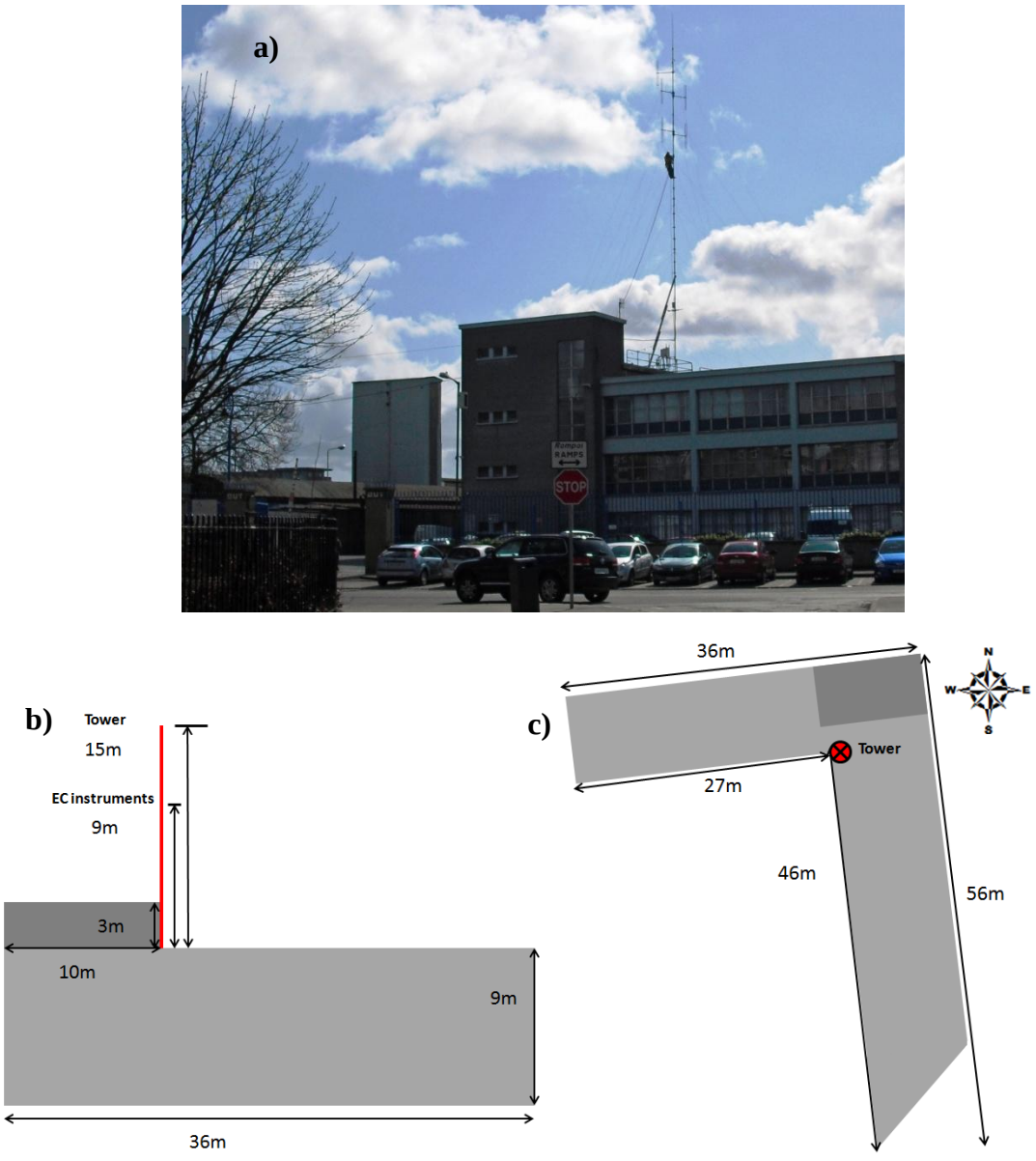

Figure 5.13 a)Photograph illustrating the location of the EC tower at marrowbone Lane b) a cross section view schematic of the building illustrating the building, tower and EC instrument heights and c) a plan view schematic showing the building dimensions in metres and the location of the EC tower.

The precipitation gauge is mounted on a roof structure south of the tower at a height of 10m agl (see Figure 5.15c) and the data loggers are housed at the base of the tower structure. Figure 5.15a-d shows images taken from the rooftop site in different directions. Directly north of the tower is a roof access point (Figure 5.15a) and connection to the building's power supply. Immediately east and west of the tower (Figure 5.15b and c respectively) are storing yards comprising of warehouses and open spaces for DCC vehicles, staff vehicles and for the storage of outdoor street lighting equipment. The roof of the DCC building is flat, made of concrete and is relatively less dark in comparison to the school roof surface (Figure 5.15d).

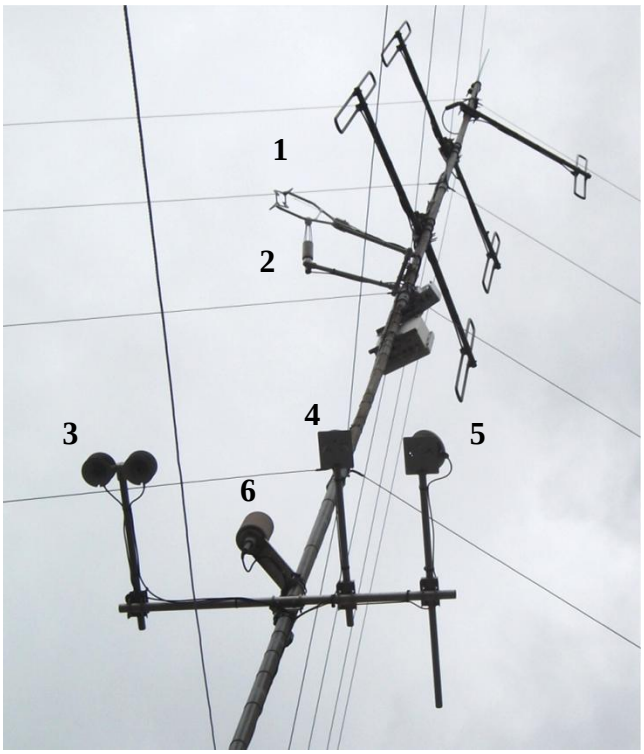

Figure 5.14 Marrowbone Lane tower equipped with a 1) sonic anemometer (CSAT3), 2) gas analyser (Li7500), 3) Net radiometer (NR01), 4) solar radiation sensor (CMP6), 5) PAR sensor (SKP215) and 6) a temperature and humidity probe (HMP45C).

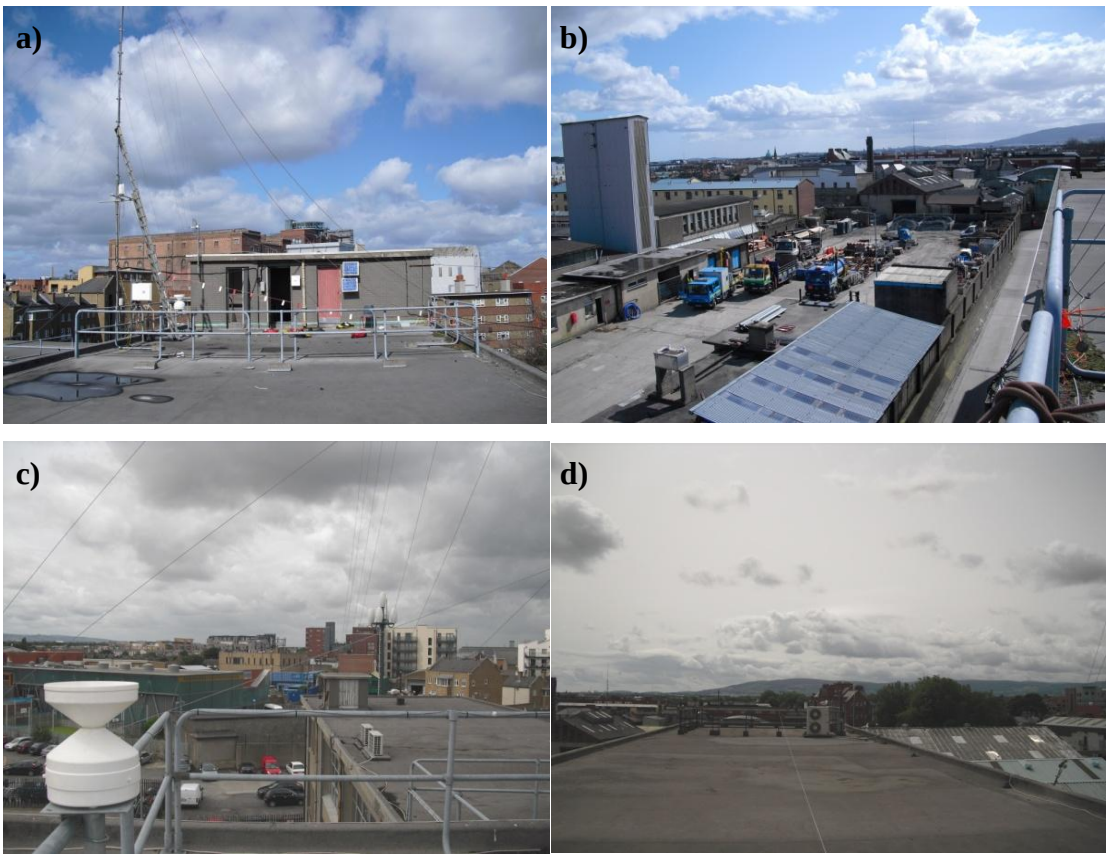

Figure 5.15 Site photos illustrating the surrounds of the EC site, a) EC mast and north facing direction, b) south east direction , c) north west direction, d) south direction with rain gauge location, e) illustrating the building roof material and the south direction, and f) the south west direction including the aluminium roof of an adjacent warehouse.

5.2.1 *Site surrounds and surface properties of urban site 1*

Beyond the immediate surrounds of the DCC building, land use is mixed and is comprised of dense residential, institutional, industrial and light commercial activities. Residential dwellings are largely located to the south west, south and south east of the EC station, while industrial and commercial activities are located to the north and to the north east. To the northwest about 400m distant is a large industrial complex (St James Gate Brewery). The residential dwellings comprise of two types: 3-4 storey apartment buildings, built in two phases, between 1991-2005 and between 1945-1960 (Figure 5.16a) and terraced housing of 1 or 2 storeys (Figure 5.16c and d), most of which was built before 1940 (CSO, 2011).

Figure 5.16 Land use in the surrounds of the EC site comprising of a) 4-5 storey apartment buildings, b) institutional buildings, and c) and d) 1 and 2 storey residential dwellings.

Significant water bodies in the vicinity of the EC station include 1) the River Liffey which is located approximately 800 m north of the site and 2) the Grand Canal located 900m south of the site (Figure 5.17). Land cover fractions representing a 1 km radius of the EC site include 54% impervious surface, 14% vegetation (includes greenspace and canopy cover), 31% built fraction and 1% water (Figure 5.17). With regard to the directional land cover fractions, the built surface fraction varies between 24-40%. For all directions the proportion of impervious surface is the greatest, ranging between 45-70%. Greenspace in the 1 km radius is relatively scarce consisting largely of grassland on the grounds of apartment complexes and institutional buildings (e.g. Figure 5.16a and b). Canopy cover extent is greatest for the wind direction sector between 285-315° accounting for 19% of the land cover. Canopy cover in this direction consists of trees on commercial premises and on the ground of St James' Hospital.

Figure 5.17 1 km radius land cover map for urban site 1 illustrating buildings, impervious surfaces, greenspace, canopy cover and street trees.

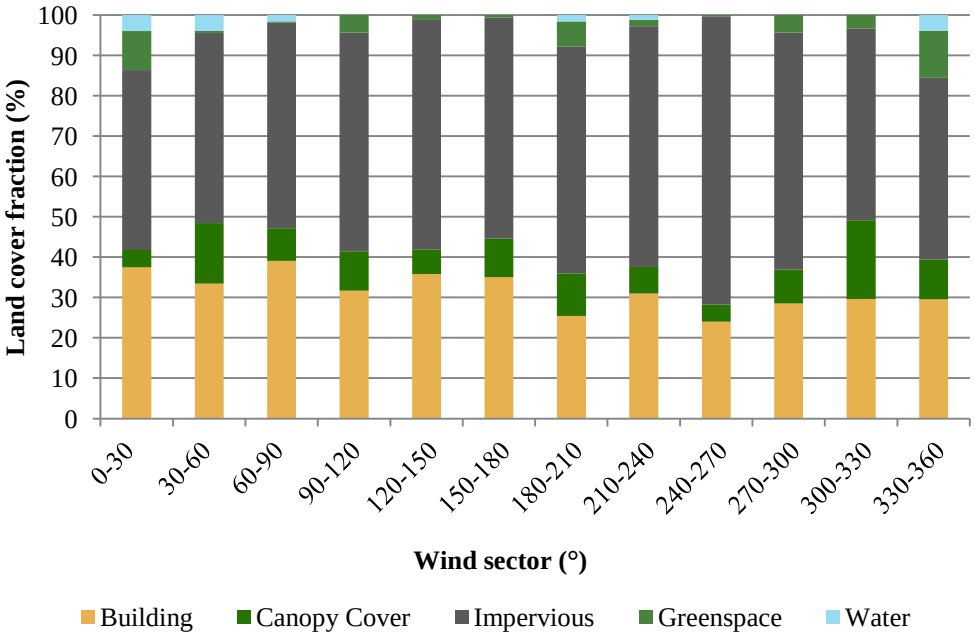

Figure 5.18 Land cover fractions for a 1 km radius of Marrowbone Lane for 12 wind sectors.

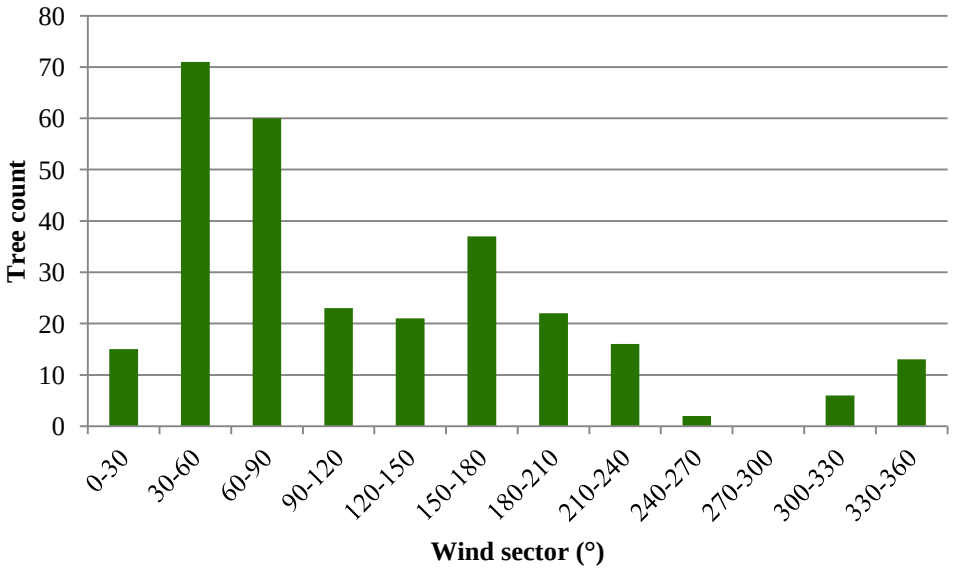

Figure 5.19 Street tree count for a 1 km radius of Marrowbone Lane for 12 wind sectors.

Street trees are relatively sparse in the west direction of the Marrowbone Lane EC station. Interestingly street trees become denser towards the north and east of the EC station approaching the city centre of Dublin (Figure 5.17 and Figure 5.19). The most common tree species include deciduous species such as, Hornbeam, Lime, London Plane and Maple and the average tree height is 8.5 m.

Figure 5.20 The building height in metres for a 1 km radius of the Marrowbone Lane EC station (Please note the scale difference in the legend in comparison to the suburban location and Kevin Street).

5.2.2 *Surface roughness properties of urban site 1*

Street widths are more variable in relation to the suburban location and are determined by three main road categories: residential or tertiary roads (street width of 11 m); regional roads (street width of 20 m) and national roads (street width of 30 m). The weighted average street width in the 1 km radius around the EC site is 16.6 m. The average building height for the 1km radius is 7.97 m but there is considerable variation; to the west, south and south east where land use is predominantly residential, the building heights are typically lower in comparison to more densely built areas to the north and north east as you approach the city centre of Dublin (Figure 5.20). The large

footprint of buildings in the northwest direction results in fewer buildings in the calculation of the average height in comparison to the north east where buildings are smaller in extent but greater in number, ranging in height from 4.57-33.83 m. As a consequence the average building height for the wind directions are relatively consistent for all wind directions (Figure 5.21). The average H/W ratio for the site is 0.48 and is consistent with medium density neighbourhoods. Average z_d is 3.57 m but there is great variation depending on the wind sector, ranging from less than 2 m to greater than 6m (Figure 5.22a). Large values generally correspond to those sectors where λ_p is also large, such as the north-west direction (Figure 5.22c), while small z_d values correspond to sectors with large open spaces, or large open streets (e.g. 210 and 240°) (Figure 5.20 and Figure 5.22a).

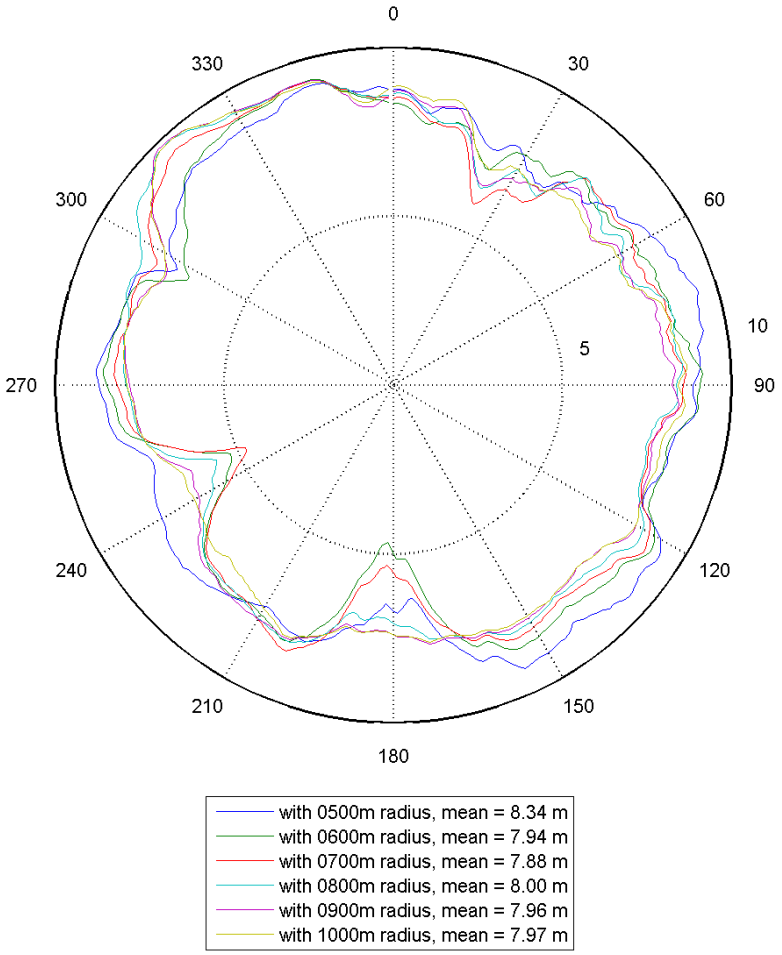

Figure 5.21 Average building heights in metres for Marrowbone Lane EC station per 1° wind sector for radiuses equal to 500, 600, 700, 800, 900, 1000 m.

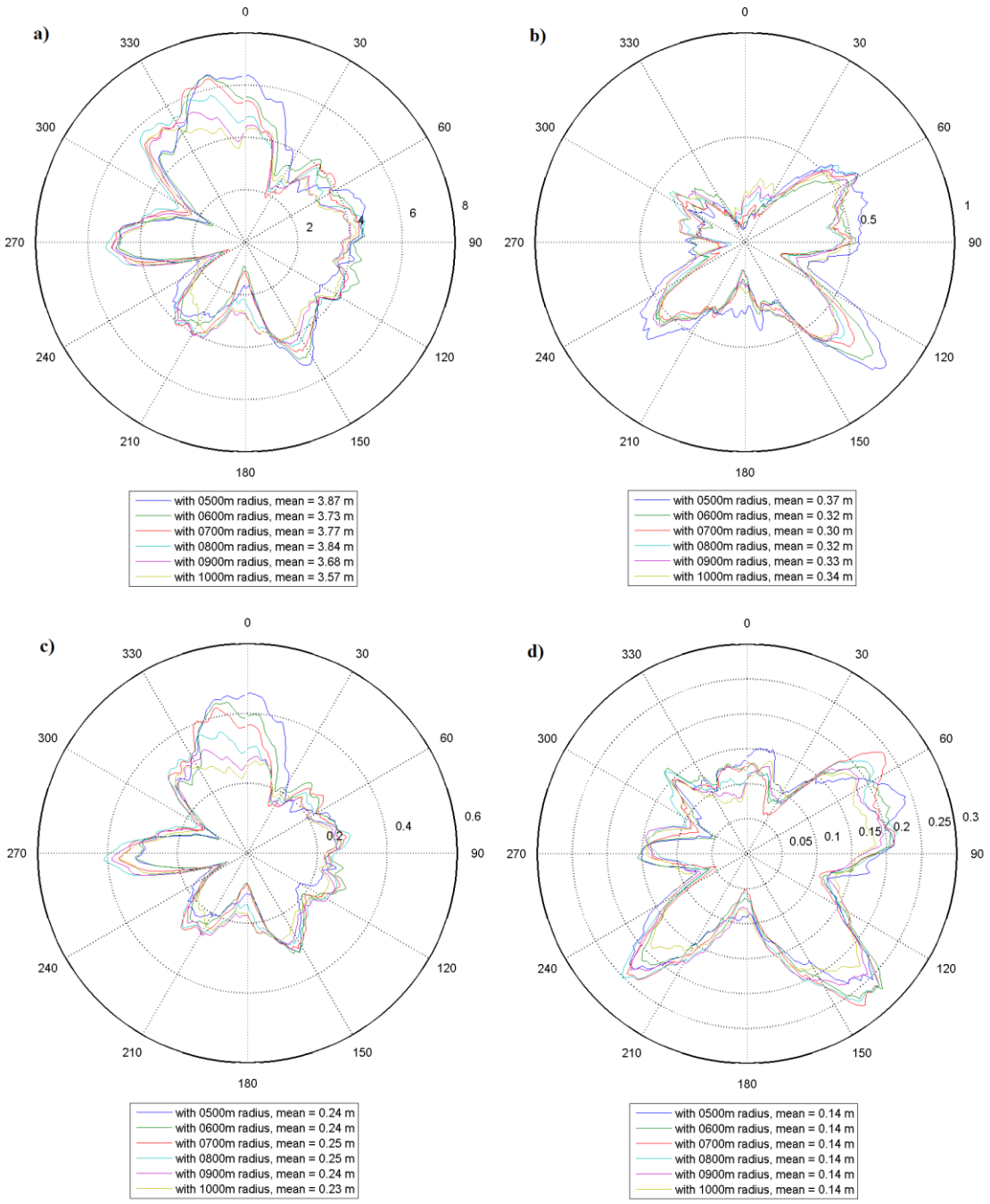

Figure 5.22 a) Zero plane displacement height in metres, b) roughness length in metres, c) plan area fraction and d) frontal area fraction for Marrowbone Lane per 1° wind direction for a radius of 500, 600, 700, 800, 900, and 1000 m.

Consistent with the literature, z_0 approaches zero at large displacement heights (e.g. z_d >4) where the log wind profile predicts that mean flow is close to zero. For small z_d values (< 4 m) z_0 displays values between 0.1 and 0.5 m. Wind sectors with large λ_p values, such as the densely built city centre to the east and residential sectors to south east and south west, correspond to the largest values calculated for z_0 (e.g. 0.5-0.8 m).

With the exception of sectors with large plan area fractions, the flow regime is most likely to be wake interference flow (e.g. wind sectors from 30-315°).

5.3 Urban Site 2 – Kevin Street

Urban site 2 is located 2 km east of Marrowbone Lane in Dublin City on the roof of the Dublin Institute of Technology (DIT), Kevin Street Campus (Figure 5.24a). The DIT building was built in 1968 and is built of pre-cast concrete with walls that are tiled.

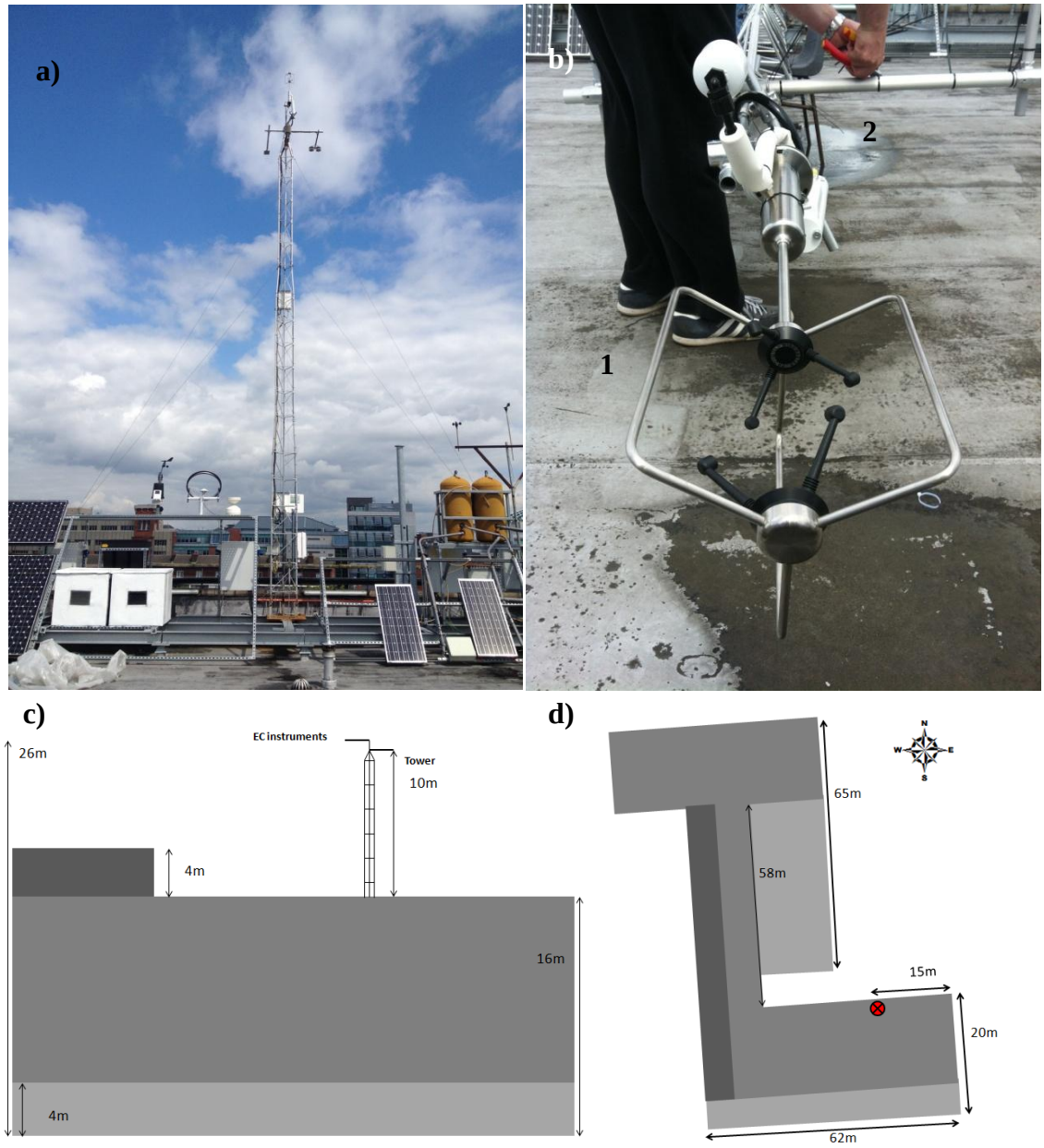

Figure 5.24 Photograph illustrating the location of the EC tower on the roof of Dublin Institute of Technology, Kevin Street, b) a photograph of the sonic anemometer (Gill WindMasterPro)(1) and enclosed path gas analyser (Li7200) (2) deployed on top of a 10 metre lattice tower, c) a cross section view illustrating the building, tower and EC instrument heights, d) a plan view schematic of the building showing its dimensions in metres and the location of the EC tower.

It has a raised ground floor (4 m above ground level), 4 storeys (each approximately 3 m in height) and a 6th floor (3 m in height) along the west side of the building (Figure 5.24c and d). The station began operating in July 2012 and the instruments are mounted to a 10 m lattice tower on the roof (Figure 5.24a, b and c). The sonic is deployed at the top of the tower and the gas analyser is secured to the base of the sonic structure (Figure 5.24b). The height of sonic and gas analyser is 27.3 and 26.9 m agl respectively. The height of the EC instruments in this regard refers to the centre point of the measurement path of the sonic, and the height of the inlet tubing of the enclosed-path gas analyser. The net radiation sensor and PAR sensor are mounted on a horizontal boom at a height of 26m agl and are orientated in a northerly direction (0°) to reduce the effects of reflections from underlying photovoltaic (PV) panels that are also located on the roof (Figure 5.23b).

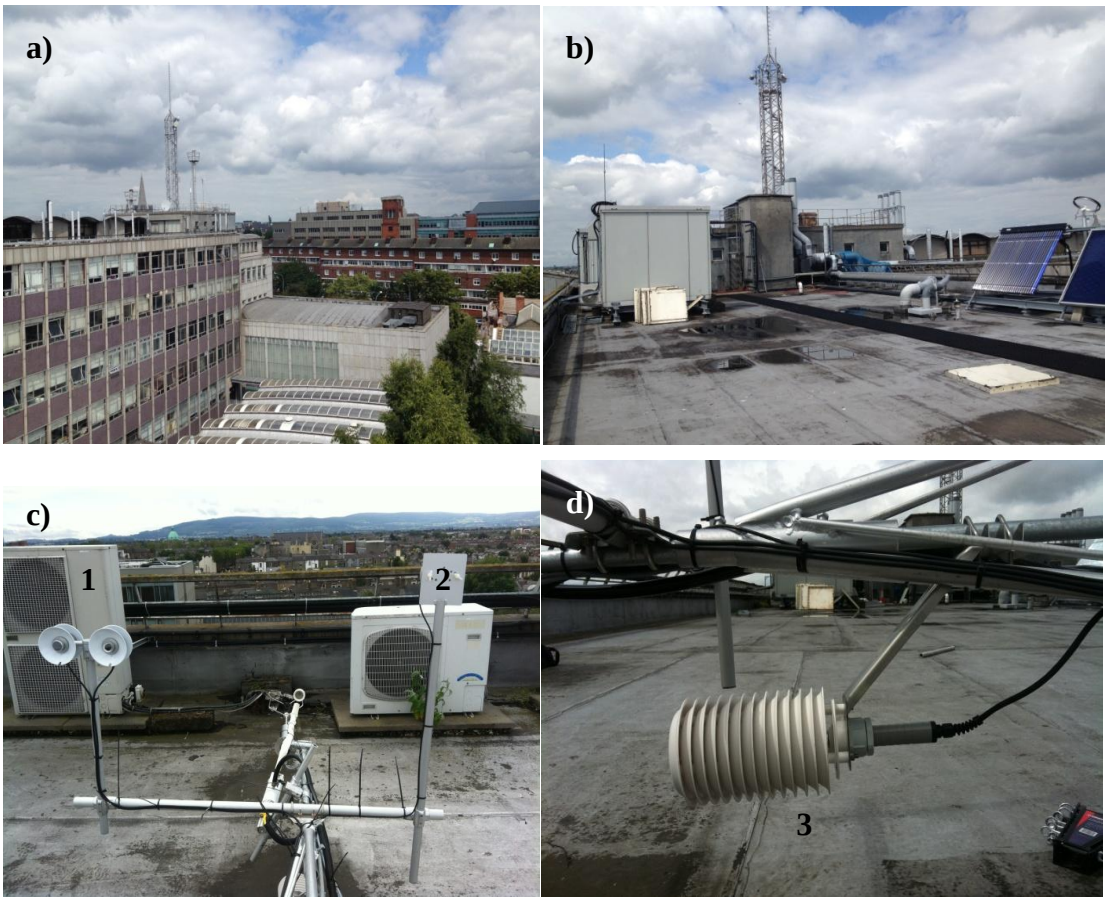

Figure 5.23 a) Photograph illustrating a) the DIT building and immediate surrounds to the north of the EC station b) the roof of Kevin Street DIT illustrating photovoltaic (PV) panels, c) 1) the net radiation sensor (NR01), 2) the mounting plate for the skyward facing PAR sensor, and d) the relative humidity and air temperature probe (HMP45C) mounted to the south point of the lattice tower.

The temperature and relative humidity probe (HMP45C) is mounted at the southern point of the lattice tower at 25.5 m agl and is housed in a radiation shield (Figure 5.23d).

The roof is flat and is covered with a waterproof membrane, with the exception of the west side of the building which has an additional storey (Figure 5.23a, b, c and d).

5.3.1 *Site surrounds and surface properties of urban site 2*

Within a 1 km radius of the EC site land use is a mix of residential dwellings, institutional buildings, commercial buildings and public parks (Figure 5.24a, b, c and d). Residential dwellings are largely confined to the sector extending from the south to the west and comprise of one, two and three storey terraced housing and three and four storey apartment complexes (Figure 5.24). Institutional and commercial buildings are located to the north and east in the direction of the city centre. Water bodies in the vicinity of Kevin Street include the River Liffey which is located approximately 900 m to the north and the Grand Canal located 800m to the south (Figure 5.25).

Figure 5.24 Land use in the surrounds of the Kevin Street DIT campus comprising of a) terrace housing, b) apartment complexes, c) institutional buildings, and d) public parks.

Figure 5.25 Map of a 1 km radius of urban site 2 located on the roof of Kevin Street DIT, illustrating land cover including building footprints, impervious surfaces (including roads, pavements, car parks and courtyards), water bodies, greenspace, canopy cover and street trees.

Land cover fractions representing a 1km radius of the EC station consist of 43% impervious surface, 17% vegetation (includes greenspace and canopy cover), 38% built fraction and 2% water (Figure 5.25 and Figure 5.26). With regard to the directional land cover fractions, the built surface fraction varies between 30-60%, with greatest fractions corresponding to the city centre direction (from 330-90°) (Figure 5.26) The proportion of impervious surface is the greatest in the west direction with fractions exceeding 60% (210-330°). This is consistent with findings for Marrowbone Lane which lies 2km to the west of Kevin Street. Approaching the city centre to the north east and east there is a greater proportion of greenspace consisting of 2 significant urban parks (St Stephen's Green and The Iveagh Gardens), where canopy cover accounts for

greater than 35% of the total land cover for their corresponding wind sectors. It is likely that the proportion of greenspace for the site is underestimated given that the majority of back gardens pertaining to residential dwellings are treated as impervious. The number of street trees is greatest along the South Circular Road and the Grand Canal, both located 500 and 750 m to the south (Figure 5.25 and Figure 5.27). There are few recorded street trees in the wind sectors corresponding to the urban parks, where trees within the public parks have not been included in the street tree inventory.

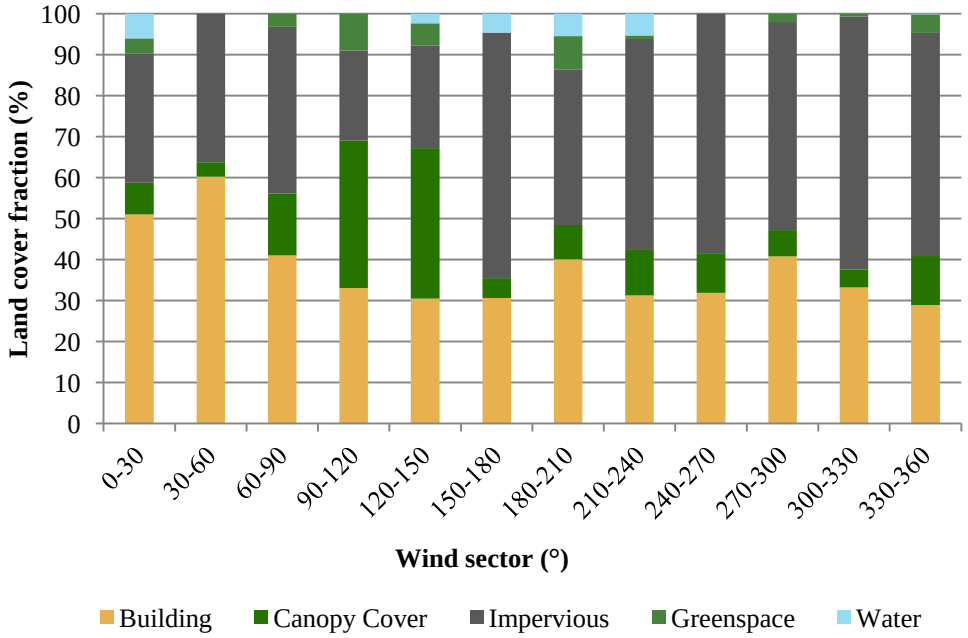

Figure 5.26 Land cover fractions for a 1 km radius of Kevin Street for 12 wind sectors.

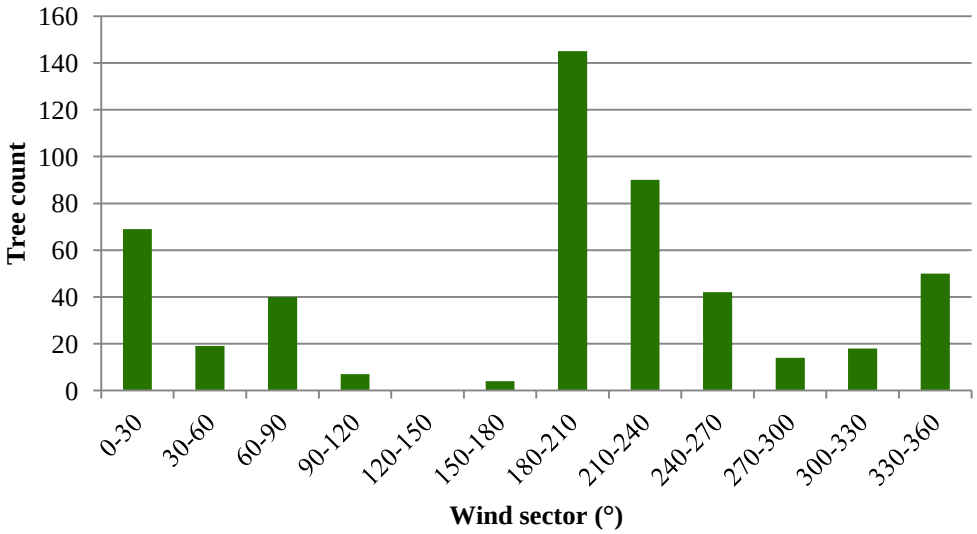

Figure 5.27 Street tree count for a 1 km radius of Kevin Street for 12 wind sectors.

5.3.2 *Surface roughness properties of urban site 2*

The distribution of building heights around the site has a clear pattern. For wind sectors 151-330° z_H is on average 6.75 m and are largely representative of residential dwellings. For the other directions (331-150°) where buildings are largely institutional and commercial, the average z_H is 11.85 m (see Figure 5.28 and Figure 5.29). For the entire 1 km radius the average z_H is 9.32 m. This will affect both z_d and z_0 and the flow regime will vary with wind direction.

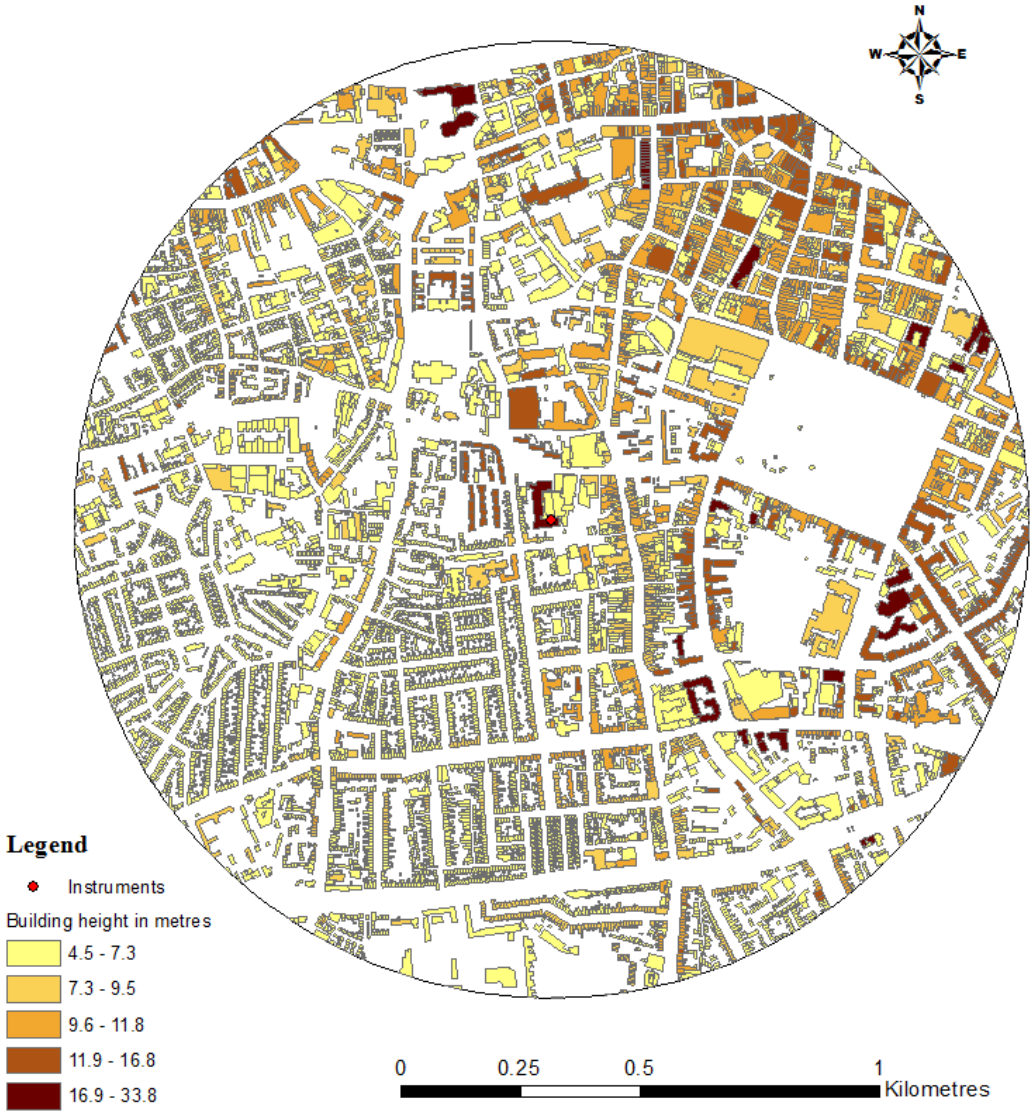

Figure 5.28 The building height in metres for a 1 km radius of the Kevin Street EC station (Please note the scale difference in the legend in comparison to the suburban location and Marrowbone Lane).

In terms of street widths, similar to Marrowbone Lane, three main road types with road widths are present in the 1 km radius: a weighted-average street width of 14.7 m was calculated for the 1 km radius. The average H/W ratio is 0.63 and is characteristic of

medium density according (Grimmond and Oke, 1999b). As previously mentioned the difference in the height and dimensions of buildings will affect the flow regime. For those areas with large plan area fractions to the north, east and south east, z_d values are on average greater than 7m. For wind sectors corresponding to the residential dwellings, z_d values are lower, on average 3.25 m and closer to the values obtained for the suburban EC station (Figure 5.30). At large z_d values, z_0 approaches zero indicating a skimming flow regime. At this site, skimming flow is most likely to occur between wind sectors 340-60° (Figure 5.30b) while airflow from other directions will contain the wake interference effects of nearby buildings. As illustrated in Figure 5.30 the frontal area fraction is relatively reduced (λ_p=0.1 m) in the wind sectors corresponding to the two urban parks, e.g. 70 and 110°.

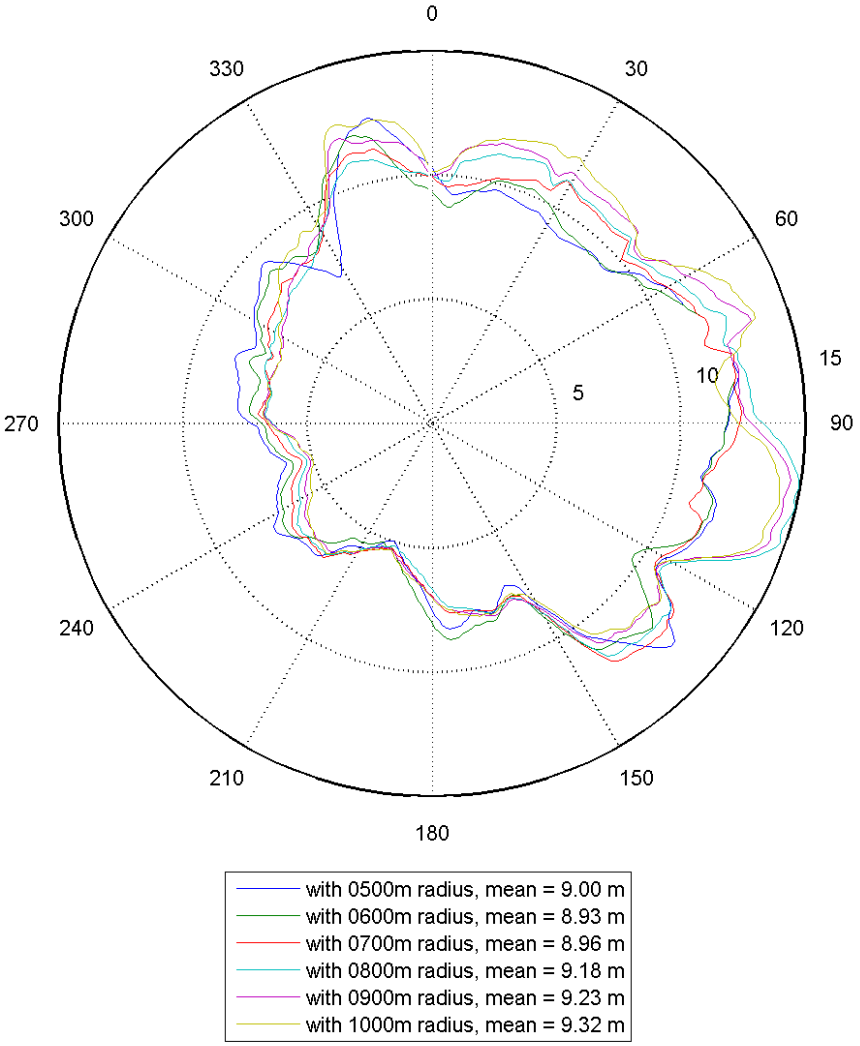

Figure 5.29 Average building heights in metres for Kevin Street EC station per 1° wind sector for radiuses equal to 500, 600, 700, 800, 900, 1000 m.

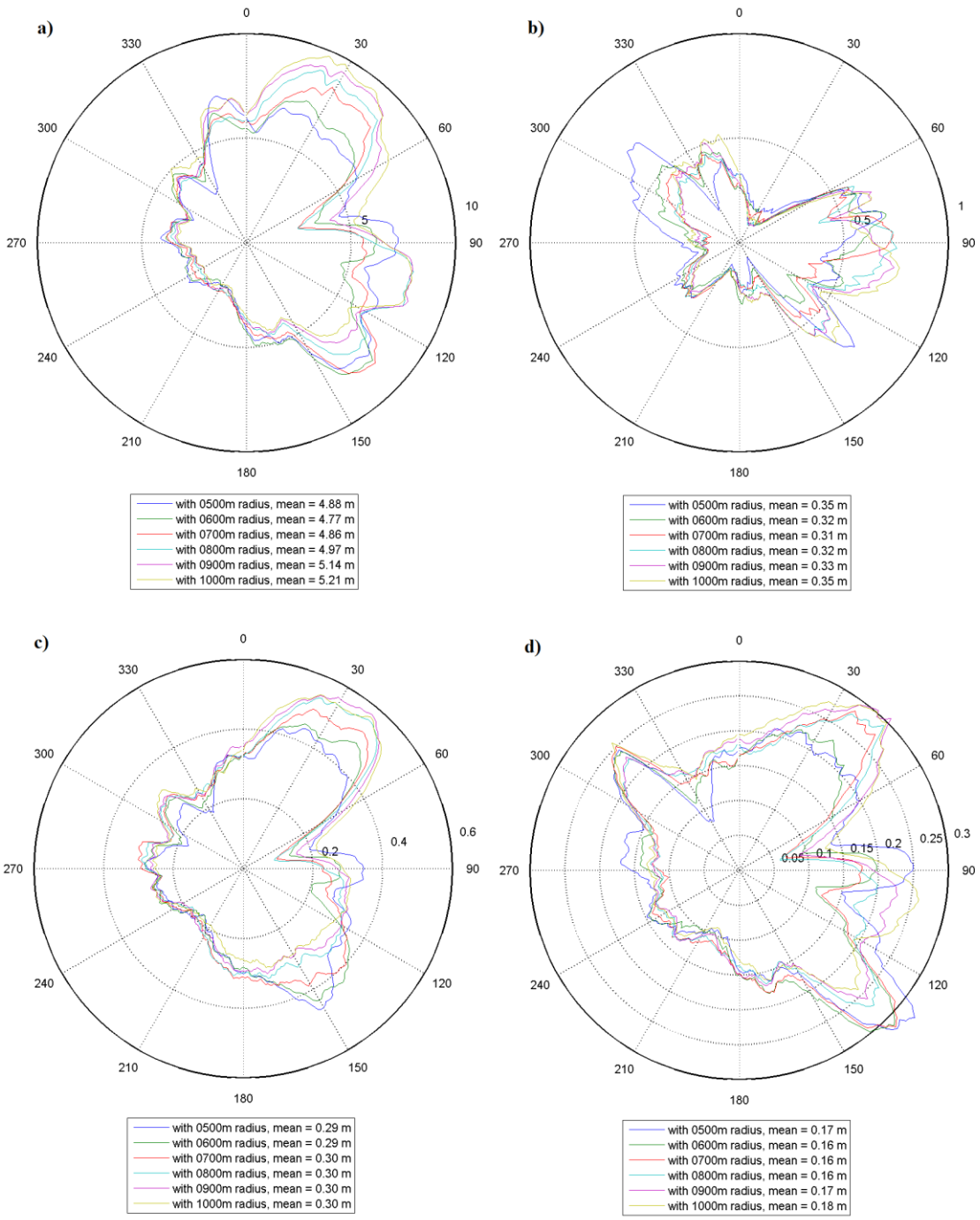

Figure 5.30 a) Zero plane displacement height in metres, b) roughness length in metres, c) plan area fraction and d) frontal area fraction for Kevin Street per 1° wind direction for a radius of 500, 600, 700, 800, 900, and 1000 m.

5.4 Discussion of the site characteristics

This chapter provided a detailed description of each of the EC stations located in Dublin. The 3 EC sites are characterised by different urban forms (e.g. geometries and land cover) and functions (e.g. residential, institutional and commercial). Table 5.1

summarises key properties and the local climate zone (LCZ) (Stewart and Oke, 2012) classification pertaining to each EC station in Dublin.

The suburban site is typical of several Dublin suburbs, which have large vegetated fractions (50%) consisting of parklands and playing fields and residential dwellings are typically 2 storey semi-detached houses with large gardens containing trees and shrubbery. Commercial activity typically consists of supermarkets and local shops. Traffic activity is greatest at commuter and school times and decreases in the middle of the day and throughout the night. The population density for the area around the suburban EC site is lower per square kilometre compared to the neighbourhoods in the city centre (Table 5.1).

Table 5.1 Site characteristics for each EC site in Dublin

Station	**Suburban site**	**Urban site1**	**Urban site 2**
Station location	**Templeogue**	**Marrowbone Lane**	**Kevin street**
Latitude(°) **Longitude (°)**	53°18'10"N 6°18'17"W	53°20'22"N 6°17'06"W	53°20'10"N 6°16'03"W
Land use	Residential/Sports Grounds/Urban park	Residential/Institutional/Commercial	Residential/Institutional / Commercial/Urban park
Period of operation	April 2010 - present	April 2010 – July 2012	July 2012 - present
Population density	1189 inh km^{-2}	4525 inh km^{-2}	4525 inh km^{-2}
LCZ	Open low rise LCZ 6	Open midrise LCZ 5	Compact midrise LCZ2 Open midrise LCZ 5
H/W	0.26	0.48	0.63
z_H	8.05	7.97	9.32
z_{Tree}	7	8.5	8
z_m	12	18	27
z_d	2.38	3.7	5.21
z_0	0.57	0.34	0.35
λ_p	0.14	0.24	0.30
λ_f	0.14	0.14	0.18
Surface cover fractions (%)			
λ_i **impervious**	34	54	43
λ_v **vegetation**	50	14	17
λ_b **building**	16	31	38
λ_w **water**	0	1	2

Traffic activity, although moderate in the vicinity of the suburban site, is relatively high for the urban EC stations, particularly at urban site 2 where large road intersections are located nearby. The 2 EC sites located in Dublin City represent more densely built neighbourhoods with higher impervious and built surface fractions. Urban site 2 has a larger greenspace fraction owing to the presence of large urban parks in the 1 km radius (Figure 5.31). Urban site 1 on the other hand is characterised by impervious spaces consisting of storing yards, car parks, courtyards and larger street widths. As a result the H/W ratio is smaller in comparison to that calculated for the surrounds of urban site 2 (0.48 versus 0.63). Analysis of the building height and footprint data for urban site 2 revealed wind sectors where the airflow and turbulent fluxes will likely possess different properties. The displacement height (z_d) in the direction of the city centre is increased relative to that pertaining to the residential surrounds of urban site 2. The measurement height of 27 m at urban site 2 is theoretically within the ISL for wind approaching from the residential sector (>2.5 z_H), however in relation to the city centre direction where building heights are greater, vertical fluxes measured at the EC site may be representative of the more complex RSL.

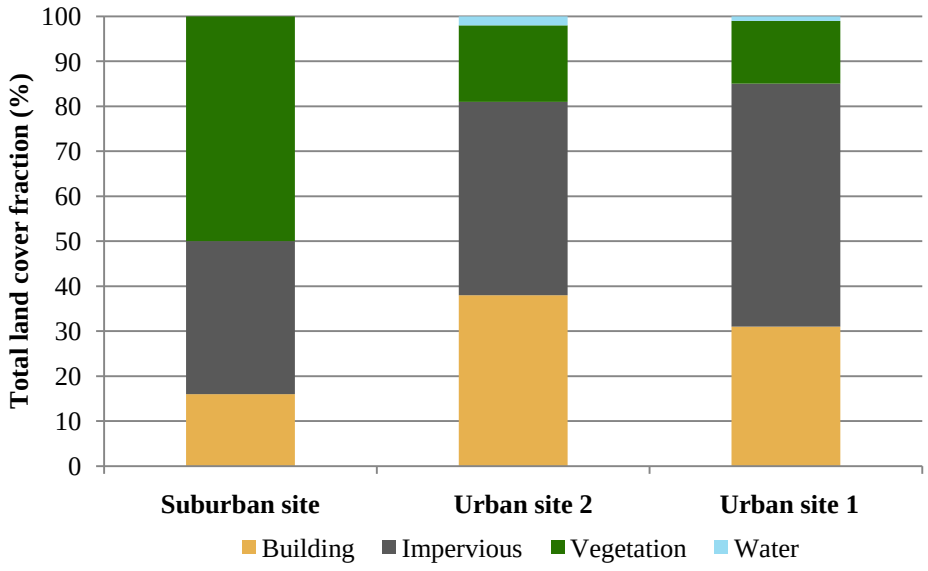

Figure 5.31 Land cover fractions for each Dublin EC Station

Differing neighbourhood surface properties, such as land cover fractions, presented for each EC station will firstly influence the radiative fluxes measured at the site. Knowledge of the surface albedo, yielded from measured observations, will determine the amount of solar radiation that is reflected. Typically vegetated surfaces, such as the suburban site, will have a higher albedo in relation to neighbourhoods, such as urban

site 1, which has a higher proportion of impervious, dark surfaces (Oke, 1987). Reflection of solar radiation (K↑) at the suburban site will likely be greater in comparison to the two urban locations. The H/W ratio will also influence the receipt of solar radiation and the emission of terrestrial radiation. Higher H/W ratios will cause multiple reflections to occur within the urban canyon leading to higher fluxes of L↑, which in turns encourages the development of the UHI effect. Secondly the neighbourhood surface properties will influences the timing, magnitude and partitioning of the turbulent heat fluxes, where, for example, the presence of water at the surface will influence the magnitude of the latent heat flux. Furthermore the presence of greenspace, particularly deciduous trees within a neighbourhood will influence the uptake and release of CO_2, serving to influence the diurnal and seasonal CO_2 flux.

Previous work undertaken by Alexander and Mills (2014) involved a city-wide classification of Dublin according to the LCZ classification scheme. This was achieved using Land Use and Land Cover (LULC) data in unison with extensive fieldwork. This work allows for the 3 EC sites to be contextualised in terms of the Greater Dublin Area (GDA), allowing for their representativeness to be ascertained. The city-wide LCZ map, shown in Figure 5.32 clearly illustrates an extensive fraction of the GDA is classified as Open Lowrise, similar to the suburban EC site. This LCZ is typically representative of two-three- storey residential dwellings with large vegetated surface fractions comprising of residential gardens, parks and playing fields (Stewart and Oke, 2012). The prevalence of Open Lowrise LCZs is important in that observations from EC campaigns such as this can be tentatively applied to greater portions of the city than the instrumented site, this is particularly important given the financial and logistical resources required to operate an EC site.

The LCZs associated with urban site 1 and urban site 2, Open Midrise and Compact Midrise respectively represent relatively smaller fractions of the GDA (Figure 5.32) nevertheless their urban form and function are likely to cause the greatest modification the local climate in the Dublin context. Furthermore it is in these LCZs that an increased understanding of the surface radiation, energy and carbon budgets are required (Arnfield, 2003; Grimmond, 2006).

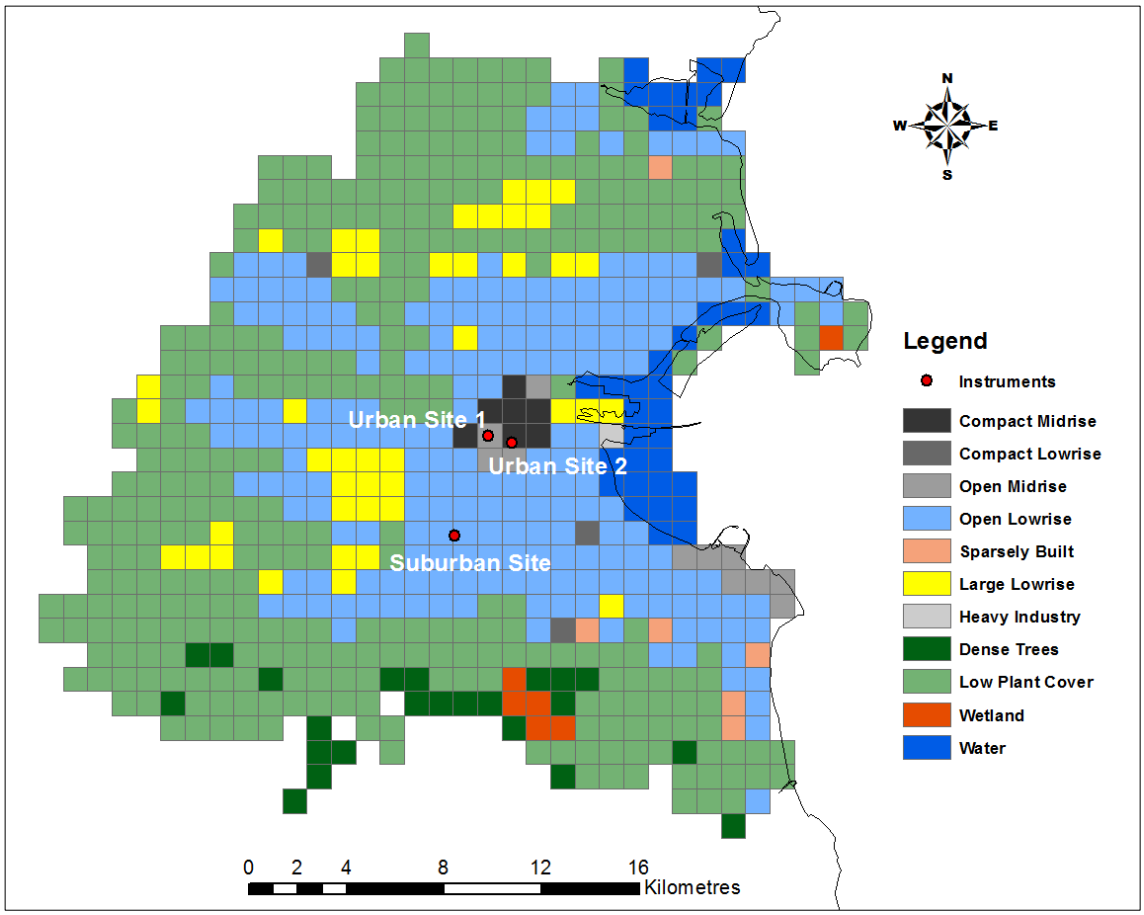

Figure 5.32 A Local Climate Zone Map for the Greater Dublin Area derived from LULC and fieldwork (Alexander and Mills, 2014), modified to include the 3 EC sites in Dublin. See legend for LCZs.

In summary this chapter has presented the three EC sites located in Dublin, each of which represents a distinctive urban neighbourhood and a unique LCZ. The geography of each of the EC site surrounds' has been illustrated using photography, land cover and building height maps. The surface roughness parameters have been calculated using morphometric methods according to Macdonald et al. (1998). This analysis has allowed the flow regime to be characterised for each EC station. This site specific information provides explanatory power when attempting to analyse the measured radiative and turbulent fluxes, particularly for differing wind directions.

Chapter 6 Results

This chapter will outline the results of an EC observation campaign in Dublin from April 2010 to December 2012. As outlined in Chapter 4 a series of post processing techniques must be performed before collating and analysing flux datasets. This chapter will provide information on 1) periods of data loss, 2) data available for processing and 3) data remaining following post-processing steps. Radiative and turbulent fluxes measured at the three EC sites will be presented and examined in conjunction with radiation source areas, flux footprint information and meteorological variables such as wind direction, atmospheric stability and rainfall. A comparison between urban and suburban sites in terms of the fluxes of radiation, energy and CO_2 is undertaken, where comparative time periods existed for both sites.

6.1 Raw data availability for processing

Data gaps throughout this investigation occur in the datasets for 2 main reasons, 1) insufficient memory card space, and 2) site inaccessibility. Largest data gaps for the suburban and urban site 1 occurred in November 2010 due to heavy snowfalls where access to the measurement sites was not possible. In this situation the data logger is programmed to overwrite data occurring first in the dataset and to append new data to the end of the dataset. As a result 26 days of data from the beginning of November 2010, before heavy snowfall, was deleted due to the lack of disk space. Other significant data losses are presented in Table 6.1

Table 6.1 EC site period of operation and data availability for processing

Site	Period of operation	Data loss period	Reason for data loss	Number of days missing	Number of days of complete data
Suburban site	8 April 2010-present	July 2010 November 2010	Lack of disk space Site inaccessible	7 26	1091
Urban site 1	9 April 2010-10 July 2012	July 2010 November 2010	Lack of disk space Site inaccessible	7 26	792
Urban site 2	17 July 2012-present	July-October 2012	Net radiometer not in operation	49	89

The longest record for the 33 month observation period is available from the suburban site and is considered as the reference EC site for Dublin. Detailed explanation of the radiative and energy fluxes will be provided in relation to the suburban site and any deviation from these results will be discussed in relation to urban site 1 and urban site 2.

6.2 Meteorological conditions for the three year observation period

As illustrated in Figure 4.1 the EC sites are located in relatively close proximity to one another (2-4 km), as a consequence synoptic conditions are broadly considered to be similar. The observation period began in 2010 with a relatively dry April where total monthly rainfall was 22.7 mm or 46% of the long term average (LTA) (e.g. 1961-1990 average for Met Éireann's nearby Merion Square station, see Figure 6.1). A high pressure system persisted throughout mid-April which gave rise to clear-sky conditions, temperatures as a result fell below zero on several nights due to increased long-wave radiative cooling (Figure 6.2). December 2010 was exceptionally cold, again coinciding with a persistent high pressure system. Minimum daily air temperatures recorded at the suburban site were below -15 °C; between December 23rd and 25th temperatures did not rise above 0 °C (Figure 6.2). Precipitation totals during the month, which includes hail and snow, was 53.8 mm or 74% of the 1961-1990 average. Periods of heavy snow showers began at the end of November 2010 (28 and 30th) and continued into early December (between December 1st and 4th). Heavy snowfalls occurred again later in the month (December 17-18th and 23rd and 24th) and due to extremely cold air temperatures snow remained at the surface during these times.

Typically the passage of high pressure systems in winter months result in periods of dry, sunny but cold conditions, for example December 2011 to March 2012 (Figure 6.2). With the exception of January 2012, these months consistently recorded below average rainfall totals. On the other hand periods of low pressure are characterised by high rainfall totals and relatively milder air temperatures due to radiative trapping by clouds. Weather patterns during mid July 2010, for example, where dominated by slow moving Atlantic depressions resulting in cloudy, unsettled and wet conditions. Rainfall totals were greater than 200% of the 1961-1990 average (Met Éireann) (Figure 6.1). Mid to late October 2011 again experienced Atlantic depressions and total rainfall recorded at the station between October 24 and 26th was 110.4 mm. Although the beginning of 2012 was relatively dry, the summer months, particularly June and July, were extremely

wet and cloudy conditions gave rise to warm but dull weather. This weather continued into September 2012 and a deep depression measuring 977 hPa (Figure 6.2b) gave rise to extremely high rainfall totals at the suburban station (67.4 mm between September 24 and 25th) causing flooding in many parts of Dublin (Met Éireann). Dry months experiencing less than 60% of the monthly LTA include April 2010, August 2010, October 2010, January 2011, April 2011, August 2011, December 2011, February 2012, March 2012 and December 2012 (Figure 6.1). This indicates relatively drier and brighter (in terms of sunshine hours) winters and springs, and relatively wet and cooler summers.

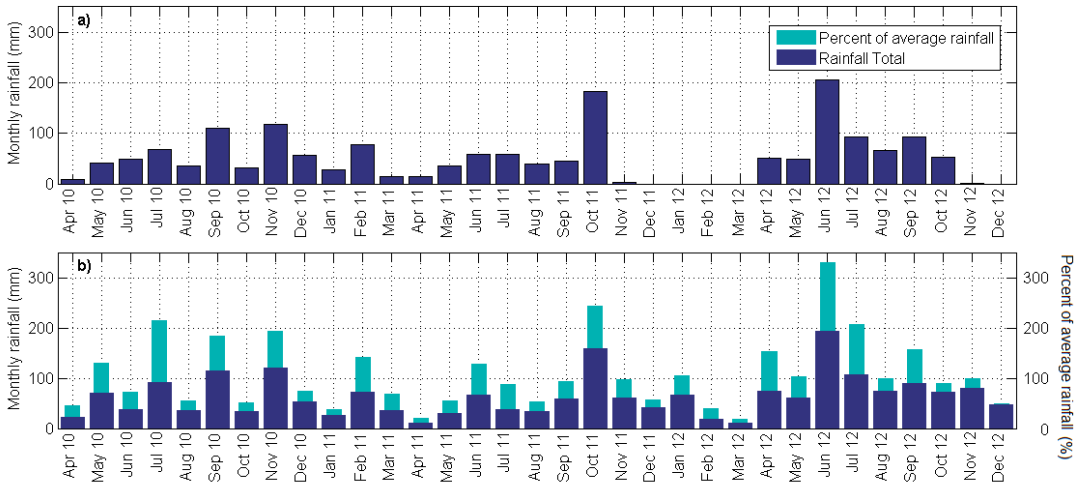

Figure 6.1 a) monthly rainfall totals recorded at the suburban site and b) Met Éireann's Merrion Square weather station in Dublin (Met Éireann) (Purple colour) indicating percent of 1961-1990 average for years 2010-2011, and 1981-2010 average from January 2012-December 2012 (Turquoise colour).

The vapour pressure deficit (VPD) represents the amount of water vapour necessary to achieve saturation and can be described as the 'drying power' of the air relative to a saturated surface (Oke, 1987:64) (Figure 6.2c). Throughout the observation period mean daily VPD ranges from 2-12 hPa at the suburban site, typically increasing with increased air temperature and moisture availability. December 2010 and January 2012 recorded the lowest mean daily VPD (~2 hPa) coincident with very cold air temperatures.

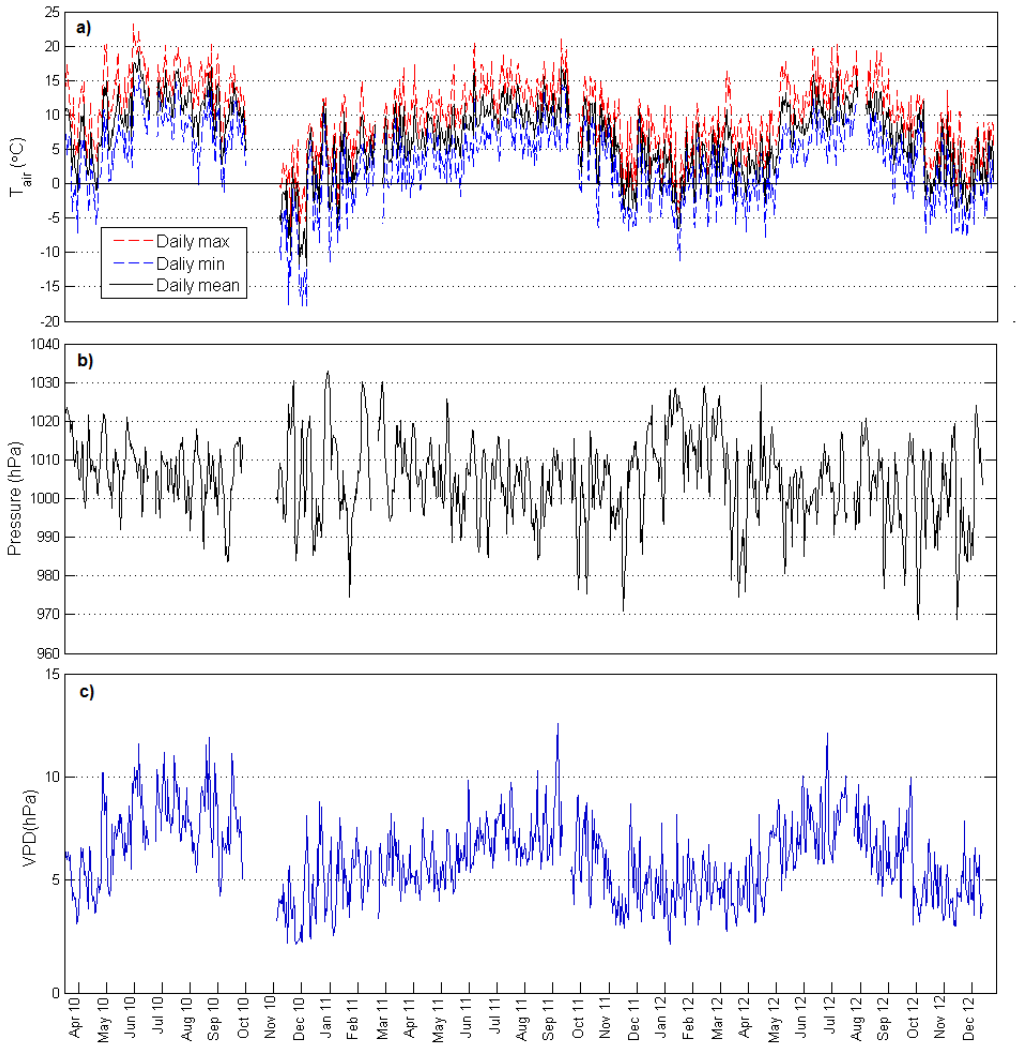

Figure 6.2 Meteorological conditions during the observation period at the suburban site: a) daily mean, minimum and maximum station air temperature, b) mean daily station pressure and c) mean daily station vapour pressure deficit (VPD).

The prevailing wind direction measured at the suburban station is from the west, north west and south west direction, accounting for 44% of all daytime hours (Daytime is defined as K↓>3 W m^{-2}). With regard to nighttime hours there is a relatively large increase in the frequency of wind from the east direction, accounting for 24% of all cases during the night relative to 12% during the daytime cases (Figure 6.3). The nighttime windspeed during easterly air flow is significantly reduced relative to westerly air flow and is classified as calm-light air flow according to the Beaufort Scale. Dublin observes a sea breeze into the night due to the UHI maintaining a positive land-sea temperature difference after sunset. This phenomenon has been reported in literature for coastal cities (Barlow, 2014). In general the majority of windspeed for westerly directions lie between 1 and 7 ms^{-1} and can be classified as a light to gentle breeze. Airflow from the north, south and north easterly directions are relatively infrequent at

the suburban station and this trend is also evident for Dublin-based Met Éireann stations (Met Éireann).

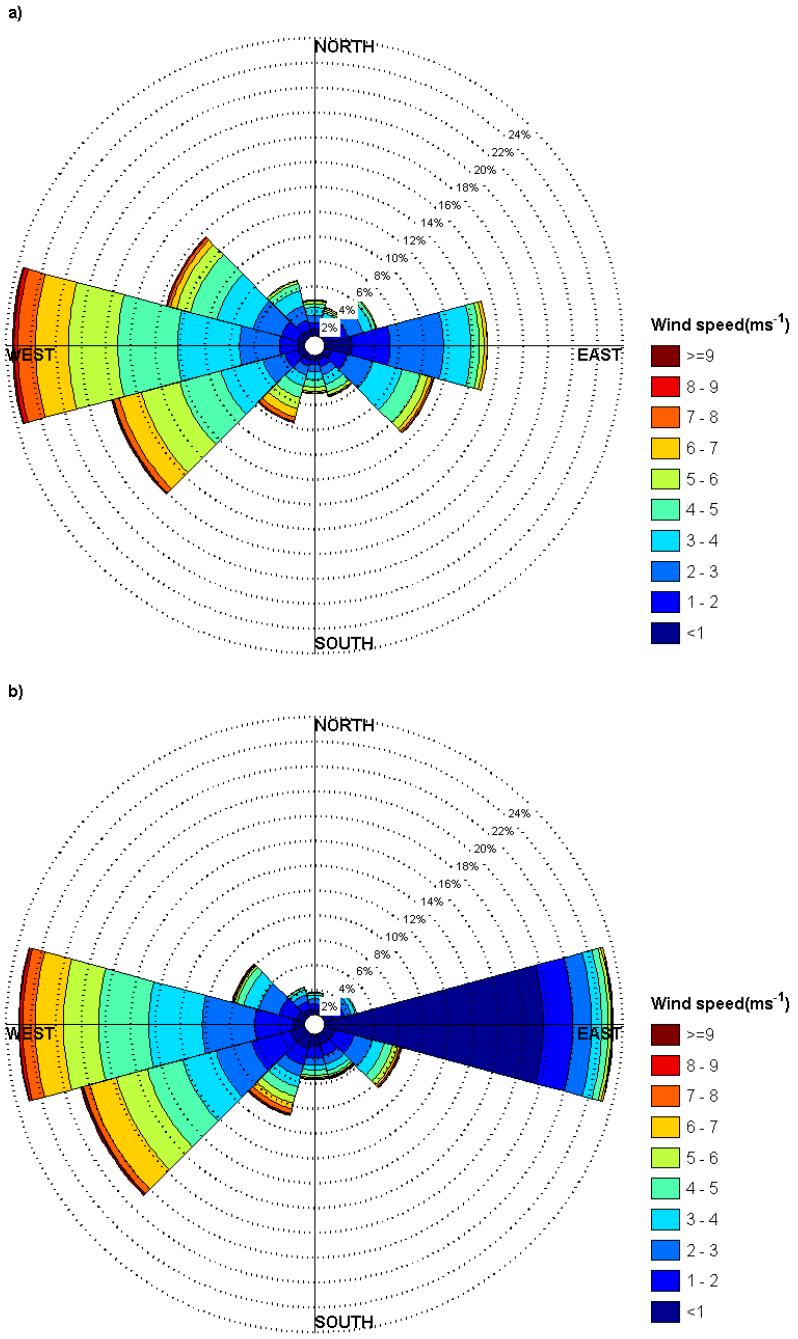

Figure 6.3 Windrose illustrating windspeed per wind direction recorded at the suburban site for a) daytime cases and b) nighttime cases. Daytime values are defined as those corresponding to values of incoming shortwave radiation (K↓) greater than 3 W m^{-2}.

The synoptic scale weather conditions, such as mean atmospheric pressure, experienced at the suburban site and urban site 1 are largely consistent over the observational campaign; however air temperature exhibited a difference throughout the observation period, in general urban air temperatures are greater than the suburban site with the average temperature difference equal to 0.8 °C (Figure 6.4). With regard to rainfall,

station cumulative totals between May 2010 and June 2012 were 1679.8 and 1368.6 mm at urban site 1 and the suburban site respectively and the difference in recorded rainfall was 311.2 mm. The cumulative rainfall for the same period at the nearby Merrion Square Met Éireann weather station in Dublin City was 1605.9 mm (Met Éireann).

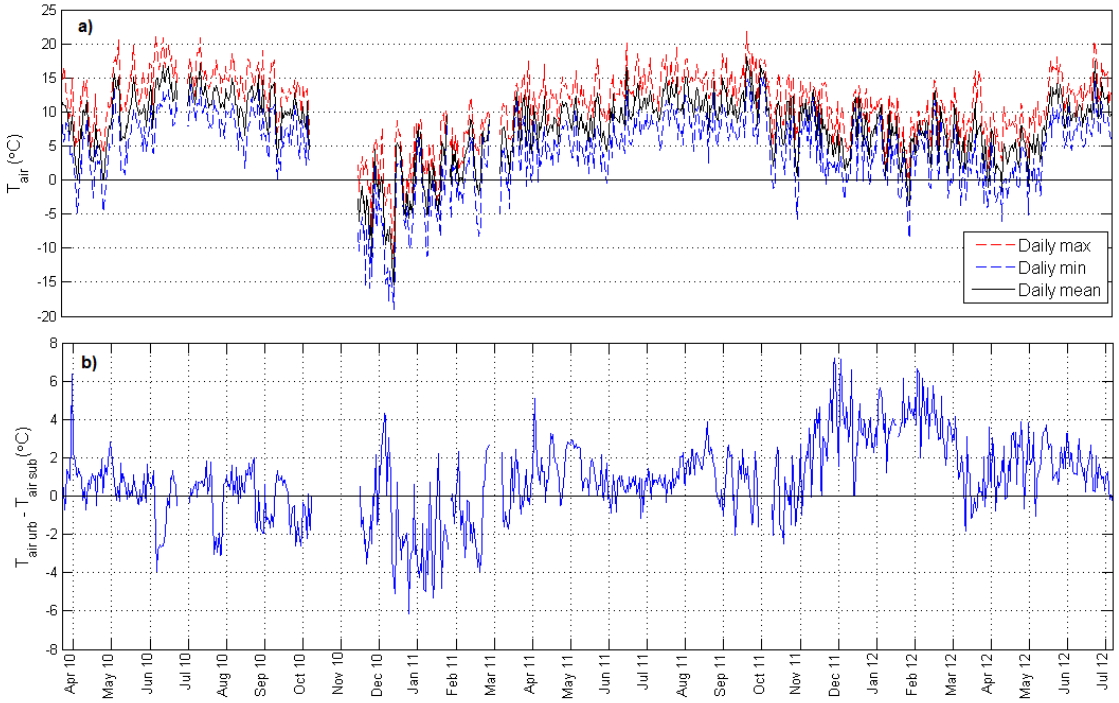

Figure 6.4 a) Mean daily station air temperature measured at urban site 1 and b) mean daily air temperature difference between urban site 1 and the suburban site.

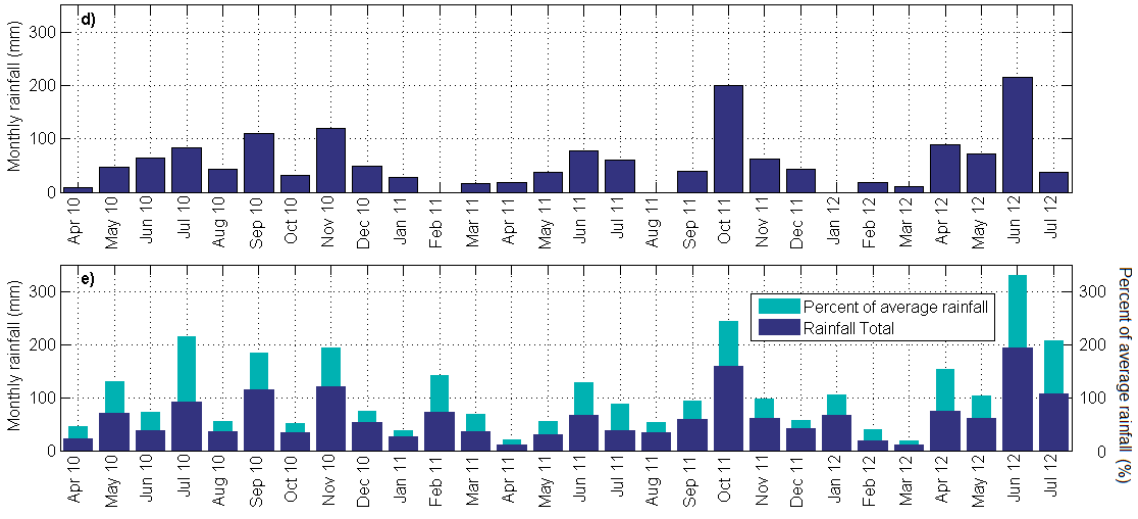

Figure 6.5 Same as Figure 6.1 for a) urban site 1 and b) Merrion Square Met Éireann weather station. Complete monthly rainfall data is not available at urban site 1 for months April 2010 and July 2012 due to the beginning and end dates of the station operation period.

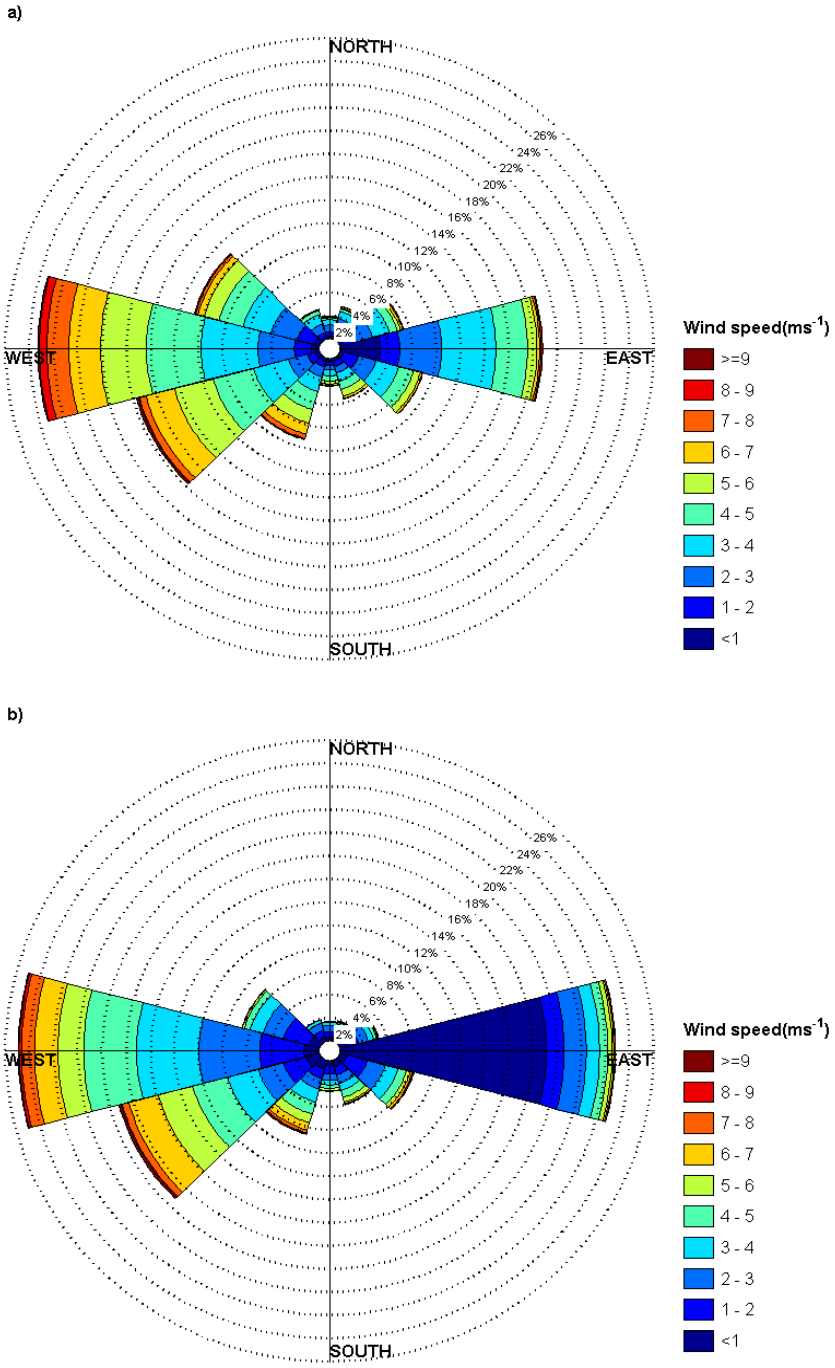

Figure 6.6 Same as Figure 6.3 for urban site 1.

With regard to urban site 1 the prevailing wind direction between April 2010 and July 2012 is westerly, accounting for 25% of all daytime hours and 27% percent of nighttime hours. The occurrence of easterly airflow at nighttime, similar to the suburban site, is also significant (25% of all cases) in unison with westerly airflow (25% of all cases). The windspeed for easterly airflow at nighttime is reduced in comparison to westerly airflow. The prevalence of airflow from the general north and south directions is limited and the greatest windspeed coincide with westerly airflow (Figure 6.6).

6.3 The radiation balance

Radiation source areas

The measured signal of a downward facing pyranometer (measuring K↑), mounted parallel to the ground, represents a circular source area. The radius of the circular source area is given by Schmid et al. (1991) (Equation 2.22) and was used to estimate the source area contributing to 95% of the instrument's signal. The size of the source area will be influenced by the height of the pyranometer above the ground; the NR01 instrument is mounted at 11, 17 and 25 m above ground level at the suburban site, urban site 1 and urban site 2. Employing Equation 2.22 the radius of the 95% source area was calculated as 48, 74 and 109 m for the suburban site, urban site 1 and urban site 2 respectively (see Figure 5.7, Figure 5.17 and Figure 5.25). See Table 5.1 for a summary of the key surface characteristics and albedo observed at each EC site.

6.3.1 *Suburban site radiation measurements*

Shortwave radiative fluxes

Observed maximum values of K↓ were 998 W m^{-2} in June 2010, 1013 W m^{-2} in June 2011 and 995 W m^{-2} in July 2012. Maximum winter time values observed at solar noon, coincident with the winter solstice, were 395 W m^{-2} in December 2010, 266 W m^{-2} in December 2011 and 292 W m^{-2} in December 2012. Half hourly averages for the three year observation period are illustrated in Figure 6.7a and demonstrate the seasonal pattern of incoming shortwave radiative in response to day length and the increasing and decreasing inclination of the Earth relative to the Sun (Figure 6.7b). During clear-sky days the suburban surface receives relatively more incoming solar radiation relative to all-sky days. In 2010, for example, the magnitude of incoming shortwave radiation observed on a clear-sky day at local solar noon was 916 W m^{-2} for June 20 (Figure 6.7a) versus a monthly median value of 650W m^{-2} (Figure 6.7d) representing all sky conditions in June 2010.

Mean monthly values represent the average magnitude of incoming shortwave radiation for all daytime hours per month. During the observation period the monthly mean values for months April and May typically receive greater than or equal to the magnitude of incoming shortwave radiation compared to June and July. The wet and dull summer of 2012 is illustrated in Figure 6.7c where monthly mean values from

March to September 2012 display little seasonality (221, 216, 224, 243, 237 and 234 W m^{-2} for April, May June, July, August and September respectively).

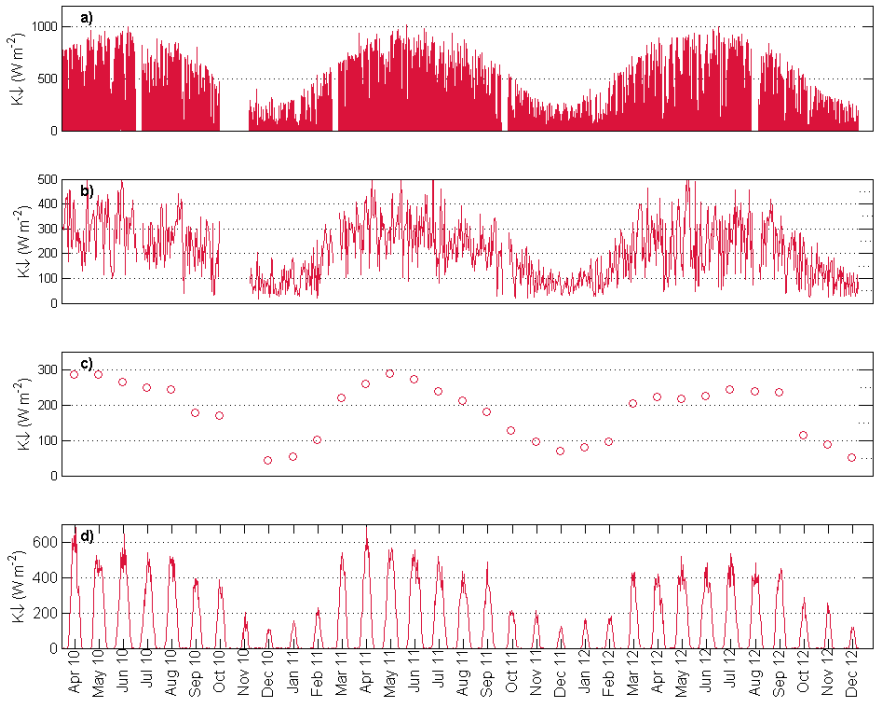

Figure 6.7 a) Half hourly, b) daily and c) monthly averages for incoming shortwave radiation and d) monthly diurnal cycles of median values observed at the suburban site. There were an insufficient number of data points available for the calculation of the monthly mean for November 2010. Note the scale difference on the y-axis for a, b, c and d.

Figure 6.8 Same as Figure 6.7 for reflected shortwave radiation.

The monthly median diurnal pattern of incoming solar radiation is illustrated in Figure 6.7d for all months (note that median and monthly average values are calculated using a total of 23 and 4 days for April 2010 and November 2010). Lowest median diurnal patterns are typically observed in December of each year (maximum values at local solar noon are 108, 135 and 119 W m^{-2} for years 2010, 2011 and 2012). The median diurnal cycles for April 2010 and 2011 observed the greatest magnitude of incoming shortwave radiation in their respective years.

The magnitude of reflected shortwave radiation is largely proportional to that received at the surface (10-12% of K↓) with the exception of two clear periods, namely the end of November 2010 and December 2010 (Figure 6.8). These cases correspond to periods of snowfall when snow remained at the surface for varying lengths of time. During these conditions the magnitude of reflected shortwave radiation increased significantly relative to their corresponding values in other years. Maximum K↑ observed in November and December 2010 was 158 and 140 W m^{-2} respectively (Figure 6.8a).

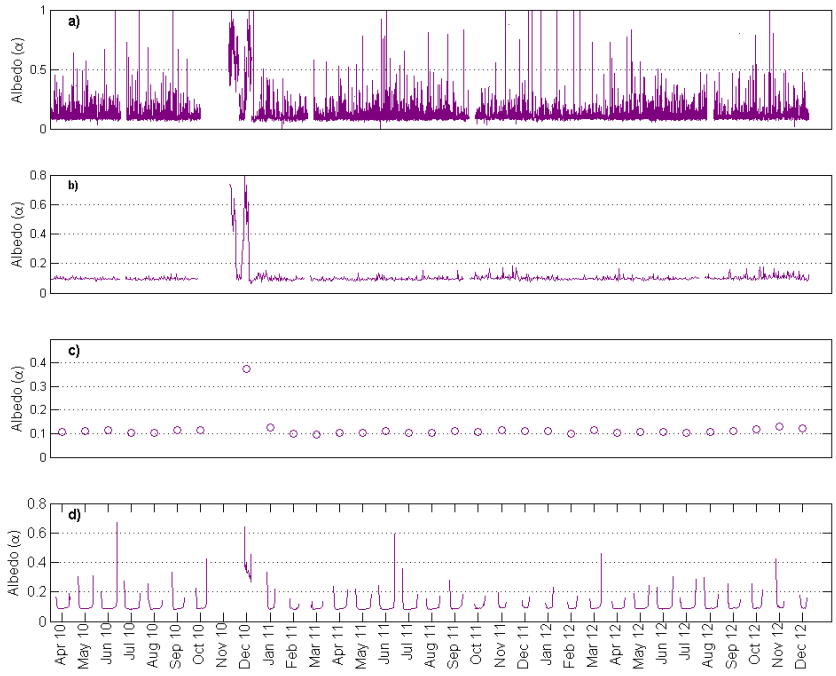

Figure 6.9 a) Half hourly b) daily, c) monthly averages for surface albedo (α) and d) monthly diurnal cycles of median values observed at the suburban site. Note the scale difference on the y-axis for a, b, c and d.

The surface albedo (α) at the suburban site is presented in Figure 6.9 and describes the proportion of K↓ that is reflected by the underlying suburban surface. Half hourly

averages vary between 0.1 and 1, representing 10 to 100% reflection of K↓. Large sustained values, for example, greater than 0.4 coincide with periods where snow remained at the surface and can be clearly seen in the daily mean α dataset (Figure 6.9b). There were an insufficient number of days available for the calculation of the monthly mean for November 2010, however the monthly mean for December 2010 reveals the increased overall α during the period of snow cover. During this time the monthly average α was three times greater (α=0.36) in comparison to all other months in the observation period where monthly average values greater than 0.12 or 12% are rarely observed (Figure 6.9c). No significant seasonal variation in α was observed throughout the entire observation as a result of differing vegetation density (e.g. Christen and Vogt, 2004). Unlike previous studies average monthly α was found to slightly increase in winter months in comparison to summer months, where mean winter α values of 0.14 and 0.11 were calculated for December, January and February (including December 2010 and excluding December 2010) versus α of 0.10 for all available June July and August data.

Longwave radiative fluxes

Maximum annual values observed were 415, 411 and 426 W m^{-2} for 2010, 2011 and 2012 respectively. The annual range was greatest in 2010, 195 W m^{-2}, this was due to the significantly cold December where lowest values of L↓ for the entire observation period were observed (219 W m^{-2}) (Figure 6.10a). In general L↓ decreases for clear-sky conditions and larger fluxes are observed during overcast, cloudy and wet conditions similar to those prevailing in months June to September 2012. Maximum values for the entire observation period were observed in June 2012 (426 W m^{-2}). Combined, the summer months of June, July and August 2012 reported the highest monthly mean values (358, 363 and 361 W m^{-2}) in comparison to corresponding months in 2010 and 2011 (Figure 6.10c). This is a result of wet and cloudy conditions that served to enhance L↓. The lowest monthly mean value was observed in December 2010 (294 W m^{-2}) followed by January and December 2011 (both observed 302 W m^{-2}).

The monthly diurnal cycle of L↓ is more complex to summarise than that of the shortwave radiative fluxes; diurnal variations are less pronounced (typically 100 W m^{-2} or less) and over the course of 30 days the average monthly diurnal median is typically a

response to a composite of several large scale synoptic weather patterns. As a consequence analysis of the monthly diurnal median values yields limited information.

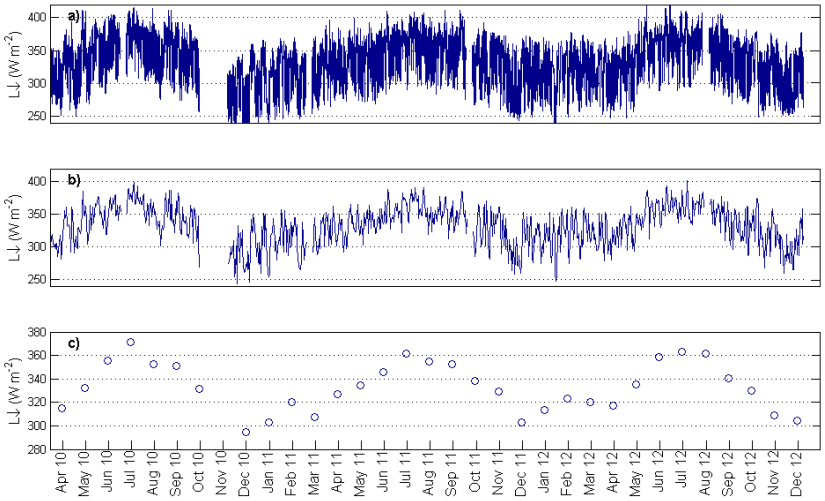

Figure 6.10 a) Half hourly b) daily and c) monthly averages for incoming longwave radiation observed at the suburban site. Note the scale difference on the y-axis for a, b, and c.

.

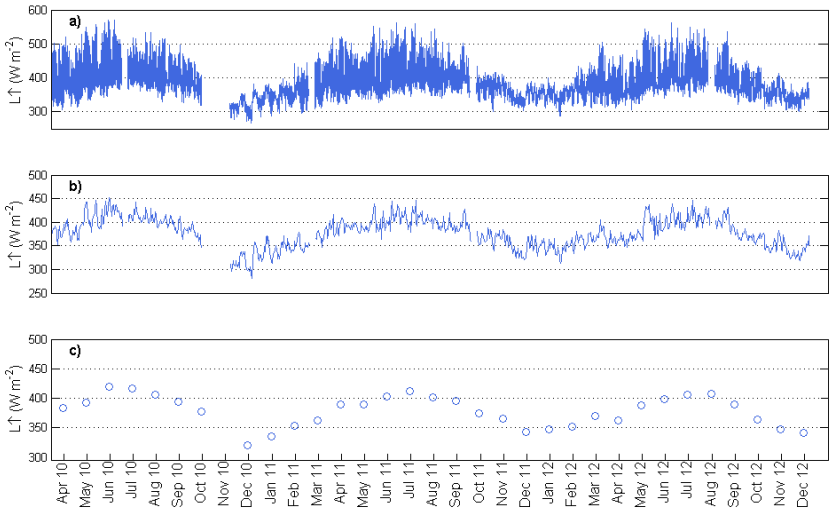

Figure 6.11 Same as Figure 6.10 but for outgoing longwave radiation observed at the suburban site.

With regard to L↑ values exhibit a more pronounced seasonal cycle in comparison to L↓. Minimum observed half hourly mean fluxes occurred in December 2010 (267 W m^{-2}) and the lowest daily mean flux observed in the month was 280 W m^{-2} (Figure 6.11 a and b). Annual maximum half hourly averages occur exclusively in June of each year; observed values in 2010, 2011 and 2012 were 569.4, 561.3 and 561.6 W m^{-2}. During the entire observation period the minimum and maximum monthly mean values occurred in

2010; monthly mean outgoing radiation was 420 W m^{-2} in June and 307 W m^{-2} in December (Figure 6.11c).

At nighttime the proportion of longwave radiation emitted from the surface relative to incoming longwave radiation (L↑/ L↓) at the suburban site ranges from 0.98 to 1.25. Over monthly timescales L↑/ L↓ is on average 1.08, however the highest monthly means observed correspond to months with little cloud cover facilitating increased nighttime longwave radiative losses, for example, April 2010 (1.14), April 2011 (1.12) and December 2011 (1.13). L↑/ L↓ approaches unity for months experiencing predominantly overcast, wet conditions when L↓ is enhanced, for example, July 2010 (1.01), October 2011 (1.04) and August 2012 (1.02).

Net all-wave radiation

Maximum annual half hourly mean values of Q* are 724 (June 2010), 745 (April 2011), and 793 W m^{-2} (July 2012) (Figure 6.12). Minimum annual half hourly values are reported in winter, for example, -75, -79, and -85 W m^{-2} for years 2010, 2011, 2012. Over a 24 hour period maximum mean daily values of Q* are significantly reduced in relation to half hourly values; the maximum daily mean observed is 222 W m^{-2} in July 2012 (Figure 6.12b). During the winter negative mean monthly values are frequently reported for Q* and indicate a net loss of energy by the surface (Figure 6.12c). The reduction in Q* in winter is evident in Figure 6.12 d where monthly median values at local solar noon range from greater than 400 W m^{-2} in summer to less than 50 W m^{-2} in winter (Figure 6.12d). Also evident from Figure 6.12 d is the difference in nocturnal loss between summer and winter. Due to the reduced receipt of energy during the day time in winter, nighttime losses are typically reduced (i.e. less negative, ~-30 W m^{-2}) compared to summer time where nocturnal values for Q* equal to -55 W m^{-2} are observed.

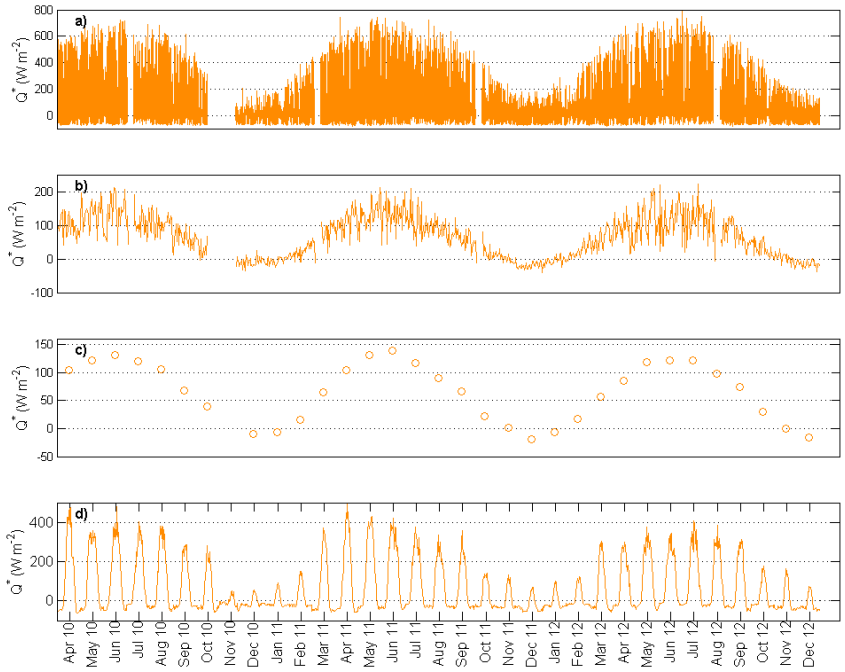

Figure 6.12 Same as Figure 6.7 but for net all-wave radiation observed at the suburban site.

This section will examine the radiation budget of urban site 1 during its operation between April 2010 and July 2012 and that of urban site 2 from October to December 2012. Given the proximity of both urban sites to the suburban site (Figure 4.1) the patterns of the urban incoming radiative fluxes (K↓ and L↓) were not expected to deviate substantially from those measured at the suburban site. This section will focus on differences in relation to suburban observations given that the overall patterns exhibited by each of the radiation components are similar on a diurnal and seasonal basis.

Figure 6.13 and Figure 6.14 show K↓ and K↑ at the two urban sites. The measured values of K↓ are similar to the suburban site. The period of snow cover in November and December 2010 is evident in the observations and the magnitude of K↑ (greater than 100 W m^{-2}) is relatively increased for the time of year (Figure 6.14). The magnitude of half hourly mean values observed in spring and summer months are consistently greater than those observed at the suburban site. Values of K↑ frequently exceed 100 W m^{-2}; observations of this magnitude only occur during snow covered periods at the suburban site (Figure 6.8a). This indicates that the urban site reflects a greater portion of K↓ than its suburban counterpart. Monthly mean values of K↑ are also greater at both urban locations with the exception of November and December 2010; at

this time it could be expected that snow remained relatively undisturbed at the suburban location relative to the urban site.

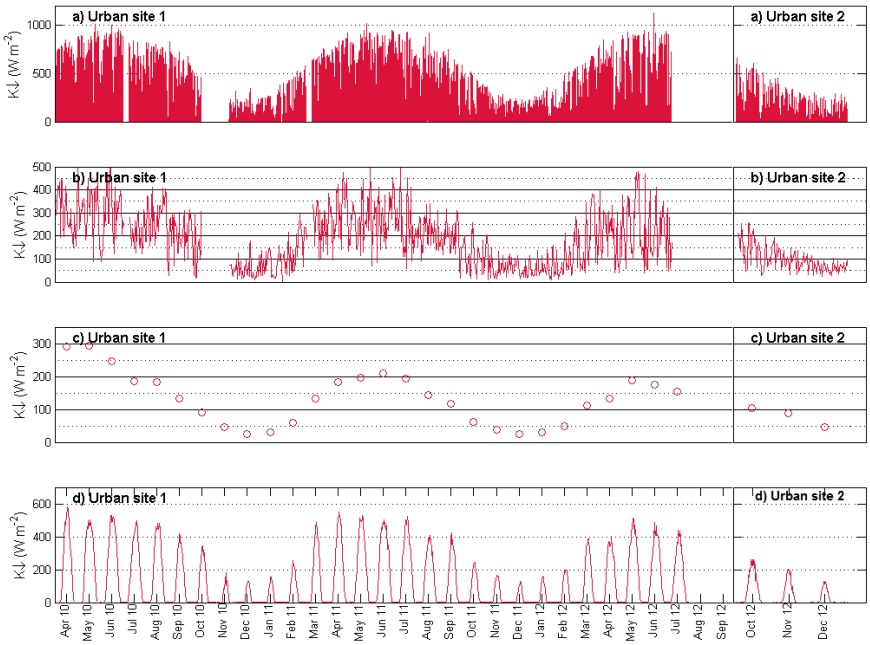

Figure 6.13 Same as Figure 6.7 but for urban site 1 and 2.

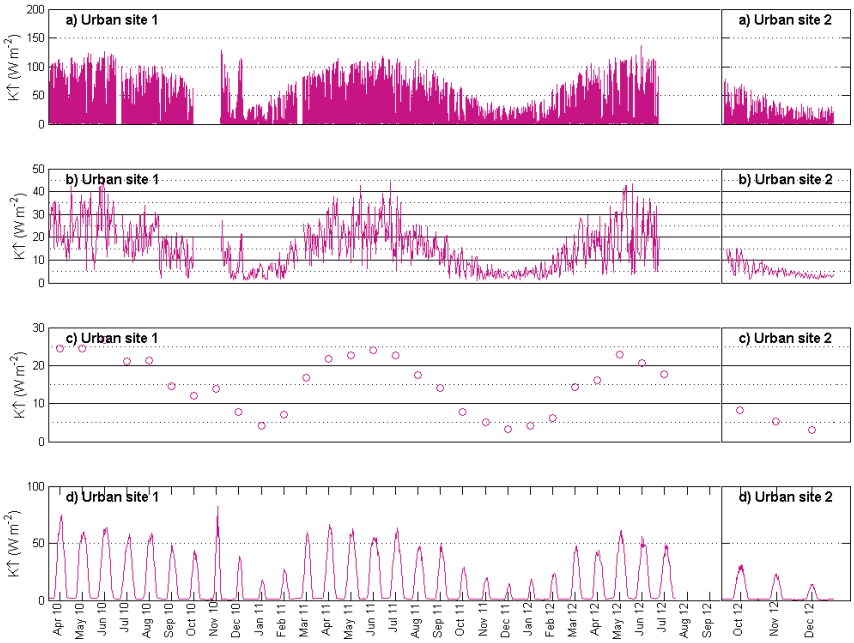

Figure 6.14 Same as Figure 6.7 for reflected shortwave radiation but for urban site 1 and 2.

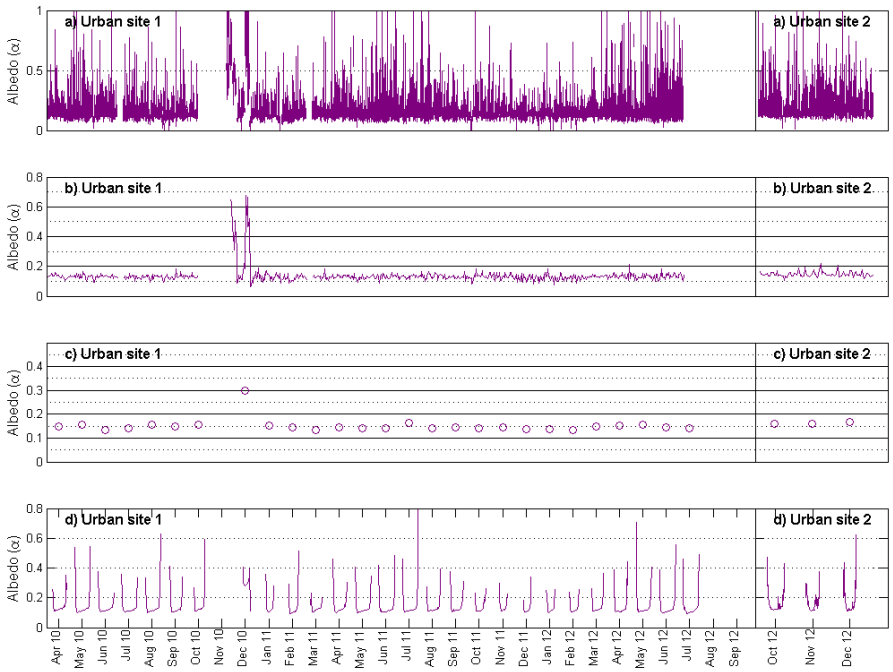

Figure 6.15 Same as Figure 6.9 but for urban site 1 and 2.

The mean daily α values observed in November and December 2010 clearly illustrate snow-cover conditions however they are relatively reduced in comparison to the suburban site due to relative disturbance of the snow cover (Figure 6.9b). Examination of the median diurnal cycle at urban site 2 revealed increased α in the afternoon (Figure 6.15d). This increase coincides with the sharp decrease in simultaneous observations of K↓ (data not shown) caused by the shadow of the adjacent mast; at this time the trend of K↓/ K↑ is altered from its typical behaviour due to instrument siting. The seasonal α is greater at the urban sites reporting 0.15, 0.14, 0.15 and 0.17 for spring, summer, autumn and winter (mean albedo for winter months in the absence of snow cover conditions is 0.14). These surface albedos are consistent with those published in the international literature however they are considerably greater than values reported previously for the suburban site in section 6.3.1 (e.g. α=0.11-0.12).

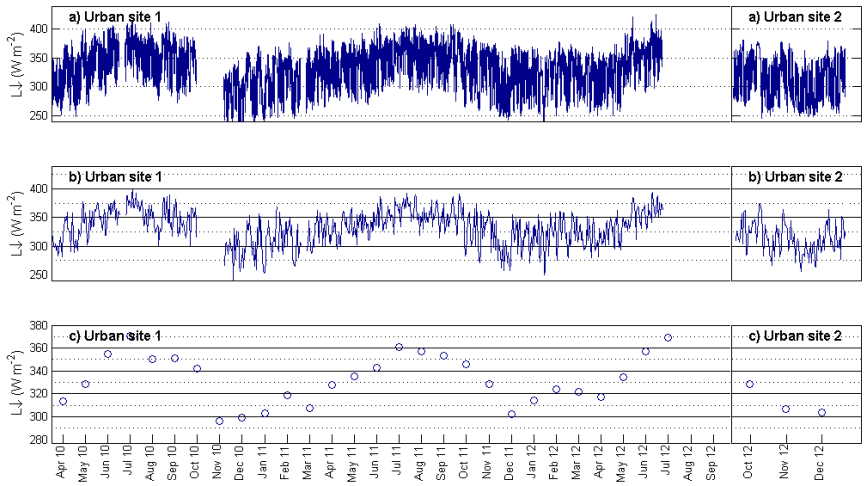

Figure 6.16 a) Half hourly b) daily and c) monthly averages for incoming longwave radiation observed at urban sites 1 and 2. Note the scale difference on the y-axis for a, b, and c.

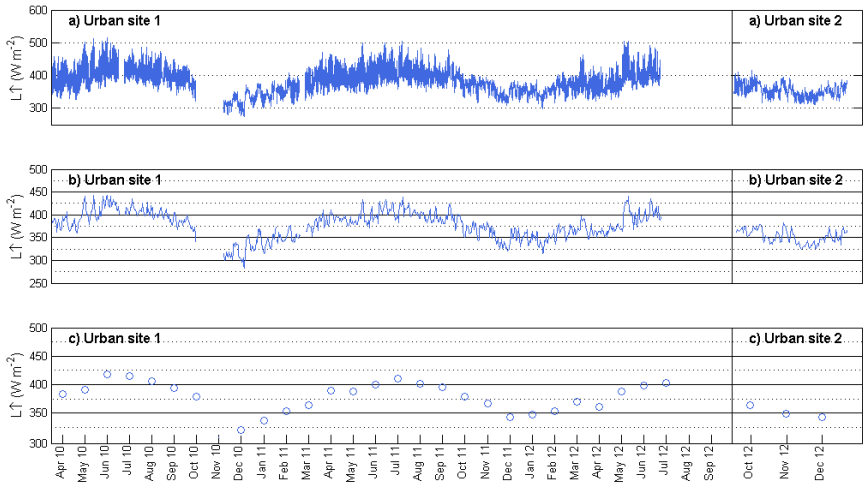

Figure 6.17 Same as Figure 6.16 for outgoing longwave radiation observed at urban sites 1 and 2.

The observations of L↓ show a spatially conservative variation between urban sites 1 and 2 and the suburban site and the time series is consistent across half hourly, daily and monthly mean values (Figure 6.11; Figure 6.16). With regard to L↑ the range of half hourly and daily means values is reduced at the urban sites. This indicates that the skin surface temperature at the urban sites is less variable over the course of the day relative to the suburban site. This is unsurprising given the geometry and higher H/W ratio at the urban sites which promote radiation trapping within the UCL (Figure 6.11 and Figure 6.17).

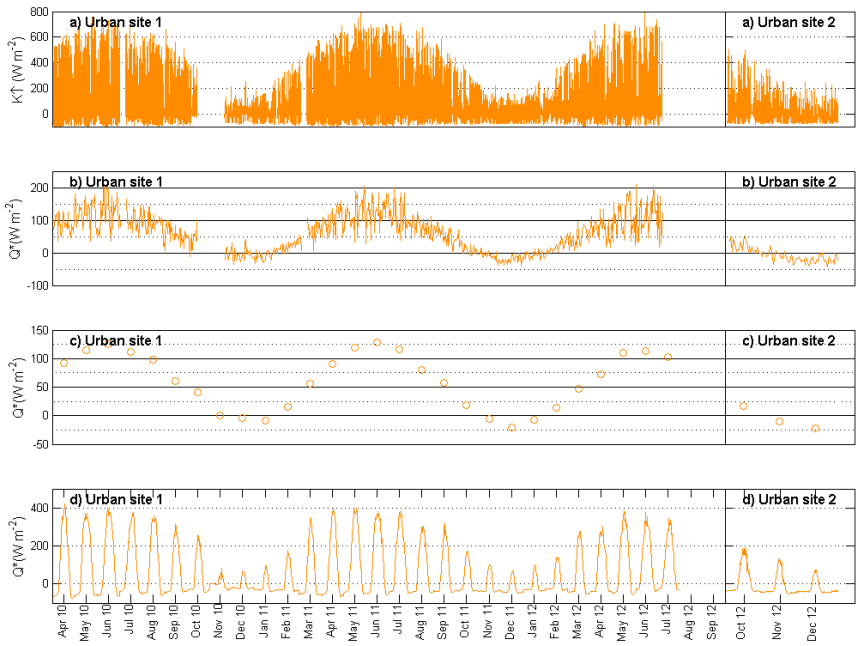

Figure 6.18 Same as Figure 6.7 for net all-wave radiation observed at urban sites 1 and 2.

The seasonal cycle of Q* observed at the urban sites reflects that of K↓. Minimum half hourly values observed are -105, -110 and -102 W m^{-2} in 2010, 2011 and 2012 respectively. While maximum half hourly values reported are 759, 838, and 872 W m^{-2} in 2010, 2011 and 2012 respectively (Figure 6.18a). Q* is significantly reduced in winter months and negative mean daily values are frequently observed, for example December 2010 and 2011 (Figure 6.18b). Median diurnal cycles also reveal relatively greater nocturnal energy loss relative to the suburban site; losses are greatest in summer, for example, -76 W m^{-2} reported in April 2010

6.4 Inter-site comparison of the radiation balance

The radiation balance components from the suburban site and urban site 1 were compared to quantify the absolute difference in K↓, K↑, L↓, L↑ and Q*. The difference in the radiation components were derived as the absolute difference in observations (W m^{-2}) between the suburban site and urban site 1 for the period between April 2010 and July 2012. Positive (negative) values indicate a relative increase (decrease) in energy observed at the suburban site and represent monthly median diurnal differences. With regard to the residual difference in K↓, the difference in monthly median values for daylight hours was exclusively positive for the observation period; in the absence of solar inputs the residual is zero (zero values are indicated as dark blue in Figure 6.19). Greatest differences occur in the spring and summer months (e.g. April to August),

particularly in May and June 2011 when greatest absolute differences in receipt of solar energy between the suburban and urban site reached 140 W m^{-2} (Figure 6.19). In the winter months when sun elevation angles are lower, the differences are smaller, typically ranging from 0-40 W m^{-2}. On average K↓ is between 7-14% greater at the suburban site relative to the urban site.

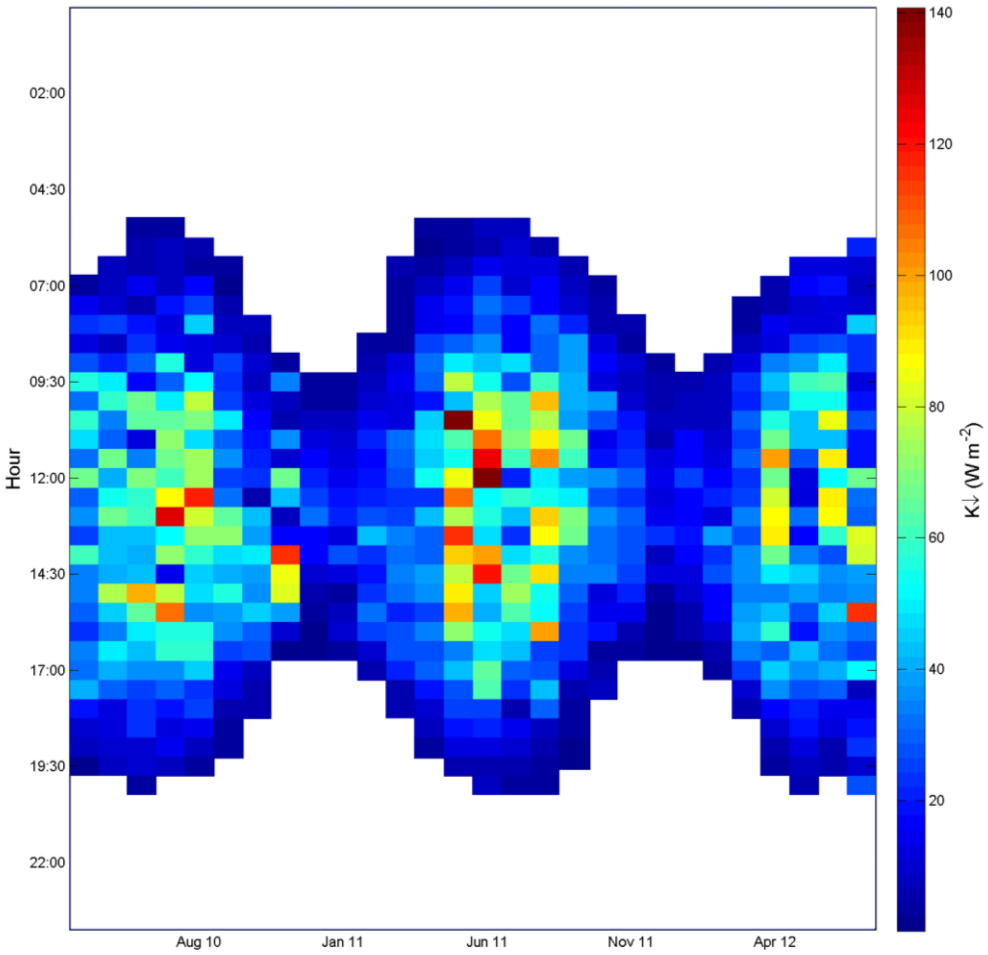

Figure 6.19 Monthly median diurnal incoming shortwave radiation residual between the suburban site and urban site 1 for months April 2010 to July 2012 for all day time hours. White areas on the plot correspond to observations of K↓ equal to zero W m^{-2}.

With regard to K↑ differences in the winter months are close to zero; this is also the case for hours close to sunrise and sunset for all seasons when the magnitude of K↓ is low (Figure 6.20). In spring, summer and autumn, at higher Sun elevations, the residual difference reveals a consistently greater magnitude of K↑ at the urban site. Typically the suburban site reflects between 5 to 25 W m^{-2} less K↑ relative to the urban surface (Figure 6.20). Exceptions to this are observed in November and December 2010 as large positive anomalies in Figure 6.20, coincident with snow cover periods at both locations.

It should be noted that the number of days of data available for the residual difference calculation for November 2010 is only 4 days. December 2010 on the other hand can be considered more representative of the difference between K↑ observed during a combination of snow cover and snow-free conditions. At this time the suburban site is observed to reflect a greater magnitude of shortwave radiation in comparison to the urban counterpart. Potential reasons for the differences during the snow events may relate to snow clearance and snow melting at each of the sites. With regard to November 2010 the increased magnitude of reflected shortwave radiation at the suburban location is likely a result of less efficient snow clearance by local government services in comparison to the city centre. While snow events in December 2010 largely coincided with the Christmas vacation, presumably when there may be an overall reduction in local government services for snow clearing, which resulted in lower inter-site differences in reflected shortwave radiation.

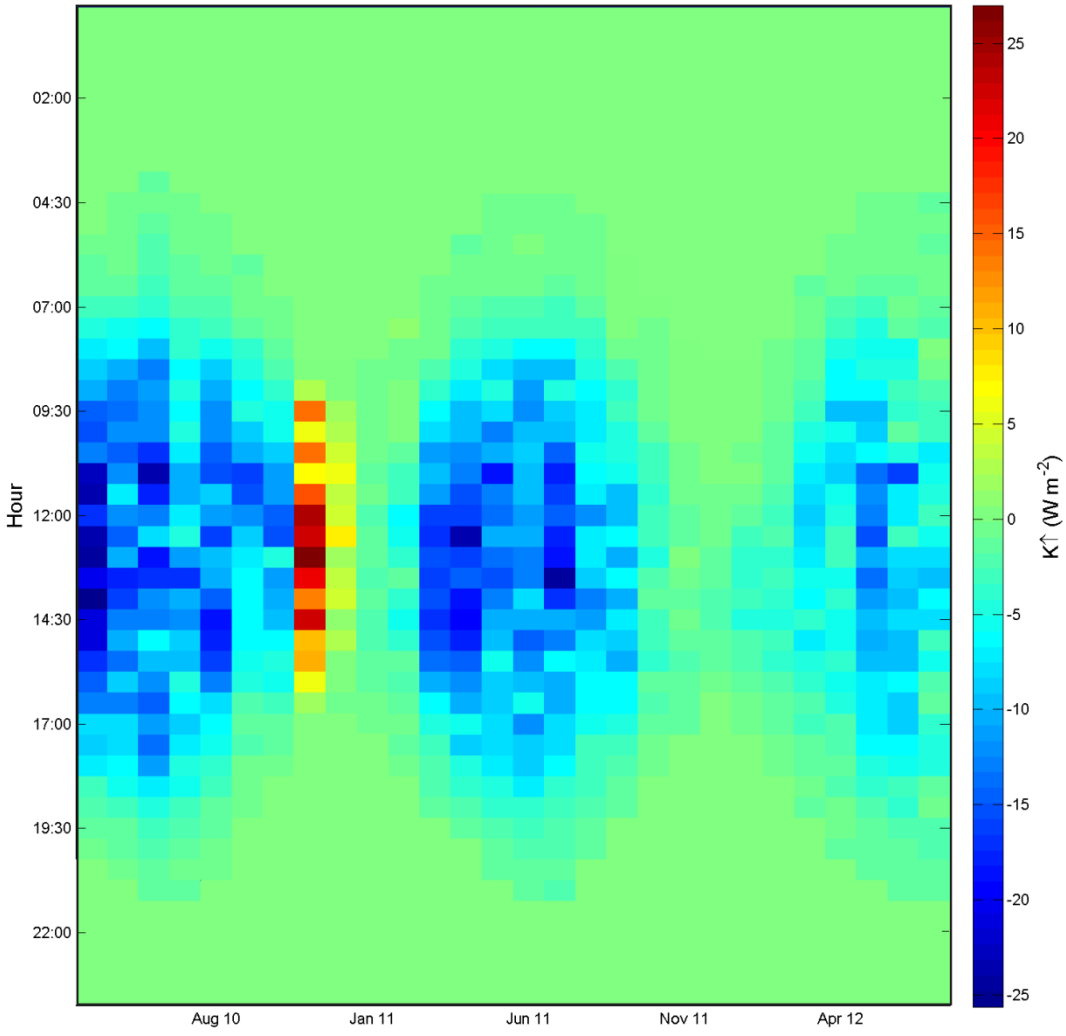

Figure 6.20 Same as Figure 6.19 for reflected shortwave radiation residual.

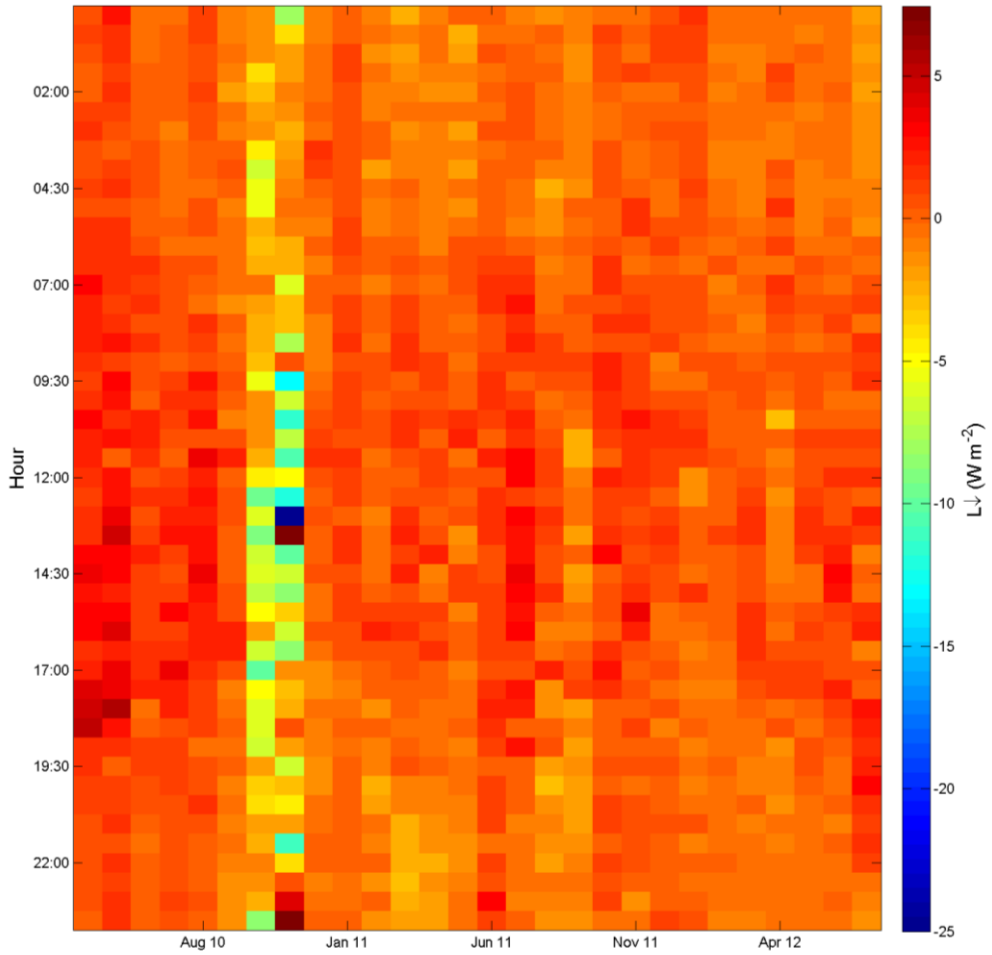

Figure 6.21 Same as Figure 6.19 for incoming longwave radiation residual for all hours.

The differences in L↓ are typically small, ±3 W m^{-2} (Figure 6.21). This is expected given that the magnitude of the flux is governed by atmospheric temperature and emissivity which do not vary substantially over distances of 3-4 km. Significant variations from this are observed in November and December 2010; at this time the suburban location receives relatively less L↓. This indicates that the UBL at the suburban location was relatively colder than its urban counterpart.

Differences in L↑ reveal a more variable pattern. Observed residual differences in winter months are the smallest, typically ranging from +5 to -5 W m^{-2} for all hours and zero for day time hours (Figure 6.22). On the other hand differences observed in months March to October each year display enhanced diurnal differences. In general for daylight hours the suburban site emits a greater magnitude of L↑ reaching +40 W m^{-2} (Figure 6.22). In the evening and into the night the residual difference displays a reverse different trend whereby L↑ at the urban site becomes relatively greater in magnitude (e.g. differences of up to -25 W m^{-2} are observed) (Figure 6.22).

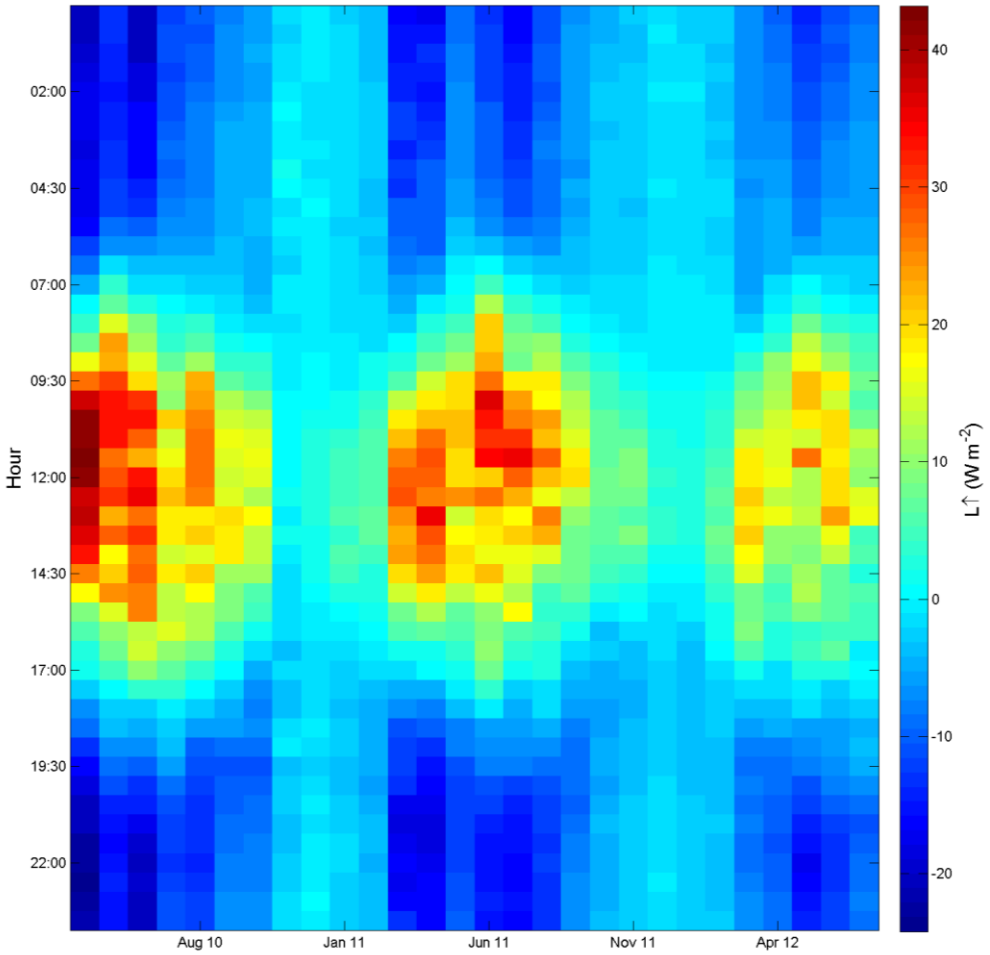

Figure 6.22 Same as Figure 6.19 for outgoing longwave radiation residual for all hours.

The difference in Q* across the two sites for the observation period is presented in Figure 6.23. Once again the difference in winter months between the sites is less pronounced owing to the overall reduction in incoming radiation (both K↓ and L↓) (Figure 6.23). The results reveal an annual cycle from 2010 to 2012 with increased Q* typically reported for nighttime hours at the suburban location; this trend is expected given the greater relative emission of L↑ at the urban site. During daytime hours the suburban site typically displays lower values for Q* relative to the urban site, the most pronounced median diurnal differences are -40 W m^{-2}; this trend is likely a result of the increased L↑ illustrated above. In some instances Q* is higher at the suburban however these cases are relative less frequent (+ 50 W m^{-2}) (Figure 6.23). Overall the relative increase in Q* at the suburban site during the night time hours is offset by losses during the day time hours. This finding supports the relative consistency in the daily and monthly mean statistics of Q* presented previously in Figure 6.12 and Figure 6.18.

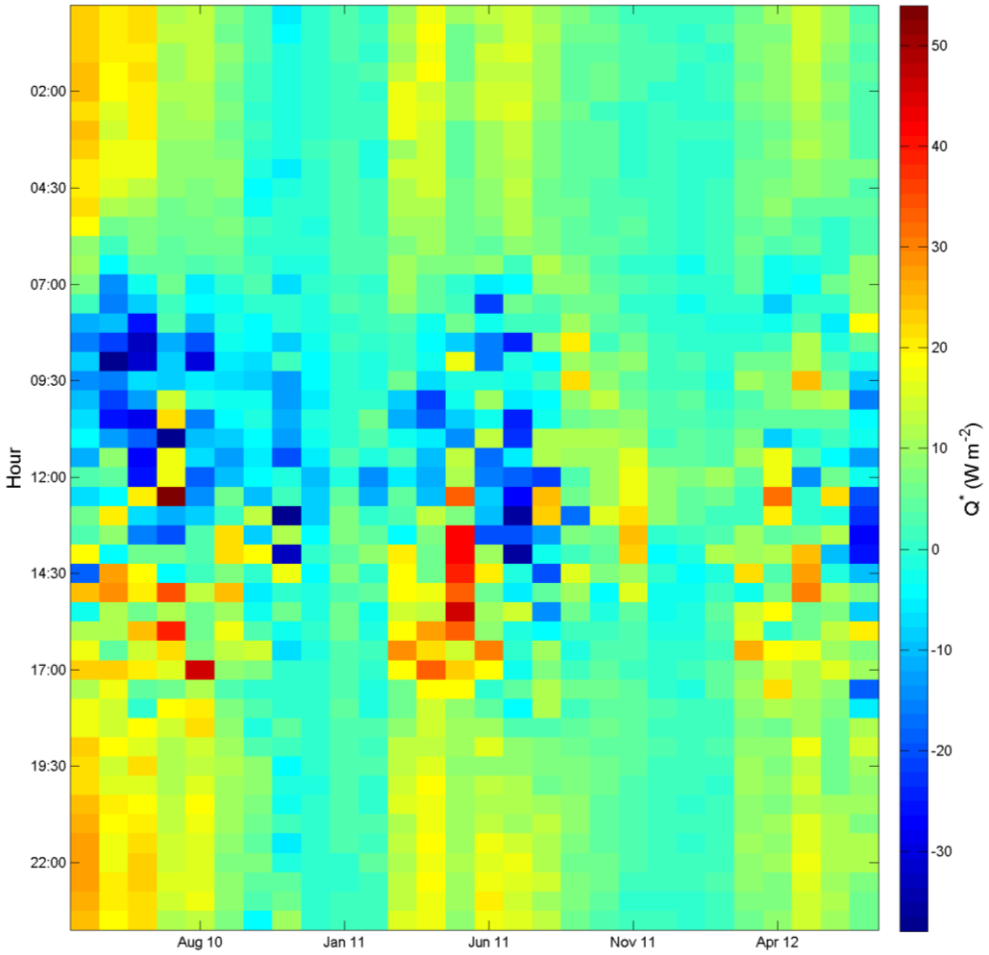

Figure 6.23 Same as Figure 6.19 for net all-wave radiation residual for all hours.

6.5 Turbulent fluxes: data availability, data gaps and quality flags

Data availability with regard to the turbulent fluxes varied for each site and each individual flux. Flux values were eliminated from analysis that corresponded to instrument diagnostic criteria, precipitation events and quality flags of class 7 or greater (see Table 4.5 and Section 4.7). The turbulent heat fluxes measured at urban site 2 were not eliminated from the dataset for reasons of precipitation as the enclosed-path gas analyser is not affected by water droplets (Burba et al., 2010). At the suburban site and urban site 1, Q_E and F_C were most affected by the data quality criteria and the percent of eliminated flux values for each station for each flux is outlined in Table 6.2.

Table 6.2 percentage of turbulent flux data discarded (%) following post-processing procedures for each EC station for each turbulent flux.

Station	Q_H	Q_E	F_C
Suburban site	31	41	35
Urban site 1	22	34	36
Urban site 2	12	26	-

Data quality flags based on Foken et al. (2004) show a relatively consistent pattern for individual fluxes across all the EC sites (Figure 6.24, Figure 6.25 and Figure 6.26). Half hourly flux estimates corresponding to quality flags of class 7, 8 and 9 are eliminated from analysis, hence all remaining flux estimates report quality flags between 1 and 6. The relative occurrence of each quality flag is presented for all sites and generally no significant difference was observed between daytime and nighttime cases (Note: The flux of CO_2 at urban site 2 is not considered in this study and is not presented in Figure 6.26).

The momentum flux (τ) consistently reports the highest relative frequency of quality flags of class 1 (e.g. greater than 77%) for all daytime and nighttime cases. This indicates that the state of turbulence observed at each EC site that regulates the fluxes of heat, water vapour and CO_2 is largely fulfilling EC requirements in terms of steady-state conditions and stationarity. Quality flags of class 5, occurring between 10-16% of all cases for τ represent conditions when there is 1) between 0-75% deviation between individual 5 minute fluxes and the 30 minute average flux and 2) between 31-100% deviation between the measured and modelled integral turbulence characteristics (ITCs).

The greatest difference in daytime and nighttime quality flags is observed in relation to the Q_H. Flags of class 1 and 2 are observed for over 80% of all daytime cases in relation to 70% at nocturnal cases at the suburban site. The relative frequency of flags 1 and 2 are 85 and 68% with regard to urban site 1 and 85 to 75% at urban site 2 for daytime and nighttime cases respectively. Quality flags of class 1 and 2 associated with the flux of latent heat (Q_E) are relatively reduced in relation to all other fluxes for all EC sites (Figure 6.24, Figure 6.25 and Figure 6.26). Daytime cases at the suburban site report the highest occurrence of quality flags of class 1 and 2 (70%), while the lowest occurrence of quality flags of class 1 and 2 are observed at urban site 1 for all cases and at nighttime at urban site 2 (50%). There is a significant proportion of quality flags of class 4 reported for both Q_E and F_C particularly at urban sites 1 (>30% for Q_E and >28% F_C

for daytime cases) (Figure 6.25). The quality flags of class 4 correspond to conditions of well-developed turbulence but non-stationarity is a concern. In physical terms this is intuitive for urban locations where turbulence is relatively well-developed for all hours (i.e. particularly at nighttime) but where the sources of heat, H_2O and CO_2 within the local-scale area are more variable in time and space in comparison to a natural surfaces.

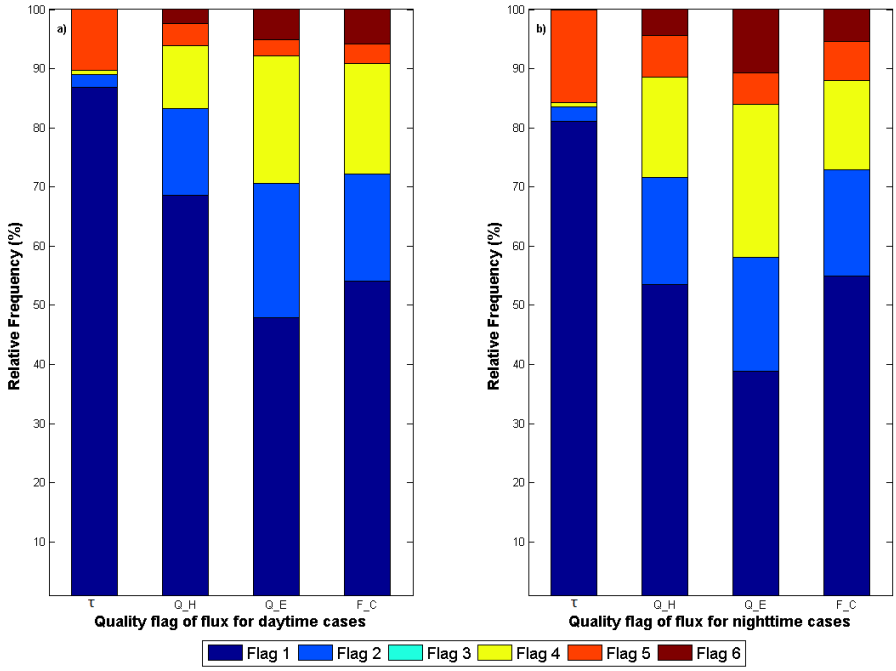

Figure 6.24 Relative frequency (%) of data quality flags for momentum (τ), sensible heat (Q_H), latent heat (Q_E) and carbon dioxide (F_C) according to Foken et al. (2004) at the suburban site for a) daytime cases and b) nighttime cases. Quality flag classes are shown in the legend.

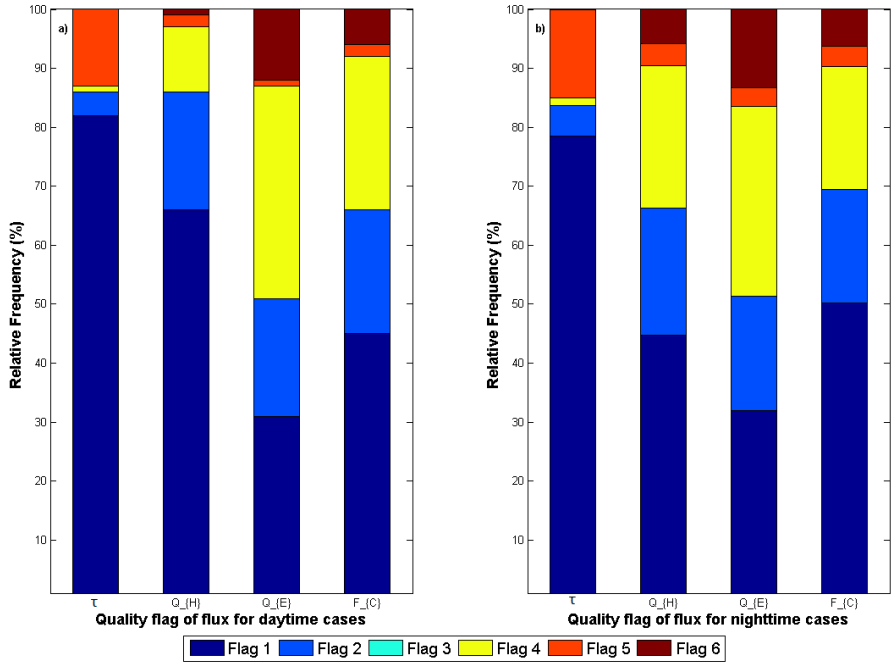

Figure 6.25 Same as Figure 6.24 for urban site 1.

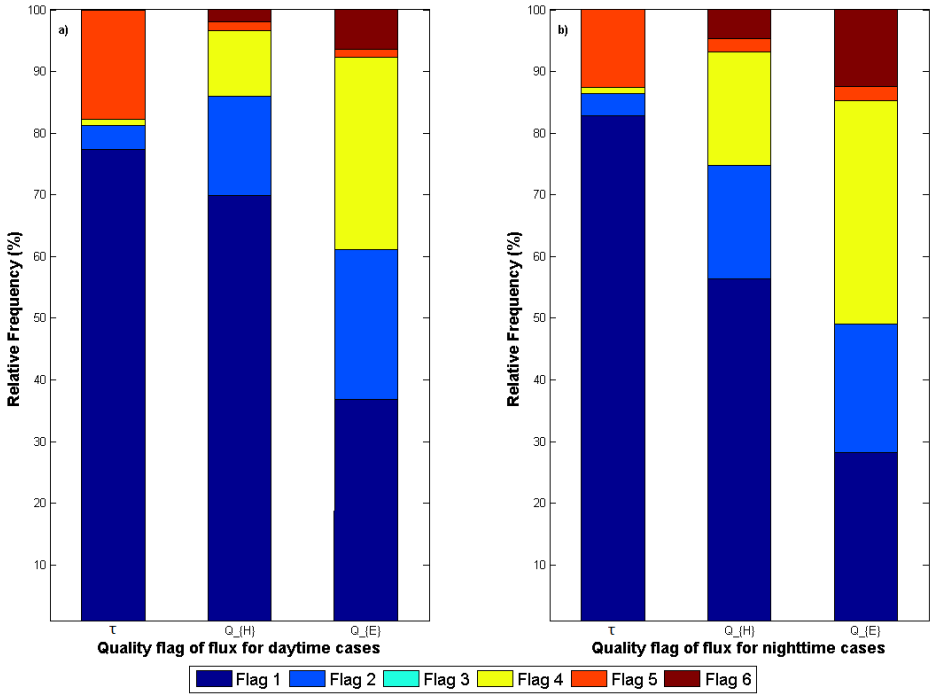

Figure 6.26 Same as Figure 6.24 for urban site 2.

6.6 Atmospheric stability

The dimensionless stability parameter (ζ) can be obtained from the measured fluxes,

$$\zeta = \frac{z'}{L}$$

Equation 6.1 Atmospheric stability parameter according to Kotthaus and Grimmond (2014a)

Where z' represents the effective height ($z' = z_m - z_d$, the difference between measurement height z_m and zero-plane displacement height z_d) and L is the Obukhov length; the sign of ζ is determined by the sign of the sensible heat flux (Q_H). Atmospheric stability can be described as the relative tendency of an air parcel to rise vertically and is an important indicator of the thermal structure of the atmospheric boundary layer. Atmospheric stability in this investigation has been classified into 4 categories, stable ($0.1 \leq \zeta$), neutral ($-0.1 \leq \zeta < 0.1$), unstable ($-0.5 \leq \zeta < -0.1$) and very unstable ($\zeta < -0.5$), and is examined for 2 time periods, April to September and October to March.

For Dublin neutral stratification is the dominant state; cloudy conditions attenuate surface heating and cooling thus weakening the development of temperature gradients and windy conditions will also serve to mix the temperature structure via mechanical convection. Neutral stratification accounts for 84, 65 and 61% of total cases at the

suburban site, urban site 1 and urban site 2 between April and September (Figure 6.27). In relation to nighttime cases neutral conditions still account for the majority of all cases and stable conditions, conducive to the formation of the stable nocturnal boundary layer, are rarely observed at both the suburban and urban locations (Figure 6.27). Similarly very unstable conditions rarely prevail and are more common at the suburban site (Figure 6.27).

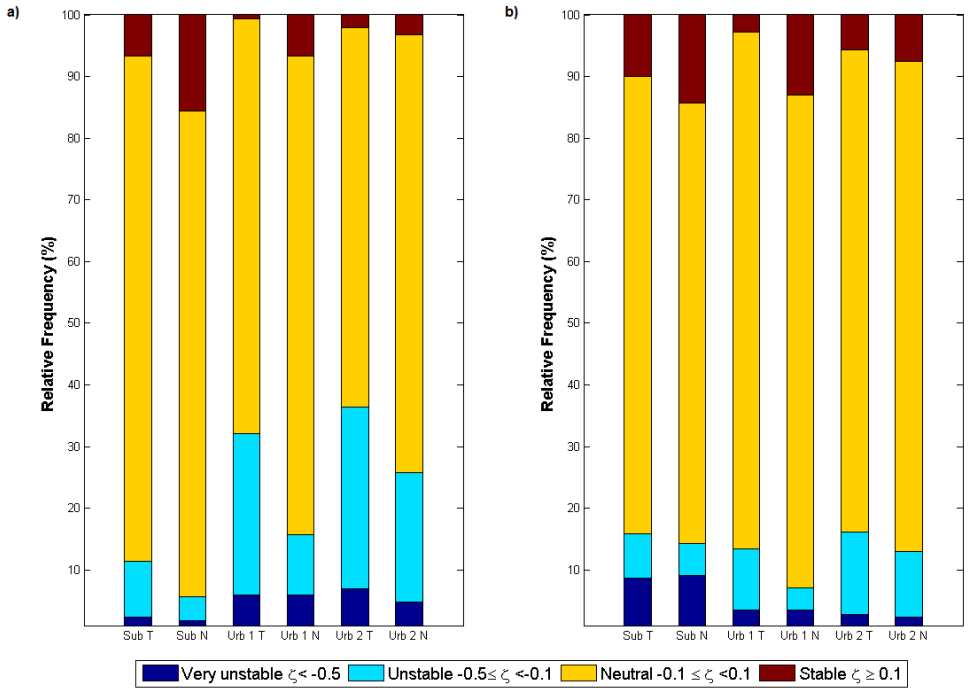

Figure 6.27 Relative frequency (%) of different atmospheric stabilities (ζ) for total or all hours (T) and night time hours (N) at the suburban site (Sub), urban site 1, (Urb 1) and urban site 2 (Urb 2) for months a) April to September and b) October to March. The stability classes are shown on the legend.

The diurnal variation of atmospheric stability is illustrated for individual EC sites in Figure 6.28, Figure 6.29 and Figure 6.30. Neutral conditions are dominant for all hours at all sites for both time periods. Exceptions to this are most pronounced at the urban sites where unstable and very unstable conditions account for between 40-50% of certain daytime hours (Figure 6.29a and Figure 6.30a). In addition, for night time cases the relative frequency of unstable conditions is more pronounced at the urban sites relative to the suburban site. This is a common observation whereby the release of heat from the urban fabric, increased surface roughness and anthropogenic heat sources serve to enhance turbulence throughout the night (Arnfield, 2003). Stably stratified conditions as a consequence are rarely observed and prevail most often at night time at the suburban location (Figure 6.28). Furthermore stable events are more frequent in months

October to March and in particular during the hours preceding sunrise; at these times the temperature of the near surface atmosphere may have cooled to temperatures below the atmosphere aloft conducive to a temperature inversion.

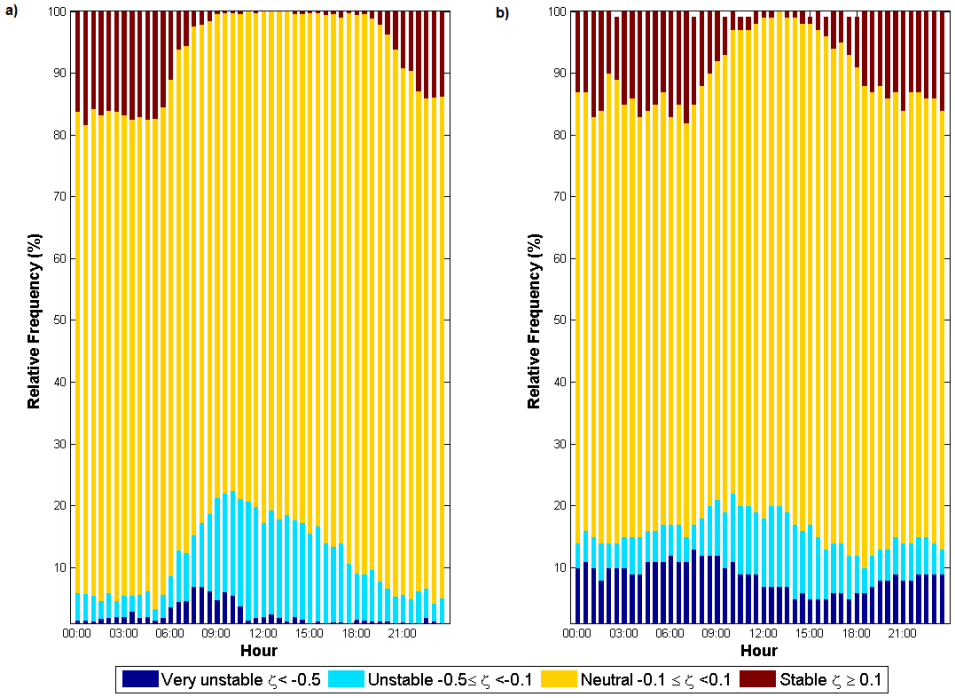

Figure 6.28 Relative frequency (%) of different atmospheric stabilities (ζ) throughout the day at the suburban site for months a) April to September and b) October to March. The stability classes are shown on the legend.

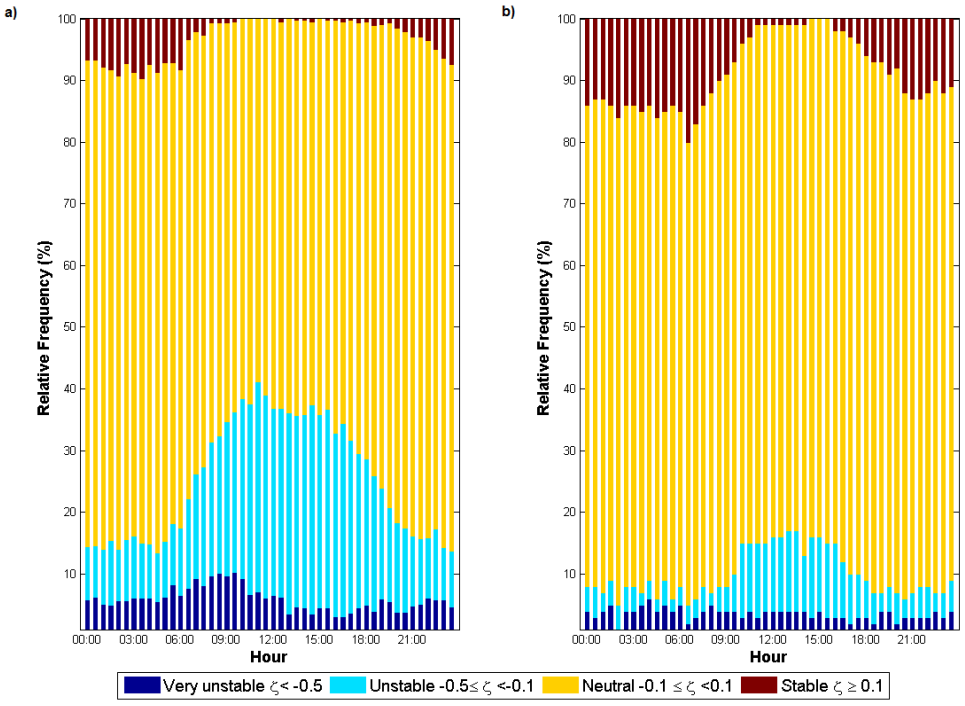

Figure 6.29 Same as Figure 6.28 for urban site 1.

With specific regard to urban site 2 there is much greater proportion of unstable conditions across April-September and October-March in relation to the two other sites (Figure 6.30). There is a corresponding decrease in the proportion of stable conditions, and this is consistent with the literature for dense city centre locations (e.g. Christen and Vogt, 2004. Increasingly dense urban locations are less likely to experience stable stratification due to increased convective turbulence from Q_F heat release and mechanically induced turbulence due to the urban form. Unstable stratification is most pronounced during the daytime hours and between Apr-sep, not surprising as they coincide with longer day length and hence increase access to solar radiation at the surface, leading to vertical temperature gradients inducing turbulence.

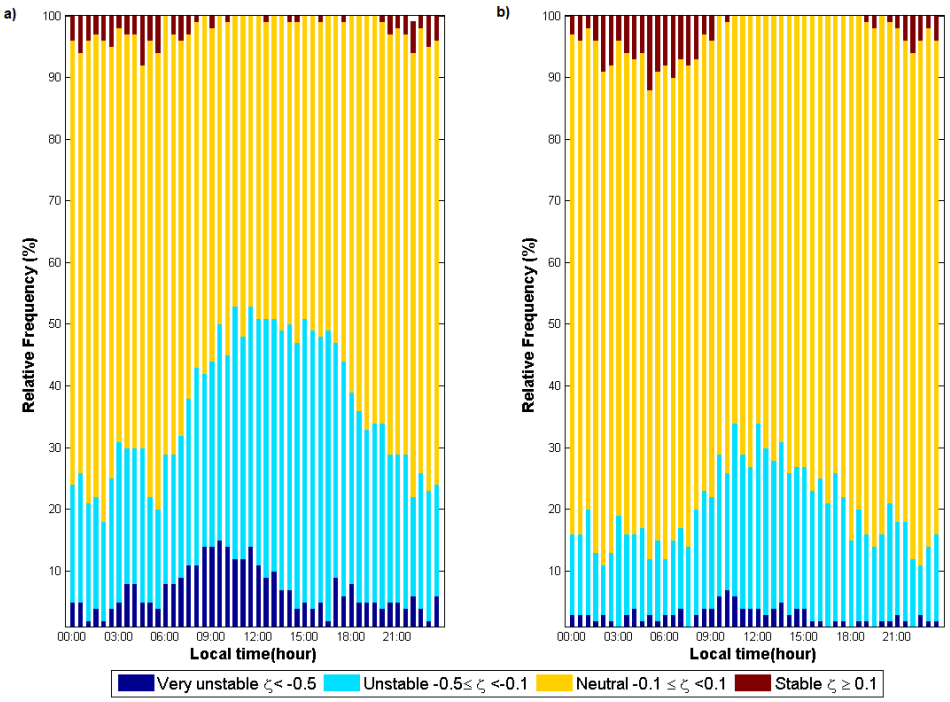

Figure 6.30 Same as Figure 6.28 for urban site 2.

Overall the frequency of unstable conditions increases for EC sites with increased impervious surface fraction, such as urban site 1 and 2, where the nature of the underlying surface typically encourages the channelling of heat into Q_H rather than Q_E. In unison with quality flag information presented earlier, analysis of the stability parameter provides confidence in night time flux estimates, in that for the majority of cases well-developed turbulent conditions prevail.

6.7 Turbulent flux footprint

Prior to an examination of the turbulent fluxes of Q_H, Q_E and F_C, the turbulent flux footprint is presented. The analytical footprint model according to Kormann and Meixner (2001) was employed within EddyPro software to determine an approximate footprint for evaluating the source contribution to the measured turbulent fluxes. This section will present upwind flux footprint distances relating to 1) the peak or maxima of the flux footprint function and 2) the upwind distance corresponding to the estimated 70% source area of the measured flux.

In strongly convective, unstable conditions, turbulence efficiently transports momentum and scalars vertically and the peak flux is yielded from between 0 to 100 metres upwind of the EC sensors at the suburban location (Figure 6.31b and d). With increasing stability however the upward motion is relatively reduced and the source area increases to distances greater than 200m upwind of the EC sensor (Figure 6.31c). As outlined earlier neutral conditions are dominant at the suburban location and the peak signal for all upwind directions is estimated to be within 50 m of the sensor location. With regard to the upwind distance representing 70% of the source area a similar relationship with stability is reported. Largest upwind distances are associated with stably stratified conditions (e.g. 600m in Figure 6.31g) whilst very unstable conditions reported upwind distances of less than 100m (Figure 6.31h).

In terms of urban sites 1 and 2 the increased measurement height (18 and 25m respectively) and displacement heights lead to increases in the upwind distances associated with the peak signal and 70% source area. That said the relationship with stability holds and largest upwind distances are associated with stable events (Figure 6.32 c and g and Figure 6.33 c and g). Urban site 2 reports considerably larger upwind distances for all stabilities; during neutral conditions the average upwind distance is between 400-800m (Figure 6.33).

The footprint model employed assumes horizontal homogeneity for z_d and z_0 in all directions surrounding the sensor location; as a result estimated flux footprint distances contain greater uncertainty due to the heterogeneity of surface roughness properties reported for the EC sites in Chapter 5. Uncertainties are likely to be reduced for the suburban site given that the displacement height and roughness length are relatively

consistent for all wind directions (Figure 5.12). Similarly at urban site 1, the displacement height and roughness length (~4 m and 0.5 m respectively) are relatively consistent for wind sectors from 30-270° and represent the wind sectors with greatest relative frequency (Figure 5.22 and Figure 6.3).

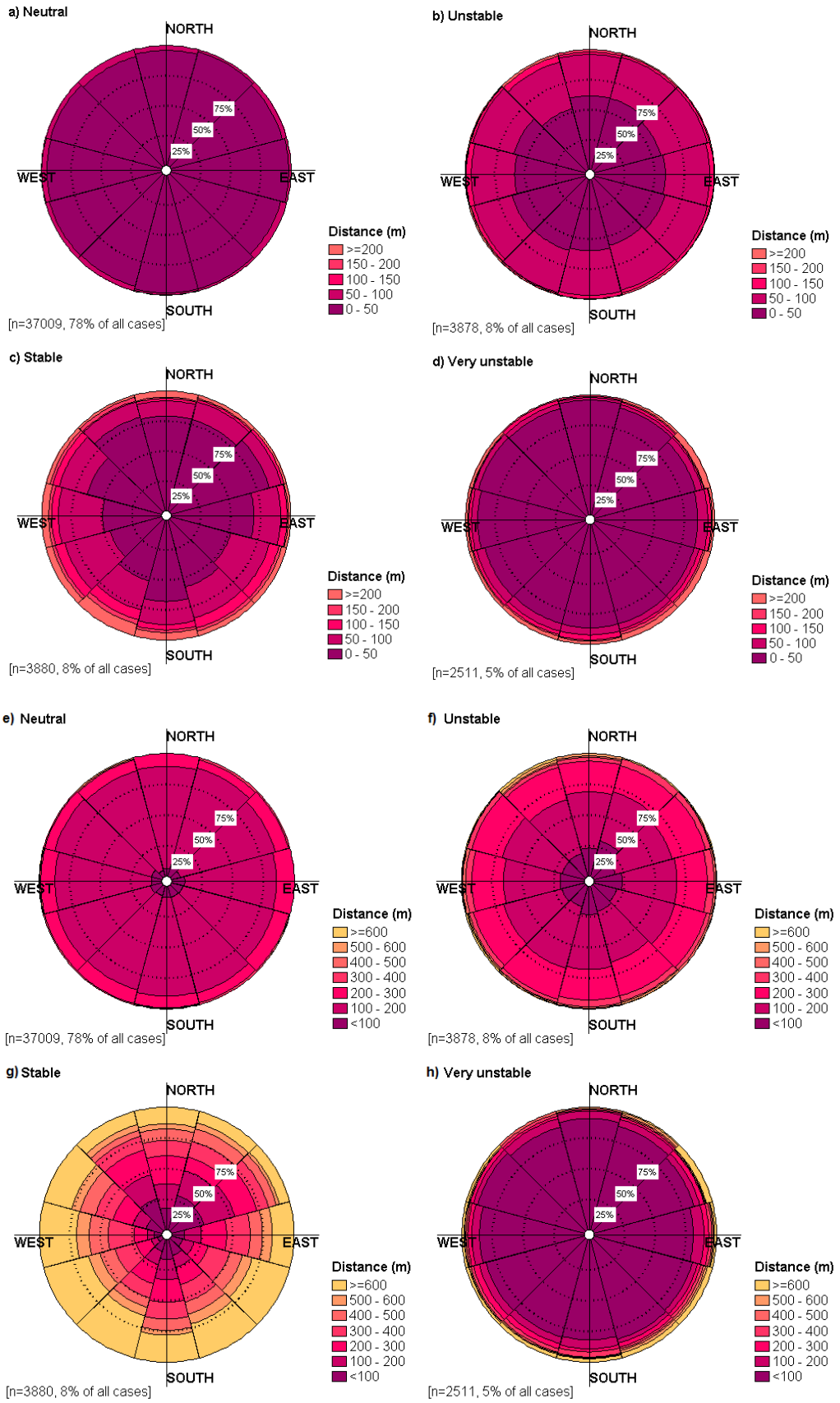

Figure 6.31 Flux footprint distance at the suburban site representing the peak flux footprint distance for a) neutral, b) unstable, c) stable and d) very unstable conditions, and the 70% upwind flux footprint distance for e) neutral, f) unstable, g) stable and h) very unstable conditions. The number of cases of each stability condition is given by the number of half hours (n) and the relative frequency (%). Distances are shown in the legend, note inter-site scale differences.

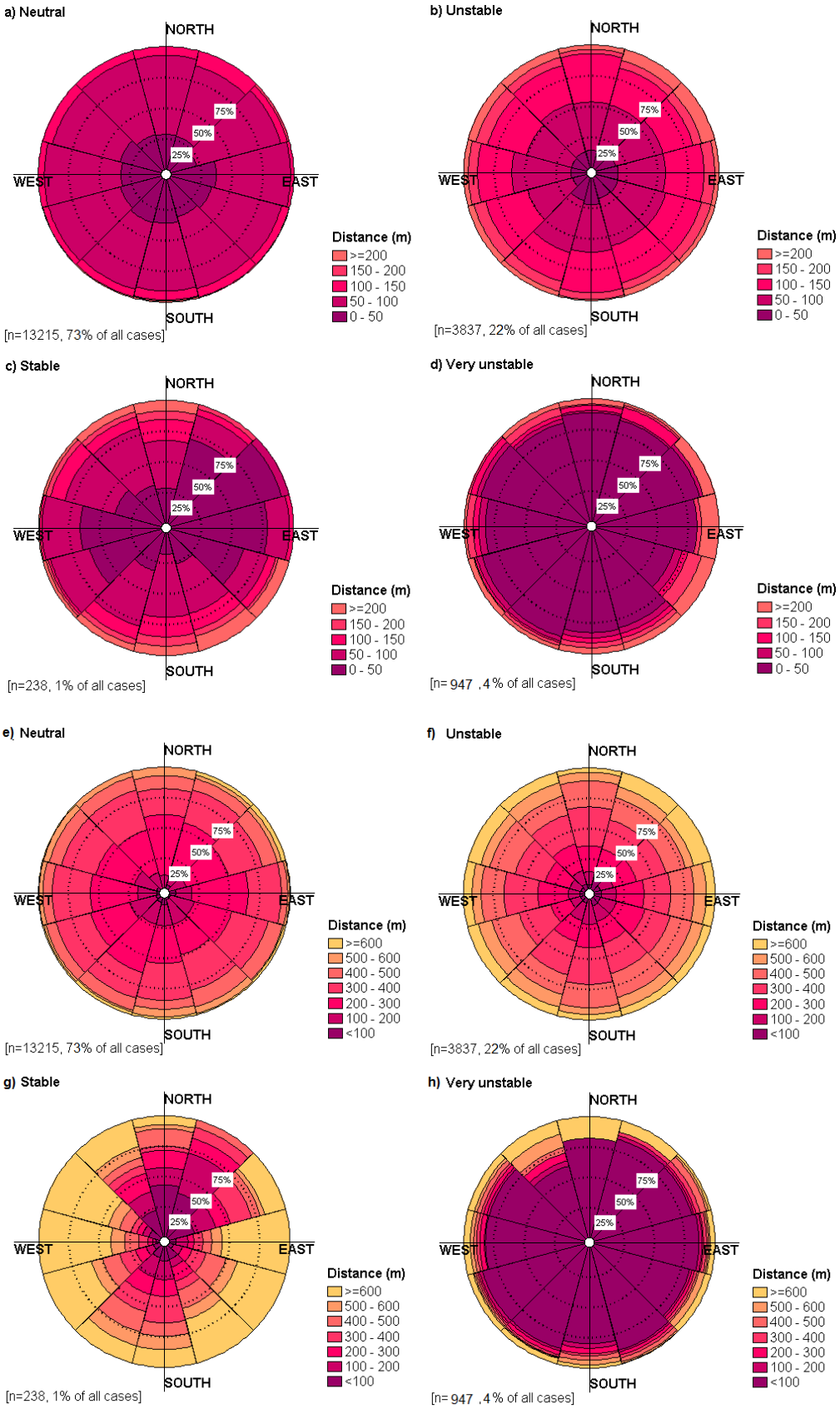

Figure 6.32 Same as Figure 6.31 for urban site 1.

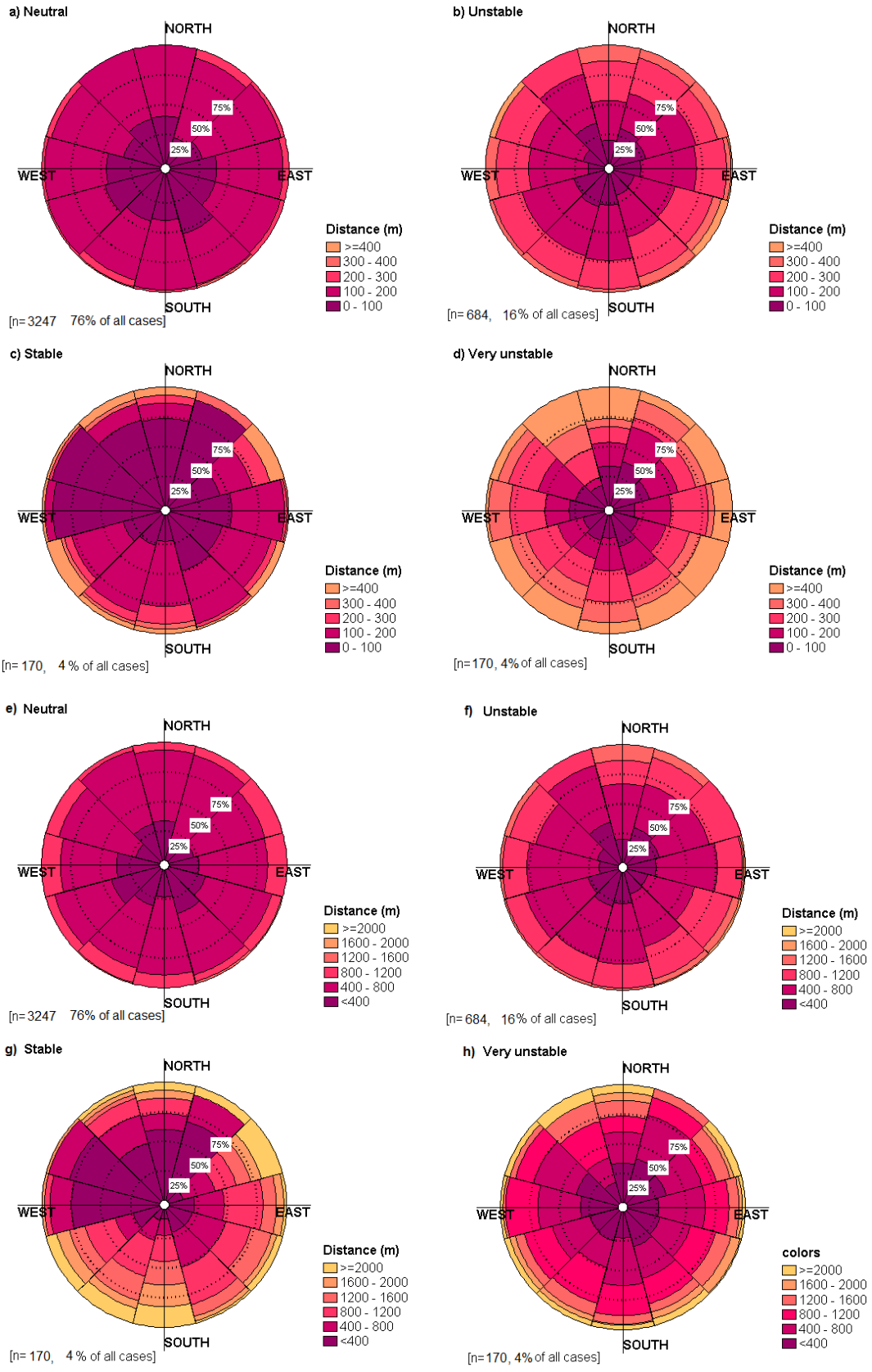

Figure 6.33 same as Figure 6.31 urban site 2 Distances are shown in the legend, note inter-site scale differences.

6.8 Turbulence, surface drag and flow distortion

The upwind surface of the EC tower, including the towers and instruments, may serve to alter or distort the approaching airflow ultimately affecting the estimated flux (Feigenwinter et al., 2012). As a result analysis of parameters, such as friction velocity (describing momentum transport), the drag coefficient and the angle of attack of the mean streamlines approaching the sonic anemometer, is useful in determining wind sectors experiencing distortion and increased roughness. In order to examine the surface roughness from the EC measurements the square root of the drag coefficient ($C_D^{0.5}$) is presented for 12 wind sectors. The angle of attack is used to determine flow distortion where data was binned into 12 wind sectors (each 30°); median values per 30° wind sector are presented for the suburban site, urban site 1 and urban site 2 in Figure 6.34, Figure 6.35 and Figure 6.36 respectively. The drag coefficient is derived from EC measurements,

$$C_D = \left(\frac{u_*}{U}\right)^2$$

Equation 6.2 The surface drag coefficient (Roth, 2000)

Where u_* is friction velocity and U (m s^{-1}) is the mean horizontal wind speed. The coefficient relates momentum transport to the mean wind speed; according to the logarithmic wind profile C_D decreases with increasing height above the roughness elements. Results from the 3 EC sites show that median values for $C_D^{0.5}$ vary according to wind sectors, increasing for wind sectors with relatively tall or isolated structures; increased values for $C_D^{0.5}$ (e.g. >0.20) however generally correspond to low frequency wind sectors, for example 330-30° (see Figure 6.34b, Figure 6.35b and Figure 6.36b). Mean $C_D^{0.5}$ for the sites are outlined in Table 6.3 and agree well with $C_D^{0.5}$ from an empirical expression derived from data in Roth (2000) (see equation 5 in Roth (2000)) where $C_D^{0.5}$ is expressed as a function of z/z_H (where z is the sensor height and z_H is the mean height of the roughness elements). Mean values of z_H outlined in Table 5.1 were employed for each EC site to determine z/z_H.

Table 6.3 Mean values of the drag coefficient derived from eddy covariance measurements and those derived from an empirical expression derived from data in Roth (2000) that is a function of z/z_H.

Parameter	Suburban site	Urban site 1	Urban site 2
z/z_H	1.5	2.25	2.89
$C_D^{0.5}$ (EC data)	0.15	0.16	0.10
$C_D^{0.5}$ (Roth, 2000)	0.17	0.13	0.11

The angle of the mean streamlines of the approaching wind is calculated using uncorrected and non-rotated wind speed measurements derived from the arctangent of observed u and vertical wind speed w (m s^{-1}). When the instantaneous wind vector is non-horizontal it has an angle of attack (ω) to the horizontal plane and the sonic anemometer,

$$\omega = \arctan \frac{w}{\sqrt{u^2 + v^2}},$$

Equation 6.3 The angle of attack (Nakai et al., 2006)

Any deviation of ω from zero indicates a local perturbation to the flow or a tilt of the instrument away from vertical. With regard to the suburban location the median angle of attack for all wind sectors is typically zero indicating limited perturbation to the flow due to surrounding roughness elements (Figure 6.34c). This wind sector corresponds to the location of an adjacent roof structure illustrated in

Figure 5.1 however wind from this direction is relatively infrequent (Figure 6.34d).

In relation to urban site 1 the angle of attack varies from 0° for all wind sectors but most significantly for sectors between 180-270°. In this direction the angle of attack is positive indicating upward deflection of the air flow, this reflects the tower position relative to the orientation and structure of the building illustrated in Figure 5.13. Wind approaching from 180-270° is forced upwards when it comes into contact with the L-shaped geometry of building. The building, unlike porous roughness elements, is impenetrable and acts as a bluff body to the airflow. That said, ω values of this magnitude can be corrected, and values greater than 5° are commonly reported in the literature (e.g. Barlow et al., 2011). Slightly negative ω values (e.g. -3°), indicating that the mean streamlines approach the sonic from above, are observed for wind sectors

corresponding to areas with relatively taller buildings (0-30°) in the immediate surrounds of the EC tower (Figure 5.29).

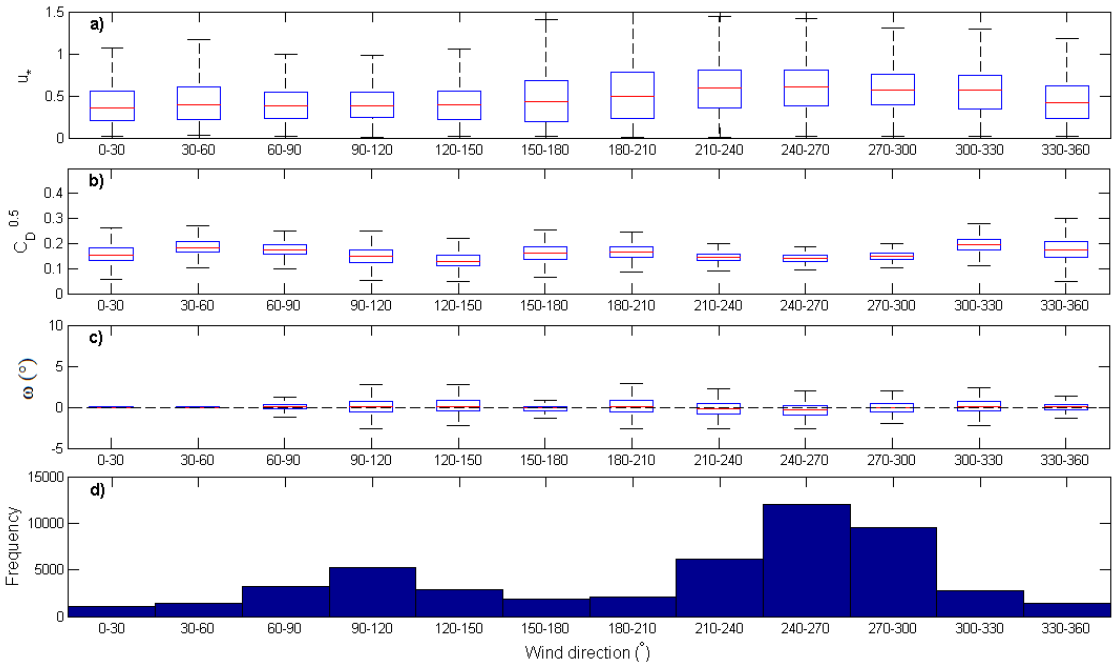

Figure 6.34 Box plots representing the median, upper quartile and lower quartile, the whisker length represents 1.5, points are determined as outliers if they are larger than $q_3 + w(q_3 - q_1)$ or smaller than $q_1 - w(q_3 - q_1)$, where q_1 and q_3 are the 25th and 75th percentiles, respectively - a) friction velocity(u_*), b) the square root of the drag coefficient ($C_D^{0.5}$) c) the angle of attack and d) histogram of the relative frequency of wind direction binned into 12 classes of 30 degrees; observations refer to those from the suburban site.

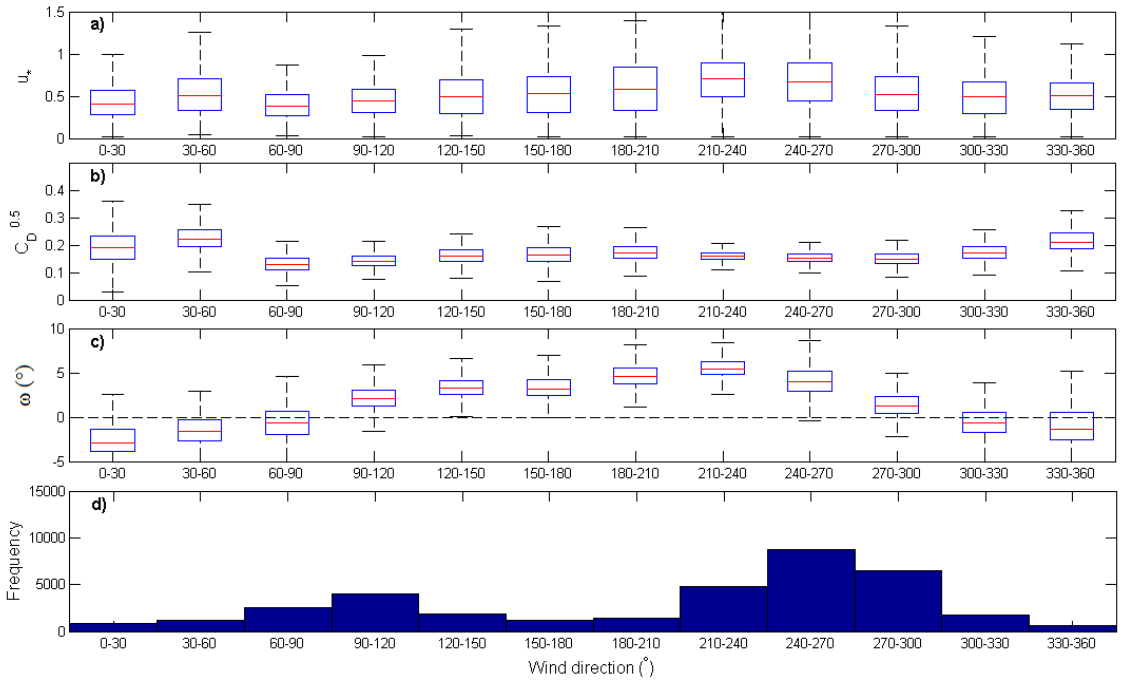

Figure 6.35 Same as Figure 6.34 for urban site 1.

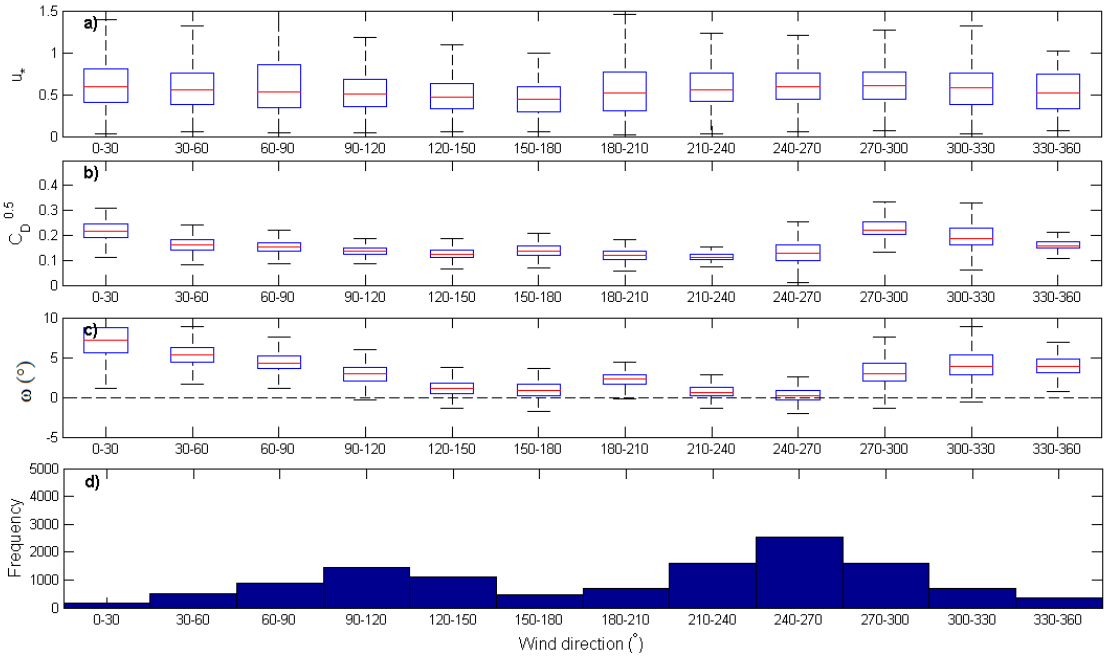

Figure 6.36 Same as Figure 6.34 for urban site 2 (Note scale difference on y-axis d relative to urban site 1 and the suburban site).

From this direction the mean streamlines come into equilibrium with the height of local roughness elements and fluxes calculated from this direction may not represent those in the ISL, but the RSL instead. Similar to above however the frequency of wind from this direction is relatively low. $C_D^{0.5}$ increases for wind sectors 0-30°, but more generally for 330-30° (Figure 6.35b). Airflow approaching from this general direction is likely to be affected by the additional storey on the urban site 1 office block (Figure 5.13).

The largest angles of attack, with a median value of 7°, observed at urban site 2 is from the northerly direction; reflecting the fact that the EC tower is located less than 2 m from the northern edge of the building (Figure 5.24). In this situation airflow stagnates upon encountering the building and is forced around the building (inducing increased surface drag) and upwards, leading to a high angle of attack (Figure 6.36). The complex geometry of the building, comprising of structures of different heights also results in high angles of attack from wind sectors with a high relative frequency of occurrence (e.g. 270-300°) (Figure 6.36). In relation to airflow approaching from wind sectors 120-270°, the angle of attack is significantly reduced indicating that the mean streamlines are parallel to the surface when approaching the sonic anemometer; the wind sectors in this regard correspond to residential areas where the building heights and surface roughness characteristics, particularly z_d, are relatively consistent (Figure 5.28 and Figure 5.30).

6.9 The surface energy budget

The surface energy budget (SEB) represents the dissipation of Q* into various surface heat fluxes within the local-scale system which give rise to distinctive local-scale climates. Radiant energy is spent via the turbulent fluxes of Q_E and Q_H and heat transferred to the substrate, ΔQ_S, which in urban areas may be soil, buildings, roofs and walls. Site-specific coefficients for the OHM will be outlined in section 6.9.1 before presenting the final, corrected and quality checked SEB fluxes for the observation period from April 2010 to December 2012. Firstly the SEB is presented according to monthly median diurnal values (and their associated upper and lower quartiles) to examine the temporal trends; daytime (nocturnal) values are classified as those with values of K↓ greater (less) than 3 Wm^{-2}. Secondly, the turbulent fluxes of Q_E and Q_H will be disaggregated into seasons and wind directions to examine their spatial variability. This spatial examination will serve to identify locations of potential bias where the surface cover and roughness for particular wind directions may differ from the local-scale neighbourhood. Finally the energy balance ratio (EBR) describing the ratio of the turbulent fluxes to available energy will be examined for all hours to determine closure of the SEB; this will be accompanied by ratios that describe the partitioning of Q* and the Bowen ratio.

6.9.1 *The storage heat flux coefficients*

Difficulties in direct measurement of ΔQ_S in an urban context have been outlined in section 3.6; as a result the magnitude of ΔQ_S in this study is estimated by two methods:

1. The residual approach in which it is obtained as the residual in the energy budget equation, that is: $\Delta Q_S \approx (Q^* + Q_F) - (Q_H + Q_E)$.
2. The Objective Hysteresis Model approach (Grimmond et al. (1991), see Equation 3.4) which is based on an empirical relationship between Q* and ΔQ_s, the nature of which is regulated by the surface cover.

With regard to the OHM approach, coefficients a_1, a_2 and a_3 are obtained from previous studies presented in Table 4 of Grimmond and Oke (1999b). A variety of coefficients are available from the published literature and their value is inherently related to the characteristics of the original study site from which they were empirically derived (Camuffo and Bernardi, 1982). The table has been modified in Table 6.4 to include the

surfaces and their coefficients relevant to the Dublin EC stations. In cases where more than one set of coefficients are available for a particular surface type an average of the coefficients was calculated (Table 6.5).

Table 6.4 Empirically derived coefficients used in the objective hysteresis model

Surface cover	Author	Regression coefficients		
1. Vegetation		a_1	a_2 (h)	a_3 (Wm^{-2})
Grass	(Doll et al., 1985)	0.32	0.54	-27.4
2. Rooftop				
Uppsala	(Taesler, 1980)	0.44	0.57	-28.9
Vancouver	(Yap, 1973)	0.17	0.10	-17
Kyoto	(Yoshida et al.,1990-91)	0.82	0.34	-55.7
	Average	0.4766	0.3366	-33.8
3.Paved/Impervious				
Concrete	(Doll et al., 1985)	0.81	0.48	-79.9
	(Asaeda et al., 1993)	0.85	0.32	-28.5
	Average	0.83	0.40	-54.2
Asphalt	(Narita et al., 1984)	0.36	0.23	-19.3
	(Asaeda et al.,1993)	0.64	0.32	-43.6
	(Anandakumar,1998)	0.82	0.68	-20.1
	Average	0.61	0.4100	-27.6
4. Water	(Souch et al., 1998)	0.5	0.21	-39.1

Table 6.5 Coefficients obtained for each Dublin EC station

Station	Surface	Weighting factor	Coefficients		
Suburban site			**a1**	**a2**	**a3**
	Greenspace	0.5	0.16	0.14	-9.60
	Rooftop	0.16	0.08	0.05	-5.42
	Concrete	0.23	0.19	0.09	-12.47
	Asphalt	0.11	0.07	0.05	-3.04
	Total	**1**	**0.50**	**0.33**	**-30.53**
Urban site 1			**a1**	**a2**	**a3**
	Greenspace	0.14	0.05	0.04	-2.69
	Rooftop	0.31	0.15	0.10	-10.50
	Concrete	0.36	0.30	0.14	-19.51
	Asphalt	0.18	0.11	0.07	-4.98
	Water	0.01	0.01	0.00	-0.39
	Total	**1**	**0.61**	**0.36**	**-38.07**
Urban site 2			**a1**	**a2**	**a3**
	Greenspace	0.17	0.05	0.05	-3.26
	Rooftop	0.38	0.18	0.13	-12.87
	Concrete	0.29	0.23	0.11	-15.18
	Asphalt	0.14	0.08	0.06	-3.87
	Water	0.02	0.01	0.00	-0.78
	Total	**1**	**0.56**	**0.35**	**-35.96**

The surface cover fractions presented in Chapter 5 are then used for the calculation of site-specific coefficients a_1, a_2 and a_3. Values of Q* are then employed according to Equation 3.4 to derive simultaneous estimates of $\Delta Q_{S\ OHM}$.

6.9.2 *The surface energy budget: temporal trends*

The SEB fluxes observed from April to December 2010 at the suburban and urban site 1 are illustrated in Figure 6.37 and Figure 6.38 respectively; values reported represent the monthly median and upper and lower quartile values. Similarly the SEB is presented for all months in 2011 and 2012 for the suburban site and urban site 1 (Figure 6.37, Figure 6.38, Figure 6.39 and Figure 6.40). SEB fluxes from urban site 2 supplement the 2012 dataset (e.g. August to December 2012 in Figure 6.42) following the cessation of urban site 1 in July 2012.

Suburban site and urban site 1: 2010

The magnitude of each flux varies in response to incoming solar radiation. Largest fluxes are observed around solar noon in months April, May, June and July. Q* is the largest flux for all months followed by Q_H and ΔQ_S which are of similar magnitude throughout the day. For both the urban and suburban site Q_E is the smallest daytime flux in the SEB, for example in April 2010 the median magnitude of Q_E relative to Q_H at local solar noon is approximately 50 versus 200 W m^{-2} at the suburban site and 25 versus 200 W m^{-2} at the urban site 1 (Figure 6.37 and Figure 6.38). Nocturnal negative values are more pronounced for ΔQ_S in comparison to the Q_H (Figure 6.37b and d).The ΔQ_S term is a significant component of the SEB at both EC sites. The median and upper and lower quartiles of the energy balance residual (RES) are shown (in green) relative to the median modelled heat storage flux calculated using the OHM ($\Delta Q_{S\ OHM}$ in black). The data shows good agreement for months with higher energy inputs via Q*; $\Delta Q_{S\ OHM}$ typically lies within the upper and lower quartiles pertaining to RES. In the winter months, for example December 2010, the OHM typically underestimates the flux into and out of the substrate; modelled median $\Delta Q_{S\ OHM}$ lies at the lower bounds of RES (shown in Figure 6.37d and Figure 6.38d). This pattern is repeated for winter months December, January and February of the following years shown in Figures 6.39-6.42.

In relation to Q_H, peak values are observed around local solar noon each month. Values are significantly reduced in winter in comparison to previous months, for example, 50 versus 300 W m^{-2} at urban site 1 in December and July 2010 respectively.

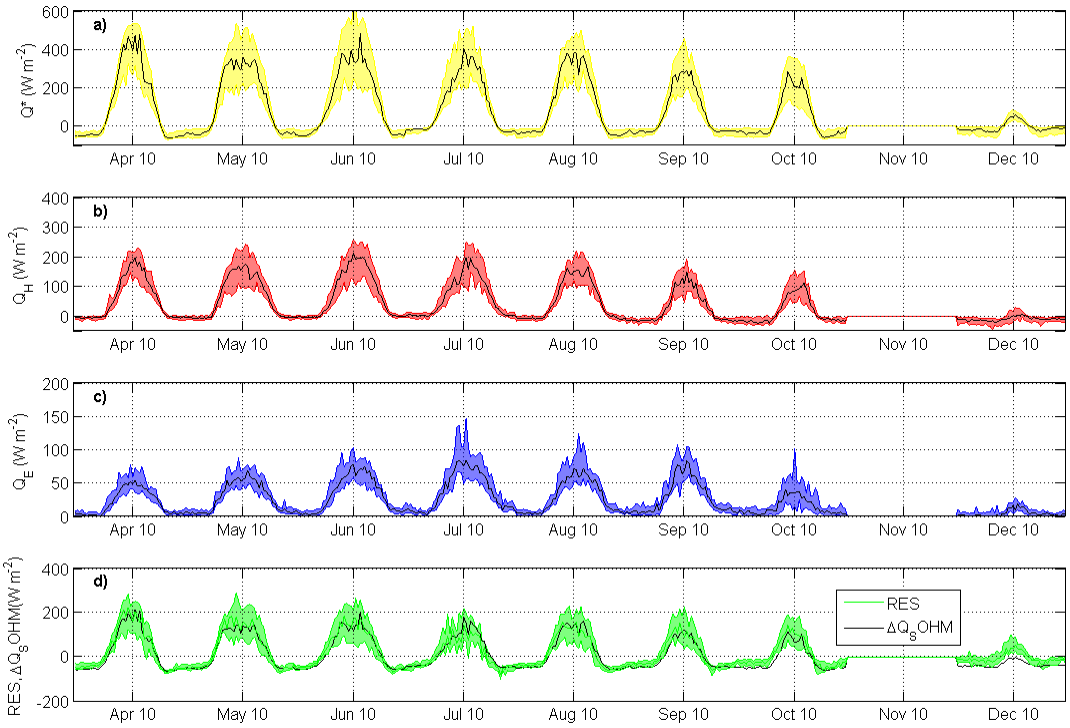

Figure 6.37 Surface energy budget for 2010 for the suburban location, a) Q*, b) Q_H, c) Q_E and d) the residual of the energy balance equation in addition to the modelled storage heat flux term, ΔQ_S $_{OHM}$. Please note scale difference on the y-axis. The black lines represent monthly median diurnal values bounded by upper and lower quartile values in colour.

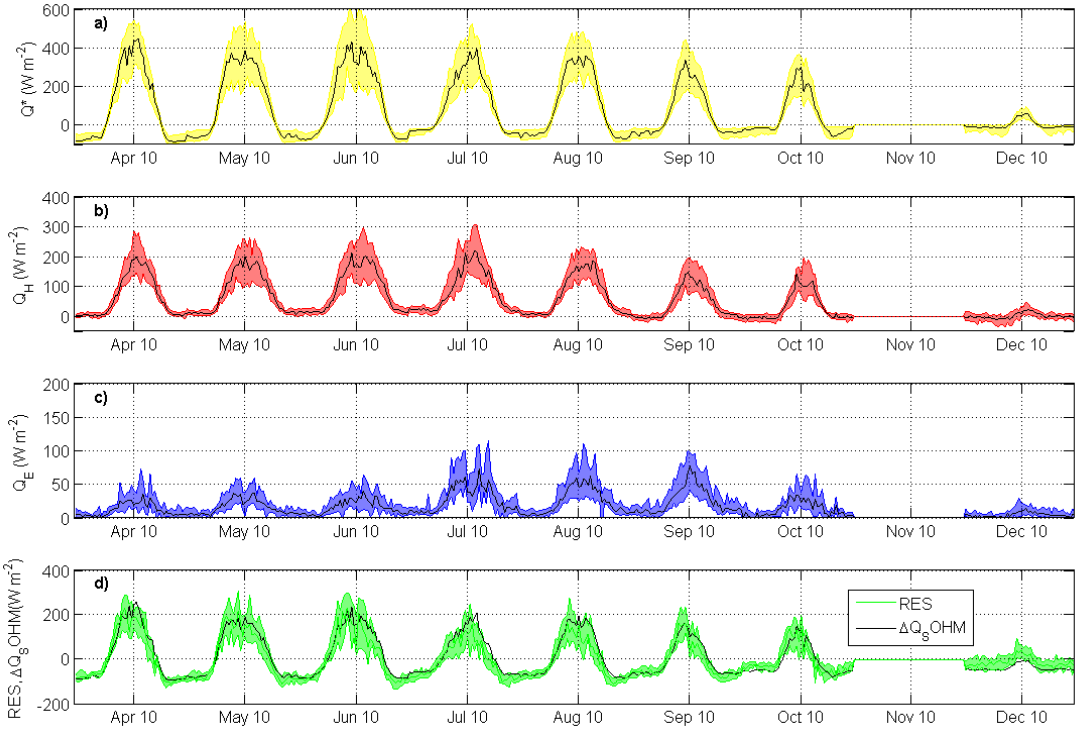

Figure 6.38 Same as Figure 6.37 for 2010 at the urban site 1.

In addition the upper quartile values reported at urban site 1 consistently exceed those of the suburban site. In spring and summer upper quartile values of 300 W m^{-2} are

observed at local solar noon at urban site 1; corresponding values rarely exceed 220 W m^{-2} at the suburban site (Figure 6.37b and Figure 6.38b).

Of all the SEB fluxes, Q_E is the only flux to remain positive in magnitude throughout the diurnal cycle each month and hence throughout the year (Figure 6.37 and Figure 6.38). The monthly diurnal profiles of Q_E peak around local solar noon at both sites, varying in magnitude from approximately 15 to 75 W m^{-2} in December and September 2010. Peak median values rarely exceed 75W m^{-2}; high upper quartile values like that observed at the suburban site in July 2010 (e.g. 150 W m^{-2}) correspond to months that received above normal precipitation (e.g. July 2010, monthly precipitation was 200% of LTA recorded at Merrion Square Met Éireann station, see Figure 6.1). This is less evident at the urban site where the potential for evaporation is reduced as rainfall does not remain as long at the surface due to a higher fraction of impervious surface fraction (Table 5.1). Inter-site differences in the median diurnal values of Q_E are less evident in months October and December 2010 when the vegetation density, serving to increase the surface area for evaporation at the suburban site, is reduced.

Suburban site and urban site 1: 2011

Similar to 2010 the monthly diurnal profiles of Q* in 2011 increase in unison with solar inputs via K↓ however greatest median values at local solar noon are observed in April 2011 (Figure 6.39 and Figure 6.40). This trend was observed at both sites and is related to the prevailing synoptic conditions in April relative to June 2011. April experienced below normal monthly precipitation, 19mm (<25% of the monthly rainfall LTA observed at the Merrion Square Met Éireann station, see Figure 6.1), indicating the prevalence of clear sky conditions and maximum receipt of incoming K↓ in comparison to June 2011; weather at this time was influenced by slow moving Atlantic depressions that gave rise to light but consistent rainfall, and indicates relatively persistent cloud cover thereby reducing K↓ (e.g. monthly precipitation was approximately 70mm or 120% of the LTA monthly rainfall observed at Merrion Square Met Éireann station).

With regard to Q_H the relative enhancement of nighttime fluxes at urban site 1 becomes more evident when examining a 12-month dataset. Higher nocturnal fluxes are particularly evident in spring and summer; the upper quartile and median values are exclusively positive throughout the night from March until August.

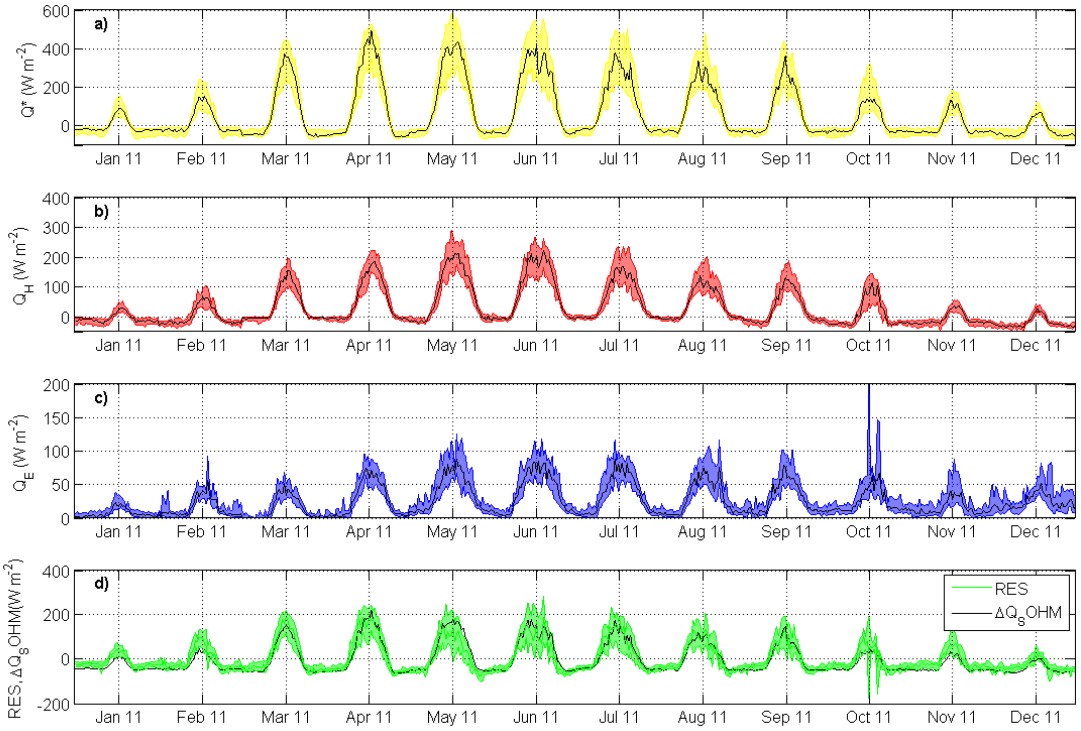

Figure 6.39 Same as Figure 6.37 for 2011 at the suburban site.

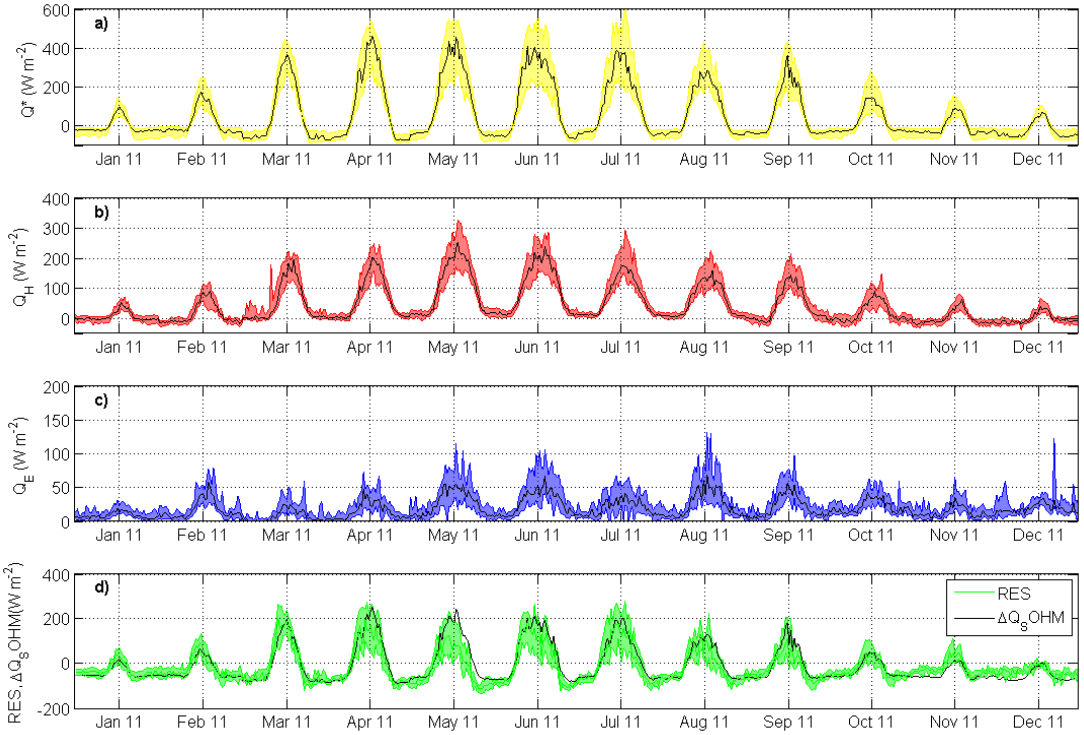

Figure 6.40 Same as Figure 6.37 for 2011 at urban site 1.

In the winter months negative nighttime values are reported but they are greater (less negative) than their suburban counterpart (Figure 6.40 and Figure 6.41). Enhanced noctural Q_H particularly in summer gives rise to the commonly observed nocturnal urban heat island (UHI) effect where urban areas typically report higher nighttime air temperatures than their suburban and rural counterparts. The relative increase in nocturnal Q_H is supported by the increased emission of nocturnal L↑ at urban site 1 in comparison to the suburban site (Figure 6.22).

Similar to 2010 median values representing Q_E reveal the greatest differences across the two EC sites. Again the magnitude of the difference is greatest for months when trees are in leaf (e.g. late April to September); differences in the peak median diurnal values between the suburban site and urban site 1 are 40 and 75 W m^{-2} in July 2011. In winter months the daytime median values observed are more consistent across the sites. Overall Q_E is more variable, the upper quartile values in particular display sharp peaks, deviating from the median value significantly (e.g. October 2011 in Figure 6.39). The increased spread in Q_E indicates the relative reliance of the flux magnitude on moisture availability which is intermittent and depends on interception of rainfall at the surface. This trend is unlike Q_H where when Q* permits the flux will increase.

Suburban site and both urban sites: 2012

Key differences observed for the SEB in 2012 at the suburban site include 1) increased Q_E in January and June in comparison to previous years, these months received 100 and over 300% of the LTA monthly rainfall observed at the Merrion Square Met Éireann station respectively (Figure 6.1), and 2) reduced median sensible heat fluxes (e.g. May, June and July) coincident with a relatively wet summer. By comparison urban site 1 observed reduced Q_E in June, and Q_H in May, June and July reported values similar to those in previous years. Despite the wet summer the urban surface was efficient in removing rainfall from the surface; as a consequence the available energy was preferentially channelled into 1) Q_H heating the near surface atmosphere and 2) the urban surbstrate via ΔQ_S (Figure 6.42).

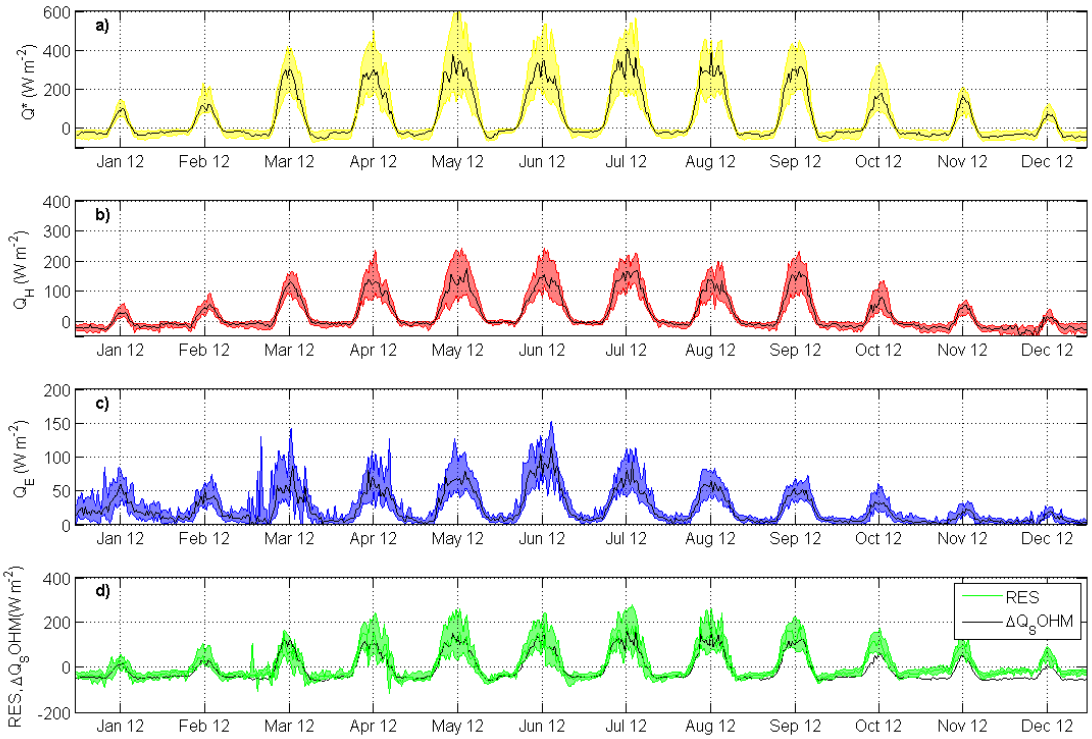

Figure 6.41 Same as Figure 6.37 for 2012 for at the suburban site.

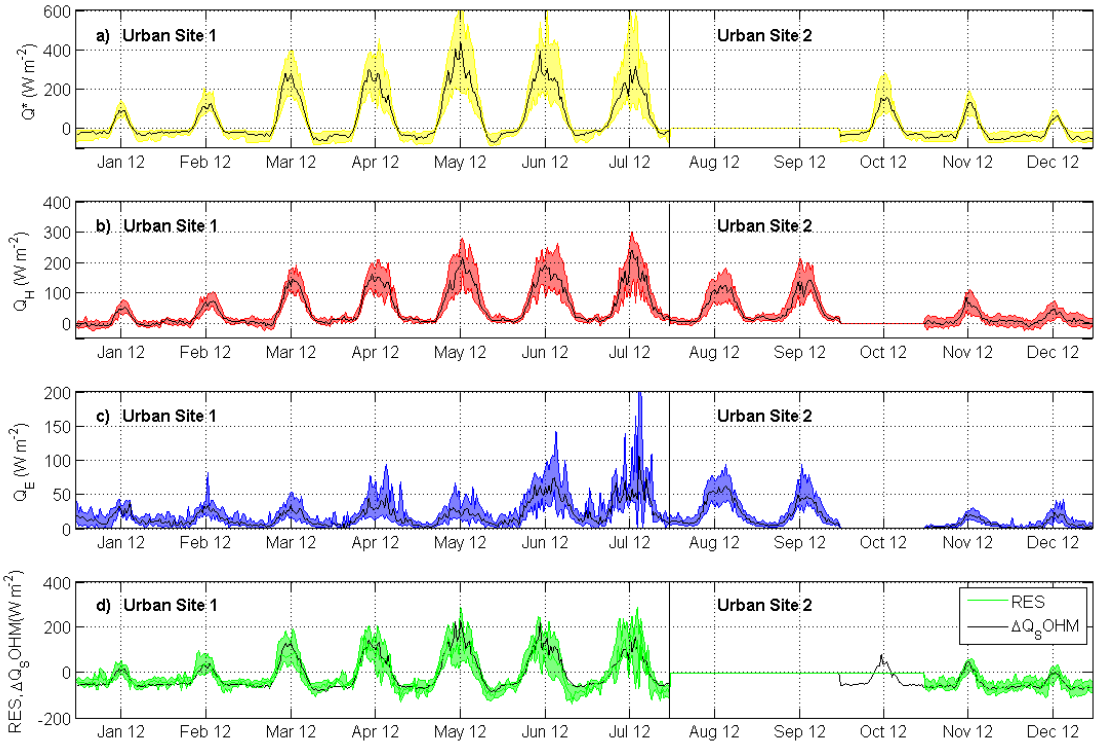

Figure 6.42 Same as Figure 6.37 for 2012 at urban site 1 and 2. Fluxes of Q_E for July 2012 are more variable, data availability in this regard consisted of only 10 days before urban site 1 ceased operation.

In August 2012 observations of the turbulent heat fluxes began at urban site 2. Throughout August and September 2012 peak median values across the suburban site

and urban site 2 are very similar in magnitude, particularly for $Q_{E,}$ such similarities were not observed relative to urban site 1. With regard to $Q_{H,}$ November and December 2012 report higher values at urban site 2, median diurnal peak values reported in December for example are 50 W m^{-2} relative to 16 W m^{-2} observed at the suburban site. Nocturnal values are also consistently greater than those observed at the suburban site which is not surprising given the increased density of urban site 2 (Figure 6.41b and Figure 6.42b).

6.9.3 *Inter-site comparison of turbulent heat fluxes*

The following represents the magnitude of difference in Q_H and Q_E in units of W m^{-2} between the suburban site and urban site 1. Median diurnal values of Q_H and Q_E are aggregated into seasons and the inter-site differences are based on a total of 27 months of quality checked turbulent fluxes. The results are presented in Figure 6.43 and Figure 6.44 where values reported greater than zero indicate times when the magnitude of the flux is greater at the suburban location relative to urban site 1 and vice versa.

With regard to the Q_E inter-site differences were observed in the spring when the flux is almost exclusively greater at the suburban site relative to urban site 1; throughout the day the absolute difference is significant, exceeding 30 W m^{-2} (Figure 6.43a). With regard to summer months the absolute difference is similar in magnitude; largest deviation occurs in unison with largest energy inputs via Q* around local solar noon. Nocturnal differences exhibit a reverse trend where Q_E is slightly greater at urban site 1; likely a result of greater unstable atmospheric conditions observed at urban site 1 indicative of enhanced turbulence (Figure 6.43b). In response to decreased day length and available energy the relative increase in Q_E at the suburban site is reduced in autumn and winter (differences range from 0-10 W m^{-2}), nevertheless the diurnal trend is similar (Figure 6.43c and d). Nocturnal differences are also reduced in response to increasingly stable night time conditions at both sites (see Figure 6.27b).

Inter-site differences relating to Q_H are typically reversed; the suburban site displays reduced fluxes in comparison to urban site 1 (Figure 6.44a, b and c). A similar situation is observed in each season, the timing of which changes in response to day length. Typically differences throughout the night and in the morning range between 10 to 15 W m^{-2}, the suburban site displays a relative increase mid-morning ranging from

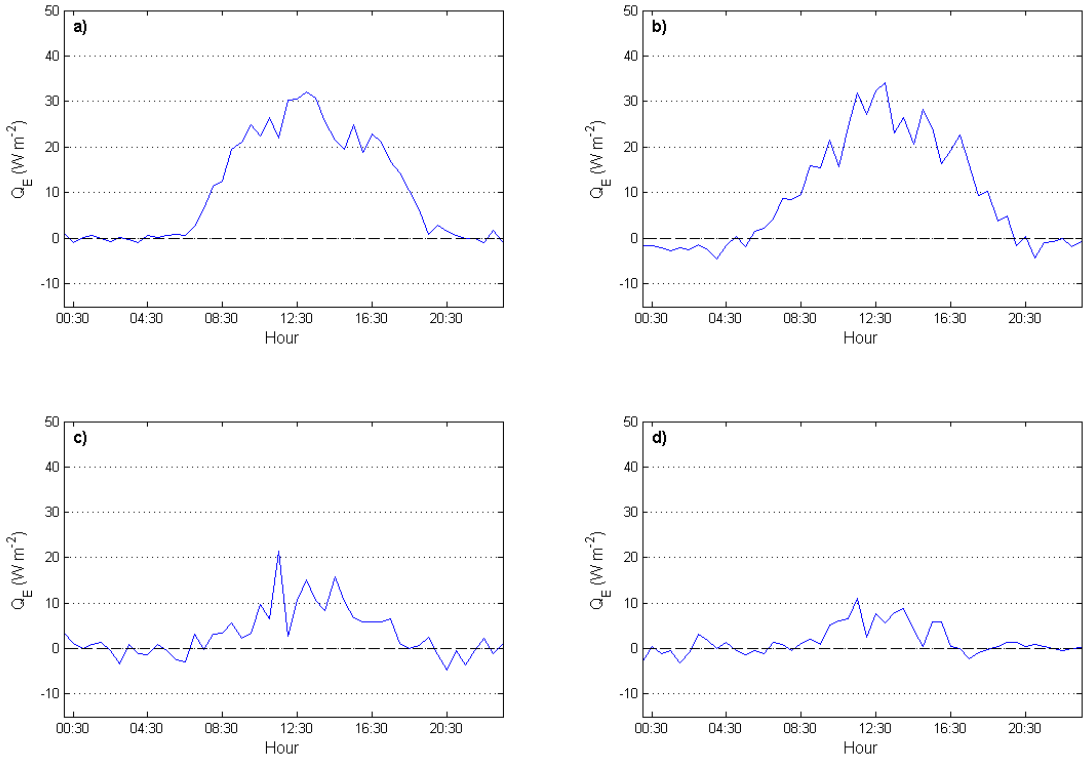

Figure 6.43 Median diurnal difference in the turbulent latent heat flux between the suburban site and urban site 1 (e.g. $Q_{E\ SUB} - Q_{E\ URB}$) for a) spring, b) summer, c) autumn and d) winter.

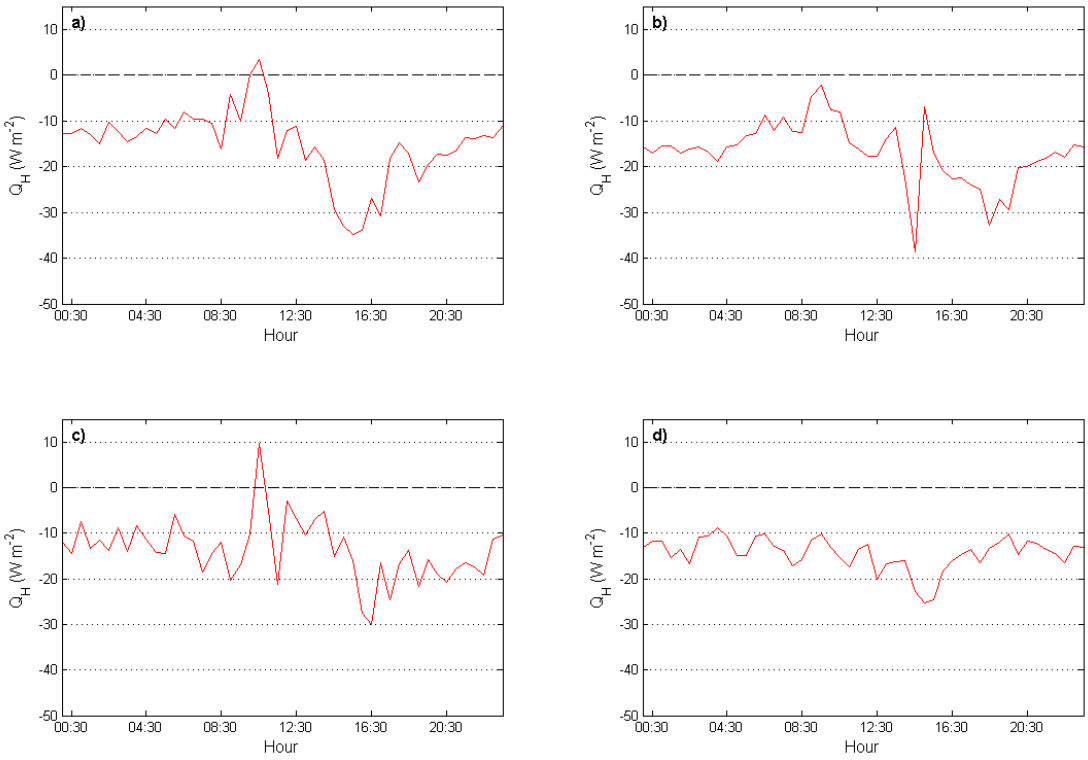

Figure 6.44 Median diurnal difference in the turbulent sensible heat flux between the suburban site and urban site 1 (e.g. $Q_{H\ SUB} - Q_{H\ URB}$) for a) spring, b) summer, c) autumn and d) winter.

09:30hrs in summer to 10:30hrs in spring and autumn (There is no observed increase in winter). Following the mid-morning peak the relative difference in Q_H increases in the afternoon at urban site 1 peaking at +38 W m^{-2} in summer; relative differences in winter are relatively reduced but are nevertheless significant (+25 W m^{-2}) (Figure 6.44). Overall Q_H is almost exclusively greater at urban site 1, indicating warmer near surface air temperatures, especially prior to sunset where observed differences are the greatest. On the other hand the suburban site is relatively cooler during the daytime as a result of increased evaporative cooling via Q_E.

6.9.4 *The turbulent heat fluxes: spatial and directional variability*

This section investigates the spatial variability of Q_E and Q_H observed at the suburban site and urban site 1. The fluxes of Q_E and Q_H are normalised according to incoming radiation (e.g. $Q\downarrow=K\downarrow+L\downarrow$) this method removes the surface attributes from the denominator. The ratios of $Q_E/Q\downarrow$ and $Q_H/Q\downarrow$ when presented according to wind sectors allow for the directional variability of fluxes to be investigated. Box plots representing the median, upper and lower quartile ratios of $Q_E/Q\downarrow$ and $Q_H/Q\downarrow$ are presented for 30° wind sectors and correspond to daytime hours ($K\downarrow$ > 3 W m^{-2}) for spring, summer, autumn and winter (see for example Figure 6.45). Similar to findings reported in the previous section inter-site differences in the ratios of $Q_E/Q\downarrow$ and $Q_H/Q\downarrow$ reveal the influence of surface cover on Q_E and Q_H; in general suburban site ratios of $Q_E/Q\downarrow$ are greater due to a larger vegetated surface fraction which promotes evaporation through transpiration. Conversely the urban site with a higher impervious surface fraction reports increased $Q_H/Q\downarrow$ particularly for spring, summer and autumn (Figure 6.45, Figure 6.46, Figure 6.47 and Figure 6.48).

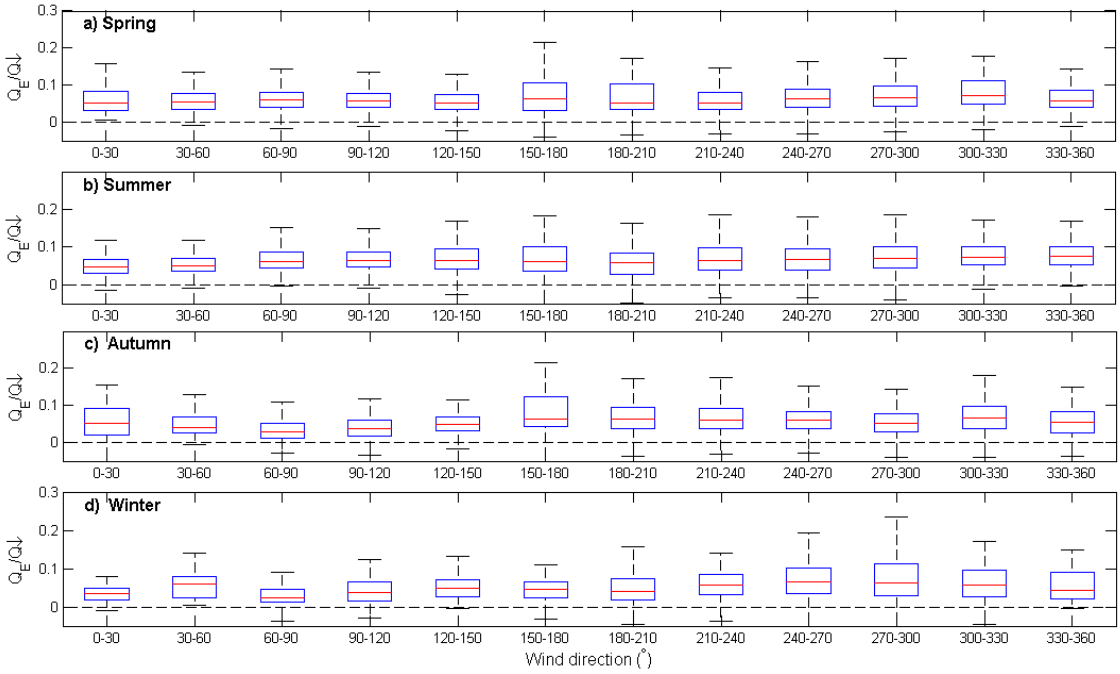

Figure 6.45 Seasonal boxplots of daytime (K↓ >3 Wm^{-2}) Q_E normalised by incoming radiation (Q↓) and wind direction for a) spring, b) summer, c) autumn and d) winter for the suburban site.

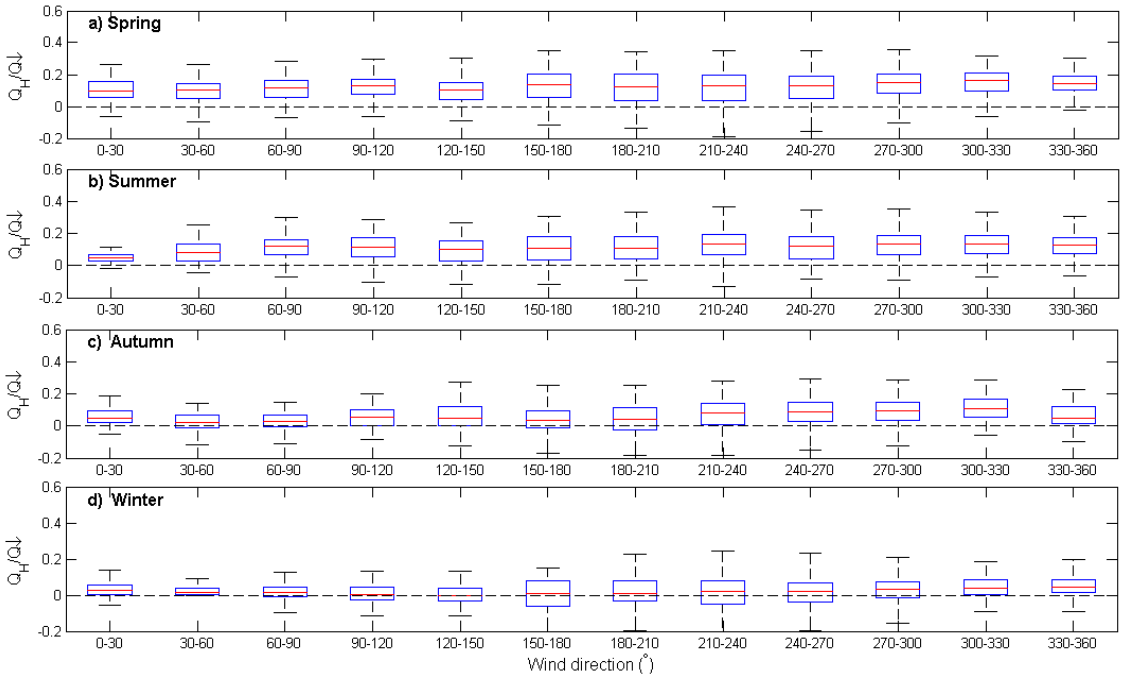

Figure 6.46 Same as Figure 6.45 for Q_H normalised by incoming radiation (Q↓) for the suburban site.

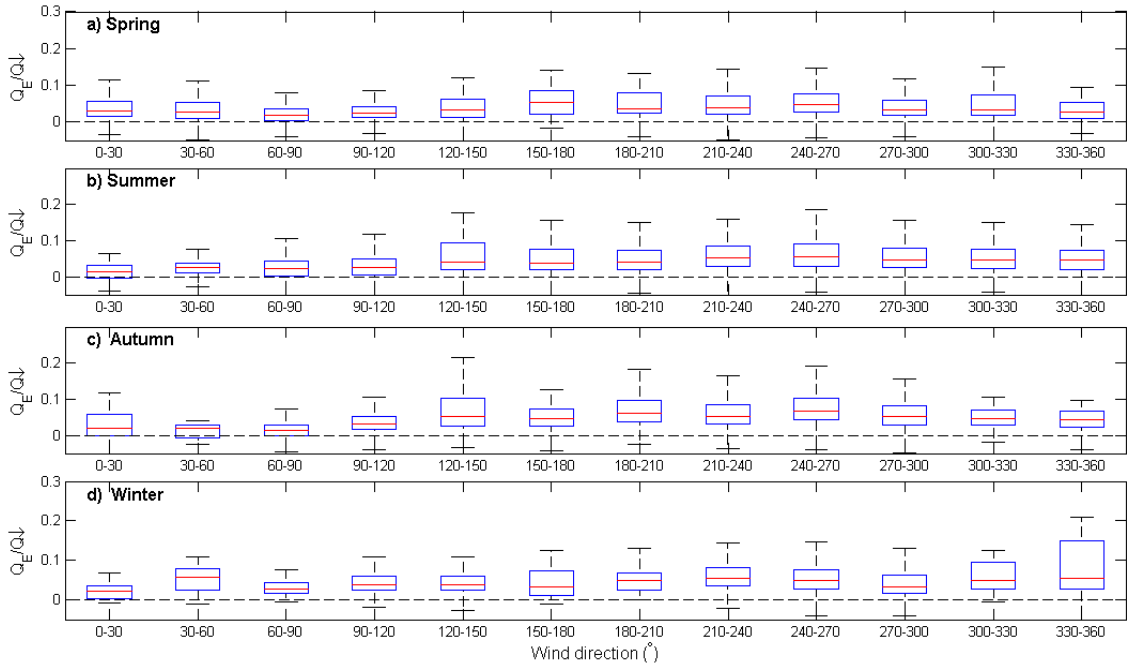

Figure 6.47 Same as Figure 6.45 seasonal Q_E normalised by incoming radiation (Q↓) for urban site 1.

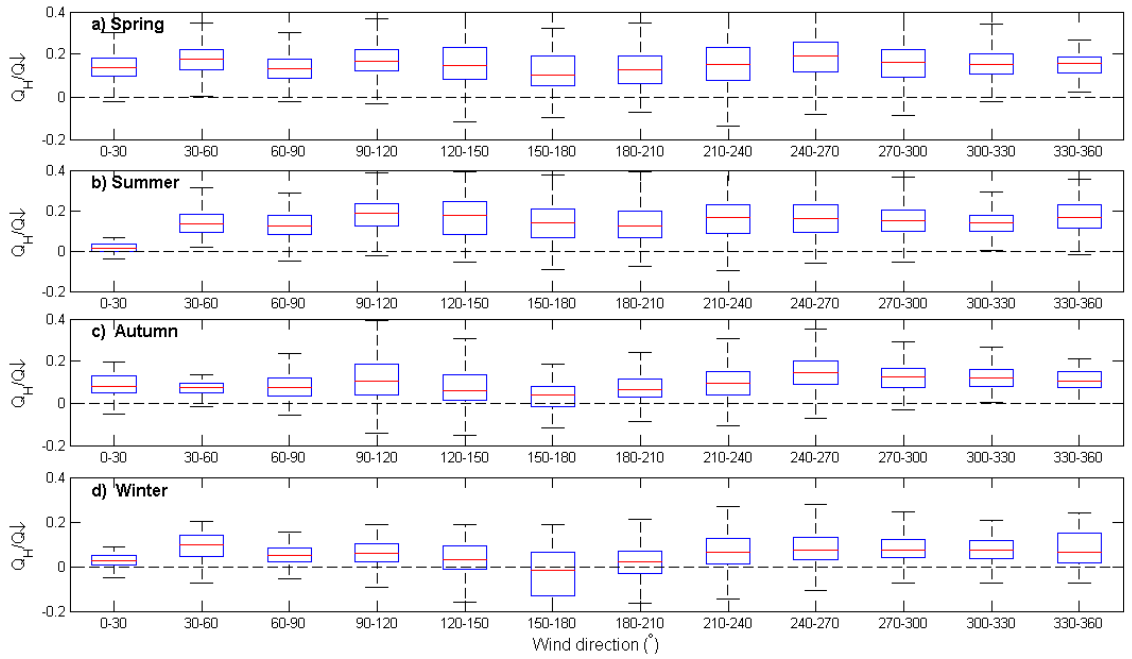

Figure 6.48 Same as Figure 6.45 seasonal Q_H normalised by incoming radiation (Q↓) for urban site 1.

In general there is little evidence of intra-site variations in $Q_E/Q\downarrow$ and $Q_H/Q\downarrow$ for different wind sectors at the suburban site. Noteworthy deviations refer to wind sector 150-180° for $Q_E/Q\downarrow$. In this direction the portion of impervious surface is >55% relative to the neighbourhood average of 34% and relates to the location of the school entrance, local shops and the car park (Figure 5.16c and Figure 5.17). The variability of $Q_E/Q\downarrow$ for this sector is large and may be a combined result of 1) large Q_E observed following

rainfall events when water remains at the surface for evaporation and 2) negligible Q_E in the absence of moisture when the surface is dry. More generally $Q_E/Q\downarrow$ corresponding to southwest-westerly air flow, between 180-300° is slightly larger, particularly in winter (Figure 6.45d). This increase is likely to be associated with higher median values reported for u_* (Figure 6.34a) and relatively wet conditions caused by frontally induced precipitation associated with these wind directions.

With regard to the spatial variability of $Q_H/Q\downarrow$ the trend is consistent for all wind sectors in all seasons (Figure 6.46 a-d). Ratios reveal evidence of seasonality and are typically smaller in autumn and winter. In general the ratios are slightly increased for westerly wind sectors; in relation to easterly wind sectors $Q_H/Q\downarrow$ is small for wind sectors 0-150°, particularly in winter. Wind speeds from these sectors are typically lower reporting lower associated values of u_* (Figure 6.3 and Figure 6.34).

Similar to the suburban site, the greatest variability in the ratios of $Q_H/Q\downarrow$ and $Q_E/Q\downarrow$ at urban site 1 are reported for wind sectors with high impervious surface cover (see Figure 5.18), for example 120-150° and 240-270° (Figure 6.47 and Figure 6.48). There is also increased variability observed in winter in both $Q_H/Q\downarrow$ and $Q_E/Q\downarrow$ for wind sector 330-360°. With regard to wind sector 0-30° the ratio of $Q_H/Q\downarrow$ in summer and winter is significantly reduced in comparison to other sectors (Figure 6.48b and d); $Q_H/Q\downarrow$ is approximately 0.02 in summer in comparison to 0.20 for wind sectors 90-120° and 120-150° (Figure 6.48b). This variability is also observed at the suburban site, where $Q_H/Q\downarrow$ is relatively small in summer and winter for 0-90° indicating evidence of synoptically driven influences (Figure 6.46b and d).

6.9.5 *Energy partitioning and energy balance closure*

Flux ratios are considered as useful parameters when attempting to identify temporal and spatial trends in the partitioning of Q*, normalising fluxes according to Q* also facilitates cross-site comparisons with the studies undertaken in other cities (Oke, 2006). Seasonal daytime flux ratios representing the partitioning of Q* between Q_E, Q_H and $\Delta Q_{S\ OHM}$ for the suburban site and urban site 1 are presented in Table 6.6. The seasonal daytime Bowen ratio (β) will be presented describing the relationship between the two turbulent fluxes (Q_H and Q_E); when its value is greater than 1 more energy is spent heating the atmosphere than evaporating water. This section will also address

energy balance closure using the energy balance ratio (see Equation 2.24). The relation between available energy (Q^*-ΔQ_S) and the turbulent heat fluxes (Q_E+Q_H) will be examined and seasonal variation in EBR will be outlined.

Results for Dublin report that Q_E/Q^* represents the smallest partitioning of Q^* in the spring and summer months at the suburban site and urban site 1, generally accounting for a greater portion of Q^* at the suburban site (Table 6.6). Q_E/Q^* ratios of 0.16 are reported at urban site 1 in the spring months, corresponding values are greater at the suburban site, 0.26 and represent the effect of a greater pervious surface fraction and higher vegetation density. During the summer Q_E/Q^* ratios increase to 0.23 and 0.30 at the urban site 1 and the suburban site respectively. Throughout the winter months the partitioning of Q^* into Q_E significantly increases and peak ratios reported are 0.46 and 0.68 for urban site 1 and the suburban site (Table 6.6). Q_E is the only flux of the SEB to remain positive throughout the year and over the course of the night and as a result it becomes an important component of the surface energy budget in winter.

In spring and summer Q_H and $\Delta Q_{S\ OHM}$ become increasingly important fluxes (Table 6.6). The dominance of Q_H/Q^* ratios is evident in summer, approaching 0.60 and 0.48 at the urban site 1 and the suburban site respectively. Partitioning of Q^* into Q_H is greater at the urban site 1 in all seasons. At the suburban site Q_H represents only 15% of Q^* in winter and negative ratios representing $\Delta Q_{S\ OHM}/Q^*$ indicate a net loss of energy from the substrate at the suburban site. $\Delta Q_{S\ OHM}/Q^*$ is relatively constant between spring and summer at both sites, relative changes in the partitioning of Q^* are reported for the turbulent fluxes instead (Table 6.6).

Table 6.6 Seasonal energy balance flux ratios for the suburban and urban site 1, seasonal values were determined from 33 and 27 months of data the suburban and urban site 1 respectively.

Ratio	Q_H/Q^*		Q_E/Q^*		$\Delta Q_{S\ OHM}/Q^*$		β (Q_H/Q_E)		EBR	
Season	**URB**	**SUB**	**URB**	**SUB**	**URB**	**SUB**	**URB**	**SUB**	**URB**	**SUB**
Spring	0.64	0.47	0.16	0.26	0.38	0.34	4.42	1.96	1.30	0.91
Summer	0.60	0.48	0.23	0.30	0.37	0.34	2.67	1.67	1.52	1.03
Autumn	0.57	0.38	0.36	0.36	0.21	0.21	1.75	1.27	1.09	0.72
Winter	0.63	0.15	0.46	0.68	-0.28	-0.21	1.16	0.28	0.87	0.63
Annual	0.61	0.37	0.33	0.40	0.17	0.17	2.50	1.30	1.23	0.85

The Bowen ratio is consistently higher at urban site 1 for all seasons (Table 6.6). This trend illustrates the relatively lower fluxes of Q_E relative to Q_H. Maximum β is reported for spring months and is 4.42 and 1.96 for urban site 1 and the suburban site; over the observational campaign spring months were relatively dry and as a consequence Q_H dominates. Minimum β is reported for winter; again the trend is consistent across the two sites. The suburban site reports β less than 1; this indicates that Q_E becomes the dominant turbulent heat flux in winter. β approaches unity at urban site 1 (e.g. 1.16) and further demonstrates the seasonality in the turbulent fluxes and the relative importance of Q_E in winter (Table 6.6).

The energy balance closure ratio (EBR in Table 6.6) describes the ratio of the sum of the turbulent heat fluxes (Q_H+Q_E) to the sum of available energy ($Q^*- \Delta Q_{S\ OHM}$). The ratios in Table 6.6 represent median diurnal values (all hours) divided into seasons. Seasonal EBR report the same pattern across the EC sites. Ratios are largest in the summer and smallest in the winter (Table 6.6). With regard to urban site 1 energy balance closure is almost achieved in the autumn (e.g. 1.09). The energy balance is over-closed in summer by almost 50%, the magnitude of the turbulent fluxes exceeds the available energy estimated by $Q^*- \Delta Q_{S\ OHM}$. On the other hand the turbulent fluxes are 13% lower than the available energy in winter. With regard to the suburban site energy balance is almost achieved in spring and summer (e.g. 0.91 and 1.03 in Table 6.6). In autumn and winter however the turbulent fluxes are lower than the available energy by 28 and 37%. The EBR representing the average total of 27 months is 0.85 and 1.23 for the suburban site and urban site 1 respectively.

In order to investigate energy balance closure further a regression analyses was performed on the data where $Q^*- \Delta Q_{S\ OHM}$ represents the independent variable and Q_H+Q_E is the dependent variable (see for example Figure 6.49). The regression analysis represents monthly median diurnal values between April 2010 and July 2012 (e.g. n= 1344 median data points for 27 months).With regard to the suburban site, the slope of the regression line is 1.17; this indicates that the sum of the turbulent heat fluxes (Q_H+Q_E) is typically greater than the available energy via $Q^*- \Delta Q_{S\ OHM.}$ The scatter around the regression line is consistent for values between 50-250 W m^{-2}, scatter increases however for higher values. In relation to low values of available energy (e.g.

<50 W m^{-2}) the sum of the turbulent fluxes is either negative or lower in magnitude (Figure 6.49).

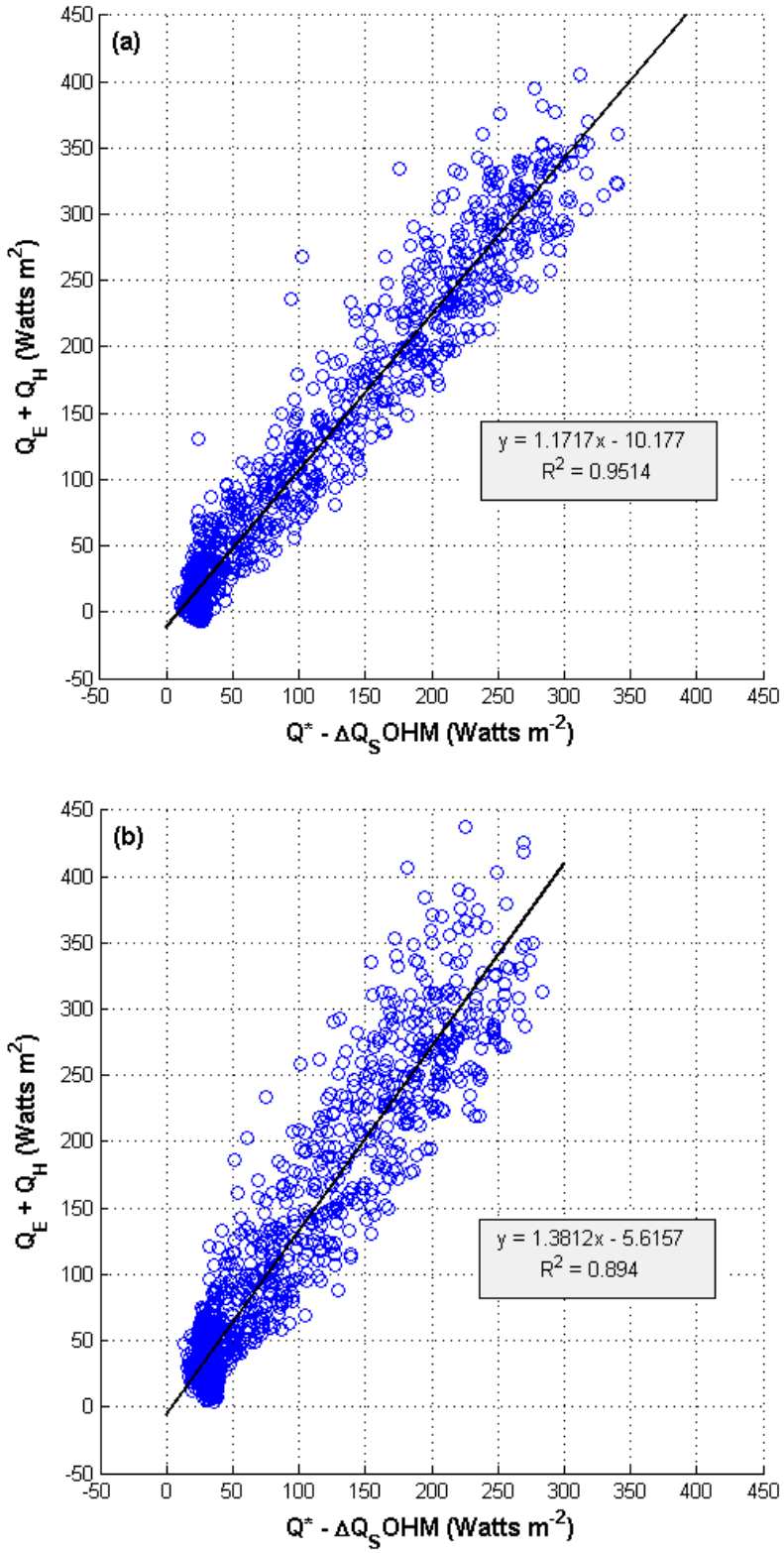

Figure 6.49 Scatter plot showing the relation between the available energy (Q^*- ΔQ_SOHM) and the sum of the turbulent fluxes (Q_E+Q_H) for a) the suburban site and b) urban site 1 between April 2010 and July 2012. Data points refer to monthly median diurnal values where n=1344.

During winter when available energy is significantly reduced the corresponding sum of the turbulent fluxes is likely to be lower in magnitude. This pattern changes for spring and summer; increased available energy (e.g. 300 W m^{-2}) leads to higher associated turbulent heat fluxes (e.g. >300 W m^{-2}) (Figure 6.49). The urban site reports similar findings however the slope of the regression line is greater (1.38) indicating that the sum of turbulent fluxes is typically greater than the available energy. Scatter around the regression line is greater particularly for values >300 W m^{-2} (Figure 6.49). There is good agreement between available energy and the sum of the turbulent fluxes for low values (e.g. <50 W m^{-2}) leading to better closure of the SEB in autumn and winter. On the other hand, greater differences are evident for larger energy inputs typically observed in spring and summer leading to over closure of the SEB (Table 6.6

6.9.6 *The anthropogenic heat flux*

Values of Q_F generated for the suburban site and urban site 1 by Alexander et al. (in review) were used to evaluate the SEB observations and the disparity in the EBRs presented above. Q_F values were estimated using the Surface Urban Energy and Water Balance Scheme (SUEWS) (Järvi et al., 2011). This scheme employs population density (inhabitants per hectare), cooling degree days (CDD) and heating degree days (HD) to generate daily Q_F for weekdays and weekends (see equation 3 of Järvi et al., 2011). Q_F was modelled for a typical climatological year (TCY) taking hourly averages from Dublin Airport from 2005-2015 (Met Éireann) and population data from the 2011 Irish Census (CSO, 2011) pertaining to the electoral divisions of the 2 EC sites (45.9 and 119.8 inhabitants per hectare at the suburban site and urban site 1 respectively) (Alexander et al., in review).

Figure 6.50 presents the monthly median diurnal cycle of Q_F for a TCY from January to December. A clear diurnal pattern is revealed for both EC sites where three peaks, indicating increased electricity usage per inhabitant, coincide with morning and evening hours when people leave for and return from work or school and thirdly the late evening when people may be more likely to require space heating. The magnitude of the monthly diurnal values broadly changes in response to ambient temperatures, for example largest values for Q_F are modelled for winter months (28 and 68 W m^{-2} in January at the suburban site and urban site 1 respectively) and smallest values during summer months (20 and 48 W m^{-2} in July at the suburban site and urban site 1

respectively). Monthly and annual mean values were generated for the 12 month modelled data set and are presented in Table 6.7. Q_F for urban site 1 is typically twice the magnitude owing to the increased population density; on an annual basis mean Q_F is 15.20 and 33.87 W m^{-2} for the suburban site and urban site 1 respectively (Table 6.7).

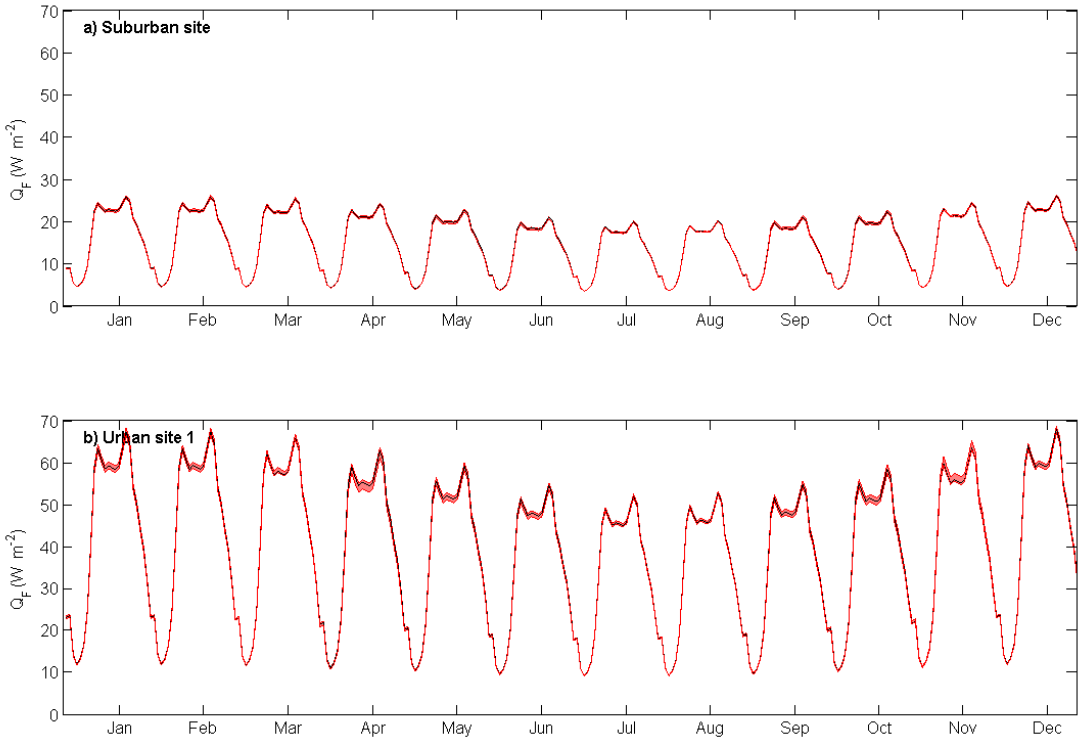

Figure 6.50 Monthly median diurnal cycles generated using data from Alexander et al. (in review) for a) the suburban site and b) urban site 1 for a typical climatological year (TCY).

Table 6.7 Seasonal and annual means of Q_F (W m^{-2}) modelled using Järvi et al. (2011).

Season	Suburban site	Urban site 1
Spring	15.76	40.90
Summer	13.33	34.68
Autumn	14.76	28.33
Winter	16.94	44.15
Annual	15.20	33.87

Given that the modelled data represents 12 months of a TCY and not the 33 month observational campaign, a direct comparison is not possible. Median diurnal cycles and seasonal averages however give an indication of the magnitude of Q_F at both EC sites and help to explain differences reported in the EBR for the observation campaign. Incorporating Q_F into the EBR according to Offerle et al. (2005b),

$$EBR = \frac{Q* + Q_F - \Delta Q_S}{Q_H + Q_E}$$

Figure 6.51 Energy balance ratio for urban areas according to Offerle et al. (2005b)

Serves to increase the magnitude of terms representing available energy ($Q* + Q_F - \Delta Q_S$) and brings them closer in magnitude to the terms representing the magnitude net turbulent energy ($Q_H + Q_E$). The slope of the regression line (1.17) for the suburban site indicated that the sum of the turbulent heat fluxes (Q_H+Q_E) is typically greater than the available energy via Q*- $\Delta Q_{S\ OHM}$. With regard to urban site 1 the slope was 1.38; the tentative application of these modelled Q_F values therefore closes the SEB at both EC sites to a greater degree than reported in previous sections (e.g. Section 6.9.5).

6.10 The CO_2 flux

In an urban context the EC method, when appropriate scale and height requirements are applied, is capable of measuring all biogenic and anthropogenic CO_2 fluxes within a local-scale neighbourhood. On an annual basis the question as to whether a neighbourhood is a net source or sink of CO_2 will depend on the relative strength of its sources and sinks. As illustrated in Figure 3.22 local-scale CO_2 sources include combustion processes related to vehicles, industry and households (e.g. space heating and cooking), respiration processes by soil, vegetation and humans, while CO_2 sinks include uptake via photosynthesis by urban vegetation.

6.10.1 *The temporal variability of F_C*

The strength of neighbourhood sources and sinks vary on a diurnal and seasonal basis and as result the flux of CO_2 (F_C) measured by the EC system exhibits distinct temporal patterns. Biogenic influences such as urban vegetation and soils serve as 1) a CO_2 sink during the day throughout the growing season day, particularly around solar noon, and 2) a CO_2 source via respiration throughout the night when photosynthesis is nil. Combustion processes linked to anthropogenic influences at the local-scale serve exclusively as CO_2 sources. For Dublin F_C reveals a distinct pattern that can largely be attributed to traffic. Similar to previous studies the sharpest peak in F_C occurs in the morning during weekdays coincident with rush hour; there is a less pronounced peak in the evening as a result of work days of varying lengths and the onset of contributions from households which varies on a seasonal basis. During benign weather conditions, when demand for space heating is negligible nocturnal emissions are assumed to be

respiration - and vehicular - related. Evening and nocturnal CO_2 fluxes in the winter suggests increased emission from space heating demand.

This section presents CO_2 fluxes measured at the suburban site and urban site 1. Suburban measurements span a total of 11 months (April 2010 to March 2011); urban site 1 measurements span a total of 26 months (April 2010 to July 2012). The diurnal variability of F_C will be presented for each season across the two locations. In the absence of detailed traffic counts and vehicle types, F_C is divided into weekday and weekend days as a means of investigating the contribution of vehicular emissions to the measured flux. It is assumed that vehicular activity is relatively reduced during the weekend at both the suburban site and urban site 1. Furthermore F_C in the summer at the suburban site is divided into two time periods, 1) June, representing summertime F_C when the school is in term and 2) summer, representing F_C in July and August when the school is closed for 8 weeks. The diurnal trend of F_C for each season will be presented for the individual sites.

Urban site: diurnal trend

At the urban site a distinctive morning peak in F_C is reported at 8hrs; this peak is observed in all seasons, values in summer and autumn are of similar magnitude, ~15 µmol m^{-2} s^{-1} and winter reports the largest peak value of 22 µmol m^{-2} s^{-1} (Figure 6.52, Figure 6.53, Figure 6.54 and Figure 6.55). The magnitude of F_C drops off following morning rush hour remaining relatively constant between 10:00-19:00hrs for spring, summer and autumn. On the other hand winter observes a second peak with a rising limb between 13:00-18:00hrs. This second peak is likely to be a combination of anthropogenic sources, namely combustion via vehicular activity and space heating.

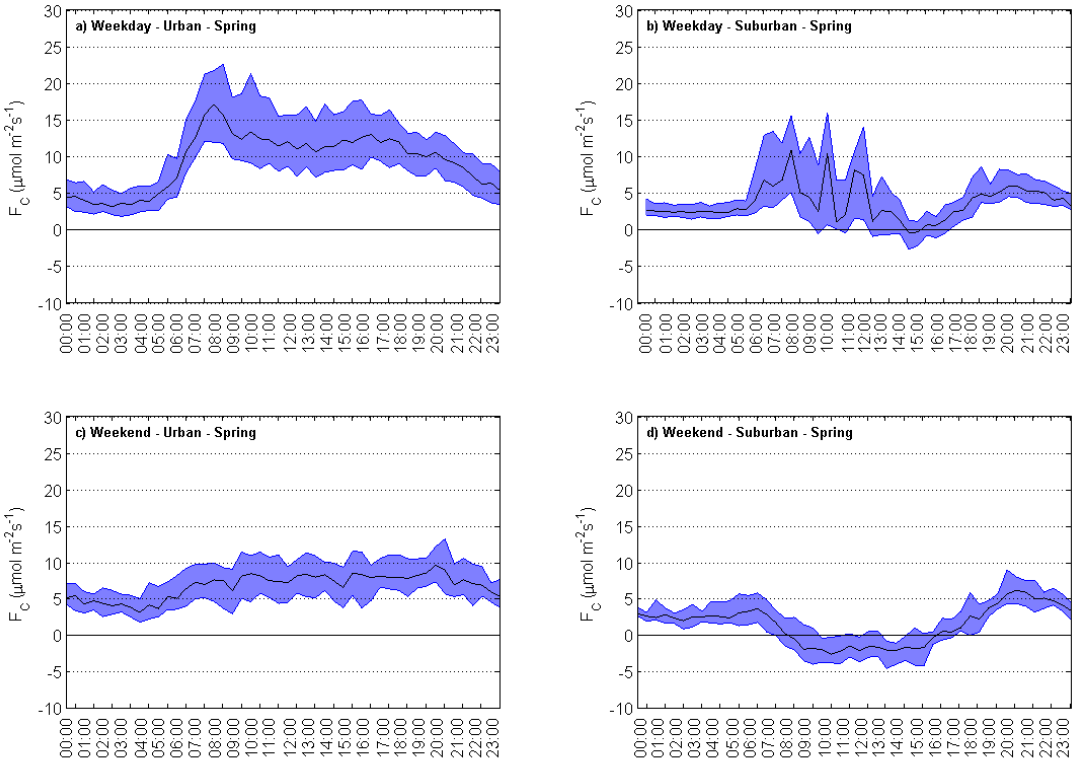

Figure 6.52 Spring median diurnal CO_2 flux (in black) showing upper and lower quartiles (in blue) observed during weekdays and weekends at urban site 1 and the suburban location.

Examination of F_C on weekend days in winter reveal no significant morning peak, indicating reduced vehicular activity, however F_C increases throughout the day, peaking at 19hrs coincident with expected increases in demand for household energy use (e.g. space heating and cooking via natural gas) (Figure 6.55c). During weekend days F_C in summer report remarkably consistent values between 00:00-18:00hrs (~5 µmol m^{-2} s^{-1}) increasing slightly in the evening (Figure 6.53c). This increase may be attributed to increased household energy use or vehicular activity. In spring and autumn weekend fluxes are again relatively consistent throughout the day (5 -10 µmol m^{-2} s^{-1}) and there are no significant peaks that could be easily attributed to traffic (Figure 6.52c and Figure 6.54c).

Nocturnal F_C for spring, summer and autumn are relatively consistent; during late evening F_C decreases from around 10-5 µmol m^{-2} s^{-1}. Early morning values between 00-06hrs typically range between 4-5 µmol m^{-2} s^{-1} (Figure 6.52a and c, Figure 6.53a and c, and Figure 6.54a and c). With regard to winter, values in the evening follow the same trend but are typically greater in magnitude by 5 µmol m^{-2} s^{-1}, indicative of increased household contributions (Figure 6.55a and c).

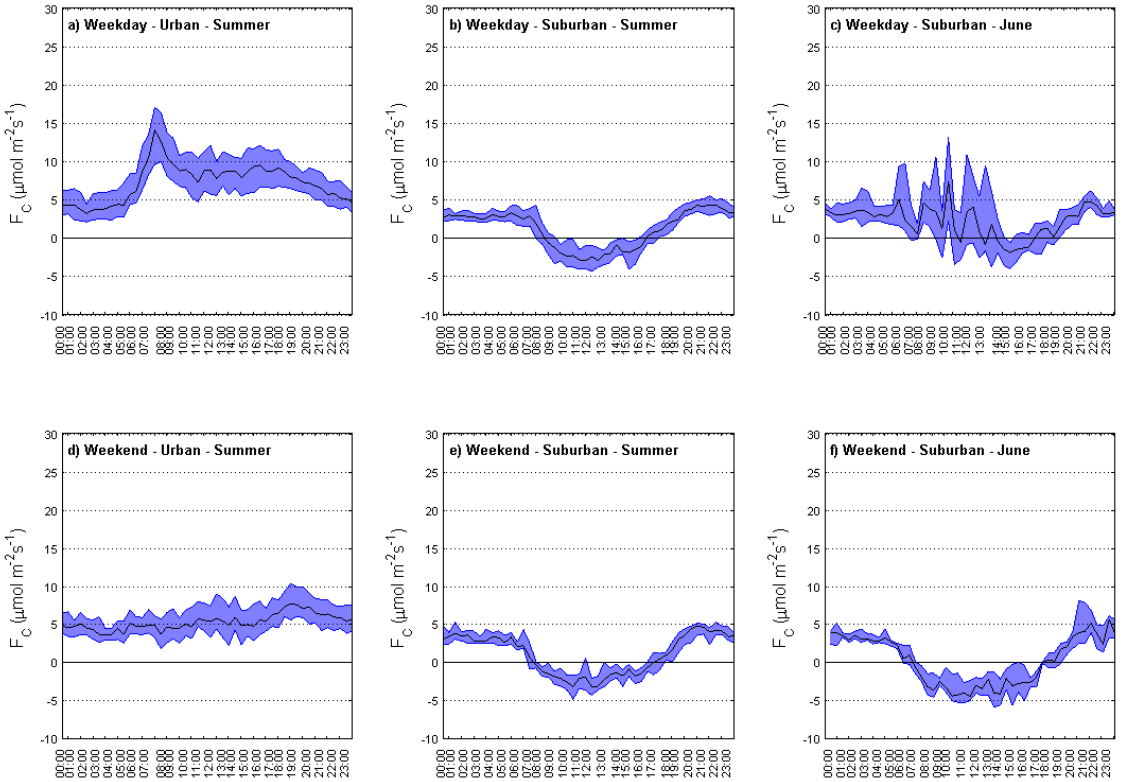

Figure 6.53 Same as Figure 6.50 for summer; with regard to the suburban site summer is separated into two plots to reflect summer months in (June) and out of school term.

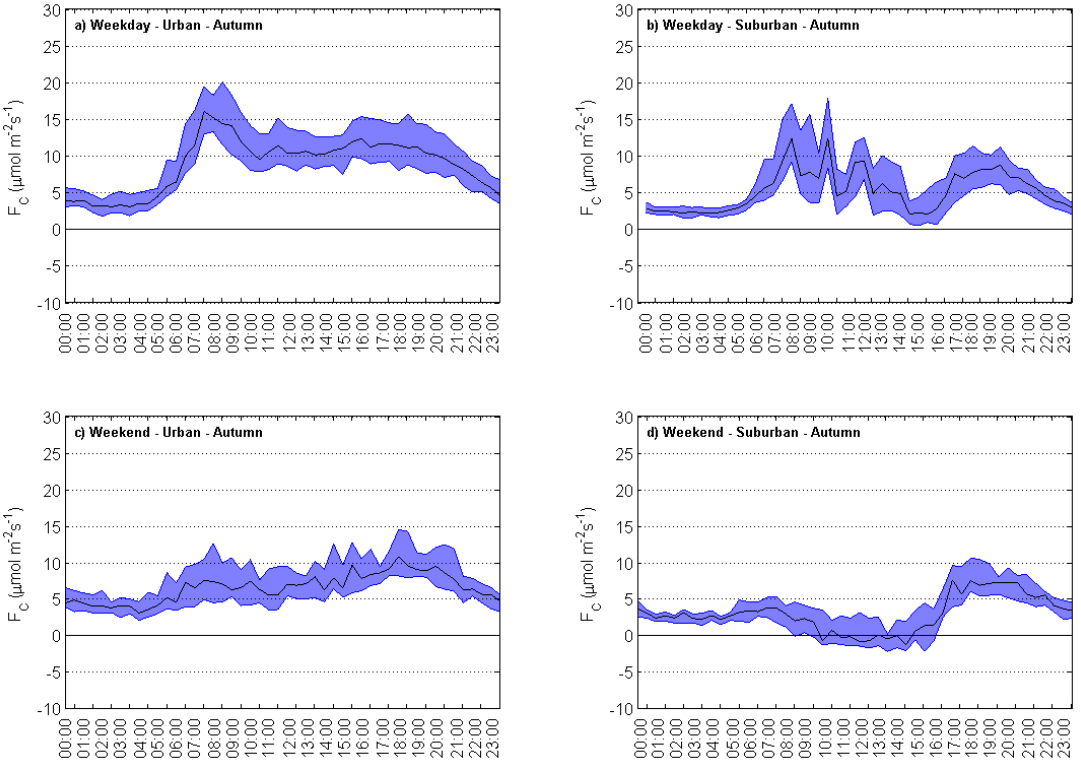

Figure 6.54 Same as Figure 6.50 for autumn at urban site 1 and the suburban site.

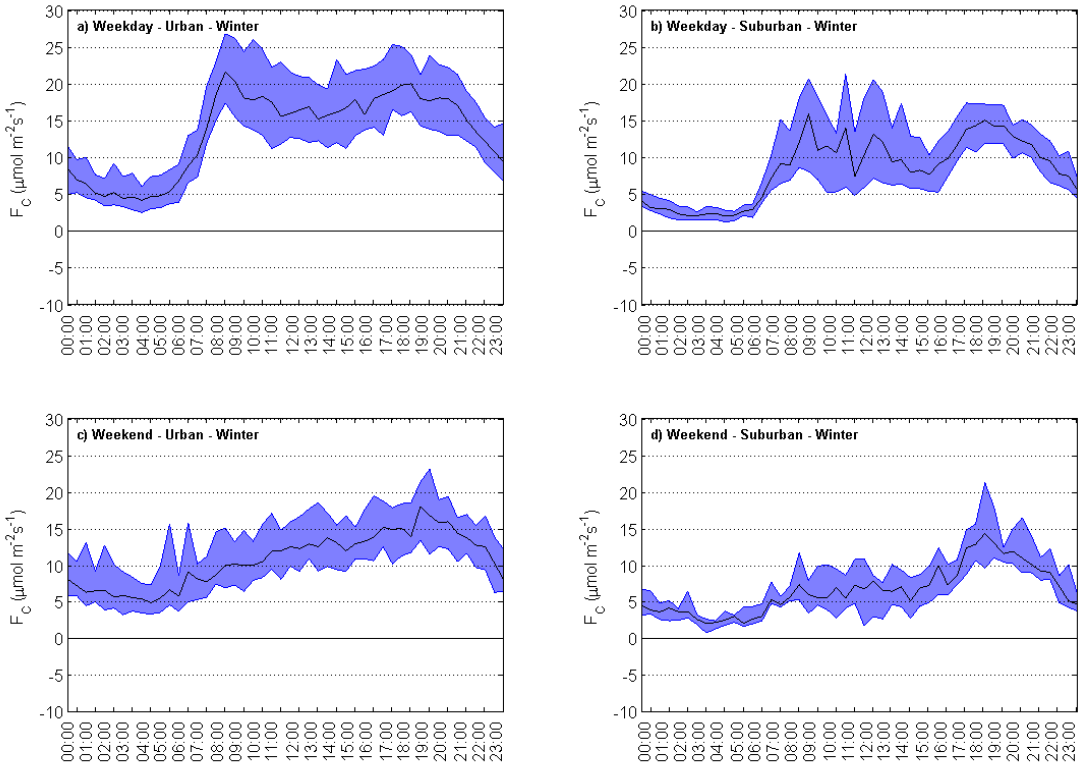

Figure 6.55 Same as Figure 6.50 for winter at urban site 1 and the suburban site.

Suburban site: diurnal trend

With the exception of summer, considered here, as July and August when the school, on which the instruments are located, is closed, the weekday diurnal trend of F_C exhibits a series of distinctive peaks between 07:00-13:00hr (Figure 6.52b, Figure 6.53c, Figure 6.54b and Figure 6.55b). These peaks are very likely a result of school-related emissions associated with traffic, space heating and human respiration given that they not observed in the summer diurnal trend of F_C when the school is closed. The timing of the morning peaks is consistent for all seasons; the peaks correspond with morning commuter and school traffic (07:00-09:00hr) and school breaks (10:00 and 12:00hr) when the pupils and staff are in the school yard. F_C begins to increase following 15:00hr coinciding with school closing times, the onset of evening commuter traffic and increased household energy use. The magnitude of the evening peak varies in magnitude according to the season. In winter the increase in F_C occurs earlier and is more pronounced; shorter day lengths and colder air temperatures increase the demand in household energy use and fluxes reach 15 µmol m^{-2} s^{-1} at 18:00hr (Figure 6.55b). F_C increases less rapidly in the evening in spring, summer and autumn and are lower in magnitude (Figure 6.52b, Figure 6.53c and Figure 6.54b).

Weekend diurnal variability in spring, summer and autumn reveal evidence that the urban vegetation is sequestering carbon (Figure 6.52d, Figure 6.53e and f, and Figure 6.54d). Values less than zero, indicative of uptake via photosynthesis, are most pronounced in June, for example, -4 μmol m^{-2} s^{-1}, when photosynthetic active radiation is greatest (Figure 6.53f). Outside of the growing season, for example in winter, F_C does not show evidence of uptake by the urban vegetation and remains positive throughout the diurnal course (Figure 6.55d). In the absence of commuter traffic there are no distinctive morning peaks reported for F_C on weekend days; large peaks are typically confined to winter evenings and are more likely to be household - as oppose to traffic - related (Figure 6.55d). It is important to note that significant uptake via urban vegetation is typically only evident during weekend days and in June when the school is closed. At these times the vegetation has an effect on the direction of F_C however anthropogenic sources during the weekdays reduce this effect.

Nocturnal trends in F_C particularly for 00:00-05:00hr are consistent in magnitude for all days and for all seasons typically ranging between 3-5μmol m^{-2} s^{-1}. This is similar to findings for a suburban location in Swindon where nocturnal values of F_C were consistent throughout the year, typically reporting values of 3μmol m^{-2} s^{-1} (Ward et al., 2013). The uniformity of the nocturnal flux throughout the year suggests that the flux is related to human respiration which does not change on a seasonal basis.

6.10.2 *The spatial variability of F_C*

This section investigates the influence of the local-scale surface cover on the F_C observed at the suburban and urban site. The magnitude of F_C is examined for individual wind sectors surrounding the EC towers. The frequency of wind from each sector is normalised so that the magnitude of F_C can be investigated consistently across all wind sectors (see for example Figure 6.56). Given that the nocturnal trend in F_C was relatively consistent for both sites the fluxes reported below correspond only to day time values (e.g. $K\downarrow > 3$ W m^{-2}) for all seasons.

Urban site: spatial variability

As reported previously the vegetation fraction at urban site 1 is limited and largely comprises of grass as oppose to trees which serve as a stronger CO_2 sink during the growing season. For wind sectors from 315-195° there is some evidence of CO_2 uptake, particularly in spring and summer (green areas in Figure 6.56a and b) however the magnitude of F_C is typically positive for all wind sectors in all seasons. The relative magnitude of F_C is generally consistent for all wind sectors; exceptions to this include wind sectors from the north and north easterly direction (345-105°) corresponding to the direction of the city centre and heavily trafficked roads such as Thomas Street which lies 200 m to the north of the EC tower (Figure 5.25). For wind sectors between 15-105° the frequency of large F_C (e.g. >24 µmol m^{-2} s^{-1}) represents over 50% of all observations in winter (Figure 6.56d); these wind sectors comprise of relatively less residential dwellings and a large density of commercial buildings that would require space heating during the work day hours (Figure 5.25).

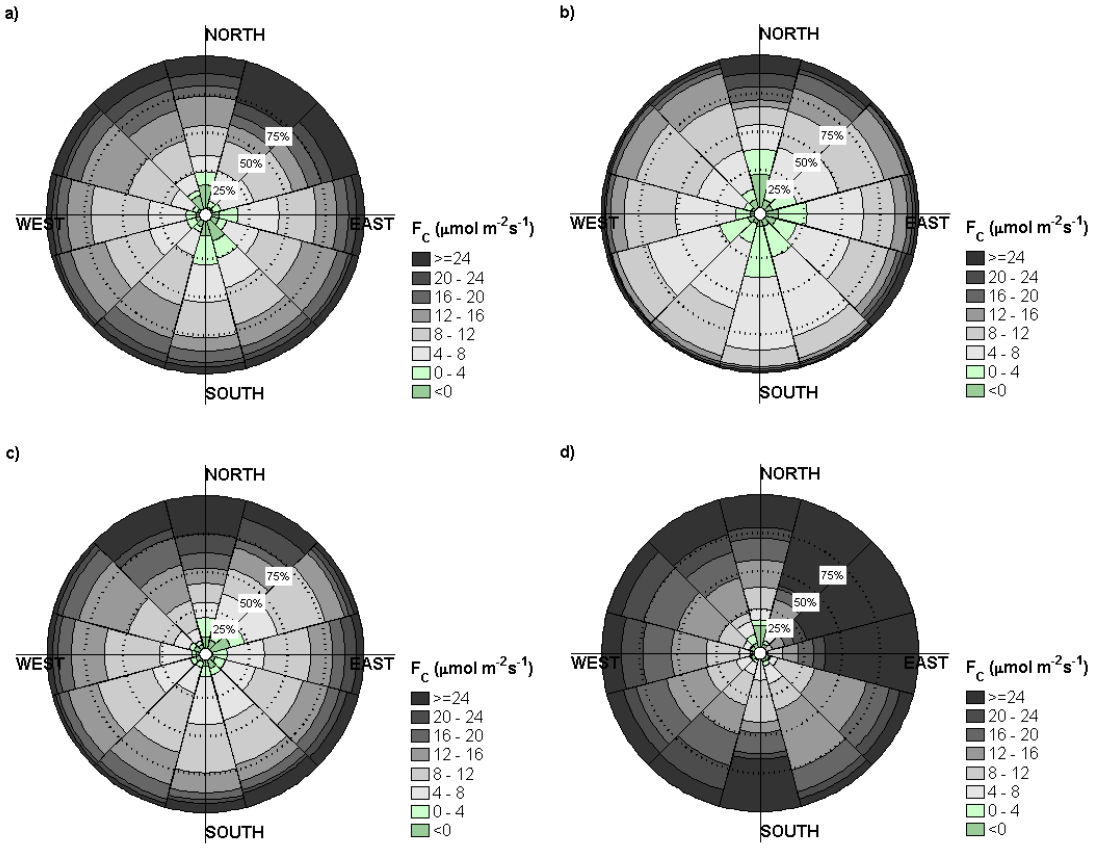

Figure 6.56 Seasonal CO_2 flux observed at urban site 1 normalised per wind sector for a) spring, b) summer, c) autumn and d) winter. The magnitude of flux (µmol m^{-2} s^{-1}) is outlined in the legend. The relative frequency of the flux magnitude per wind sector is outline by the dashed circles, e.g. 25, 50 and 75%.

Suburban site: spatial variability

F_C at the suburban location reveals a spatially variable trend when examined according to wind sectors (Figure 6.57). When vegetation is active the spatial variability of F_C is most pronounced; the spatial distribution of urban vegetation serves to modulate the effect of anthropogenic CO_2 release in spring, summer and autumn for certain wind sectors (Figure 6.57 a, b and c). When vegetation is dormant in winter this modulating effect is diminished and the magnitude of F_C is spatially more consistent (Figure 6.57 d). The 70% source area corresponding to F_C was estimated to represent an area approximately 200 m upwind of the EC tower during neutral conditions (Figure 6.31e). On closer examination of this area there is evidence to suggest F_C is lower in the easterly direction for all seasons; roads in this direction are exclusively residential typically accessed by local residents and there is a greater fraction of greenspace within the 200-300m radius (Figure 6.58). Greatest uptake via photosynthesis is also evident for this sector together with wind sectors in the northeast and north where F_C indicates uptake for over 50% of observations (Figure 6.57b).

F_C in all seasons corresponding to the southerly wind sector is relatively large (165-195°); this direction corresponds to the school entrance and local shops which is heavily trafficked at school opening and closing times (Figure 5.6c). With regard to wind sectors from the general west direction between 195-345°, F_C is relatively large in all seasons; in summer there is evidence of CO_2 uptake for certain sectors but this is largely offset by the presence of two regional roads, Wainsfort Road to the northwest and Templeville Road to the southwest (Figure 6.58).

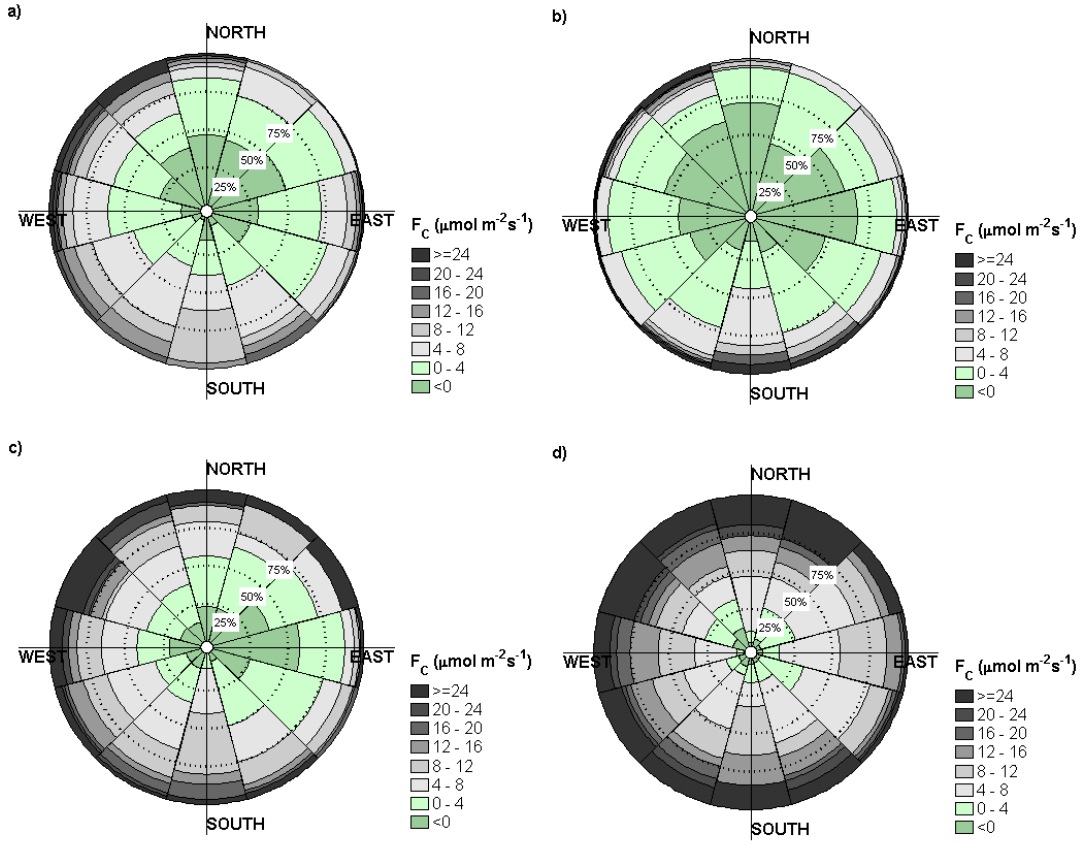

Figure 6.57 Same as Figure 6.54 for the suburban site.

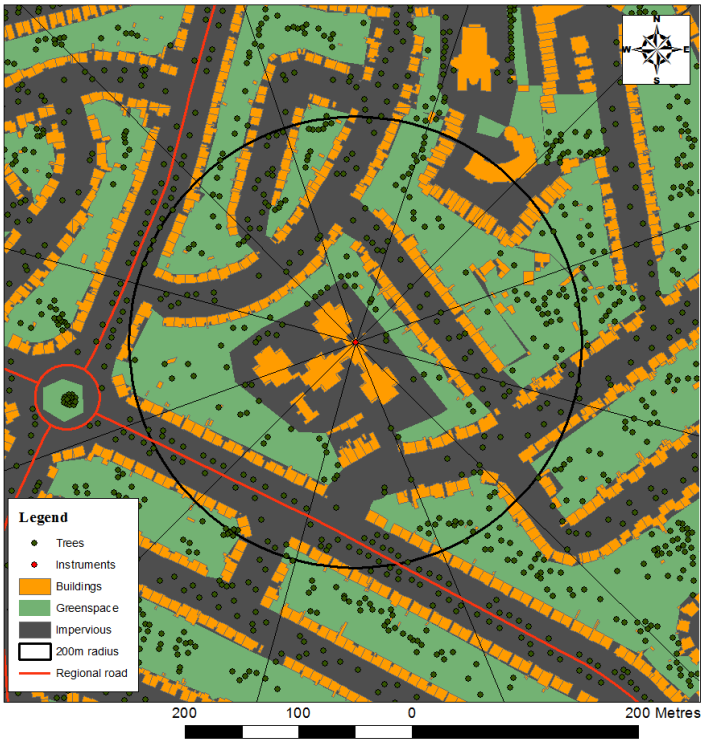

Figure 6.58 Map illustrating the land cover in a 200m radius of the suburban location.

The anthropogenic sources dominate despite the dense presence of street trees along these transects. Household (e.g. space heating and cooking) and vehicle emissions are the main contributors to winter F_C, relatively lower magnitudes corresponding to the east wind sectors are attributed to differences in the road type given that housing fraction is largely consistent for all wind sectors (Figure 5.8). In the summer urban vegetation, serving to uptake CO_2, is capable of offsetting some of the anthropogenic influences although sources from traffic at this time are reduced due to the closure of the school and the negligible demand for space heating. In summary it was found that combined, the density of housing and roads (e.g. local or regional) had a greater influence on the magnitude of F_C in comparison to the density of urban vegetation (e.g. number of trees). F_C was positive for the majority of observations, particularly for wind sectors corresponding to regional roads and the school junction.

6.11 Summary of the results

This chapter presented the key findings from the EC observation period spanning almost 3 years in Dublin. Inter-annual variations in the meteorological conditions resulted in observations representing a range a snow free and snow cover periods. In terms of spring and summer, spring months were typically dry indicative of clear-sky conditions. Very often K↓ was reported as larger in spring relative to summer months coincident with the summer solstice. An inter-site comparison revealed differences in the radiation budget components, particularly with regard to K↓ and K↑, which in turn affected α.

Post-processing and quality flagging of the estimated turbulent fluxes revealed that the EC fluxes were of good quality for the majority of day and night time cases; conditions of non-stationarity is a concern sometimes, however conditions of well-developed turbulence were largely fulfilled. The fluxes of Q_E and F_C were most affected by post-processing techniques given that they rely on relatively dry conditions for accurate measurement by open-path gas analysers. As a result a large percentage of Q_E and F_C data was discarded for subsequent analysis. On the other hand Q_H, which is not as affected by precipitation events and instrumental issues, reported better quality flags and a greater portion of the data was attained for subsequent analysis.

In general neutral conditions are dominant for day and night time conditions for each EC site, however increasing instability was reported for EC sites with increasing

impervious surface fraction; stable atmospheric conditions were rarely observed. The estimated flux footprint was presented for each EC site and revealed increasing footprint distances for stable atmospheric conditions. Potential flow distortion was investigated for all wind sectors at the 3 EC sites. The urban sites reported the highest angles of attack for northerly wind sectors where the frequency of this wind direction is relatively rare. The suburban site reported consistent values for all wind sectors and the angle of attack rarely deviated from 0° this was attributed the uniformity of the roughness elements here.

The OHM was employed to model ΔQ_S and estimates agreed reasonably well with those derived using the energy balance residual method (RES), particularly when Q* is large. Both fluxes were examined in unison with Q* and the turbulent heat fluxes Q_E and Q_H. The magnitude of the fluxes varied according to energy inputs via Q*, peak diurnal values are typically reported around local solar noon in all months. Nocturnal values indicate a greater loss of energy by the urban surface relative to its suburban counterpart, particularly in summer when day length and Q* are greater. The spatial variability of the turbulent fluxes revealed inter-site differences for both of the turbulent heat fluxes; Q_E is typically greater at the suburban site in all seasons while Q_H is consistently greater at the urban site for all seasons ($Q_E/Q\downarrow$ on average 0.05 at the suburban site versus 0.02 at urban site 1 in JJA, and $Q_H/Q\downarrow$ on average 0.13 at the suburban site versus 0.18 at urban site 1 in JJA). $Q_E/Q\downarrow$ and $Q_H/Q\downarrow$ were also examined at the suburban and urban site 1 and revealed relatively little evidence of intra-site differences per wind direction. Noteworthy intra-site differences corresponded to wind sectors with an increased impervious fraction relative to the local-scale average.

The temporal and spatial variability of F_C was presented for all seasons in relation to the suburban site and urban site 1. Temporal variability revealed a distinct weekday and weekend pattern at both sites evident in all seasons; the difference in these patterns is largely attributed to emissions from vehicular activity. Morning peaks observed at the suburban site revealed distinctive peaks associated with school opening hours, school-related traffic and human respiration. Emissions from domestic energy use and space heating became evident in the evening in the autumn and winter months. Evidence of CO_2 sequestration at the suburban site was reported in spring, summer and autumn. This uptake was most pronounced during weekend days when traffic activity in the

neighbourhood was reduced. Urban site 1 revealed large morning peaks associated with commuter traffic, the magnitude of which varied according to season (e.g. 15 and 22 μmol m^{-2} s^{-1} in summer and winter respectively). The morning peak was substantially reduced for weekend days particularly in spring and summer. An analysis of the spatial variability of F_C indicated greater emissions for the wind sectors corresponding to the city centre of Dublin. With regard to the suburban site uptake of CO_2 was greatest for wind directions corresponding to residential roads, whilst higher F_C was associated with regional roads with greater traffic activity.

Chapter 7 Discussion and Conclusions

The purpose of this chapter is to interpret the research findings for Dublin and to contextualise the research in the international literature. The chapter will discuss the thesis findings relating to the radiation balance, the surface energy budget and CO_2 flux for Dublin, in addition to outlining any findings specific to this study. The chapter will also identify limitations of the research associated with 1) observational techniques including the siting and use of certain micro-meteorological instruments and 2) methodological techniques concerning data processing in EC software, post-processing and data quality. These limitations will be presented in unison with specific recommendations for current and future urban EC investigations. Recommendations for future work will be set out, in addition to key policy-relevant implications of the research. Finally the thesis conclusions are presented.

7.1 Discussion of thesis findings

7.1.1 *Radiation budget*

The results of the radiation budget for Dublin revealed temporal patterns broadly consistent with mid-latitude cities in the Northern hemisphere (e.g. London, Kotthaus and Grimmond, (2014a)); largest K↓ was typically observed in summer months however there was evidence of high receipt of K↓ in spring. This variability is as result of relatively clear-sky conditions prevailing in spring for the observation period. Results pertaining to α revealed values consistent with the published literature, for example values between 0.08 to 0.20 have commonly been reported for cities (e.g. Adebayo, 1990; Christen and Vogt, 2004; Offerle et al., 2005a; Frey et al., 2011; Goldbach and Kuttler, 2013). Interestingly α was lower in magnitude at the suburban location, where there is a larger greenspace surface fraction than both urban sites (e.g. 0.10 versus ~0.13). The instrument at the suburban site is mounted 6 metres above the school roof surface which is dark asphalt; this surface typically has a low α (e.g. 0.05-0.20 from Oke, 1987) serving to reflect a smaller proportion of K↓ than more common suburban surfaces beyond the school grounds (see Table 3.2). The cosine response of the downward facing pyranometer means that the surface immediately below the instrument exercises the greatest influence on the measured signal. As a consequence measurements of K↑ at the suburban site were affected by the placement of the sensor. The concrete roof surface at urban site 1 is broadly consistent with the local-scale

surrounds and is not considered to induce bias into the radiation data set (see Figure 5.15 and Figure 5.16). When compared with the roof surface at the suburban site however it is relatively lighter and therefore reflected a greater magnitude of K↓ and hence a higher α.

In addition to the roof surface the circular source area of the downward facing pyranometer 'sees' surface materials typical of the suburban site, such as concrete, grass and trees (see Figure 5.5). Initially during the observation period the school yard was exclusively asphalt and concrete. Astro-turf material replaced much of the school yard during school term breaks between July 2012 and July 2013 (Figure 5.4b and d). α from January to May 2013 were examined in comparison to those for the preceding years to determine whether a significant difference in α was observed prior to and after the school yard was resurfaced as this affected almost 28% of the FOV of the downward facing pyranometer. α was highest for March 2013 in relation to March 2011 and 2012 (0.12 in 2013 versus 0.09 and 0.11 in 2010 and 2011 respectively) however this was as a result of the snowfall that occurred in mid-late March 2013; other observed months in 2013 did not reveal significant increases or decreases in comparison to previous years. Yaghoobian et al. (2010) reports astro-turf albedo values from modelling experiments using the Temperature of Urban Facets model (TUF3D) for a South Carolina suburb. The surface albedo reported for the investigation was 0.08 and is similar to the albedo of asphalt, and would therefore support the findings here of a lack of variability in α before and after the new surface was laid.

Snowfall events throughout November and December 2010 gave rise to distinctive differences in the radiation budgets of the suburban site and urban site 1. Key differences were revealed in the observations relating to K↑ and α. Monthly mean α of 0.3 (urban site 1) and 0.4 (suburban site) in December 2010 were similar to findings reported by Bergeron and Strachan (2012) for α observed at two suburban sites (0.30-0.45) in winter in Montreal, Canada (Latitude 45°N). Whilst daily mean α of >0.6 during snow cover days were comparable to a rural site in Montreal (0.70-0.85) (Bergeron and Strachan, 2012).

With regard to incoming radiative fluxes, K↓ is reduced at urban site 1 relative to the suburban site and typically absolute differences are ~60 W m^{-2} in summer months and

<40 W m^{-2} in winter. The percentage decrease is 7.5% and 10% in summer and winter respectively; increased attenuation of K↓ at urban site 1 is expected in winter due to increased energy use and atmospheric pollution concentration (Oke, 1987). Similar findings were recently reported by Frey et al. (2011) for three EC sites of differing urban surface types in Cairo. In general K↓ increased in magnitude from the city (Cairo University) to the urban fringe (suburban-desert site) and differences for all sky conditions were greatest around local solar noon (e.g. 62 W m^{-2}). Diminutions in K↓ of 22% between cities and their rural surrounds have been reported for cities such as Mexico City (Jáuregui and Luyando, 1999), however pollution concentrations in Dublin are unlikely to be as high compared to such mega cities.

In relation to L↓ the observations in Dublin reveal slightly higher values during the day at urban site 1 and spatially consistent values throughout the night; daytime differences however largely range between ±3 W m^{-2}. Small inter-site ranges in relation to L↓ were also reported for 1) Cairo where differences for all sky conditions were typically <2.5 W m^{-2} (Frey et al., 2011) and 2) Oberhausen where differences of ±9 W m^{-2} (or 2%) were reported between a suburban and urban site.

The school roof surface affected L↑ at the suburban site as seen from the residual difference between the suburban site and urban site 1 measurements (Figure 6.22). Throughout the daytime L↑ at the suburban site was consistently greater than L↑ at urban site 1. On the other hand nocturnal values reported greater emission of L↑ at urban site 1. Surfaces with a low albedo will absorb a greater magnitude of K↓ during daylight hours leading to higher surface skin temperatures revealed in L↑. The dark asphalt roof material at the suburban site can therefore be considered as thermally extreme becoming very hot (cold) during the daytime (nighttime) particularly under cloud-free conditions. Nocturnal differences in L↑ between the suburban site and urban site 1 can also be explained due to differential cooling rates at the 2 locations. A lower H/W ratio (0.26), coupled with a larger vegetated fraction allow the suburban location to cool more rapidly relative to urban site 1 that has a higher H/W ratio (0.48). Typically urban areas consistently report higher L↑ as a result of higher skin surface temperatures and radiative trapping effects by the urban geometry. Goldbach and Kuttler (2013) report increases of +32-58 W m^{-2}, accounting for between 9-16% of L↑, at their urban site in Oberhausen relative to the suburban site. Observations for Dublin in this regard

are therefore different to the published literature and can largely be attributed to the nature of the school roof surface.

Oke (1974) was the first to suggest that that intra-site differences in Q* between urban and rural areas were unlikely to deviate substantially from one another. In general reduced K↓ is compensated for by lower albedo (and hence higher K↑); as a result K* among urban and rural sites are typically similar. With regard to longwave energy, increased L↓ due to enhanced emissivity in urban areas will be offset by increased L↑ due to higher surface temperatures leading to similar L*. As a result Q* between urban and rural sites are spatially consistent. This trend is evident in the literature, for example in Basel, Switzerland (Christen and Vogt, 2004) and Łodz, Poland (Offerle et al., 2006a) where differences in Q* across multiple sites of differing surfaces were small (e.g. <1 W m^{-2} in Basel based on 1 year of data).

With regard to Dublin, higher K* at the suburban site via increased K↓ and decreased K↑ were not offset by corresponding losses via L* at urban site 1. As a consequence Q* at the suburban site is greater for the observation period (average difference for all hours: +9%). This is however consistent with long term observations in Oberhausen, Germany, where the maximum differences observed for Q* between the suburban and urban site were 35 W m^{-2} or 10% (Goldbach and Kuttler, 2013). Q* measured over three winter seasons in Montreal, Canada, also report relative increases in Q* at the suburban site relative to the urban site (average difference is +20-30 W m^{-2} for all hours and +2-10 W m^{-2} for nighttime hours) and the authors attribute this increase to a higher α at the urban site, similar to the situation observed in Dublin (Bergeron and Strachan, 2012).

Intra-daily differences in Q* across the observation sites in Dublin again report findings similar to those reported in the literature; typically Q* is greater at urban site 1 during the day (average difference +8 W m^{-2}, +4.5%) and lower during the night (average difference -6 W m^{-2}, -17%) due to increased radiative losses via L↑. In general results for Dublin are consistent with the international literature relating to long term observational campaigns. Small reported inter-site differences in Q* are largely induced by upwelling fluxes K↑ and L↑; the school roof surface is a good absorber of K↓ due to

its lower α, and as a consequence it is a good emitter of L↑. This point demonstrates the importance of appropriate instrument siting in the urban domain.

7.1.1 *Turbulent flux footprint*

At the suburban location the peak distance relating to neutral conditions is typically 50m from the sensor location with the 70% source area originating from between 0-300m upwind of the sensor. Results in this case are consistent for all wind directions (Figure 6.31a and e). On the other hand, the radiometer circular source area radius is 48m (diameter of approximately 100m) comprising largely of the school roof, yard and vegetated gardens from adjacent houses (Figure 5.5). As expected the upwind distance of the flux footprint exceeds that of the radiation source area. Although the peak signal of the calculated flux will largely correspond to the surfaces seen by the radiometer (e.g. the school roof and surrounding school yard), the 70-90% flux source area is influenced by surfaces extending beyond the school grounds that comprise of relatively greater fractions of vegetation. As a consequence Q*, determined here by largely asphalt surfaces with a low surface albedo, is likely to be overestimated in comparison to Q* measured over a residential garden, for example in Swindon which would likely have a lower α (Ward et al., 2013).

With regard to urban site 1, the radiometer circular source area radius is approximately 74m (diameter of approximately 150m); during neutral conditions (prevailing during 73% of all cases) the peak signal originates from between 50-100m upwind of the sensors and the extent of the corresponding 70% upwind distance is typically between 300-400m. The surface cover fractions and land use at urban site 1 do not vary significantly between the source area seen by the radiometer and that contributing to the turbulent fluxes. With the exception perhaps of the northerly wind sector (e.g. the location of the Guinness Brewery), for all directions within 400m of the EC site there are no atypical land cover fractions, such as increased water or vegetated surfaces, or land uses that would observe substantially different Q* in relation to that measured by the radiometer.

The situation at urban site 2 is more complex given the increased measurement height of the sensors, and hence the extent of the surface contributing to the measurements. The radiometer circular source area radius is approximately 109m (diameter of

approximately 220m). For neutral conditions the modelled peak signal contributing to the measured flux is estimated at between 0-200m upwind of the sensors; the corresponding 70% footprint extent is typically between 0-800 metres upwind but can extend beyond 800m for all wind directions (Figure 6.33e). As shown in Chapter 5 there are substantial differences in the surface roughness and land cover in the surrounds of urban site 2. Large vegetated parks are located approximately 600m east of the sensor location, plan and frontal area fractions vary, increasing in the north east and south east directions coincident with Dublin city centre. The spatial distribution of sources and sinks of heat and moisture are therefore more variable and measured fluxes may not always represent the underlying surface measured by the radiometer. Future research with regard to urban site 2 should include the stratification of the turbulent heat fluxes and the CO_2 flux into wind sectors representing 1) LCZ 2 compact midrise (~330-150°) and 2) LCZ 3 compact lowrise (~151-329°). Analysis of the fluxes in this regard will allow for a more robust interpretation of the fluxes. This is similar to approaches employed at EC sites in Essen, Germany and Helsinki, Finland where fluxes were representative of differing surfaces depending on the wind direction (see Kordowski and Kuttler, 2010; Järvi et al., 2012). Given that the prevailing wind direction corresponds to the LCZ compact lowrise it is likely that for the majority of the time the fluxes will be representative of the ISL. This assumption is supported when considered in unison with the quality flags reported in Section 6.5 that indicate a high relative frequency of stationary conditions (>60% for day time cases for Q_E). An analysis of quality flags per wind sector will likely yield a greater relative frequency of steady-state conditions in relation to LCZ compact lowrise.

7.1.2 *Turbulent heat fluxes*

The turbulent heat fluxes for Dublin revealed increased Q_E at the suburban site while Q_H was larger at urban site 1. This inter-site variability was reported for all seasons however differences were more pronounced in summer; maximum median diurnal values were 220 and 205 W m^{-2} for Q_H and 110 and 60 W m^{-2} for Q_E at urban site 1 and the suburban site (Table 7.1). In winter the median diurnal values were similar across the sites, 90 and 80 W m^{-2} for Q_H at urban site 1 and the suburban site, and 50 W m^{-2} for Q_E at both sites. Very similar values obtained for urban site 1 were reported for a dense urban location in London, which is also classified as LCZ Compact Midrise (Kotthaus and Grimmond, 2014a). In terms of suburban locations turbulent heat flux results for

Dublin compare very closely with those reported for Swindon which has the same climate (e.g. maritime-temperate climate) (Ward et al., 2013) (Table 7.1). The EC systems are deployed in neighbourhoods of similar density (LCZ open lowrise) and the urban form is similar, comprising of mainly 2 storey residential houses with vegetated gardens.

International comparisons are more readily made when flux ratios are reported. In winter Q_E/Q^* represented the greatest flux ratio at the suburban site and urban site 1 (0.68 and 0.46 respectively) indicating the relative dominance of Q_E in the winter SEB. The increase in Q_E in winter affects the Bowen ratio, where β approaches unity at the urban site (1.16) and is less than 1 at the suburban site (0.28). With regard to the suburban site similar findings have been stated for suburban locations such as Swindon (<1), Christchurch (0.28-2.11) (Spronken-Smith, 2002), Oberhausen (0.47) (Goldbach and Kuttler, 2013) and Łódź (0.30) (Offerle et al., 2006a) (see Table 7.1). With regard to urban sites internationally, winter β is typically reported as >2, for example Goldbach and Kuttler (2013) report β of 4.40 in January, while β during September is reduced to 1.41; this is in contrast to findings observed here. Observational campaigns for winter months are relatively limited however findings from a winter time campaign in Montreal indicate that β is between 3-4 at their urban and suburban locations (Bergeron and Strachan, 2012). With regard to summer β, urban site 1 is largely in agreement with published findings, for example β of 2.67 for Dublin is almost identical to β of 2.62 observed at an urban location in Basel (Christen and Vogt, 2004). Furthermore an urban location in Helsinki reports β of 2 for all hour conditions (Vesala et al., 2008) (Table 7.1).

With regard to Q_H/Q^* summer values for urban site 1 report findings similar to an old urban core location in Marseille (0.60 versus 0.69 respectively) (Grimmond et al., 2004) (Table 7.1). For a dense urban location in London the partitioning of Q^* into Q_H is likely to be of similar magnitude to both Dublin and Marseille (Kotthaus and Grimmond, 2014a).

Table 7.1 Reproduced and updated from Goldbach and Kutller (2013) outlining urban/suburban energy balance studies of EC measurement examples (in situ) with respect to Q_H and Q_E fluxes

Authors	Location	Site characteristics	Height (z in m agl)	Duration	Q_H maximum (W m^{-2})	Q_E maximum (W m^{-2})	Q_H/Q^* (daytime mean values, $Q^* > 0$ W m^{-2})	Q_E/Q^*	Q_H/Q_E (β)
This study	Dublin, Ireland	Urban site 1	18	09 April 2010- 12 July 2012	220(Su) [a] 90(Wi) [a]	60(Su) [a] 50(Wi) [a]	0.60(Su) 0.63(Wi)	0.23(Su) 0.46(Wi)	2.67 (Su) 1.16(Wi)
		Suburban	12	08 April 2010- 31 December 2012	205(Su) [a] 80(Wi) [a]	110(Su) [a] 50(Wi) [a]	0.49(Su) 0.15(Wi)	0.30 (Su) 0.65(Wi)	1.67(Su) 0.28(Wi)
Ward et al. (2013, 2014)	Swindon, UK	Suburban	12.5	09 May 2011- 30 April 2012	189(Su)[a] 48(Wi) [a]	121(Su)[a] 48(Wi) [a]	0.45 (Jun) 0.20 (Wi)	0.34(Jun)	1.6(Su) <1(Wi)
Kotthaus and Grimmond (2014a)	London, UK	Urban (KSS)	49	November 2009- March 2012	~230(Su) [a] ~150(Wi)[a]	~65(Su) [a] ~30(Wi) [a]	n.a.	n.a.	~4-11
Goldbach and Kuttler (2013)	Oberhausen, Germany	Urban	32	15 August 2010 -15 April 2011	159(Su) [b]	123(Su) [b] 55 [b]	0.40(Su) 1.21(Wi)	0.35(Su) 0.24(Wi)	1.41(Sep) 4.40(Jan)
		Suburban	30		127(Su) [b]	232(Su) [b] 76 [b]	0.26(Su) 0.20(Wi)	0.86(Su) 0.27(Wi)	0.47(Sep) 0.64(Jan)
Velasco et al. (2011)	Mexico City, Mexico	Urban	27	March 2006	220 [c]	100 [c]	0.38	0.13	2.91
Frey et al. (2011)	Cairo, Egypt	Urban	27	20 November 2007- 20 February 2008	105 [b]	40 [b]	n.a	n.a.	1.9
		Suburban-agricultural	1.9		78 [b]	130 [b]			0.1
		Suburban-desert	1.9		115 [b]	25 [b]			6.7

Table7.1 (*Continued.*)[1]

Authors	Location	Site characteristics	Height (z in m agl)	Duration	Q_H maximum (W m^{-2})	Q_E maximum (W m^{-2})	Q_H/Q^* (daytime mean values, $Q^* > 0$ W m^{-2})	Q_E/Q^*	Q_H/Q_E (β)
Balogun et al. (2009)	Kansas City, USA	Suburban	35	01 August 2004-17 August 2004	160 (n.a.)[c]	280 (n.a.)[c]	0.21(0.22)[d]	0.46(0.46)[d]	0.48(0.47)[d]
Vesala et al. (2008)	Helsinki, Finland	Urban	31	01December 2005-31 August 2006	300 (225)[d]	60 (150)[d]	n.a.	n.a.	Ca. 5 (2)
Newton et al. (2007)	Miami, USA	Suburban	40	13 May 1995-21 June 1995	260[b]	160[b]	0.42	0.27	1.55
Offerle et al. (2006a, 2006b)	Łódź, Poland	Urban	37	01 January 2001-31 December 2002	180-220 (100)[f]	110 (90)[f]	0.44	n.a.	1.83
		Suburban	41	16 August 2002-27 August 2002	90.9 (36.6)[d]	112.5(58.5)[d]	0.30	n.a.	0.30
Christen and Vogt (2004)	Basel, Switzerland	Urban Suburban	32 16	24 June 2002-12 July 2002	200[g] 168[g]	88[g] 134[g]	0.48[g] 0.37[g]	0.18[g] 0.30[g]	2.62[g] 1.23[g]
Grimmond et al. (2004)	Marseille, France	Urban	20.7	16 June 2001-14 July 2001	390[b]	100[b]	0.69	0.17	4.17
Moriwaki and Kanda (2004)	Tokyo, Japan	Suburban	29	May 2001-April 2002	108 (47)[h]	61(8)[h]	0.49(0.40)[h]	0.28(0.07)[h]	1.77(5.81)[h]
Spronken-Smith (2002)	Christchurch, New Zealand	Suburban	20	29 January 1996-18 Februrary1996, 16 July 1997-09 August 1997	275 (70)[i]	100(20)[i]	0.46(0.16)[i]	0.22(0.10)[i]	0.28-2.11

[1] See next page for explanation of abbreviations and superscripted letters.

Su:Summer; Wi:Winter; Jan:January; Sep:September; n.a.: not available

[a] Maximum monthly median diurnal value within the study period.

[b] Maximum mean hourly value within the study period.

[c] Maximum mean hourly value during clear an calm weather conditions (all days).

[d] Daytime mean value during clear and calm weather conditions (all days).

[e] Maximum mean hourly value from June to August within an urban (vegetation) sector.

[f] Maximum mean hourly value from May to June (during wintertime).

[g] Daytime mean value from 11:00 to 15:00 CET.

[h] Daily mean value in July (February).

[i] Maximum mean hourly value during clear and calm weather conditions in the summer months (in the winter months).

The three locations have similar combined surface fractions of vegetation and water, for example, 15, 19 and 11% for Dublin, London and Marseille respectively. A large sealed surface fraction, serving to drain water away from the surface at these sites, promotes the channelling of Q* into heating the near surface atmosphere. Q_E/Q^* and Q_H/Q^* for suburban locations in Oberhausen, Christchurch, Tokyo, Miami and Basel agree well with Dublin indicating a good degree of consistency in suburban EC observations across different climates and continents (Table 7.1).

Ratios representing $Q_E/Q\downarrow$ and $Q_H/Q\downarrow$ per wind sector are rarely reported in the literature however values are available for London (Kotthaus and Grimmond, 2014b) and Swindon (Ward et al., 2013). In relation to a complex location in London, $Q_H/Q\downarrow$ and $Q_E/Q\downarrow$ varied according to wind direction ($Q_H/Q\downarrow$ was 8-32% and $Q_E/Q\downarrow$ was 1.5-4.5%). To avoid a directional bias due to frontally induced precipitation from the south west direction, only periods reporting dry conditions in the preceding 12 hrs were employed in the spatial investigation (Kotthaus and Grimmond, 2014b). Following this no single causal factor was identified for observed directional patterns; instead the relations between the ratios and the surface cover fractions were deemed complex and may be related to variations in the surface roughness and turbulence structure of EC tower surrounds (Kotthaus and Grimmond, 2014b). In relation to results for Swindon ratios relating to $Q_E/Q\downarrow$ were more correlated to surface cover fractions; a greater proportion of $Q\downarrow$ was used in evaporation for the most vegetated sectors (>10%) in relation to the least-vegetated sectors (6-8%) (Ward et al., 2013).

Ratios of $Q_E/Q\downarrow$ and $Q_H/Q\downarrow$ reported for the suburban site and urban site 1 in Dublin suggest relatively consistent median values for each wind sector. This directional consistency is reported for all seasons; some exceptions were reported for wind sectors with greater impervious surface fractions than the local-scale average. For example $Q_E/Q\downarrow$ corresponding to wind sector 150-180° at the suburban site illustrates greatest variability in spring summer and autumn (indicated by maximum whisker lengths in the boxplot, see Figure 6.45) and has an impervious fraction of 54% versus the site average of 34%. Increased variability in the magnitude of Q_E is likely attributed to periods of surface wetting and drying. Furthermore the surface cover in the 200 m upwind distance of the sensor is almost exclusively impervious (Figure 6.58); other wind sectors in this regard are punctuated with vegetated surfaces in 200m upwind distance which would serve to modulate Q_E (Figure 6.58).

With regard to urban site 1 increased variability in both $Q_H/Q\downarrow$ and $Q_E/Q\downarrow$ was observed in winter for wind sector 330-360°. The median ratios were broadly consistent with other wind sectors however upper quartile (UQ) ratios were larger than those for other wind sectors particularly in relation to Q_E/Q^* (e.g. 16% UQ value versus 7% UQ value for the predominant wind sector, 240-270°) (Figure 6.47d and Figure 6.48d). On closer inspection of the roughness characteristics, the wind sector 330-360° corresponds to higher mean building heights and large associated values reported for z_d and $C_D^{0.5}$; as a result surface fluxes in winter from this direction may be representative of the increasingly complex RSL. This wind sector represents a relatively small fraction of observations (<4% of total cases) and as a result effects on the total flux dataset are not considered to be significant.

In terms of inter-site differences the suburban site ratios of $Q_E/Q\downarrow$ are greater due to a larger vegetated surface fraction which promotes evaporation, for example median summer values of 8 and 5% were observed at the suburban site and urban site 1 respectively for the predominant wind sector (240-270°). Values at Swindon compare well with the suburban site whilst values reported for urban site 1 are at the upper bounds of those reported for London by Kotthaus and Grimmond (2014b). With regard to $Q_H/Q\downarrow$ median summer values for wind sector 240-270° are 11 and 17% at the suburban site and urban site 1 respectively and indicate the effect of a higher impervious surface fraction on the partitioning of energy.

Unlike Kotthaus and Grimmond (2014b) this investigation included fluxes after rainfall events, as a result there are slight observed increases in $Q_E/Q\downarrow$ for south-west to west wind sectors 180-300° that are likely attributed to frontally induced precipitation. Slight increases in median ratios were also observed for $Q_H/Q\downarrow$ prompting an analysis of u_* and wind speed observations. With regard to the suburban site wind speeds from these wind sectors are typically higher (e.g. >4 m s^{-1}, Figure 6.3) with higher associated u_* (e.g. 0.3-0.4 m s^{-1}, Figure 6.34a). Similarly at urban site 1, the slightly higher ratios corresponded to wind sectors with higher wind speeds (e.g. >4 m s^{-1}, Figure 6.6) and higher u_* (e.g. 0.6-0.7 m s^{-1}, Figure 6.35a). The median values of both $Q_H/Q\downarrow$ and $Q_E/Q\downarrow$ are broadly consistent across all sectors at the suburban site and urban site 1. The spatially consistent findings suggest that both EC systems are located sufficiently within their associated LCZs and that the relative consistency in surface cover fractions per wind sectors result in a spatially-blended local-scale signal for all seasons.

7.1.3 *The energy balance ratio and the storage heat flux*

The annual mean EBR at the suburban site was 0.85. Given the directional consistency reported for the turbulent heat fluxes it is less likely that non-closure is a result of differences in the upwind flux footprint. In addition the net radiation sensor effectively 'sees' the same portion of the underlying surface regardless of wind direction. This suggests that non-closure is more likely to be a result of a slight mismatch in the source areas of the net radiation sensor and the EC system. Sensor placement at the suburban site introduces bias in Q* and subsequently into estimates of $\Delta Q_{S\ OHM}$ given its dependency on the magnitude and timing of Q*. $\Delta Q_{S\ OHM}$ at the suburban site was found to agree well with estimates using the residual method (RES) when Q* was large; greater variability between the storage estimates are reported however during winter when Q* is significantly reduced. In winter $\Delta Q_{S\ OHM}$ is typically too negative in comparison to RES (e.g. -36 versus -18 W m^{-2}), this as a consequence leads to greater apparent available energy via $Q^*-\Delta Q_{S\ OHM}$ than is observed via the sum of Q_E+Q_H. Similar findings for the suburban site were reported by Ward et al. (2013) for Swindon where energy balance closure of around 100% was reported in summer, while in winter the energy balance was over closed by 20% (EBR ~0.8). The authors attribute the magnitude of the negative nocturnal flux to the negative a_3 coefficient in the OHM (e.g. a_3=-27 W m^{-2} in Swindon and a_3=-30 W m^{-2} at the suburban site, see Table 6.5). This

coefficient represents the magnitude of ΔQ_S when Q* is zero. This is likely to be too negative for winter however empirically-derived coefficients of a_3, such as those reported in Table 6.4, would need to be extended to include more winter-based observations that might yield more representative coefficients when Q* is reduced or negative in magnitude. Modelled annual mean values of Q_F (approximately 15 W m^{-2}) tentatively applied the suburban site SEB fluxes indicated greater agreement between the net available energy terms and net turbulent heat terms of the EBR. A more comprehensive investigation of Q_F, taking into account vehicular activity, will improve our understanding of the SEB at the suburban site, nevertheless the values presented in Section 0 provide a first estimate of Q_F. Similar to the suburban site estimates of ΔQ_S $_{OHM}$ at urban site 1 were shown to agree well with RES; inconsistencies were again observed between the storage estimates for small and negative values of Q* in winter (e.g. -38 and -50 W m^{-2} for RES and ΔQ_S $_{OHM}$ when Q* is -20 W m^{-2}) leading to EBRs of 0.87. This was similar to findings reported for Łódź, where values of 0.9 were reported for an urban location (Offerle et al., 2005b). Q_F estimates for urban site were typically double the magnitude or greater than those reported for the suburban site (annual mean of approximately 34 W m^{-2}). When the Q_F term is considered in the EBR (e.g. according to Offerle et al., 2005b) better agreement in the magnitude of the net available energy terms and net turbulent heat terms is achieved.

7.1.4 *The CO_2 flux*

This section will discuss key similarities and differences observed for F_C across the suburban and urban sites. The section will also address a key research question which is to determine whether the suburban site and urban site 1 are net sources or sinks of CO_2. Net seasonal and annual estimates of carbon exchange corresponding to the two neighbourhoods will be presented and key comparisons will be made with the international published literature.

The directional variability of F_C reported at the suburban site and urban site 1 revealed peak fluxes corresponding to wind sectors aligned with main roads and busy road intersections. This was similar to findings reported for locations in Melbourne (Coutts et al., 2007), Beijing (Song and Wang, 2012), Helsinki (Järvi et al., 2012), Swindon (Ward et al., 2013) and Essen (Kordowski and Kuttler, 2013). F_C at both Dublin sites report morning peaks coincident with commuter traffic. At urban site 1 F_C drops off following

morning rush hour and remains relatively constant throughout the day with the exception of winter. The median magnitude of the morning F_C peak at urban site 1 is reduced in summer relative to winter (e.g. 14 versus 22 µmol m^{-2} s^{-1} respectively). It is a constant source of CO_2 indicated by positive F_C for all days and all seasons. Results for Dublin in this regard are broadly consistent with temporal trends reported in the international literature. Peak values consistent with morning commuter traffic are commonly reported, the magnitude of which typically increases in winter. An urban location in Montreal for example, reports similar values for urban site 1 with regard to peak morning fluxes (e.g.11 versus 28 µmol m^{-2} s^{-1} in summer and winter respectively) (Bergeron and Strachan, 2012).

On the other hand the suburban site reports uptake in 3 seasons of the year, namely weekend days in spring and autumn and all days in summer. The diurnal trend in F_C is influenced by local anthropogenic sources associated with the school (e.g. vehicular traffic and respiration), vehicular traffic and domestic energy use. Nevertheless the role of vegetation as a local sink is apparent and serves to modulate F_C, particularly in summer when median F_C at midday is -4 µmol m^{-2} s^{-1}. F_C observed in Swindon reported similar seasonal values where mean uptake at midday in July 2011 was <-5 µmol m^{-2} s^{-1} (Ward et al., 2013). Unlike the suburban site however, F_C in Swindon does not reveal significant anthropogenic influences during the day, instead biogenic influences dominate the diurnal trend in summer. With regard to nocturnal values, inter-site differences in F_C for spring, summer and autumn across the sites rarely exceeded 2 µmol m^{-2} s^{-1}; in winter inter-site differences reported are 4 µmol m^{-2} s^{-1}. This trend is quite conservative given the difference in both the urban density (e.g. the built fraction) and population density (e.g. 1189 versus 4525 inh km^{-2}) of the suburban and urban site respectively (CSO, 2011).

The net seasonal and annual exchange for each site is presented in Table 7.2 and supports international findings. Similar to suburbs of Chicago (Grimmond et al., 2002), Swindon (Ward et al., 2013) and Essen (Kordowski and Kuttler, 2010) the urban vegetation at the suburban site has an effect during the day and in the growing season however it is not enough to offset the local-scale anthropogenic sources on a seasonal or annual basis. As a consequence the suburban site in Dublin is a net source of CO_2 (see Table 7.2). The mean daily carbon release (averages of monthly mean diurnal cycles)

ranges from 1.4 g C m^{-2} day^{-1} in summer to 8.3 C g m^{-2} day^{-1} in winter. Interestingly when weekend days in June were examined (e.g. in the absence of school-related influences, see Figure 6.43f) the mean daily exchange was 0.2 C g m^{-2} day^{-1} indicating that uptake via photosynthesis was close to offsetting all carbon release from the neighbourhood.

Table 7.2 Mean daily exchange of carbon (C) estimated for each season and estimated net total exchange of C at the suburban site and urban site 1. Missing daily data are gap filled using the equivalent monthly mean daily values.

Station	**Mean daily release (g C m^{-2} day^{-1})**				**Mean annual release (kg C m^{-2} $year^{-1}$)**
Season	Spring	Summer	Autumn	Winter	Year
Suburban site	3.4	1.4	5.2	8.3	1.67
Urban site 1	9.2	7.1	8.6	13.2	3.47

Mean daily carbon release observed at urban site 1 is consistently greater than the suburban site for all seasons (Table 7.2). Inter-site differences in the mean daily release of carbon are greatest in the summer; the urban site reports values 5 times greater than those reported for the suburban site. Inter-site differences are significantly reduced in winter (1.6 times) indicating the increase in domestic space heating and the absence of a vegetative role in offsetting suburban anthropogenic emissions. It should also be noted that CO_2 fluxes representing winter at the suburban site correspond to measurements from December 2010 and January and February 2011; December was the coldest on record according to observations at Met Éireann's Dublin Airport synoptic station (Met Éireann, 2010). Similarly very low air temperatures were observed at the suburban location at this time, minimum air temperatures observed reached –17° C (Figure 6.2a). Extremely low air temperatures would have increased the demand for space heating causing increased anthropogenic CO_2 contributions relative to typical winter air temperatures.

On an annual basis the two sites are net sources of CO_2. The estimated net annual release of carbon at the urban site is double that at the suburban location, 3.47 versus 1.67 kg C km^{-2} yr^{-1} (Table 7.2). This is unsurprising given 1) the limited vegetation fraction at urban site 1 (14%) relative to the suburban site (50%) which has relatively larger number of deciduous trees (Figure 5.7) and 2) the increased anthropogenic sources of CO_2 at urban site 1 relative to suburban site 1. In terms of international

findings, the estimated values for Dublin broadly correspond to values for similar LCZs (Table 7.3). Winter and annual estimates for the suburban site are very similar to a suburb of Montreal (Bergeron and Strachan, 2011) and Swindon (Ward et al., 2013); this indicates a relative consistency for findings representing the Open lowrise LCZ (Table 7.3).

Table 7.3 Table reproduced and modified from Christen (2014) to include seasonal and annual measured mass fluxes of carbon dioxide (F_C), at the suburban site and urban site 1 in Dublin. The locations are sorted by increased annual F_C (kg C m^{-2} $year^{-1}$). In many cases the values are multi-year averages. Positive numbers are net exchange of CO_2 from the surface to the atmosphere (emissions dominate), while negative numbers are cases where uptake dominates and CO_2 is sequestered by the urban biosphere rather than emitted. LCZ refers to the Local Climate Zone classification (Stewart and Oke, 2012) and λb is the plan area fraction of buildings in the tower source area (as reported by the various studies). In most cases, results are for long-term turbulent source areas (all wind directions), with the exception of 'Essen-Grugapark' where a conditional average of only an urbanised sector is shown.

Site	LCZ	λb	Daily Fco_2 (g C m^{-2} day^{-1}) Summer	Daily Fco_2 (g C m^{-2} day^{-1}) Winter	Annual Fco_2 (kg C m^{-2} $year^{-1}$) Year	References
Baltimore-Club Hill, USA (39°N)	Open lowrise	14%	-0.9	+3.8	+0.35	Crawford et al. (2011)
Montreal-Roxboro, Canada (46°N)	Open lowrise	12%	+0.5	+8.2	+1.48	Bergeron and Strachan (2011)
Suburban site, Dublin (53°N)	Open lowrise	16%	+1.4	+8.3	+1.67	This study
Swindon, UK (52°N)	Open lowrise	16%	+0.6	+9.5	+1.84	Ward et al. (2013)
Melbourne-Preston, Australia (38°S)	Open lowrise	46%	+5.9	+7.6	+2.31	Coutts et al. (2007)
Łódź-Lipowa, Poland (52°N)	Compact midrise	30%	+6.0	+9.9	+2.94	Pawlak et al. (2011)
Tokyo-Kugahara, Japan (36°N)	Compact lowrise	33%	+6.8	+10.6	+3.35	Moriwaki and Kanda (2004)
Urban site 1, Dublin (53°N)	Open midrise	31%	+7.1	+13.2	+3.47	This study
Basel-Klingelbergstrasse, Switzerland (48°N)	Compact midrise	38%	+6.8	+10.6	+3.63	Lietzke and Vogt (2013)
Essen-Grugapark, Germany (46°N)	Compact lowrise	59%	+5.9	+19.5	+3.94	Kordowski and Kuttler (2010)
Montréal-Rue des Écores, Canada (46°N)	Compact lowrise	27%	+9.8	+23.4	+5.64	Bergeron and Strachan (2011)
Vancouver-Sunset, Canada (49°N)	Open lowrise	29%	+16.4	+21.4	+6.71	Christen et al. (2011)

Open lowrise locations with higher (lower) built surface fractions revealed higher (lower) annual F_C (e.g. Baltimore, λb=14% versus Melbourne λb=46%, Table 7.3). The only location to report net seasonal uptake (e.g. -0.9 g C m^{-2} day^{-1} in summer) is a well-vegetated suburb of Baltimore, in this situation the vegetated surface fraction comprising of trees and grass accounted for 67% of the local-scale area. The role of the local-scale urban vegetation was almost strong enough to offset annual anthropogenic emissions (e.g. +0.35 kg C m^{-2} $year^{-1}$) (Crawford et al., 2011) (Table 7.3).

Weissert et al. (2014) recommends integrating available datasets from various methods to assess the mitigation potential of urban vegetation. Given the tree data available for the suburban and urban sites, future work may include allometric approaches similar to those employed by Velasco et al. (2013) who estimated CO_2 storage and sequestration rates per tree per year (kg $tree^{-1}$ $year^{-1}$) for a suburban location in Singapore. An analysis of the storage and sequestration rates of individual trees in the footprint of the Dublin EC sites would increasingly inform the role of vegetation and the directional variability of F_C reported in this thesis. The temporal and directional variability of F_C reported for both the suburban site and urban site 1 indicates a strong contribution from vehicular emissions to the total flux. Analysis of traffic flow and traffic fleet data would complement the research undertaken here and would strengthen the argument for a modal shift from private vehicle use to public transport. The effectiveness of such a shift would require an extension of current Irish government strategies, such as the cycle to work scheme, to beyond the working population, particularly given the influence of school-related traffic reported here.

7.1.5 *Fulfilment of eddy covariance assumptions*

This section examines the results of the observation campaign under the consideration of EC theoretical assumptions. It will discuss data quality in the context of urban international studies and outline why the results presented in the thesis are considered to be of good quality and representative of fluxes in the ISL. The 2 important criteria, steady state and well-developed turbulent conditions are evaluated by applying objective stationarity tests and examining the integral turbulence characteristics (ITCs) according to Foken et al. (2004) which simply describe the relationship between the standard deviation of a turbulent parameter and its associated flux or covariance.

Results of the stationarity test can be employed as a means to evaluate whether measurements are representative of the spatially-blended inertial sublayer (ISL) were fluxes are constant with height (Stull, 1988). Conditions of non-stationarity over an averaging period indicate inconsistencies in the vertical transport of heat and moisture more indicative of the RSL. Application of stationarity tests are considered as an effective and objective means for determining good quality flux estimates (Aubinet et al., 1999). Detailed information on the outcome of stationarity tests are limited in the urban EC literature nevertheless results from EC campaigns in Mexico City, Helsinki, Edinburgh and London can be presented. Velasco et al. (2009) report that stationarity criteria (e.g. where deviation of the 30 minute flux with 6 sub-interval 5 minute fluxes is less than 30%) were met greater than 70% of the time for F_C in Mexico City. Results relating to Dublin are similar whereby stationarity criteria are met for 70 and 67% of total available daytime fluxes of F_C for the suburban site and urban site 1 respectively. While findings for 3 urban EC sites in Helsinki report data rejection percentages of 18, 23 and 14% for F_C due to stationarity criteria (Nordbo et al., 2013). Nemitz et al. (2002) apply a different stationarity test following Dutaur et al. (1999) for Edinburgh, the net effect of which was 18% data rejection for F_C. In relation to EC measurements undertaken at a height of 190m agl in London, only 6% of data were rejected due to non-stationarity according to Foken et al. (2004); this indicates that EC system (circa 22 times the mean building height) was located well within the ISL and sometimes reported decoupling from the underlying surface (Helfter et al., 2011).

With regard to tests on the fulfilment of good turbulent conditions, the Dublin EC sites reported a high percentage of quality flags of class 1 and 2, particularly for the momentum flux (>80%). Flags of quality class 1 and 2 represent deviation of the measured ITCs of less than 30% from modelled ITCs indicating sufficient turbulent conditions. A high proportion of flags of quality 1 and 2 coupled with atmospheric stability and u_* datasets indicates that adequate turbulent conditions prevailed for the majority of the observational campaign; this increased for EC sites of increased building density. In general turbulence criteria are largely fulfilled in urban investigations and stable stratification of the UBL, suppressing vertical mixing, is rarely observed (e.g. Kanda and Moriwaki, 2004; Nordbo et al., 2012b; Kotthaus and Grimmond, 2014a).

Employing the EC technique assumes that advective effects via ΔQ_A are negligible when the measurement tower is located sufficiently within a homogeneous land surface; this allows for the properties of the air flow to come into equilibrium with the underlying surface (Oke, 2007). The suburban site and urban site 1 selected for this investigation largely satisfy the theoretical assumptions of horizontal homogeneity in the urban domain being located sufficiently within their associated LCZs (Figure 5.32). The directional consistency of the turbulent flux magnitudes (e.g. ratios $Q_E/Q\downarrow$ and $QH/Q\downarrow$) for each wind sector supports this point and advective effects are therefore assumed to be minimal. Urban site 2, located in Dublin city centre is more complex and presents challenges when interpreting the turbulent fluxes. As outlined the EC tower is located at a boundary of two distinctive LCZs (Figure 5.32); horizontal gradients may develop inducing advective effects. Nevertheless urban EC studies have been undertaken along similar boundaries and future work will require careful stratification and analysis of the turbulent heat and CO_2 fluxes.

7.2 Observational and methodological considerations

The research undertaken relies on direct measurements of meteorological variables in the urban domain. The EC method is well-established internationally and allows for the continuous, non-intrusive measurement of surface-atmospheric exchanges. Placement of the micro-meteorological instruments is however of significant importance and affects the validity and representativeness of the fluxes. With regard to the suburban site the placement of the net radiometer on the roof of St Pius X School meant that the source area of the downward facing pyranometer and pyrgeometer largely comprised of the dark asphalt roof surface. This surface has different properties than the surrounds of the suburban site which comprises of a range of lighter and more vegetated surfaces; as a result the upwelling radiation fluxes of $K\uparrow$ and $L\uparrow$ and α were affected. Similar to the published literature the findings suggest that placement of net radiometers requires careful consideration of the site surrounds and identification of erroneous surfaces that will obstruct complete measurement of all incoming and outgoing radiation fluxes (Oke, 2007; Kotthaus and Grimmond, 2014b). It is suggested that multiple net radiometers in the vicinity of the EC sensors will allow for an increasingly spatial representation of Q* in more complex urban locations.

The precipitation gauge at the suburban site was mounted on a structure adjacent to the measurement tower and was not sheltered from the building. Whilst this is beneficial in that the interception of rainfall was not affected, maintenance of the instrument was difficult and hence precipitation observations became more uncertain in between cleaning due to the build up of debris and algae in the gauge. Nevertheless precipitation from a standard weather station on the school grounds was used to supplement periods of suspect and/or missing data.

Precipitation observations were used in unison with EC instrument diagnostics and quality flagging criteria to determine periods when 1) measurement accuracy is reduced relating to the sonic anemometer and infrared gas analyser and 2) the theoretical EC assumptions are not met via stationarity and turbulence criteria. Percentages of data rejection relating to these criteria were substantial, particularly for Q_E and F_C measured by the open-path gas analysers at the suburban site (31 and 41%) and urban site 1 (22 and 34%) (Table 6.2). Similar data rejection percentages have been reported in the international literature, for example, Nordbo et al. (2013) report data rejection of between 29-45% for Q_E and 14-23% for F_C at the 3 urban EC sites in Helsinki. Similarly, Goldbach and Kuttler (2012) report 60 and 61.5% rejection of the total flux data at their urban and suburban site respectively. A long term observation period spanning five years in Baltimore, USA, reports data availability of 53.3% relating to hourly estimates of F_C (this ranges between 45.4 to 72.3% per month) (Crawford et al., 2011).

Feigenwinter et al. (2012) in a review of urban EC measurements suggest that EC investigators should follow the established processing techniques applied in homogeneous environments whilst taking particular care to address potential flow distortion by the immediate surrounds of the EC site. An analysis of the angle of attack at each of the Dublin EC sites yielded different results. The suburban site angle of attack rarely deviated from 0° indicating limited flow distortion from the site surrounds. Urban site 1 reported increased angles of attack, for example -3° to +5° that are likely a result of taller buildings in the northerly direction and the building geometry in the southerly direction. The relative frequency of wind from these sectors was rare. In relation to urban site 2 deflection angles were the greatest (e.g. 7° corresponding to the northern edge of the building) however for the frequent wind directions deflection was 3° or less.

International findings report angles of attack of 3-13° for Helsinki (Nordbo et al., 2012) and 6-8° for London (Barlow et al., 2011). In the case of the 3 Dublin EC sites the angles of attack were within acceptable ranges of ±45° reported for the deployed sonic anemometers and are consistent with the published literature relating to EC towers in urban areas. Therefore flow distortion by the towers and site surrounds at the Dublin EC sites is not considered to be severe. Careful siting of the instruments is important however knowledge of the prevailing synoptic scale conditions at a location should inform the appropriate siting of the instruments. Whilst urban site 2 is subject to micro-scale building effects, the frequency of wind from the most affected wind sectors is relatively small (<5%). Coupled with information on the building effects/flow distortion effects, urban climatologists can account for these inaccuracies and limitations via data post-processing techniques, quality flagging techniques and via visual inspection of the flux.

Observational challenges in the urban domain may arise due to issues regarding physical site access and network access. In the case of Dublin site access did not pose a significant problem and data could be physically retrieved with relative ease. A lack of network access at the suburban site meant that physical data retrieval was required and that high frequency data and instrument diagnostics could not be monitored in real time. This was similar to urban site 1 and had implications for data availability; where problems cannot be readily identified the risk of data loss due to instrument problems or power supply issues increased. On the other hand network access allowed for real time monitoring of high frequency data and instrument diagnostics at urban site 2. This is increasingly necessary where Li7200 gas analysers are deployed which require flow modules to regulate air flow in the sampling tube. Problems identified from off-site inspection of the real-time diagnostics allowed for instrument problems to be identified relatively quickly. As suggest by Mauder et al. (2013) urban EC investigators should also record high resolution instrument diagnostics to allow for tests on high-frequency data, this would allow for sub-half hourly problems to be accounted for without the necessity to remove the entire half hour flux estimate from the analysis, if you replace the instantaneous measurements with NAN values the periods of instrumental problems may be short, accounting for less than 10% for example of the 30 min interval. This measure would likely retain a greater proportion of processed data.

An enclosed-path gas analyser (Licor model Li7200) was deployed at urban site 2 to measure atmospheric CO_2 and H_2O; the instrument has optimal features in comparison to open-path gas analysers (Burba et al., 2010). In this investigation the relative percent of data rejection with regard to Q_E and F_C measured by the Li7200 was reduced (Table 6.2). In addition flux estimates during precipitation events were not removed from data analysis. This allows for Q_E to be measured during and after rainfall periods when the flux is likely to be largest in magnitude. The reported fluxes for urban site 2 were of similar magnitude to those observed at the suburban site (e.g. Figure 6.41 and Figure 6.42). This point raises concerns regarding the representativeness of fluxes estimated by widely used open-path gas analysers (e.g. Licor model Li7500), particularly in temperate climates experiencing frequent rainfall. It is common practice to remove turbulent fluxes from the record during and after precipitation events; this post-processing technique essentially induces a bias towards dry conditions in the record, and an overall underestimation of Q_E. The Li7200 has optimal features in that rainfall does not affect the measurement of atmospheric CO_2 and H_2O; as a result the percent of data rejection is reduced for Q_E and F_C relative to Li7500 measured fluxes (Table 6.2).

A direct comparison of open – and enclosed – path gas analysers was beyond the scope of this thesis however an investigation of this kind would be beneficial and would yield detailed information about the relative effects of each gas analyser on data retention. Nordbo et al. (2012) reports findings for Q_E from closed – and open – path gas analysers; the results suggest similar flux magnitudes on average however maximum values of Q_E were typically higher for the closed-path analyser suggesting that it is more capable of measuring the extreme values, during or following precipitation events. In addition significant data gaps in the Q_E record pertaining to open-path analyser did not appear in the simultaneous record of the closed-path analyser suggesting greater data retention.

As outlined in Chapter 4 multiple EC software are currently available for processing high frequency raw data. The software comparison did reveal inconsistencies in the application of published data despiking algorithms (see Appendix II for more details). This applied to all three of the software compared whereby, for example fluxes from wind sectors corresponding to the c-clamp structure of the sonic anemometer were not flagged according to the conditions proposed by Foken et al. (2004) and outlined

previously (Table 4.4). Overall however when the resultant data was compared, the fluxes of Q_H, Q_E and F_C yielded very similar flux estimates. Following the software comparison, EddyPro was identified as the most flexible software package for use in urban EC investigations. It is freely available and is frequently updated to implement novel correction methods; more importantly comprehensive output file are provided in addition to up-to-date manual documentation. A software comparison of this nature has not been undertaken in the urban domain and provided useful insights into the limitations and benefits of certain software for application in urban EC investigations. In addition the software comparison supports previous findings carried out in software comparisons undertaken for managed ecosystems (e.g. Mauder et al. 2007b; Mauder et al., 2008; Fratini and Mauder, 2014). The comparison undertaken in the urban domain used 12 weeks of data as oppose to previously published work that typically used smaller datasets of between 5 days to 4 weeks; in this regard the comparison findings, reported in Chapter 4, provide additional confidence in EC software.

A recommendation of relevance to EC software developers is the incorporation of land cover and building height data sets representing urban areas in the estimation of the turbulent flux footprint. At present there are no operational models available for urban environments that account for topography and spatial variability in the roughness elements; instead analytical models like those employed here for Dublin developed by Kormann and Meixner (2001) assume horizontal homogeneity. Despite their limitations analytical models account for non-neutral stratification, often observed in urban areas, and are frequently employed in urban EC investigations as an approximation of the flux footprint (e.g. Helfter et al., 2011; Nordbo et al., 2013; Goldbach and Kuttler, 2013).

Despiking tests in current EC software vary in their application and their associated output. Most software test the plausibility (see Table 4.2) of each data point; if it lies outside of particular bounds it is deemed as physically implausible (Vickers and Mahrt, 1997). At present the EddyPro software outputs the number of spike events per half hour and per variable alongside windspeed and wind direction data. In this way it is possible to explore the number of spike events occurring according to wind direction and according to time. Whilst this does not provide the user with data at a higher resolution it is nonetheless useful to examine this data for erroneous or unusual trends

that could indicate micro-scale effects similar to those reported in London by Kotthaus and Grimmond (2012).

If current trends continue it is anticipated that the number of EC systems in urban areas will increase. Whilst the urban domain requires increased consideration in terms of instrument siting, the field should strive to develop uniform data acquisition, data processing and post-processing techniques. In doing so the techniques should be straightforward where possible and practically feasible in their application. For example inspection of individual half hourly ogives and cospectral curves is somewhat unrealistic; instead EC investigators should inspect these at the outset of the observational campaign, and for different times of day and atmospheric stabilities to determine the most appropriate averaging period for calculating covariances. Where convergence of ogives did not occur in Dublin (see Figure 4.13) it was found that application of a dynamical averaging period was not possible in any EC available software, furthermore there was no evidence of the use of dynamic averaging periods in the literature. More realistic methods to ensure that theoretical assumptions are met are via the objective application of quality tests like those set out in Foken et al. (2004). The flagging system employed in this method is more useful for the urban domain than methods proposed Mauder and Foken (2004) where data quality is assigned as 0, 1 or 2 representing best quality, standard quality and worst quality data that should be discarded. The user in this case does not yield as much information about the fulfilment of the theoretical tests in comparison to quality flags of class 1-9.

7.3 Research implications

The drag coefficient, relating the momentum flux to the mean wind profile is an important parameter for numerical weather prediction models and wind-profile predictions. However there are few urban based observations available to support the theoretical logarithmic wind profile in urban areas (Roth, 2000). This investigation contributes to the small but growing number of urban observations. Mean $C_D^{0.5}$ derived here (0.15, 0.16 and 0.10 for the suburban site, urban site 1 and urban site 2 respectively) using EC measurements agrees well with the published literature, for example Weber and Kordowski (2010) report mean $C_D^{0.5}$ equal to 0.13 and 0.15 at an urban and suburban location in Essen, Germany. Estimates for Dublin derived from an empirical expression based on different urban observations as reported in Roth (2000)

agree well with those derived from the EC measurements. Both values presented in Table 6.3 for $C_D^{0.5}$ lie on the empirical curve for the drag coefficient as a function of z/z_H. When compared to international values from over ten EC sites outlined in Nordbo et al. (2013) the 3 EC sites are also likely to collapse on the curve predicted by the logarithmic profile.

The surface albedo (α) derived from EC measurements here will also prove useful for application in numerical models particularly given the range of values reported here as a result of snow free and snow cover conditions observed during the observation period. The urban surface of Dublin reported α typical of winter time conditions reported for rural and suburban locations in Montreal, Canada which has a continental climate (Bergeron and Strachan, 2012). The atmospheric stability parameter (ζ) presented here provides detailed datasets for 3 urban locations of differing density. This parameter is important for air pollution dispersion models and gives an indication of the near-surface atmosphere's ability to disperse harmful pollutants emitted at or close to the surface. This investigation contributes to a relatively small number of investigations that report detailed information relating to ζ at half-hourly to hourly timescales (e.g. Lietzke and Vogt, 2013). The nocturnal UBL for Dublin tends towards neutral and unstable stratification as a result of heat released from the urban substrate, similar to findings reported internationally (e.g. Arnfield, 2003; Christen and Vogt, 2004; Grimmond et al., 2004; Weber and Kordowski, 2010; Kotthaus and Grimmond, 2014a; Nordbo et al., 2013). In Dublin unstable conditions increased in frequency with increasing building density. Furthermore the development of the stable nocturnal UBL is rare and occurs most often at the suburban site; this is similar to findings observed in Basel where the occurrence of stable conditions decreased with increasing urban density (Christen and Vogt, 2004). The relative paucity of observed stable atmospheric conditions in urban areas has implications for numerical model validation, particularly since these conditions are conducive to poor air quality episodes.

The observation campaign spanning almost 3 years represents a broad range of synoptic conditions, the simultaneous measurements at the suburban site and urban site 1 allowed for changes in the estimated fluxes to be examined under different external forcings. Seasonal average synoptic conditions varied over the observational campaign and several anomalies were reported, for example, December 2010 was reported as the

coldest on record (Met Éireann) and the summer of 2012 reported 188% of seasonal LTA rainfall for Casement Aerodrome station near Dublin (Met Éireann). Long term EC observations such as those reported in this thesis are important from a numerical modelling perspective whereby testing and validation can be undertaken for a range of initial conditions. Furthermore simultaneous datasets that include site-specific parameters (e.g. α, ζ and $C_D^{0.5}$, z_0 and z_d) from within the same city allow for more educated selection of parameters for city-wide numerical simulations. From an observations perspective the simultaneous datasets also allowed for a more informed interpretation of the research findings, for example, with regard to α and $K\uparrow$ at the suburban site. Results containing bias were more readily identified that may have otherwise been accounted for in the absence of two simultaneous EC datasets.

Data losses can be significant, as described in Section 7.2. In most situations these can be reduced with the use of an enclosed-path gas analyser (e.g. model Li7200) and real-time monitoring of raw data. The financial cost of operating and maintaining EC systems in addition to auxiliary instruments is significant, particularly given that anywhere between 20-60% of the data will be unsuitable for data analysis. The financial demand of such observational campaigns has implications for the international urban climate community when there is an imperative to extend these measurements to cities located in developing countries which may not have access to the same resources.

Common flux and flow characteristics are becoming increasingly evident from the published literature; mid-latitude, developed cities, particularly suburbs, are well-represented in the international urban flux network. The data presented in this thesis contributes to this category, representative of maritime temperate climates, Cfb according to the Köppen Classification System. EC campaigns in this category also include those undertaken in Copenhagen, London, Swindon, Essen, Oberhausen, Edinburgh, Melbourne, Christchurch and Vancouver. The focus of undertaking single tower EC measurements campaigns in the future should be shifted towards cities of differing urban morphologies that represent other climate classifications.

7.4 Final conclusions

The research presented was the first attempt at investigating radiative, energy and CO_2 fluxes over an urban surface in Ireland. Key inter-site differences in the radiation

balance were observed where Q* is reduced by between 7.5-10% at the urban site. Examination of key parameters such as the surface albedo demonstrated the importance of the appropriate siting of radiation and EC sensors in the urban domain. The turbulent heat fluxes were analysed in unison with surface cover and roughness properties; inter-site differences related to the magnitude of the Q_E and Q_H were attributed to site-specific surface cover fractions. The suburban location with a high vegetation fraction (50%) reported consistently higher Q_E throughout the year. While the urban site with a small vegetation surface fraction (14%) reported consistently higher Q_H in all seasons. Inter-site differences were most pronounced in summer when Q_H was +30 and +15 W m^{-2} at local solar noon and throughout the night time at the urban location. With regard to Q_E the suburban location was reported as the most effective evaporation area; this trend was more pronounced in winter when Q_E became the dominant turbulent heat flux reporting Bowen ratios less than 1. The storage heat flux was a significant component of the surface energy budget and was slightly greater in magnitude at the urban site. Flux ratios representing $\Delta Q_S/Q^*$ report negative values in winter indicating a seasonal loss of heat from the urban substrate; this is expected given that annual net heat storage must be negligible. Direct treatment of the Q_F via inventory methods was beyond the scope of this study however anthropogenic contributions of heat and moisture are considered to be included in the measured fluxes. Energy balance ratios greater than 1 reported for the urban and suburban sites (EBR of 1.2) indicate this contribution of Q_F to the measured turbulent heat fluxes.

The relative strength of the turbulent heat fluxes gives rise to distinct local climates and as a result knowledge of their timing, partitioning and magnitude is central to understanding inter-city, local-scale climate variations in addition to identifying adverse local-climate conditions experienced by urban dwellers. Simultaneous observations allowed for the spatial variability of the surface energy budgets to be investigated. In winter with reduced Q* the surface energy budget was relatively uniform across the suburban and urban sites. On the other hand summer time reported a reduction in evaporative cooling via Q_E and an intensification of Q_H at urban site 1, where energy is preferentially channelled into heating the near surface atmosphere. The increased partitioning of Q_H in summer time is significant as it coincides with greater risk of the occurrence of extreme heat events (EHEs). Furthermore energy stored in the substrate and released during the night will only serve to enhance nocturnal near surface

temperatures, conducive to extreme UHI conditions. Increased sealed surface fractions, like that reported for urban site 1 intensifies the channelling of Q* into Q_H and raises air temperatures. Simple urban design measures that increase the pervious fraction of urban areas will serve to enhance their evaporation potential and hence the production of cool air. In developed cities brown field sites could be redeveloped into vegetated spaces. In order to ensure sufficient water is available for evaporation a combination of irrigation and water retention strategies would need to coincide with the extension of pervious surfaces in cities. With regard to cities in construction careful consideration of the synoptic climate conditions must be considered in urban design. For example prior knowledge of the wind climatology facilitates the design and orientation of urban canyons that promote ventilation.

The research also undertook the first attempt at estimating emissions of CO_2 from the urban surface of Dublin via direct methods and contributes to a small urban global database of CO_2 fluxes. Global gridded CO_2 emissions at a spatial scale of 0.1°, like those presented in Figure 1.2 remain too coarse to ascertain the precise emissions from cities and their surrounds. The results of annual emissions presented here are +1.67 and +3.47 kg C m^{-2} yr^{-1} for the suburban site and urban site 1 and are consistent with international findings, particularly for corresponding LCZs. Emissions estimates such as these will be important for city-inventory validation aimed at ascertaining the precise contribution of cities to the global carbon budget particularly given that they account for CO_2 sinks in their measurement (e.g. Helfter et al., 2011). The latter point is important given that net effect of city efforts to mitigate CO_2 emissions via tree planting initiatives remains unaccounted for in traditional inventory approaches. The National Atmospheric Emissions Inventory (NAEI) in the England for example omits both biosphere and human exhalation contributions to estimated fluxes which are accounted for with EC flux estimates.

Using the LCZ classification scheme as a conceptual framework we can begin to make tentative estimates about the emission of CO_2 for greater portions of the Greater Dublin Area (GDA). Previous work undertaken by Alexander and Mills (2014) presented in Chapter 5 complements the research undertaken here; the city-wide LCZ map clearly disaggregates the GDA into 1 kilometre square grids, each representative of an LCZ. Although the urban site was estimated to emit double the CO_2 compared to the suburban

site the relative extent of Open lowrise LCZs in the GDA is significant. This LCZ accounts for >200 grid squares compared to 11 for Open midrise. From a mitigation perspective it could be suggested that geographically-focussed mitigation strategies should target Open lowrise type settlements for greatest efficacy.

Population projections for the GDA indicate a population increase of 400,000 people between 2016-2031; this accounts for two thirds of the total projected growth for Ireland (CSO, 2013). This growth has significant implications for urban planning and land use. In order to accommodate for an increasing population, green field sites located on the urban fringes of the GDA, currently classified as Low Plant LCZs will most likely be affected (Figure 5.32). In order to avoid significant land use change on the urban periphery, which will serve to increase reliance on private vehicle use and anthropogenic emissions, urban design must implement strategies to develop brown field sites and limit traditional development patterns that lead to sprawling low density settlements.

Urban climate studies are overcoming initial problems in the field associated with defining urban climate effects according to simple urban versus rural definitions. This progression has been demonstrated via the widespread use of LCZs to describe and report observational findings, for example, related to the CO_2 flux. Increasingly informed cross-site comparisons can be made and provide EC investigators with explanatory power when reporting observations in relation to other international findings. Use of the LCZ system has also highlighted particular LCZs that we know relatively little about (e.g. Lightweight lowrise), particularly with regard to (sub) tropical climates. This research contributes to a growing EC database related to cities in developed countries with typically maritime temperate climates (Cfb). The EC observational network needs to be extended to include measurements from rapidly urbanising countries such as India, China and Nigeria. In the absence of EC observations it can be argued that certain urban landscapes (e.g. central business districts) worldwide do not differ substantially in their physical form and that useful climate information from measurement and modelling techniques could be applied to new cities under construction. On the other hand the development of light lowrise settlements on the fringes of cities in developing countries are home to an increasing

portion of the urban population of large and mega cities worldwide; for these urban morphologies we know relatively little.

Understanding the nature of the urban boundary layer (UBL) is imperative; it is where a growing proportion of humans reside and work and as a result it must be a sustainable environment in which to conduct these activities. Investigating local-scale climates within the UBL is of paramount importance if we wish to improve the skill of numerical modelling techniques and create urban areas that are more resilient to future projected climate change. Urban design needs to consider human dwellers as direct and active users of the urban atmosphere, which as this research has shown, is altered by both the urban from (e.g. increased air temperatures via Q_H as a result of increased impervious surfaces) and the urban function (e.g. via the emission of waste heat, moisture and pollutants). In the absence of this consideration cities will continue to be constructed in such a way that they generate outdoor climates that are harmful to human health.

Bibliography

Adebayo, Y.R. (1990) Aspects of the variation in some characteristics of radiation budget within the urban canopy of Ibadan. *Atmospheric Environment. Part B. Urban Atmosphere*. **24**(1), 9–17.

Aida, M., Yaji, M. (1979) Observations of atmospheric downward radiation in the Tokyo area. *Boundary-Layer Meteorology*. **16**(3), 453–465.

Alexander, P.J., Mills, G. (2014) Local Climate Classification and Dublin's Urban Heat Island. *Atmosphere*. **5**(4), 755–774.

Alexander, P.J., Fealy, R., Mills, G. (*in review*) Simulating the impact of different urban development pathways on the local climate: a case study of a mid-latitude city. Submitted to: *Landscape and Urban Planning. Manuscript number: LAND-D-15-00596.*

Allwine, K.J., Leach, M.J., Stockham, L.W., Shinn, J.S., Hosker, R.P., Bowers, J.F., Pace, J.C. (2004) *Overview of Joint Urban 2003—an atmospheric dispersion study in Oklahoma City*. In: Symposium on Planning, Nowcasting and Forecasting in the Urban Zone, Seattle, WA, American Meteorological Society.

Allwine, K.J., Shinn, J.H., Streit, G.E., Clawson, K.L., Brown, M. (2002) Overview of URBAN 2000: A multiscale field study of dispersion through an urban environment. *Bulletin of the American Meteorological Society*. **83**(4), 521–536.

Anandakumar, K. (1999) A study on the partition of net radiation into heat fluxes on a dry asphalt surface. *Atmospheric Environment*. **33**(24), 3911–3918.

Andres, R.J., Marland, G., Fung, I., Matthews, E. (1997) *Geographic Patterns of Carbon Dioxide Emissions from Fossil-Fuel Burning, Hydraulic Cement Production, and Gas Flaring on a One Degree by One Degree Grid Cell Basis: 1950 to 1990*. Carbon Dioxide Information Analysis Centre, Oak Ridge National Laboratory: Oak Ridge, Tennessee; Environmental Science Division No. 4646.

Arnfield, A.J. (2003) Two decades of urban climate research: a review of turbulence, exchanges of energy and water, and the urban heat island. *International Journal of Climatology*. **23**(1), 1–26.

Arya, P.S. (2001) *Introduction to micrometeorology*. Second Edition. London: Academic press.

Asaeda, T., Ca, V.T. (1993) The subsurface transport of heat and moisture and its effect on the environment: a numerical model. *Boundary-Layer Meteorology*. **65**(1-2), 159–179.

Asefi-Najafabady, S., Rayner, P.J., Gurney, K.R., McRobert, A., Song, Y., Coltin, K., Huang, J., Elvidge, C., Baugh, K. (2014) A multiyear, global gridded fossil fuel CO2 emission data product: Evaluation and analysis of results. *Journal of Geophysical Research: Atmospheres*. **119**(17), 10–213.

Aubinet, M., Feigenwinter, C., Heinesch, B., Laffineur, Q., Papale, D., Reichstein, M., Rinne, J., Gorsel, E.V. (2012) Nighttime Flux Correction. In Aubinet, M., Vesala, T., Papale, D., eds. *Eddy Covariance*. Springer Atmospheric Sciences. Springer Netherlands, pp. 133–157.

Aubinet, M., Grelle, A., Ibrom, A., Rannik, Ü., Moncrieff, J., Foken, T., Kowalski, A.S., Martin, P.H., Berbigier, P., Bernhofer, C., Clement, R., Elbers, J., Granier, A., Gunwald, T., Morgenstern, K., Pilegaard, C., Rebmann, Snijders, W., Valentini, R., Vesala, T. (1999) Estimates of the annual net carbon and water exchange of forests: the EUROFLUX methodology. *Advances in Ecological Research*. **30**, 113–175.

Baldocchi, D.D. (2003) Assessing the eddy covariance technique for evaluating carbon dioxide exchange rates of ecosystems: past, present and future. *Global Change Biology*. **9**(4), 479–492.

Balogun, A.A., Adegoke, J.O., Vezhapparambu, S., Mauder, M., McFadden, J.P., Gallo, K. (2009) Surface Energy Balance Measurements Above an Exurban Residential Neighbourhood of Kansas City, Missouri. *Boundary-Layer Meteorology*. **133**(3), 299–321.

Barlow, J.F., Harrison, J., Robins, A.G., Wood, C.R. (2011) A wind-tunnel study of flow distortion at a meteorological sensor on top of the BT Tower, London, UK. *Journal of Wind Engineering and Industrial Aerodynamics*. **99**(9), 899–907.

Barriopedro, D., Fischer, E.M., Luterbacher, J., Trigo, R.M., García-Herrera, R. (2011) The Hot Summer of 2010: Redrawing the Temperature Record Map of Europe. *Science*. **332**(6026), 220–224.

Bergeron, O., Strachan, I.B. (2012) Wintertime radiation and energy budget along an urbanization gradient in Montreal, Canada. *International Journal of Climatology*. **32**(1), 137–152.

Brazel, A., Selover, N., Vose, R., Heisler, G., others (2000) The tale of two climates-Baltimore and Phoenix urban LTER sites. *Climate Research*. **15**(2), 123–135.

Brest, C.L. (1987) Seasonal albedo of an urban/rural landscape from satellite observations. *Journal of Climate and Applied Meteorology*. **26**(9), 1169–1187.

Burba, G. (2013) *Eddy Covariance Method for Scientific, Industrial, Agricultural and Regulatory Applications: A Field Book on Measuring Ecosystem Gas Exchange and Areal Emission Rates*. LI-COR Biosciences.

Burba, G.G., McDermitt, D.K., Grelle, A., Anderson, D.J., Xu, L. (2008) Addressing the influence of instrument surface heat exchange on the measurements of CO2 flux from open-path gas analyzers. *Global Change Biology*. **14**(8), 1854–1876.

Burba, G., Schmidt, A., Scott, R.L., Nakai, T., Kathilankal, J., Fratini, G., Hanson, C., Law, B., McDermitt, D.K., Eckles, R., others (2012) Calculating CO2 and H2O eddy covariance fluxes from an enclosed gas analyzer using an instantaneous mixing ratio. *Global Change Biology*. **18**(1), 385–399.

Campbell Scientific (2004) Model HMP45C temperature and relative humidity probe instruction manual (version 8/04), Logan, Utah.

Campbell Scientific (2014) CSAT3 Three dimensional sonic anemometer instruction manual, Logan, Utah.

Central Statistics Office, (2011) *Census 2011 Profile 1: Town and County*. Cork.

Central Statistics Office, (2011) *Census 2011 Profile 4: The roof over our heads – Housing in Ireland*. Cork.

Central Statistics Office, (2013) *Regional Population Projections 2016 - 2031*. Cork.

Christen, A. (2014) Atmospheric measurement techniques to quantify greenhouse gas emissions from cities. *Urban Climate*. **10**(2), 241-260.

Christen, A., Coops, N.C., Crawford, B.R., Kellett, R., Liss, K.N., Olchovski, I., Tooke, T.R., Van Der Laan, M., Voogt, J.A. (2011) Validation of modeled carbon-dioxide emissions from an urban neighborhood with direct eddy-covariance measurements. *Atmospheric Environment*. **45**(33), 6057–6069.

Christen, A., Vogt, R. (2004) Energy and radiation balance of a central European city. *International Journal of Climatology*. **24**(11), 1395–1421.

Coutts, A.M., Beringer, J., Tapper, N.J. (2007) Characteristics influencing the variability of urban CO2 fluxes in Melbourne, Australia. *Atmospheric Environment*. **41**(1), 51–62.

Cowling, E.B., Chameides, W.L., Kiang, C.S., Fehsenfeld, F.C., Meagher, J.F. (1998) Introduction to special section: Southern Oxidants Study Nashville/Middle Tennessee Ozone Study. *Journal of Geophysical Research: Atmospheres (1984–2012)*. **103**(D17), 22209–22212.

Cowling, E.B., Chameides, W.L., Kiang, C.S., Fehsenfeld, F.C., Meagher, J.F. (2000) Introduction to special section: southern oxidants study Nashville/Middle Tennessee ozone study, Part 2. *Journal of Geophysical Research: Atmospheres (1984–2012)*. **105**(D7), 9075–9077.

Crawford, B., Grimmond, C.S.B., Christen, A. (2011) Five years of carbon dioxide fluxes measurements in a highly vegetated suburban area. *Atmospheric Environment*. **45**(4), 896–905.

Cros, B., Durand, P., Cachier, H., Drobinski, P., Frejafon, E., Kottmeier, C., Perros, P.E., Peuch, V.-H., Ponche, J.-L., Robin, D., others (2004) The ESCOMPTE program: an overview. *Atmospheric Research*. **69**(3), 241–279.

Van Dijk, A., Kohsiek, W., de Bruin, H.A. (2003) Oxygen sensitivity of krypton and Lyman-α hygrometers. *Journal of Atmospheric and Oceanic Technology*. **20**(1), 143–151.

Doll, D., Ching, J.K.S., Kaneshiro, J. (1985) Parameterization of subsurface heating for soil and concrete using net radiation data. *Boundary-Layer Meteorology*. **32**(4), 351–372.

Doran, J.C., Berkowitz, C.M., Coulter, R.L., Shaw, W.J., Spicer, C.W. (2003) The 2001 Phoenix Sunrise experiment: vertical mixing and chemistry during the morning transition in Phoenix. *Atmospheric Environment*. **37**(17), 2365–2377.

Doran, J.C., Bian, X., de Wekker, S.F.J., Edgerton, S., Fast, J.D., Hubbe, J.M., Shaw, W.J., Whiteman, C.D., Abbott, S., King, C. (1998) The IMADA-AVER boundary layer experiment in the Mexico City area. *Bulletin of the American Meteorological Society*. **79**(11), 2497–2508.

Doran, J.C., Fast, J.D., Horel, J. (2002) The VTMX 2000 campaign. *Bulletin of the American Meteorological Society*. **83**(4), 537–551.

Dutaur, L., Cieslik, S., Carrara, A., Lopez, A. (1999) *The detection of non-stationarity in the determination of deposition fluxes*. In: Proceedings of EUROTRAC Symposium 1998, Vol. 2. WIT Press, Southampton, pp. 171–176.

Eugster, W., Senn, W. (1995) A cospectral correction model for measurement of turbulent NO2 flux. *Boundary-Layer Meteorology*. **74**(4), 321–340.

Fast, J.D., Doran, J.C., Shaw, W.J., Coulter, R.L., Martin, T.J. (2000) The evolution of the boundary layer and its effect on air chemistry in the Phoenix area. *Journal of Geophysical Research: Atmospheres (1984–2012)*. **105**(D18), 22833–22848.

Feigenwinter, C., Vogt, R., Christen, A. (2012) Eddy Covariance Measurements Over Urban Areas. In Aubinet, M., Vesala, T., Papale, D., eds. *Eddy Covariance*. Springer Atmospheric Sciences. Springer Netherlands, pp. 133–157.

Ferreira, M.J., de Oliveira, A.P., Soares, J. (2013) Diurnal variation in stored energy flux in São Paulo city, Brazil. *Urban Climate*. **5**, 36–51.

Finnigan, J.J. (2004) A re-evaluation of long-term flux measurement techniques Part II: coordinate systems. *Boundary-Layer Meteorology*. **113**(1), 1–41.

Finnigan, J.J., Clement, R., Malhi, Y., Leuning, R., Cleugh, H.A. (2003) A Re-Evaluation of Long-Term Flux Measurement Techniques Part I: Averaging and Coordinate Rotation. *Boundary-Layer Meteorology*. **107**(1), 1–48.

Foken, T. (2008a) *Micrometeorology*. Second Edition. Berlin Heidelberg: Springer.

Foken, T. (2008b) The energy balance closure problem: an overview. *Ecological Applications*. **18**(6), 1351–1367.

Foken, T., Aubinet, M., Leuning, R. (2012a) The Eddy Covariance Method. In Aubinet, M., Vesala, T., Papale, D., eds. *Eddy Covariance*. Springer Atmospheric Sciences. Springer Netherlands, pp. 1–19.

Foken, T., Göockede, M., Mauder, M., Mahrt, L., Amiro, B., Munger, W. (2004) Post-field data quality control. In Lee, X., Massman, W.J., Law, B.E. eds. *Handbook of Micrometeorology*. Springer, pp. 181–208.

Foken, T., Jegede, O.O., Weisensee, U., Richter, S.H., Handorf, D., Görsdorf, U., Vogel, G., Schubert, U., Kirzel, H.J., Thiermann, V. (1997) Results of the LINEX-96/2 Experiment. Dt Wetterdienst, Forsch, Entwicklung, Arbeitsergebnisse, Dt Wetterdienst, Gerschäftsbereich Forshung und Entwicklung, Offenbach am Main, pp 75.

Foken, T., Leuning, R., Oncley, S.R., Mauder, M., Aubinet, M. (2012b) Corrections and Data Quality Control. In Aubinet, M., Vesala, T., Papale, D., eds. *Eddy Covariance*. Springer Atmospheric Sciences. Springer Netherlands, pp. 133–157.

Foken, T., Skeib, G., Richter, S.H. (1991) Dependence of the integral turbulence characteristics on the stability of stratification and their use for Doppler-Sodar measurements. *Meteorologische Zeitschrift*. **41**.

Foken, T., Wichura, B. (1996) Tools for quality assessment of surface-based flux measurements. *Agricultural and Forest Meteorology*. **78**(1), 83–105.

Fratini, G., Ibrom, A., Arriga, N., Burba, G., Papale, D. (2012) Relative humidity effects on water vapour fluxes measured with closed-path eddy-covariance systems with short sampling lines. *Agricultural & Forest Meteorology*. **165**, 53–63.

Fratini, G., Mauder, M. (2014) Towards a consistent eddy-covariance processing: an intercomparison of EddyPro and TK3. *Atmospheric Measurement Techniques Discussions*. **7**(3), 2107–2126.

Gaffney, J.S., Marley, N.A., Drayton, P.J., Doskey, P.V., Kotamarthi, V.R., Cunningham, M.M., Baird, J.C., Dintaman, J., Hart, H.L. (2002) Field observations of regional and urban impacts on NO2, ozone, UVB, and nitrate radical production rates in the Phoenix air basin. *Atmospheric Environment*. **36**(5), 825–833.

Garratt, J.R. (1980) Surface influence upon vertical profiles in the atmospheric near-surface layer. *Quarterly Journal of the Royal Meteorological Society*. **106**(450), 803–819.

Garratt, J.R. (1994) *The atmospheric boundary layer*. Cambridge university press.
Gioli, B., Toscano, P., Lugato, E., Matese, A., Miglietta, F., Zaldei, A., Vaccari, F.P. (2012) Methane and carbon dioxide fluxes and source partitioning in urban areas: The case study of Florence, Italy. *Environmental Pollution*. **164**, 125–131.

Gill Instruments (2010) Windmaster Pro sonic anemometer user manual (Document no.1561-PS-0001), Lymington, UK.

Goldbach, A., Kuttler, W. (2013) Quantification of turbulent heat fluxes for adaptation strategies within urban planning. *International Journal of Climatology*. **33**(1), 143–159.

Gorbarenko, E.V., Abakumova, G.M. (2011) Radiation balance variations of underlying surface from the long-term observations of the Meteorological Observatory of the Moscow State University. *Russian Meteorology and Hydrology*. **36**(6), 383–391.

Goulden, M.L., Munger, J.W., FAN, S.-M., Daube, B.C., Wofsy, S.C. (1996) Measurements of carbon sequestration by long-term eddy covariance: Methods and a critical evaluation of accuracy. *Global Change Biology*. **2**(3), 169–182.

Grimmond, C.S.B. (1998) Aerodynamic roughness of urban areas derived from wind observations. *Boundary-Layer Meteorology*. **89**(1), 1–24.

Grimmond, C.S.B. (2006) Progress in measuring and observing the urban atmosphere. *Theoretical and Applied Climatology*. **84**(1-3), 3–22.

Grimmond, C.S.B., Christen, A. (2012) Flux measurements in urban ecosystems. *Invited article in Flux-Letter–Newsletter of Fluxnet*. **5**(1), 1–7.

Grimmond, C.S.B., Cleugh, H.A., Oke, T.R. (1991) An objective urban heat storage model and its comparison with other schemes. *Atmospheric Environment. Part B. Urban Atmosphere*. **25**(3), 311–326.

Grimmond, C.S.B., King, T.S., Roth, M., Oke, T.R. (1998) Aerodynamic roughness of urban areas derived from wind observations. *Boundary-Layer Meteorology*. **89**(1), 1–24.

Grimmond, C.S.B., Oke, T.R. (1995) Comparison of heat fluxes from summertime observations in the suburbs of four North American cities.

Grimmond, C.S.B., Oke, T.R. (1999a) Aerodynamic Properties of Urban Areas Derived from Analysis of Surface Form. *Journal of Applied Meteorology*. **38**(9), 1262–1292.

Grimmond, C.S.B., Oke, T.R. (1999b) Heat storage in urban areas: Local-scale observations and evaluation of a simple model. *Journal of Applied Meteorology*. **38**(7), 922–940.

Grimmond, C.S.B., Oke, T.R. (2002) Turbulent heat fluxes in urban areas: Observations and a local-scale urban meteorological parameterization scheme (LUMPS). *Journal of Applied Meteorology*. **41**(7).

Grimmond, C.S.B., Roth, M., Oke, T.R., Au, Y.C., Best, M., Betts, R., Carmichael, G., Cleugh, H., Dabberdt, W., Emmanuel, R., Freitas, E., Fortuniak, K., Hanna, S., Klein, P., Kalkstein, L.S., Liu, C.H., Nickson, A., Pearlmutter, D., Sailor, D., Voogt, J. (2010) Climate and More Sustainable Cities: Climate Information for Improved Planning and Management of Cities (Producers/Capabilities Perspective). *Procedia Environmental Sciences*. **1**, 247–274.

Grimmond, C.S.B., Salmond, J.A., Oke, T.R., Offerle, B., Lemonsu, A. (2004) Flux and turbulence measurements at a densely built-up site in Marseille: Heat, mass (water and carbon dioxide), and momentum. *Journal of Geophysical Research: Atmospheres*. **109**(D24).

Grimmond, C.S.B., Souch, C., Hubble, M.D. (1996) Influence of tree cover on summer-time surface energy balance fluxes, San Gabriel Valley, Los Angeles. *Climate Research*. **6**(1), 45–57.

Ham, J.M., Heilman, J.L. (2003) Experimental test of density and energy-balance corrections on carbon dioxide flux as measured using open-path eddy covariance. *Agronomy Journal*. **95**(6), 1393–1403.

Harman, I.N., Best, M.J., Belcher, S.E. (2004) Radiative exchange in an urban street canyon. *Boundary-Layer Meteorology*. **110**(2), 301–316.

Hartmann, D.L., Tank, A.M.G.K., Rusticucci, M., Alexander, L.V., Brönnimann, S., Charabi, Y., Dentener, F.J., Dlugokencky, E.J., Easterling, D.R., Kaplan, A., Soden, B.J., Thorne, P.W., Wild, M. and Zhai, P.M. (2013) Observations: Atmosphere and Surface. In T. F. Stocker, D. Qin, G. K. Plattner, M. Tignor, S. K. Allen, J. Boschung, A. Nauels, Y. Xia, V. Bex, P. M. Midgl, eds. *Climate Change 2013: The Physical Science Basis. Contribution of Working Group I to the Fifth Assessment Report of the Intergovernmental Panel on Climate Change*. Cambridge, United Kingdom and New York, USA: Cambridge University Press, 159–254.

Helfter, C., Famulari, D., Phillips, G.J., Barlow, J.F., Wood, C.R., Grimmond, C.S.B., Nemitz, E. (2011) Controls of carbon dioxide concentrations and fluxes above central London. *Atmospheric Chemistry and Physics*. **11**(5), 1913–1928.

Heusinkveld, B.G., Jacobs, A.F.G., Holtslag, A.A.M., Berkowicz, S.M. (2004) Surface energy balance closure in an arid region: role of soil heat flux. *Agricultural and Forest Meteorology*. **122**(1), 21–37.

Horst, T.W. (1997) A simple formula for attenuation of eddy fluxes measured with first-order-response scalar sensors. *Boundary-Layer Meteorology*. **82**(2), 219–233.

Horst, T.W., Lenschow, D.H. (2009) Attenuation of scalar fluxes measured with spatially-displaced sensors. *Boundary-Layer Meteorology*. **130**(2), 275–300.

Horst, T.W., Weil, J.C. (1994) How far is far enough?: The fetch requirements for micrometeorological measurement of surface fluxes. *Journal of Atmospheric and Oceanic Technology*. **11**(4), 1018–1025.

Hsieh, C.-I., Katul, G., Chi, T. (2000) An approximate analytical model for footprint estimation of scalar fluxes in thermally stratified atmospheric flows. *Advances in Water Resources*. **23**(7), 765–772.

Hsieh, C.-M., Aramaki, T., Hanaki, K. (2007) Estimation of heat rejection based on the air conditioner use time and its mitigation from buildings in Taipei City. *Building and Environment*. **42**(9), 3125–3137.

Hukseflux Thermal Sensor (2007) Four-component net-radiation sensor manual (NR01) (Version 0816), Delft, The Netherlands.

Hussain, M., Lee, B.E. (1980) A wind tunnel study of the mean pressure forces acting on large groups of low-rise buildings. *Journal of Wind Engineering and Industrial Aerodynamics*. **6**(3-4), 207–225.

Ibrom, A., Dellwik, E., Flyvbjerg, H., Jensen, N.O., Pilegaard, K. (2007) Strong low-pass filtering effects on water vapour flux measurements with closed-path eddy correlation systems. *Agricultural and Forest Meteorology*. **147**(3), 140–156.

Järvi, L., Grimmond, C.S.B., Christen, A. (2011) The surface urban energy and water balance scheme (SUEWS): Evaluation in Los Angeles and Vancouver. *Journal of Hydrology*. **411**(3), 219–237.

Järvi, L., Nordbo, A., Junninen, H., Riikonen, A., Moilanen, J., Nikinmaa, E., Vesala, T. (2012) Seasonal and annual variation of carbon dioxide surface fluxes in Helsinki, Finland, in 2006–2010. *Atmospheric Chemistry and Physics*. **12**(18), 8475–8489.

Järvi, L., Rannik, Ü., Mammarella, I., Sogachev, A., Aalto, P.P., Keronen, P., Siivola, E., Kulmala, M., Vesala, T. (2009) Annual particle flux observations over a heterogeneous urban area. *Atmospheric Chemistry and Physics*. **9**(20), 7847–7856.

Jauregui, E., Luyando, E. (1999) Global radiation attenuation by air pollution and its effects on the thermal climate in Mexico City. *International Journal of Climatology*. **19**(6), 683–694.

Jonsson, P., Eliasson, I., Holmer, B., Grimmond, C.S.B. (2006) Longwave incoming radiation in the Tropics: results from field work in three African cities. *Theoretical and Applied Climatology*. **85**(3-4), 185–201.

Kaimal J.C. and Finnigan J.J. (1994) *Atmospheric Boundary Layer Flows: Their Structure and Measurement*. Oxford: Oxford University Press.

Keogh, S., Mills, G., Fealy, R. (2012) The energy budget of the urban surface: two locations in Dublin. *Irish Geography*. **45**(1), 1–23.

Kipp and Zonen (2013) CMP series instruction manual (Document no. V1311), Delft, The Netherlands.

Kljun, N., Calanca, P., Rotach, M.W., Schmid, H.P. (2004) A simple parameterisation for flux footprint predictions. *Boundary-Layer Meteorology*. **112**(3), 503–523.

Kljun, N., Rotach, M.W., Schmid, H.P. (2002) A three-dimensional backward Lagrangian footprint model for a wide range of boundary-layer stratifications. *Boundary-Layer Meteorology*. **103**(2), 205–226.

Kondo, A., Ueno, M., Kaga, A., Yamaguchi, K. (2001) The influence of urban canopy configuration on urban albedo. *Boundary-Layer Meteorology*. **100**(2), 225–242.

Kordowski, K., Kuttler, W. (2010) Carbon dioxide fluxes over an urban park area. *Atmospheric Environment*. **44**(23), 2722–2730.

Kormann, R., Meixner, F.X. (2001) An Analytical Footprint Model For Non-Neutral Stratification. *Boundary-Layer Meteorology*. **99**(2), 207–224.

Kotthaus, S., Grimmond, C.S.B. (2014a) Energy exchange in a dense urban environment – Part I: Temporal variability of long-term observations in central London. *Urban Climate.* **10**(2), 261-280.

Kotthaus, S., Grimmond, C.S.B. (2014b) Energy exchange in a dense urban environment – Part II: Impact of spatial heterogeneity of the surface. *Urban Climate.* **10**(2), 281-307.

Kotthaus, S., Grimmond, C.S.B. (2012) Identification of Micro-scale Anthropogenic CO2, heat and moisture sources – Processing eddy covariance fluxes for a dense urban environment. *Atmospheric Environment*. **57**, 301–316.

Landsberg, H.E. (1981) *The urban climate*. Academic Press.

Lee, X., Massman, W.J., Law, B.E. (2004) *Handbook of micrometeorology: a guide for surface flux measurement and analysis*. The Netherlands: Springer.

Lemonsu, A., Grimmond, C.S.B., Masson, V. (2004) Modeling the surface energy balance of the core of an old Mediterranean city: Marseille. *Journal of Applied Meteorology*. **43**(2).

Lettau, H. (1969) Note on aerodynamic roughness-parameter estimation on the basis of roughness-element description. *Journal of Applied Meteorology*. **8**(5), 828–832.

Licor Biosciences (2007) Li-7500 CO2/H2O Analyser, Instruction manual, Lincoln, Nebraska (Publication no. 63-09204).

Licor Biosciences (2012) Li-7200 CO2/H2O Analyser, Instruction manual, Lincoln, Nebraska (Publication no. 984-10564).

Licor Biosciences (2015) *Licor Environmental Home: Eddy Covariance Systems – Eddy Pro.* Available at: http://www.licor.com/env/products/eddy_covariance/eddypro.html (accessed 30 June 2015).

Lietzke, B., Vogt, R. (2013) Variability of CO2 concentrations and fluxes in and above an urban street canyon. *Atmospheric Environment*. **74**, 60–72.

Liu, H., Peters, G., Foken, T. (2001) New equations for sonic temperature variance and buoyancy heat flux with an omnidirectional sonic anemometer. *Boundary-Layer Meteorology*. **100**(3), 459–468.

Liu, H.Z., Feng, J.W., Järvi, L., Vesala, T. (2012) Four-year (2006–2009) eddy covariance measurements of CO 2 flux over an urban area in Beijing. *Atmospheric Chemistry and Physics*. **12**(17), 7881–7892.

Loridan, T., Grimmond, C.S.B. (2012) Characterization of energy flux partitioning in urban environments: links with surface seasonal properties. *Journal of Applied Meteorology and Climatology*. **51**(2), 219–241.

Macdonald, R.W., Griffiths, R.F., Hall, D.J. (1998) An improved method for the estimation of surface roughness of obstacle arrays. *Atmospheric Environment*. **32**(11), 1857–1864.

Mammarella, I., Launiainen, S., Gronholm, T., Keronen, P., Pumpanen, J., Rannik, Ü., Vesala, T. (2009) Relative humidity effect on the high-frequency attenuation of water vapor flux measured by a closed-path eddy covariance system. *Journal of Atmospheric and Oceanic Technology*. **26**(9), 1856–1866.

Martilli, A., Clappier, A., Rotach, M.W. (2002) An urban surface exchange parameterisation for mesoscale models. *Boundary-Layer Meteorology*. **104**(2), 261–304.

Massman, W., Clement, R. (2004) Uncertainty in eddy covariance flux estimates resulting from spectral attenuation. In Lee, X., Massman, W.J., Law, B.E. eds. *Handbook of micrometeorology*. Springer, pp. 67-99.

Masson, V. (2000) A physically-based scheme for the urban energy budget in atmospheric models. *Boundary-Layer Meteorology*. **94**(3), 357–397.

Matese, A., Gioli, B., Vaccari, F.P., Zaldei, A., Miglietta, F. (2009) Carbon dioxide emissions of the city center of Firenze, Italy: measurement, evaluation, and source partitioning. *Journal of Applied Meteorology and Climatology*. **48**(9), 1940–1947.

Mathsworks, (2015) *Regstats regression diagnostics*. Available at: http://uk.mathworks.com/help/stats/regstats.html?s_tid=srchtitle (accessed 23 June 2015).

Mauder, M., Foken, T. (2004) *Documentation and instruction manual of the Eddy-Covariance software package TK2*. Univ., Abt. Mikrometeorologie.

Mauder, M., Foken, T. (2011) *Documentation and instruction manual of the Eddy-Covariance software package TK3*. Univ., Abt. Mikrometeorologie.

Mauder, M., Foken, T., Clement, R., Elbers, J.A., Eugster, W., Grünwald, T., Heusinkveld, B., Kolle, O. (2008) Quality control of CarboEurope flux data–Part 2: Inter-comparison of eddy-covariance software. *Biogeosciences*. **5**(2).

Mauder, M., Jegede, O.O., Okogbue, E.C., Wimmer, F., Foken, T. (2007a) Surface energy balance measurements at a tropical site in West Africa during the transition from dry to wet season. *Theoretical and Applied Climatology*. **89**(3-4), 171–183.

Mauder, M., Oncley, S.P., Vogt, R., Weidinger, T., Ribeiro, L., Bernhofer, C., Foken, T., Kohsiek, W., De Bruin, H.A.R., Heping Liu (2007b) The energy balance experiment EBEX-2000. Part II: Intercomparison of eddy-covariance sensors and post-field data processing methods. *Boundary-Layer Meteorology*. **123**(1), 29–54.

Mauder, M., Cuntz, M., Drüe, C., Graf, A., Rebmann, C., Schmid, H.P., Schmidt, M., Steinbrecher, R. (2013) A strategy for quality and uncertainty assessment of long-term eddy-covariance measurements. *Agricultural & Forest Meteorology*. **169**, 122–135.

McCarthy, M.P., Best, M.J., Betts, R.A. (2010) Climate change in cities due to global warming and urban effects. *Geophysical Research Letters*. **37**(9).

Meagher, J.F., Cowling, E.B., Fehsenfeld, F.C., Parkhurst, W.J. (1998) Ozone formation and transport in southeastern United States: overview of the SOS Nashville/Middle Tennessee ozone study. *Journal of Geophysical Research: Atmospheres (1984–2012)*. **103**(D17), 22213–22223.

Menut, L., Vautard, R., Flamant, C., Abonnel, C., Beekmann, M., Chazette, P., Flamant, P.H., Gombert, D., Guédalia, D., Kley, D., others (2000) Measurements and modelling of atmospheric pollution over the Paris area: an overview of the ESQUIF Project. In *Annales Geophysicae*. Springer, pp. 1467–1481.

Mestayer, P.G., Durand, P., Augustin, P., Bastin, S., Bonnefond, J.-M., Bénech, B., Campistron, B., Coppalle, A., Delbarre, H., Dousset, B., others (2005) The urban boundary-layer field campaign in Marseille (UBL/CLU-ESCOMPTE): set-up and first results. *Boundary-Layer Meteorology*. **114**(2), 315–365.

Met Éireann, (2010) *Met Éireann Monthly Weather Bulletin*, Dublin, 288, April 2010, 1-16.

Met Éireann, (2010) *Met Éireann Monthly Weather Bulletin*, Dublin, 290, June 2010, 1-16.

Met Éireann, (2010) *Met Éireann Monthly Weather Bulletin*, Dublin, 295, November 2010, 1-16.

Met Éireann, (2010) *Met Éireann Monthly Weather Bulletin*, Dublin, 296, December 2010, 1-16.

Met Éireann, (2010) *Met Éireann Climate Annual 2010*, Dublin, 1-28.

Met Éireann, (2011) *Met Éireann Climate Annual 2011*, Dublin, 1-28.

Met Éireann, (2012) *Met Éireann Climate Annual 2012*, Dublin, 1-28.

Met Éireann, (2012) *Met Éireann Monthly Weather Bulletin*, Dublin, 314, June 2012, 1-16.

Mills, G. (2006) Progress toward sustainable settlements: a role for urban climatology. *Theoretical and Applied Climatology*. **84**(1-3), 69–76.

Mills, G. (2007) Cities as agents of global change. *International Journal of Climatology*. **27**(14), 1849–1857.

Mills, G. (2008) Luke Howard and The Climate of London. *Weather*. **63**(6), 153–157.
Moncrieff, J.B., Massheder, J.M., De Bruin, H., Elbers, J., Friborg, T., Heusinkveld, B., Kabat, P., Scott, S., Søgaard, H., Verhoef, A. (1997) A system to measure surface fluxes of momentum, sensible heat, water vapour and carbon dioxide. *Journal of Hydrology*. **188**, 589–611.

Moncrieff, J., Clement, R., Finnigan, J., Meyers, T. (2004) Averaging, detrending, and filtering of eddy covariance time series. In Lee, X., Massman, W.J., Law, B.E. eds. *Handbook of micrometeorology*. Springer, pp. 7–31.

Moore, C.J. (1986) Frequency response corrections for eddy correlation systems. *Boundary-Layer Meteorology*. **37**(1-2), 17–35.

Moriwaki, R., Kanda, M. (2004) Seasonal and diurnal fluxes of radiation, heat, water vapor, and carbon dioxide over a suburban area. *Journal of Applied Meteorology*. **43**(11), 1700–1710.

Munger, J.W., Loescher, H.W., Luo, H. (2012) Measurement, Tower, and Site Design Considerations. In M. Aubinet, T. Vesala, & D. Papale, eds. *Eddy Covariance*. Springer Atmospheric Sciences. Springer Netherlands, pp. 21–58.

Nakai, T., Van Der Molen, M.K., Gash, J.H.C., Kodama, Y. (2006) Correction of sonic anemometer angle of attack errors. *Agricultural and Forest Meteorology*. **136**(1), 19–30.

Nakai, T., Iwata, H., Harazono, Y. (2011) Importance of mixing ratio for a long-term CO2 flux measurement with a closed-path system. *Tellus B*. **63**(3), 302–308.

Nakai, T., Shimoyama, K. (2012) Ultrasonic anemometer angle of attack errors under turbulent conditions. *Agricultural and Forest Meteorology*. **162**, 14–26.

Narita, K., Sekine, T., Tokuoka, T. (1984) Thermal properties of urban surface materials: Study on heat balance at asphalt pavement. *Geographical Review of Japan*. **57**, 639–651.

Nemitz, E., Gallagher, M.W., Duyzer, J.H., Fowler, D. (2002) Micrometeorological measurements of particle deposition velocities to moorland vegetation. *Quarterly Journal of the Royal Meteorological Society*. **128**(585), 2281–2300.

Newton, T., Oke, T.R., Grimmond, C.S.B., Roth, M. (2007) The suburban energy balance in Miami, Florida. *Geografiska Annaler: Series A, Physical Geography*. **89**(4), 331–347.

Ng, E., Yuan, C., Chen, L., Ren, C., Fung, J.C.H. (2011) Improving the wind environment in high-density cities by understanding urban morphology and surface roughness: A study in Hong Kong. *Landscape and Urban Planning*. **101**(1), 59–74.

Ningal, T., Mills, G., Smithwick, P. (2010) An inventory of trees in Dublin city centre. *Irish Geography*. **43**(2), 161–176.

Nordbo, A., Järvi, L., Vesala, T. (2012) Revised eddy covariance flux calculation methodologies–effect on urban energy balance. *Tellus B*. **64**.

Nordbo, A., Järvi, L., Haapanala, S., Moilanen, J., Vesala, T. (2013) Intra-City Variation in Urban Morphology and Turbulence Structure in Helsinki, Finland. *Boundary-Layer Meteorology*. **146**(3), 469–496.

Nunez, M., Eliasson, I., Lindgren, J. (2000) Spatial variations of incoming longwave radiationin Göteborg, Sweden. *Theoretical and Applied Climatology*. **67**(3-4), 181–192.

Nunez, M., Oke, T.R. (1977) The Energy Balance of an Urban Canyon. *Journal of Applied Meteorology*. **16**(1), 11–19.

Oda, T., Maksyutov, S. (2011) A very high-resolution (1 km X 1 km) global fossil fuel CO2 emission inventory derived using a point source database and satellite observations of nighttime lights. *Atmospheric Chemistry and Physics*. **11**(2), 543–556.

Offerle, B., Grimmond, C.S.B., Fortuniak, K. (2005b) Heat storage and anthropogenic heat flux in relation to the energy balance of a central European city centre. *International Journal of Climatology*. **25**(10), 1405–1419.

Offerle, B., Grimmond, C.S.B., Fortuniak, K., Kłysik, K., Oke, T.R. (2006b) Temporal variations in heat fluxes over a central European city centre. *Theoretical and Applied Climatology*. **84**(1-3), 103–115.

Offerle, B., Grimmond, C.S.B., Fortuniak, K., Pawlak, W. (2006a) Intraurban differences of surface energy fluxes in a central European city. *Journal of Applied Meteorology and Climatology*. **45**(1), 125–136.

Offerle, B., Grimmond, C.S.B., Oke, T.R. (2003) Parameterization of net all-wave radiation for urban areas. *Journal of Applied Meteorology*. **42**(8), 1157–1173.

Offerle, B., Jonsson, P., Eliasson, I., Grimmond, C.S.B. (2005a) Urban modification of the surface energy balance in the West African Sahel: Ouagadougou, Burkina Faso. *Journal of Climate*. **18**(19).

Ohashi, Y., Genchi, Y., Kondo, H., Kikegawa, Y., Yoshikado, H., Hirano, Y. (2007) Influence of air-conditioning waste heat on air temperature in Tokyo during summer: numerical experiments using an urban canopy model coupled with a building energy model. *Journal of Applied Meteorology and Climatology*. **46**(1), 66–81.

Oikawa, S., Meng, Y. (1995) Turbulence characteristics and organized motion in a suburban roughness sublayer. *Boundary-Layer Meteorology*. **74**(3), 289–312.

Oke, T.R. (1974) *Review of urban climatology 1968-1973*. Technical Note No. 134, World Meteorological Organization Geneva.

Oke, T.R. (1979) *Review of urban climatology, 1973-1976*. Technical Note No. 539, World Meteorological Organization Geneva.

Oke, T.R. (1987) *Boundary Layer Climates*. Second Edition. London: Routledge.

Oke, T.R. (1988a) Street design and urban canopy layer climate. *Energy and Buildings*. **11**(1-3), 103–113.

Oke, T.R. (1988b) The urban energy balance. *Progress in Physical Geography*. **12**(4), 471–508.

Oke, T.R. (1995) The Heat Island of the Urban Boundary Layer: Characteristics, Causes and Effects. In J. E. Cermak, A. G. Davenport, E. J. Plate, & D. X. Viegas, eds. *Wind Climate in Cities*. NATO ASI Series. Springer Netherlands, pp. 81–107.

Oke, T.R. (2004) *Initial guidance to obtain representative meteorological observations at urban sites*. World Meteorological Organization Geneva.

Oke, T.R. (2006) Towards better scientific communication in urban climate. *Theoretical and Applied Climatology*. **84**(1-3), 179–190.

Oke, T.R. (2007) Siting and Exposure of Meteorological Instruments at Urban Sites. In Borrego, C., Norman, A.L., eds. *Air Pollution Modeling and Its Application XVII*. Springer US, pp. 615–631.

Oke, T.R., Cleugh, H.A. (1987) Urban heat storage derived as energy balance residuals. *Boundary-Layer Meteorology*. **39**(3), 233–245.

Oke, T.R., Kalanda, B.D., Steyn, D.G. (1981) Parameterization of heat storage in urban areas. *Urban Ecology*. **5**(1), 45–54.

Oleson, K.W., Bonan, G.B., Feddema, J., Vertenstein, M., Grimmond, C.S.B. (2008) An urban parameterization for a global climate model. Part I: Formulation and evaluation for two cities. *Journal of Applied Meteorology and Climatology*. **47**(4), 1038–1060.

Park, M.-S., Joo, S.J., Lee, C.S. (2013) Effects of an urban park and residential area on the atmospheric CO2 concentration and flux in Seoul, Korea. *Advances in Atmospheric Sciences*. **30**(2), 503–514.

Parlow, E. (2003) The urban heat budget derived from satellite data. *Geographica Helvetica*. **58**(2), 99–111.

Pawlak, W., Fortuniak, K., Siedlecki, M. (2011) Carbon dioxide flux in the centre of Łódź, Poland—analysis of a 2-year eddy covariance measurement data set. *International Journal of Climatology*. **31**(2), 232–243.

Pearcy, R.W. (1989) Radiation and light measurements. In R. W. Pearcy, J. R. Ehleringer, H. A. Mooney, & P. W. Rundel, eds. *Plant Physiological Ecology*. Springer Netherlands, pp. 97–116.

Pearlmutter, D., Berliner, P., Shaviv, E. (2005) Evaluation of urban surface energy fluxes using an open-air scale model. *Journal of Applied Meteorology*. **44**(4), 532–545.

Piringer, M., Grimmond, C.S.B., Joffre, S.M., Mestayer, P., Middleton, D.R., Rotach, M.W., Baklanov, A., Ridder, K.D., Ferreira, J., Guilloteau, E., Karppinen, A., Martilli, A., Masson, V., Tombrou, M. (2002) Investigating the surface energy balance in urban areas – recent advances and future needs. *Water, Air and Soil Pollution: Focus*. **2**(5-6), 1–16.

Piringer, M., Joffre, S., Baklanov, A., Christen, A., Deserti, M., Ridder, K.D., Emeis, S., Mestayer, P., Tombrou, M., Middleton, D., Baumann-Stanzer, K., Dandou, A.,

Karppinen, A., Burzynski, J. (2007) The surface energy balance and the mixing height in urban areas—activities and recommendations of COST-Action 715. *Boundary-Layer Meteorology*. **124**(1), 3–24.

Ramamurthy, P., Pardyjak, E.R. (2011) Toward understanding the behavior of carbon dioxide and surface energy fluxes in the urbanized semi-arid Salt Lake Valley, Utah, USA. *Atmospheric Environment*. **45**(1), 73–84.

Rannik, Ü., Sogachev, A., Foken, T., Göckede, M., Kljun, N., Leclerc, M.Y., Vesala, T. (2012) Footprint Analysis. In M. Aubinet, T. Vesala, & D. Papale, eds. *Eddy Covariance*. Springer Atmospheric Sciences. Springer Netherlands, pp. 211–261.

Roberts, S.M. (2010) *Three-dimensional radiation flux source areas in urban areas*. Vancouver: University of British Columbia. Ph.D. thesis, The University of British Columbia, Vancouver, Canada, 214 pp.

Roberts, S.M., Oke, T.R., Grimmond, C.S.B., Voogt, J.A. (2006) Comparison of four methods to estimate urban heat storage. *Journal of Applied Meteorology and Climatology*. **45**(12), 1766–1781.

Robine, J.-M., Cheung, S.L.K., Le Roy, S., Van Oyen, H., Griffiths, C., Michel, J.-P., Herrmann, F.R. (2008) Death toll exceeded 70,000 in Europe during the summer of 2003. *Comptes Rendus Biologies*. **331**(2), 171–178.

Rotach, M.W. (1999) On the influence of the urban roughness sublayer on turbulence and dispersion. *Atmospheric Environment*. **33**(24), 4001–4008.

Rotach, M.W. (1995) Profiles of turbulence statistics in and above an urban street canyon. *Atmospheric Environment*. **29**(13), 1473–1486.

Rotach, M.W. (2001) Simulation of urban-scale dispersion using a Lagrangian stochastic dispersion model. *Boundary-Layer Meteorology*. **99**(3), 379–410.

Rotach, M.W., Vogt, R., Bernhofer, C., Batchvarova, E., Christen, A., Clappier, A., Feddersen, B., Gryning, S.-E., Martucci, G., Mayer, H., Mitev, V., Oke, T.R., Parlow, E., Richner, H., Roth, M., Roulet, Y.-A., Ruffieux, D., Salmond, J.A., Schatzmann, M., Voogt, J.A. (2005) BUBBLE – an Urban Boundary Layer Meteorology Project. *Theoretical and Applied Climatology*. **81**(3-4), 231–261.

Roth, M. (2000) Review of atmospheric turbulence over cities. *Quarterly Journal of the Royal Meteorological Society*. **126**(564), 941–990.

Roth, M. (2007) Review of urban climate research in (sub)tropical regions. *International Journal of Climatology*. **27**(14), 1859–1873.

Roth, M., Oke, T.R. (1994) Comparison of modelled and "measured" heat storage in suburban terrain. *Contributions to Atmospheric Physics*, **67**, 149-156.

Sailor, D.J. (2011) A review of methods for estimating anthropogenic heat and moisture emissions in the urban environment. *International Journal of Climatology*. **31**(2), 189–199.

Sailor, D.J., Lu, L. (2004) A top–down methodology for developing diurnal and seasonal anthropogenic heating profiles for urban areas. *Atmospheric Environment*. **38**(17), 2737–2748.

Sánchez, J.M., Caselles, V., Rubio, E.M. (2010) Analysis of the energy balance closure over a FLUXNET boreal forest in Finland. *Hydrology and Earth System Sciences*. **14**(8), 1487–1497.

Schmid, H.P. (1994) Source areas for scalars and scalar fluxes. *Boundary-Layer Meteorology*. **67**(3), 293–318.

Schmid, H.P., Cleugh, H.A., Grimmond, C.S.B., Oke, T.R. (1991) Spatial variability of energy fluxes in suburban terrain. *Boundary-Layer Meteorology*. **54**(3), 249–276.

Schotanus, P., Nieuwstadt, F.T.M., De Bruin, H.A.R. (1983) Temperature measurement with a sonic anemometer and its application to heat and moisture fluxes. *Boundary-Layer Meteorology*. **26**(1), 81–93.

Schuepp, P.H., Leclerc, M.Y., MacPherson, J.I., Desjardins, R.L. (1990) Footprint prediction of scalar fluxes from analytical solutions of the diffusion equation. *Boundary-Layer Meteorology*. **50**(1-4), 355–373.

Sogachev, A., Menzhulin, G.V., Heimann, M., Lloyd, J. (2002) A simple three-dimensional canopy–planetary boundary layer simulation model for scalar concentrations and fluxes. *Tellus B*, **54**(5), 784–819.

Skye Instruments (2007) Photosynthetic active radiation sensor (SKP 215), Powys, UK.

Soegaard, H., Møller-Jensen, L. (2003) Towards a spatial CO_2 budget of a metropolitan region based on textural image classification and flux measurements. *Remote Sensing of Environment*. **87**(2), 283–294.

Song, T., Wang, Y. (2012) Carbon dioxide fluxes from an urban area in Beijing. *Atmospheric Research*. **106**, 139–149.

Souch, C., Grimmond, C.S.B., Wolfe, C.P. (1998) Evapotranspiration rates from wetlands with different disturbance histories: Indiana Dunes National Lakeshore. *Wetlands*. **18**(2), 216–229.

Spronken-Smith, R.A. (2002) Comparison of summer-and winter-time suburban energy fluxes in Christchurch, New Zealand. *International Journal of Climatology*. **22**(8), 979–992.

Spronken-Smith, R.A., Oke, T.R. (1998) The thermal regime of urban parks in two cities with different summer climates. *International Journal of Remote Sensing*. **19**(11), 2085–2104.

Stewart, I.D. (2011) A systematic review and scientific critique of methodology in modern urban heat island literature. *International Journal of Climatology*. **31**(2), 200–217.

Stewart, I.D., Oke, T. (2009) Classifying urban climate field sites by 'local climate zones': The case of Nagano, Japan. In *Seventh International Conference on Urban Climate*.

Stewart, I.D., Oke, T.R. (2012) Local Climate Zones for Urban Temperature Studies. *Bulletin of the American Meteorological Society*. **93**(12), 1879–1900.

Steyn, D.G., Bottenheim, J.W., Thomson, R.B. (1997) Overview of tropospheric ozone in the Lower Fraser Valley, and the Pacific'93 field study. *Atmospheric Environment*. **31**(14), 2025–2035.

Stoy, P.C., Mauder, M., Foken, T., Marcolla, B., Boegh, E., Ibrom, A., Arain, M.A., Arneth, A., Aurela, M., Bernhofer, C., Cescatti, A., Dellwik, E., Duce, P., Gianelle, D., van Gorsel, E., Kiely, G., Knohl, A., Margolis, H., McCaughey, H., Merbold, L., Montagnani, L., Papale, D., Reichstein, M., Saunders, M., Serrano-Ortiz, P., Sottocornola, M., Spano, D., Vaccari, F., Varlagin, A. (2013) A data-driven analysis of energy balance closure across FLUXNET research sites: The role of landscape scale heterogeneity. *Agricultural and Forest Meteorology*. **171–172**, 137–152.

Stull, R. B. (1988) *An Introduction to Boundary Layer Meteorology*. London: Kluwer Academic Publishers.

Sutton, O. G. (1953) *A study of physical processes in the lowest layers of the Earth's atmosphere*. London: McGraw-Hill.

Svensson, M.K. (2004) Sky view factor analysis–implications for urban air temperature differences. *Meteorological Applications*. **11**(03), 201–211.

Svirejeva-Hopkins, A., Schellnhuber, H.J., Pomaz, V.L. (2004) Urbanised territories as a specific component of the Global Carbon Cycle. *Ecological Modelling*. **173**(2), 295–312.

Taesler, R. (1980) *Studies of the development and thermal structure of the urban boundary layer in Uppsala*. Meteorologiska Institutionen.

Taha, H. (1997) Urban climates and heat islands: albedo, evapotranspiration, and anthropogenic heat. *Energy and Buildings*. **25**(2), 99–103.

Tapper, N.J. (1984) Prediction of the downward flux of atmospheric radiation in a polluted urban environment. *Australian Meteorological Magazine*. **32**(2).

Terjung, W.H., Louie, S.S.-F. (1973) Solar radiation and urban heat islands. *Annals of the Association of American Geographers*. **63**(2), 181–207.

Thomas, C., Foken, T. (2002) Re-evaluation of integral turbulence characteristics and their parameterisations. In 15th Symposium on Boundary Layers and Turbulence. American Meteorological Society.

Turnipseed, A.A., Blanken, P.D., Anderson, D.E., Monson, R.K. (2002a) Energy budget above a high-elevation subalpine forest in complex topography. *Agricultural and Forest Meteorology*. **110**(3), 177–201.

Turnipseed, A.A., Blanken, P.D., Anderson, D.E., Monson, R.K. (2002b) Energy budget above a high-elevation subalpine forest in complex topography. *Agricultural and Forest Meteorology*. **110**(3), 177–201.

United Nations (2014) *World Urbanization Prospects: The 2014 Revision, Highlights*. United Nations, New York.

Van der Hoven, I. (1957) Power spectrum of horizontal wind speed in the frequency range from 0.0007 to 900 cycles per hour. *Journal of Meteorology*. **14**(2), 160–164.

Velasco, E., Pressley, S., Allwine, E., Westberg, H., Lamb, B. (2005) Measurements of CO2 fluxes from the Mexico City urban landscape. *Atmospheric Environment*. **39**(38), 7433–7446.

Velasco, E., Pressley, S., Grivicke, R., Allwine, E., Coons, T., Foster, W., Jobson, B.T., Westberg, H., Ramos, R., Hernández, F., others (2009) Eddy covariance flux measurements of pollutant gases in urban Mexico City. *Atmospheric Chemistry and Physics*. **9**(19), 7325–7342.

Velasco, E., Roth, M. (2010) Cities as net sources of CO2: Review of atmospheric CO2 exchange in urban environments measured by eddy covariance technique. *Geography Compass*. **4**(9), 1238–1259.

Vesala, T., Kljun, N., Rannik, Ü., Rinne, J., Sogachev, A., Markkanen, T., Sabelfeld, K., Foken, T., Leclerc, M.Y. (2008) Flux and concentration footprint modelling: State of the art. *Environmental Pollution*. **152**(3), 653–666.

Vickers, D., Mahrt, L. (1997) Quality control and flux sampling problems for tower and aircraft data. *Journal of Atmospheric and Oceanic Technology*. **14**(3), 512–526.

Vogt, R., Christen, A., Rotach, M.W., Roth, M., Satyanarayana, A.N.V. (2006) Temporal dynamics of CO2 fluxes and profiles over a Central European city. *Theoretical and Applied Climatology*. **84**(1-3), 117–126.

Voogt, J.A., Oke, T.R. (2003) Thermal remote sensing of urban climates. *Remote Sensing of Environment*. **86**(3), 370–384.

Ward, H.C., Evans, J.G., Grimmond, C.S.B. (2013) Multi-season eddy covariance observations of energy, water and carbon fluxes over a suburban area in Swindon, UK. *Atmospheric Chemistry and Physics*. **13**(9), 4645–4666.

Ward, H.C., Evans, J.G., Grimmond, C.S.B. (2014) Multi-scale sensible heat fluxes in the suburban environment from large-aperture scintillometry and eddy covariance. *Boundary-Layer Meteorology*. **152**(1), 65–89.

Waterra (2012) Aerodynamic rain gauge (ARG 100) instruction manual, Solihull, UK.

Webb, E.K., Pearman, G.I., Leuning, R. (1980) Correction of flux measurements for density effects due to heat and water vapour transfer. *Quarterly Journal of the Royal Meteorological Society*. **106**(447), 85–100.

Weber, S., Kordowski, K. (2010) Comparison of atmospheric turbulence characteristics and turbulent fluxes from two urban sites in Essen, Germany. *Theoretical and Applied Climatology*. **102**(1-2), 61–74.

Weissert, L.F., Salmond, J.A., Schwendenmann, L. (2014) A review of the current progress in quantifying the potential of urban forests to mitigate urban CO2 emissions. *Urban Climate*. **8**, 100–125.

White, J.M., Eaton, F.D., Auer Jr, A.H. (1978) The net radiation budget of the St. Louis metropolitan area. *Journal of Applied Meteorology*. **17**(5), 593–599.

Wilczak, J.M., Oncley, S.P., Stage, S.A. (2001) Sonic Anemometer Tilt Correction Algorithms. *Boundary-Layer Meteorology*. **99**(1), 127–150.

Wilks, D.S. (2011) *Statistical Methods in the Atmospheric Sciences.* Third Edition. Oxford: Academic Press.

Wilson, K., Goldstein, A., Falge, E., Aubinet, M., Baldocchi, D., Berbigier, P., Bernhofer, C., Ceulemans, R., Dolman, H., Field, C. (2002) Energy balance closure at FLUXNET sites. *Agricultural and Forest Meteorology*. **113**(1), 223–243.

Wood, C.R., Lacser, A., Barlow, J.F., Padhra, A., Belcher, S.E., Nemitz, E., Helfter, C., Famulari, D., Grimmond, C.S.B. (2010) Turbulent flow at 190 m height above london during 2006–2008: A climatology and the applicability of similarity theory. *Boundary-Layer Meteorology*. **137**(1), 77–96.

World Bank, 2015 CO_2 emissions (metric ton per capita) 2011-2014.Available at: http://data.worldbank.org/ (accessed 30 June 2015).

Yaghoobian, N., Kleissl, J., Krayenhoff, S.E. (2010) Modeling the Thermal Effects of Artificial Turf on the Urban Environment. *Journal of Applied Meteorology and Climatology*. **49**(3), 332–345.

Yap, D. H., 1973: Sensible heat fluxes in and near Vancouver, B.C. Ph.D. thesis, The University of British Columbia, Vancouver, Canada, 177 pp.

Yoshida, A., Tominaga, K., Watatani, S. (1991) Field measurements on energy balance of an urban canyon in the summer season. *Energy and Buildings*. **15**(3), 417–42.

APPENDIX I

Data storage and retrieval methods

Voltage output signals are converted to a physical number via software installed on the data loggers hence nominal conversion is not necessary in subsequent data processing. Data is recorded on site via Campbell Scientific data loggers, models CR3000 and CR1000. Data is stored on compact flash drives in three separate binary files before being converted to table-oriented ASCII format (TOA5) using Campbell Scientific's LoggerNet conversion software. The data files are as follows:

1) TOA5_XXXX_cr1000.dat
2) TOA5_XXXX_flux.dat
3) TOA5_XXXX_ts.data.dat

Where XXXX is a four digit number corresponding to the EC station number. Data file 1 from the CR1000 data contains one hour totals of measurements from the rain gauge, one hour averages the PAR sensor and the global radiation sensor for the suburban site and urban site 1. Data file 2 contains preliminary half hourly fluxes calculated on site via the data logger. In addition the file contains half hourly diagnostics from the both the CSAT3 and Li7500 and half hourly averaged air temperature, relative humidity, and net radiation data. Data file 3 contains 10 Hz data from the CSAT3 (wind velocities in the u, v and w directions), sonic derived air temperature (Ts), mass densities of CO_2 and H_2O, pressure from the Li7500 and ambient air temperature from the HMP45C. Fast response air temperature data from a finewire thermocouple (FW05), located within the sonic measurement path was initially available at the time of instrument deployment in September 2009, however due to instrument failure observations are not available for the remainder of the study. When the 10 Hz data is converted to ASCII format the data file must be split into smaller files so that processing can be achieved in EC software. The data is split into half-hourly files. Within most EC software filename convention requires date and time stamps in each filename. The files are therefore named as follows:

TOA5_XXXX-YYYY_MM_DD_hhmm.dat

Where TOA5 refers to Table Oriented ASCII file format version 5, XXXX refers to station number, YYYY is Year, MM is month of year, DD is day of month, hh is hour of day, mm is minute of hour. Each file has no header lines, values are comma separated, and each comprises of 18,000 rows and 13 columns. Columns one to four contain timestamp information, column five contains the record number logged by the CR3000, columns six, seven, and eight contain wind velocity measurements in the u_x, u_y, and u_z direction and the sonic temperature is reported in column nine. The Li7500 measurements are reported in columns 10 and 11 and the instrument derived pressure measurements are reported in column 13. Finally column 12 contains ambient absolute air temperature from the PRT. The column originally storing fast response air temperature measurements from the finewire thermocouple, now reported as missing values or NaNs, are removed from the split data files. At this time all other values assigned by the data logger as NaNs are replaced with -999 for ingestion into EC software.

APPENDIX II

Table II.1 Despiking algorithm parameters as described in the original paper by Vickers and Mahrt (1997), and their implementation in the software

Despiking Algorithm	Vickers and Mahrt (1997)	EddyPro Vickers and Mahrt (1997)	EddyUH Vickers and Mahrt (1997)	TK3.1 Mauder et al. (2013)
Window size in data points [1]	3000	3000	3000	18000*
Movement of the window in data points	1	1500 *	400 *	None*
Measure of central tendency	Mean (μ)	Mean (μ)	Mean (μ)	Median
Measure of dispersion	Standard deviation (σ)	Standard deviation (σ)	Standard deviation (σ)	Median absolute deviation
Initial multiplier of σ	3.5	3.5	3.5 (5 for vertical wind velocity)	7
Multiplication factor of σ	0.1	Unknown*	0.3*	N/A
Number of consecutive spikes permitted	3	3	3	3
Replacement of spike	LI	EV or LI	LI*	EV,LV or LI
Enumeration of a spike event (SE)	1 spike = 1 SE 3 consecutive spikes = 1 SE	1spike = 1 SE 3 consecutive spikes = 1 SE	1 spike = 1 SE 3 consecutive spikes = 3 SEs	1 spike = 1 SE 3 consecutive spikes = 1 SE
Number of iterations	Until no more spikes are detected	Up to 20	Up to 4	None
Threshold percentage of spikes	1	1	1	1
Number of spikes per variable given in an output file	-	Yes	Yes	No

[1]= per 30 minute interval according to 10Hz data frequency
* = software user is not capable of changing the parameter/selection (i.e. not user settable)
N/A = not applicable
Linear interpolation (LI), error value (EV), last value (LV)